Development of Sulfonated Poly(Ether Ether Ketone) Polymer-Based Solid Polymer Electrolyte Membranes for Fuel Cell Application

By
MAMTA KUMARI
CHEM01201304012

Bhabha Atomic Research Centre

A thesis submitted to the

Board of Studies in Chemical Sciences

In partial fulfillment of requirements
for the Degree of

DOCTOR OF PHILOSOPHY

of

HOMI BHABHA NATIONAL INSTITUTE

November, 2018

Homi Bhabha National Institute

Recommendations of the Viva Voce Committee

As members of the Viva Voce Committee, we certify that we have read the dissertation prepared by **Ms. Mamta Kumari** titled **"Development of Sulfonated Poly(Ether Ether Ketone) Polymer-Based Solid Polymer Electrolyte Membranes for Fuel Cell Application"** and recommend that it may be accepted as fulfilling the thesis requirement for the award of Degree of Doctor of Philosophy.

Chairman – Prof Manmohan Kumar Manmohan Kumar **Date:** 06/11/2018

Guide / Convener – Prof R.C. Bindal **Date:** 06/11/18

Examiner – Prof. Neetu Jha Neetu Jha **Date:** 6 Nov 2018

Co-guide & Member 1 - Prof H.S. Sodaye **Date:** 06/11/2018

Member 2- Prof Y.K. Bhardwaj **Date:** 06/11/18

Member 3- Prof A.K. Pandey Pandey **Date:** 6.11.2018

Technology Advisor & Member 4 - Prof. A.K. Satpati **Date:** 06/11/18

Final approval and acceptance of this thesis is contingent upon the candidate's submission of the final copies of the thesis to HBNI.

I/We hereby certify that I/we have read this thesis prepared under my/our direction and recommend that it may be accepted as fulfilling the thesis requirement.

Date: 06/11/2018

Place: Mumbai

(Prof. H. S. Sodaye)
Co-Guide

(Prof. R. C. Bindal)
Guide

STATEMENT BY AUTHOR

This dissertation titled "**Development of Sulfonated Poly(Ether Ether Ketone) Polymer-Based Solid Polymer Electrolytes Membranes for Fuel Cell Application**" has been submitted in partial fulfillment of requirements for an advanced degree at Homi Bhabha National Institute (HBNI) and is deposited in the Library to be made available to borrowers under rules of the HBNI.

Brief quotations from this dissertation are allowable without special permission, provided that accurate acknowledgement of source is made. Requests for permission for extended quotation from or reproduction of this manuscript in whole or in part may be granted by the Competent Authority of HBNI when in his or her judgment the proposed use of the material is in the interests of scholarship. In all other instances, however, permission must be obtained from the author.

Mamta Kumari
06/11/2018
(Mamta Kumari)

DECLARATION

I, hereby declare that the investigation presented in the thesis titled "**Development of Sulfonated Poly(Ether Ether Ketone) Polymer-Based Solid Polymer Electrolytes Membranes for Fuel Cell Application**" has been carried out by me. The work is original and has not been submitted earlier as a whole or in part for a degree / diploma at this or any other Institution / University.

Mamta Kumari
06/11/2018
(Mamta Kumari)

List of Publications arising from the thesis

Publications in Refereed Journal:

a. Published

1. **"**Properties and morphology studies of proton exchange membranes based on cross-linked sulfonated poly (ether ether ketone) for electrochemical application: Effect of cross-linker chain length", **Mamta Kumari**, Hemant S. Sodaye, DebasisSen and Ramesh C. Bindal**,** Solid State Ionics, 2018, Volume 316, Pages 75-84.
2. **"**Effect of Phosphotungstic Acid Blending on Properties of Sulfonated Poly (ether ether ketone)-Poly(ethylene glycol) Cross-linked Membranes**", Mamta Kumari**, Hemant S. Sodaye and Ramesh C. Bindal, Journal of Applied Polymer Science,2018, Volume 135, Pages 46667.
3. "Cross-linked sulfonated poly(ether ether ketone)-poly ethylene glycol /silica Organic–inorganic nanocomposite membrane for fuel cell application**" Mamta Kumari**, Hemant S. Sodaye and Ramesh C. Bindal, Journal of Power Sources**,** 2018, Volume 398, Pages 137-148

b. Under preparation

1. Organic–inorganic crosslinked and nanocomposite membranes derived from sulfonated poly(ether ether ketone) - Poly(ethylene glycol) /TiO_2 via sol–gel process for fuel cell application.
2. Nano composite membrane based on sulfonated poly(ether ether ketone)/ZrO_2 for fuel cell application.

Other Publications:

a. Conference/Symposium

1. "Specific ion effects on the permselectivity of cation exchange membrane based on sulfonated poly(ether ether ketone)", **Mamta Kumari**, H. S. Sodaye and R. C. Bindal, in DAE-BRNS eighth biennial symposium on **"**Emerging Trends in Separation Science and Technology (SESTEC-2018)" held during May 23-26, 2018 at BITS Pilani, K.K. Birla Goa Campus, Zuarinagar, Goa, India.
2. "Fuel cell performance of organic-inorganic nanocomposite polymer electrolyte membrane", **Mamta Kumari**, H. S. Sodaye and R. C. Bindal, Oral presentation in "Conference on Electrochemistry in Advanced Materials, Corrosion and Radiopharmaceuticals (CEAMCR-2018)", held on February 15-17, 2018 at DAE convention center, Anushaktinagar, Bhabha Atomic Research center, Mumbai, India.
3. "SPEEK-PEG-TiO_2 Based Composite-Cross linked Membrane for Fuel Cell Application", **Mamta Kumari**, H. S. Sodaye and R. C. Bindal, oral presentationin "6th International Conference on Advances in Energy Research (ICAER) 2017" held on december12–14, 2017 at IIT Bombay, Mumbai, India.
4. "Hydrocarbon polymer based composite - Cross linked proton exchange membrane for fuel cell application", **Mamta Kumari**, H. S. Sodaye and R. C. Bindal, Poster presentation in "6th International Hydrogen & Fuel Cell Conference (IHFC) – 2017" held during December 10-12, 2017 at Hotel Hyatt, Pune, India.
5. "Nano composite - Cross linked proton exchange membrane for fuel cell application", **Mamta Kumari**, H. S. Sodaye, and R. C. Bindal**,** oral presentation in "International

Conference on Nanotechnology: Ideas, Innovations & Initiatives-2017 (ICN:3i-2017)" held on 6–8 December 2017 at IIT Roorkee, Roorkee, India.

6. "Fuel cell performance of SPEEK-PEG-PWA composite membrane" **Mamta Kumari,** H. S. Sodaye and R. C. Bindal, oral presentation in"2nd International Conference on Battery & Fuel Cell Technology" held on July 27-28, 2017 at Hotel Holiday Inn, Rome, Italy.
7. "Permeability studies of Sulfonated and Cross-linked Poly(ether ether Ketone) [SPEEK] Membranes",**Mamta Kumari**, H. S. Sodaye and R. C. Bindal, poster presentationin DAE-BRNS seventh biennial symposium on "Emerging Trends in Separation Science and Technology (SESTEC-2016)", held on May 17-20, 2016 at IIT Guwahati, Guwahati, Assam, India.
8. "Development of Cation Exchange Membrane for Use in Bipolar Membranes", **Mamta Kumari**, H. S. Sodaye, R. C. Bindal and P. K. Tewari, oral presentation in "DAE-BRNS Theme Meeting on Membrane Separations for Fuel Cycle Applications (MEMSEP–2013)" held on September 16-18, 2013 at Multipurpose Hall, Training School Hostel, Anushaktinagar, Mumbai, India.
9. "Development of indigenous heterogeneous Bipolar membrane for regeneration of acid and base from Sodium Nitrate",**Mamta Kumari**, S. R. Bhole, H. S. Sodaye and R. C. Bindal,poster presentation in"Indian Desalination Association- Asia pacific Desalination Association (InDA-APDA) Conference 2016", held on February 11-12, 2016 at Hotel Ambassador Pallava, Chennai.

Mamta Kumari
06/11/2018
(Mamta Kumari)

DEDICATED

TO

MY FAMILY

ACKNOWLEDGEMENTS

It feels great satisfaction and joy to present my dissertation work and acknowledge those who have really matters me the most. First and Foremost, I would like to express my sincere gratitude to my research guide, Prof. (Dr.) R. C. Bindal, Head membrane development section and desalination division, BARC, for giving me the opportunity. He provided me the freedom to work and think independently, and the mentoring to guide me in right direction.

My especial gratitude to my co-guide, Dr. H. S. Sodaye for boosting me with his technical knowledge & expertise; for conferring me with unbound motivation and enthusiasm during the course of the PhD. I have learnt a lot from him.

I would like to thank all the doctoral committee members i.e. Dr. Y. K. Bharadwaj, Dr. A. K. Pandey, Dr. A. K. Satpati including respected chairman, Dr. Manmohan Kumar and earlier chairperson Dr. B.S. Tomar for their constructive and critical evaluation of my work during the course of the studies. My Special thanks for their valuable comments and thoughtful ideas that enabled me to shape and converge the area of work.

I sincerely acknowledge Dr. P. K. Tewari for his suggestion during my research papers writing that helped me a lot to improve my writing skills. I heartily acknowledge Dr. Soumitra Kar for all his precious help and tremendous cooperation during the course of research work. I am grateful to my senior Dr. Avishek Pal for his precious help specially learning the instrumental techniques at the beginning of my research periods which helped me lot. It is also my great pleasure to thank Mr. S.R. Bhole for his continuous help and support. My gratitude and special thanks goes for the entire staff members of MDS: Mr. R. B. Bramhane. Mr. Amit K. Singha, Mr. P. P. Surve, Mr. U. R. More, Mr. N. T. Kambar and Mrs. Amritha Gowri for their continuous in-lab support in carrying out the entire research work. I express my warm gratitude's to my dear friends and lab

mates including Amita Bedar and Bitan ghosh for their help and support and making my daily lab work enjoyable and fun. I thank all those who have helped me directly or indirectly in the successful completion of my thesis.

There is no need of formal words to thank my entire family including my parents, Mr. Rudra Mohan Tiwari and Mrs. Kamala Tiwari; my sisters, Archana Tiwari and Shreya Tiwari and my brother Abhishek Tiwari for their love and continuous support. My parents are the greatest motivational force behind me in completing my work and perhaps no word of acknowledgment is sufficient for them.

I am thankful to the persons who have shown me no interest in my work so that I have become more determined to finish my work anyway. Finally I thank My Almighty for everything.

List of Abbreviations

Abbreviation	**Full form**
AFC	Alkaline fuel cell
AFM	Atomic force microscopy
ATR	Attenuated total reflection
BAM1G	Ballard advanced materials 1st generation
BAM2G	Ballard advanced materials 2nd generation
BAM3G	Ballard advanced material 3rd generation
BSE	Backscattered electrons
CCM	Catalyst-coated membrane
CHP	Combined heat and power
DC	Direct current
DMFC	Direct methanol fuel cell
DS	Degree of sulfonation
DVB	Divinylbenzene
EDX	Energy dispersive x-ray
EIS	Electrochemical impedance spectroscopy
EOD	Electro-osmotic drag
EW	Equivalent weight
FCEV	Fuel cell electric vehicle
FESEM	Field emission scanning electron microscopy
FT	Fourier transform
FTIR	Fourier transform infrared spectroscopy
GDL	Gas diffusion layer
GE	General electric
HHV	Higher heating value
HOR	Hydrogen oxidation reaction
HPA	Heteropolyacid
IEC	Ion exchange capacity

IPN	Interpenetrating polymer network
IRE	Internal reflection element
IS	Impedance spectroscopy
LHV	Lower heating value
MCFC	Molten carbonate fuel cell
MEA	Membrane electrode assembly
MMT	Montmorillonite
MSA	Methanesulfonic acid
MW	Molecular weight
NASA	National aeronautics and space administration
OCV	Open circuit voltage
ORR	Oxygen reduction reaction
PA	Phosphoric acid
PAE	Poly(aryl ether)
PAEK	Poly(aryl ether ketone)
PAFC	Phosphoric acid fuel cell
PBI	Poly(benzimidazole)
PEFC	Polymer electrolyte fuel cell
PEG	Poly(ethylene glycol)
PEM	Proton exchange membrane
PEMFC	Proton exchange membrane fuel cell
PES	Poly(arylene ether sulfone)
PFSA	Perfluorosulfonic acid
PPQ	Poly(phenylquinoxaline)
PPZ	Polyphosphazene
PSSA	Polystyrene-sulphonic acid
PTFE	Polytetrafluoroethylene
PVDF	Poly (vinylidene fluoride)
PVP	Poly (vinylpyrrolidone)
RH	Relative humidity
RMS	Root mean square

SAXS	Small angle x-ray scattering
SE	Secondary electron
SOFC	Solid oxide fuel cell
SPEEK	Sulfonated poly(ether ether ketone)
SPI	Sulphonated polyimide
TFS	Poly (trifluorostyrene)
TGA	Thermo gravimetric analysis
TOC	Total organic carbon
TPA/PWA	Tungstophosphoric acid
UTM	Universal testing machine
YSZ	Yttria stabilized zirconia

CONTENTS

CHAPTER-1 Introduction

CHAPTER-2 Instrumental techniques

CHAPTER-3 Synthesis and Characterization of SPEEK and SPEEK-PEG Cross-linked Membranes

Chapter-4 Effect of Phosphotungstic Acid Blending on Properties and Performance of Sulfonated Poly(ether ether ketone)-Poly(ethylene glycol) Cross-linked Membranes

Chapter-5 Synthesis and Characterization of Cross-linked Sulfonated poly(ether ether ketone)-poly(ethylene glycol) / MO_2 (M=Si, Ti and Zr) Organic-Inorganic Nanocomposite Membrane

SYNOPSIS

Fuel cell is an advanced power system for the future, that is sustainable, clean and environment friendly. Proton exchange membrane fuel cells (PEMFCs), with the advantages of high power density and efficiency, low operating temperature, fast start-up, noiseless feature, static nature and safe handling are being developed as an alternative to conventional internal combustion engines, secondary batteries, and other power sources [1, 2]. In the last few decades, much effort has been devoted to develop PEMFCs, and significant advancement has been achieved. However, their commercialization has not been achieved and the major problem is the prohibitive cost and durability of the component materials (membrane electrolyte, bipolar plate and Pt electro catalyst) [3-5].

One of the key components of PEMFCs is the polymer electrolyte membrane (PEM), which functions as an electrolyte to conduct protons from the anode to the cathode and also acts as separator for preventing intermixing of the reactant gasses (H_2 and O_2). To date, the perfluorinated sulfonic acid (PFSA) membranes like Nafion have been perceived as most suitable PEMs because of their high proton conductivity and stability [6]. However, their high cost, performance loss at higher temperatures (above 80°C) or at low humidity (below 80% RH), high fuel cross over etc., impedes the large scales commercialization of PEMFCs [7, 8].

Aromatic hydrocarbon-based membranes are a promising alternative to PFSA membranes due to their low cost, good stability (thermal and mechanical), processability and wide latitude to tune the chemistry. During the last few decades, sulfonated poly(arylene ether ketone)s (SPAEK) [9, 10], sulfonated poly(imide) (SPI) [11], sulfonated poly(arylene ether sulfone)s (SPAES) [12, 13], and acid-doped polybenzimidazole (PBI) [14, 15], etc. have been extensively studied by different research groups. Among the numerous hydrocarbon polymers, sulfonated poly(ether ether ketone)

(SPEEK) is a good candidate on account of its low cost, high glass transition temperature and high proton conductivity, which depend on their degree of sulfonation (DS). SPEEK membranes with high DS exhibit high proton conductivity and ion exchange capacity (IEC). However, higher IEC that is responsible for high degree of swelling results in poor mechanical and dimensional stability, which is unfavorable for electrochemical applications [16]. In order to improve the mechanical and dimensional stability, many modifications have been carried out, like cross-linking [17, 18], blending with other polymers [19], semi-interpenetrating polymer networks [20], addition of inorganic fillers etc. [21].

Present thesis is focused on the synthesis, characterization and performance evaluation of proton exchange membranes based on sulfonated poly(ether ether ketone) (SPEEK) polymer with an aim to develop solid polymer electrolyte (SPE) membranes for fuel cell application. Different strategies were adopted to improve the electrochemical and mechanical properties of SPEEK, e.g., cross-linking with polyethylene glycol (PEG), blending with inorganic additive (phosphotungustic acid), sol-gel method for *in-situ* synthesis of silica (SiO_2), titania (TiO_2) and zirconia (ZrO_2) within the polymer matrix. Various techniques were applied to investigate the conductivity, mechanical strength, thermal stability, chemical stability, morphology etc. of the synthesized membranes. All the membranes performance study were carried out in H_2/O_2 fuel cell. This thesis is divided into six chapters and the content of each chapter is briefly summarized below.

Chapter-1: Introduction

In this chapter, a brief introduction of fuel cell and different types of fuel cells has been explained. Emphasis is given to the PEMFC and their components. As the present study mainly deals with the synthesis and characterization of proton exchange membrane and their performance study in fuel cell, an overview and the literature survey of different types of proton exchange membranes i.e. fluorinated, partially fluorinated, hydrocarbon polymer based etc., membranes have been given. The properties and limitations of commercially available PFSA membrane, i.e., Nafion have been illustrated and also the advantages of hydrocarbon polymers over that of the fluorinated polymers is given. The structure, properties and different modification methods of the SPEEK polymer based membranes have been discussed.

Chapter-2: Instrumental techniques

This chapter deals with the instrumental techniques used to investigate the electrochemical, mechanical, structural, thermal and morphological properties of solid polymer electrolyte membranes. The working principle of all the techniques is briefly mentioned in this chapter. These techniques includes electrochemical Impedance spectroscopy (EIS), Fourier Transform Infrared Spectroscopy (FTIR), Universal testing machine (UTM), Thermo gravimetric analysis (TGA), Field Emission Scanning Electron Microscopy (FESEM) - Energy Dispersive X-ray (EDX), Atomic force microscopy (AFM), Small Angle X-ray scattering (SAXS).

Chapter-3 Synthesis and Characterization of SPEEK and SPEEK-PEG Cross-linked Membranes

This chapter presents the synthesis and characterizations of SPEEK and SPEEK-PEG cross-linked membranes. The degree of sulfonation and ion exchange capacity of the synthesized SPEEK was evaluated by back titration method. Cross-linking is an effective and simple method of improving the chemical and mechanical properties of polymer membrane. The polymer morphology is also transformed during the cross-linking process. In this work a series of cross-linked membranes have been synthesized by using six different molecular weight of poly ethylene glycol (PEG) [200, 400, 600, 3000, 6000, 10,000 Da] as cross-linkers to investigate the effect of cross-linker chain length on membrane morphology and properties. Membranes topography and morphology were investigated by using AFM and SAXS, which showed that there was formation of cluster like structure, and hydrophilic-hydrophobic phase separation occurs after cross-linking that makes the membranes mechanically stronger and reduces its swelling in water at higher temperature. Membrane properties were found to be strongly dependent on the cross-linker chain length. PEG-400 and PEG-600 cross-linked membrane gave desirable properties in terms of overall membrane performance such as proton conductivity (0.095 S cm^{-1}), mechanical strength, and membrane durability etc. These two membranes (SPEEK-PEG-400 and SPEEK-PEG-600) performance was studied in H_2/O_2 fuel cell. To explore its utilization in the methanol fuel cell, the methanol permeability of the SPEEK-PEG-400 membrane was evaluated and compare with Nafion, which showed lower permeability than Nafion up to 55°C.

Chapter-4 Effect of Phosphotungstic Acid Blending on Properties and Performance of Sulfonated Poly(ether ether ketone)-Poly(ethylene glycol) Cross-linked Membranes

This study showed the effect of phosphotungstic acid (PWA) blending in sulfonated poly(ether ether ketone) (SPEEK) and poly(ethylene glycol) (PEG) cross-linked membrane in terms of electrochemical and mechanical properties. PWA is a good inorganic modifier because of its unique properties like high conductivity, thermal stability, high selectivity and non-corrosive nature. A series of SPEEK-PEG-PWA membranes were fabricated where PEG-600 is used as an interpenetrating polymer network (IPN) type cross-linker and PWA as an inorganic additive. PWA weight percentage was varied from 0% to 50%. All the membranes were equilibrated with water at room temperature (27 ºC) and elevated temperature (60 ºC) and their properties were investigated. SEM with EDX studies were used to ascertain the tungsten concentration remaining in the membrane after treatment in water at higher temperature. A systematic decrease in the tungsten concentration was seen with the increase in the initial tungsten percentage. Membrane blended with

10% PWA showed the best properties among all, i.e., highest conductivity (0.11 S cm^{-1}), mechanical strength and chemical stability. Membranes with 10% tungsten and without tungsten were studied in H_2/O_2 fuel cell. The membrane blended with 10 wt% PWA gave 33% more power density than the membrane without PWA.

Chapter-5: Synthesis and Characterization of Cross-linked Sulfonated poly(ether ether ketone)-poly(ethylene glycol) / MO_2 (M=Si, Ti and Zr) Organic-Inorganic Nanocomposite Membrane

This chapter deals with synthesis, characterization and performance studied of organic–inorganic nano-composite membranes. In this study, a series of SPEEK-PEG/MO_2 (M = Si, Ti and Zr) membranes were fabricated where, PEG-400 is used as an (IPN)-type cross-linker as well as dispersant to homogeneously distribute silica/titania/zirconia nanoparticles in the membrane, which are synthesized by in-situ sol-gel method. Polyols (PEG) are highly beneficial for controlling inorganic particle nucleation, growth and agglomeration of nanoparticles as PEG adhere on the particle surface (especially on oxides) and serve as colloidal stabilizers. The synergistic effect of cross-linking and inorganic additive on the membranes electrochemical and mechanical properties, and fuel cell performance were investigated. Experimental results reveal that nanocomposite membrane has better properties than pristine SPEEK-PEG membrane, e.g., conductivity, form stability, mechanical strength, thermal and oxidative stability etc. The hydrogen bond between –OH group of PEG, MO_2 and sulfonic acid (–SO_3H) facilitated better dispersion and improved the compatibility between the organic and inorganic components. FE-SEM and AFM images showed that the SiO_2, TiO_2 and ZrO_2 particles are distributed homogeneously without aggregation. The EDX mapping images of silicon, titanium and zirconium also supported the FE-SEM images and the elemental map's spectrum revealed the complete conversion of precursor to silica, titania and zirconia. The nanocomposite membranes with optimum amount of MO_2 have shown good form stability in water up to 80 °C, whereas without nanoparticles added sample has shown excessive swelling beyond 60 °C in water. This chapter is divided into three parts to discuss the results/outcomes of all the three MO_2 (Si, Ti and Zr) different types of nanocomposite membranes separately:

SPEEK-PEG/SiO_2

The weight percentage of SiO_2 in the SPEEK-PEG/SiO_2 Nano composite membranes was varied from 2.5, 5, 7.5, 10 to 12.5% and the best properties were observed for10wt% of SiO_2 e.g. maximum conductivity of 0.185 S cm^{-1} at 80 °C and 100% RH and optimum water uptake and showed mechanical strength of 16 to 25 MPa and the percent elongation in the range of 150 to 230%.

SPEEK-PEG/TiO_2

The weight percentage TiO_2 was varied in the steps of 2.5, 5, 7.5 to 10 wt% to prepare PEEK-PEG/TiO_2 nano composite membranes. The membrane with 7.5 wt% TiO_2 has shown the best properties i.e., maximum conductivity of 0.180 S cm^{-1} at 80 °C and 100% RH and optimum water uptake. The mechanical strength of all the membrane was found in the range of 16 to 29 MPa and the percent elongation in the range of 120 to 220%.

SPEEK-PEG/ZrO_2

The weight percentage of ZiO_2 was varied from 2.5, 5, 7.5 to 10% to prepare PEEK-PEG/ZrO_2 nanocomposite membranes. Membrane with 7.5 wt% ZrO_2 has shown the best properties among all other wt% of ZrO_2, i.e., maximum conductivity of 0.170 S cm^{-1} at 80 °C and 100% RH and optimum water uptake and all membranes have shown good mechanical properties i.e. the mechanical strength in the range of 16 to 32 MPa and the percent elongation in the range of 100 to 205%.

The membranes were found thermally stable up to 250 °C well above the low and medium temperature PEM fuel cell application. The nanocomposite membranes with optimum weight % of MO_2, i.e., 10% SiO_2, 7.5% TiO_2 and 7.5% ZrO_2 were studied individually in the H_2/O_2 fuel cell and compared with pristine SPEEK-PEG membrane up to 60 °C. The maximum power density due to the addition of MO_2 nanoparticles was enhance to more than twofold higher at 60 °C. The durability studies of the membranes in the fuel cell were carried out by measurement of OCV.

Chapter-6: Conclusions, Implications and Future perspectives

In this chapter, the summary and conclusions of the work carried out in the thesis have been given. The cross-linking of the highly sulfonated SPEEK resulted in water insoluble SPEEK-PEG membrane that has conductivity comparable with the commercially available membranes. The conductivity of the membrane was enhanced by addition of the inorganic heteropolyacid. The SPEEK-PEG membrane has a good form stability up to 60 °C. The form stability of pristine SPEEK-PEG membrane was further improved significantly by addition of inorganic metal oxide nanoparticles that formed an interpenetrating network of inorganic and organic moieties. The form stability of these membranes was further enhanced up to 80 °C in water. These membranes were studied in H_2/O_2 fuel cell and their performance are compared.

In addition to the fuel cell application, the in-house developed membranes can find several other promising applications like, (i) separation of components such as salts or acids and bases from electrolyte solutions (e.g., electro dialysis, electro-electrodialysis, bipolar electrolysis etc.), (ii) chlor-alkali industry for the production of alkali and chlorine, (iii) pure water electrolysis for production of hydrogen and oxygen and (iv) direct methanol fuel cell or redox flow batteries etc.

The possibility and advantage of usage of in-house developed composite membranes in high temperature proton exchange membrane fuel cell (HT-PEMFC) is also highlighted in this chapter.

References:

[1] F. Barbir, PEM fuel cells: theory and practice, Academic Press 2012.

[2] K.V. Kordesch, G.R. Simader, Environmental impact of fuel cell technology, Chemical Reviews, 95 (1995) 191-207.

[3] Y. Shao, G. Yin, Z. Wang, Y. Gao, Proton exchange membrane fuel cell from low temperature to high temperature: material challenges, Journal of Power Sources, 167 (2007) 235-242.

[4] D.P. Wilkinson, J. Zhang, R. Hui, J. Fergus, X. Li, Proton exchange membrane fuel cells: materials properties and performance, CRC Press2009.

[5] L. Mao, L. Jackson, T. Jackson, Investigation of polymer electrolyte membrane fuel cell internal behaviour during long term operation and its use in prognostics, Journal of Power Sources, 362 (2017) 39-49.

[6] O. Savadogo, Emerging membranes for electrochemical systems: Part II. High temperature composite membranes for polymer electrolyte fuel cell (PEFC) applications, Journal of Power Sources, 127 (2004) 135-161.

[7] S. Peighambardoust, S. Rowshanzamir, M. Amjadi, Review of the proton exchange membranes for fuel cell applications, International journal of hydrogen energy, 35 (2010) 9349-9384.

[8] J. Zhang, Z. Xie, J. Zhang, Y. Tang, C. Song, T. Navessin, Z. Shi, D. Song, H. Wang, D.P. Wilkinson, High temperature PEM fuel cells, Journal of power Sources, 160 (2006) 872-891.

[9] S. J. Zaidi, S. D. Mikhailenko, G. Robertson, M. Guiver, S. Kaliaguine, Proton conducting composite membranes from polyether ether ketone and heteropolyacids for fuel cell applications, Journal of Membrane Science, 173 (2000) 17-34.

[10] P. Xing, G. P. Robertson, M. D. Guiver, S. D. Mikhailenko, S. Kaliaguine, Sulfonated poly (aryl ether ketone) s containing the hexafluoroisopropylidene diphenyl moiety prepared by direct copolymerization, as proton exchange membranes for fuel cell application, Macromolecules, 37 (2004) 7960-7967.

[11] B. Zhang, J. Ni, X. Xiang, L. Wang, Y. Chen, Synthesis and properties of reprocessable sulfonated polyimides cross-linked via acid stimulation for use as proton exchange membranes, Journal of Power Sources, 337 (2017) 110-117.

[12] Y. T. Hong, C. H. Lee, H. S. Park, K.A. Min, H. J. Kim, S. Y. Nam, Y. M. Lee, Improvement of electrochemical performances of sulfonated poly (arylene ether sulfone) via incorporation of sulfonated poly (arylene ether benzimidazole), Journal of Power Sources, 175 (2008) 724-731.

[13] Y. Yang, Z. Shi, S. Holdcroft, Synthesis of Sulfonated Polysulfone-b lock-PVDF Copolymers: Enhancement of Proton Conductivity in Low Ion Exchange Capacity Membranes, Macromolecules, 37 (2004) 1678-1681.

[14] H. Zheng, M. Mathe, Enhanced conductivity and stability of composite membranes based on poly (2, 5-benzimidazole) and zirconium oxide nanoparticles for fuel cells, Journal of Power Sources, 196 (2011) 894-898.

[15] H. -L. Lin, T. -H. Tang, C. -R. Hu, T. L. Yu, Poly (benzimidazole)/silica-ethyl-phosphoric acid hybrid membranes for proton exchange membrane fuel cells, Journal of Power Sources, 201 (2012) 72-80.

[16] J. Millichamp, T. J. Mason, T. P. Neville, N. Rajalakshmi, R. Jervis, P. R. Shearing, D. J. Brett, Mechanisms and effects of mechanical compression and dimensional change in polymer electrolyte fuel cells–a review, Journal of Power Sources, 284 (2015) 305-320.

[17] S. D. Mikhailenko, G. P. Robertson, M. D. Guiver, S. Kaliaguine, Properties of PEMs based on cross-linked sulfonated poly (ether ether ketone), Journal of membrane science, 285 (2006) 306-316.

[18] P. Knauth, H. Hou, E. Bloch, E. Sgreccia, M. Di Vona, Thermogravimetric analysis of SPEEK membranes: thermal stability, degree of sulfonation and cross-linking reaction, Journal of Analytical and Applied Pyrolysis, 92 (2011) 361-365.

[19] H. Zhang, X. Li, C. Zhao, T. Fu, Y. Shi, H. Na, Composite membranes based on highly sulfonated PEEK and PBI: morphology characteristics and performance, Journal of Membrane Science, 308 (2008) 66-74.

[20] C. Fang, X. N. Toh, Q. Yao, D. Julius, L. Hong, J. Y. Lee, Semi-interpenetrating polymer network proton exchange membranes with narrow and well-connected hydrophilic channels, Journal of Power Sources, 226 (2013) 289-298.

[21] R. Nagarale, W. Shin, P.K. Singh, Progress in ionic organic-inorganic composite membranes for fuel cell applications, Polymer Chemistry, 1 (2010) 388-408.

LIST OF FIGURES

LIST OF TABLES

CHAPTER-1

Introduction

1.1 Fuel cell

1.1.1 Fuel cells-relevance and importance

Fossil fuels, which meet 80% of the world’s energy demand today, are limited and will eventually be depleted because the rate of fossil fuel consumption is significantly higher than the rate of the fossil production by nature. Additionally, they are also the source of serious environmental problems, such as global warming, climate change, melting of ice caps, rising sea levels, acid rains, pollution, ozone layer depletion etc.[1,2] A single approach cannot solve the energy crisis and environmental challenges facing the world. Therefore, efforts are being made worldwide to develop ‘clean’ energy technologies. Hydrogen and Fuel cells are an integral part of the clean energy portfolio. Hydrogen can be produced from diverse resources, both renewable (hydro, wind, solar, biomass, geothermal) and non-renewable (coal, natural gas, nuclear), and fuel cells can generate electricity efficiently from a number of fuels, including hydrogen, methanol, ethanol, biogas, natural gas etc.[3,4] Fuel cells are environmental friendly devices for energy conversion, power generation, and one of the most promising candidates as zero-emission power sources.[5] Fuel cells powered by hydrogen have high power densities and efficient in converting chemical energy to electrical energy. Output from these fuel cells is free from undesired compounds such as nitrogen oxides, carbon monoxide and residual hydrocarbons that are generally produced by internal combustion engines. Even carbon dioxide which is a major component in greenhouse emissions is absent in hydrogen fuel cells. Membrane based fuel cells have low operating temperature, fast start-up, noiseless feature, static nature and safe handling are being developed as an alternative to conventional internal combustion engines, secondary batteries, and other power sources. Hence due to their clean exhaust technologies and high energy efficiencies, transportation by fuel cell electric vehicles (FCEV) is an attractive approach and is an effective solution to the inevitable petroleum shortage.[6,7]

1.1.2 What is a fuel cell ?

A fuel cell is an electrochemical energy conversion device that converts chemical energy of fuel directly into direct current (DC) electricity.[8] Typically, a process of electricity generation from fuels involves several energy conversion steps, namely:

- Combustion of fuel converts chemical energy of fuel into heat,
- This heat is then used to boil water and generate steam,
- Steam is used to run a turbine in a process that converts thermal energy into mechanical energy, and finally
- Mechanical energy is used to run a generator that generates electricity.

A fuel cell circumvents all these processes and generates electricity in a single step by electrochemical combination of a fuel and oxidant without involving any moving parts. The fuel cell operates quietly and efficiently, and when hydrogen is used as fuel, it produces only heat and water as byproduct. Therefore, a fuel cell zero or low emissions device. A fuel cell is in some aspects similar to a battery. It has an electrolyte, and negative and positive electrodes, and it generates DC electricity through electrochemical reactions. However, unlike a battery, a fuel cell requires a constant supply of fuel and oxidant. In addition, the electrodes in a fuel cell do not undergo chemical changes. All fuel cells consist of an anode, to which the supplied fuel is oxidized, a cathode, to which the supplied oxidant (e.g., oxygen) is reduced, and an electrolyte, which allows the flow of ions between the anode and cathode,[1] illustrated in Figure 1.1.

The first fuel cell was invented by Sir William Grove in 1839 and he named it as ‘gaseous voltaic battery’. He used Platinum electrodes and Sulfuric acid electrolyte, and hydrogen and oxygen as reactants. The basic principle behind this first fuel cell is to obtain electricity and water by reversing the electrolysis process.

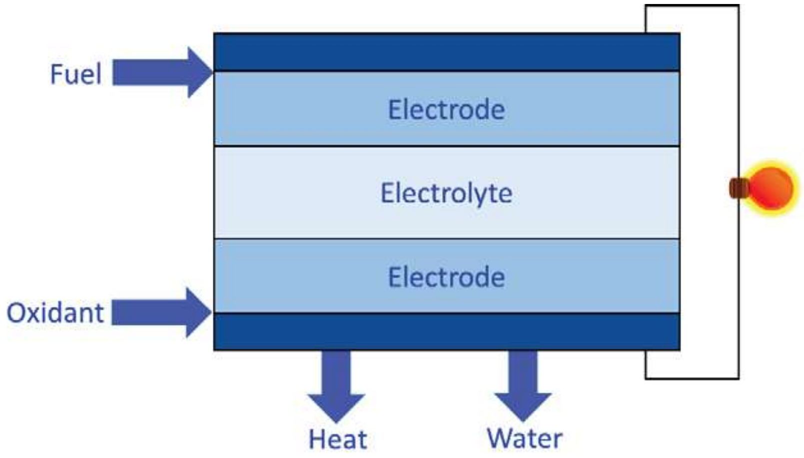

Figure 1.1: Schematic representation of a fuel cell.

1.1.3 Fuel cells classification

Basically fuel cells are classified according to their operational and constructional parameters, i.e., based on fuel requirement, working temperature and electrolyte used etc. The choice of electrolyte is the main deciding feature of a fuel cell along with power-up time, type of fuel, migration of ions, materials used in the cell construction and its stack components. Thus, fuel cells are primarily characterized by the nature of their electrolyte used. The six most common fuel cell types are: [9,10]

- Alkaline fuel cells (AFCs),
- Molten carbonate fuel cells (MCFCs),
- Phosphoric acid fuel cells (PAFCs),
- Solid oxide fuel cells (SOFCs),
- Polymer electrolyte fuel cells (PEFCs) or proton exchange membrane fuel cells (PEMFCs),
- Direct methanol fuel cells (DMFCs)

Alkaline fuel cell (AFC)

Alkaline fuel cells (AFCs) are the first fuel cell technologies that was put into practice to generate electricity from hydrogen. They were successfully used in the U.S. space program having a duel advantage of producing water and electrical energy on board spacecraft. In these fuel cells an aqueous solution of potassium hydroxide is used as the electrolyte and a variety of non-precious metals as a catalyst (e.g. Nickel, various types of activated carbon, metal oxides, silver, gold etc.) at the anode and cathode.[11] The AFCs generate electricity from hydrogen in which hydroxyl ion (OH^-) from potassium hydroxide migrates from the cathode to the anode. At the anode, hydrogen gas reacts with the OH^- ions to produce water and release electrons, illustrated in Figure 1.2.

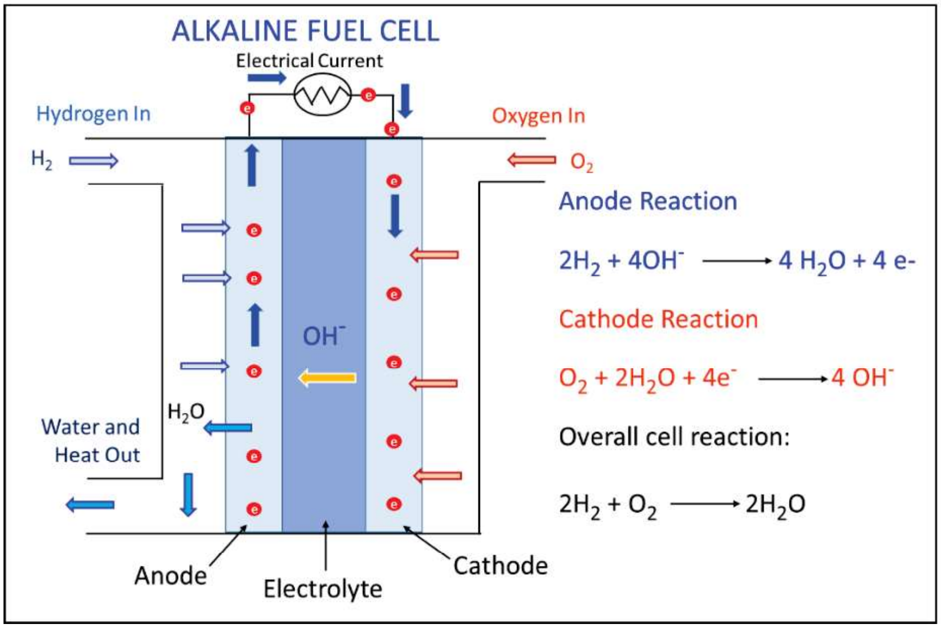

Figure 1.2: Schematic representation of an alkaline fuel cell (AFC).

These fuel cells have high efficiencies (above 60%). Other advantage is, it produce potable water in addition to electricity, therefore, they have been a choice for spacecrafts. One of the major drawbacks of the AFCs is that it is susceptible to poisoning by carbon dioxide (CO_2). In fact, even the small amount of CO_2 in the air can dramatically affect cell performance and durability due to carbonate formation. The carbonates can lead to potential blockage of the electrolyte pathways and/or electrode pores. Another disadvantage is, if the electrolyte solution is higher or below the required level, it can lead to electrode flooding or electrode drying.[12]

Molten carbonate fuel cells (MCFCs)

Molten carbonate fuel cells (MCFCs) are high temperature cells operating at approximately 600–700 °C. MCFCs use a molten mixture of alkali metal carbonates – usually a binary mixture of lithium and potassium, or lithium and sodium carbonates, which is retained in a porous, chemically inert ceramic matrix of beta-alumina solid electrolyte (BASE). BASE is an isomorphic form of aluminum oxide complexed with a mobile ion such as Na^+, K^+ or Li^+. In MCFCs the electrolytes are heated to 650°C, and the salts melt and conduct carbonate ions (CO_3^{2-}) from the cathode to the anode.[13] At the anode, hydrogen gas reacts with the oxidizing agent, namely CO_3^{2-} from the electrolyte and form water and carbon dioxide, while electrons released to the external circuit are transferred to the cathode. At the cathode, a reduction reaction of the oxygen and carbon dioxide occurs and forms carbonate ions that is released to the electrolyte, illustrated in Figure 1.3.

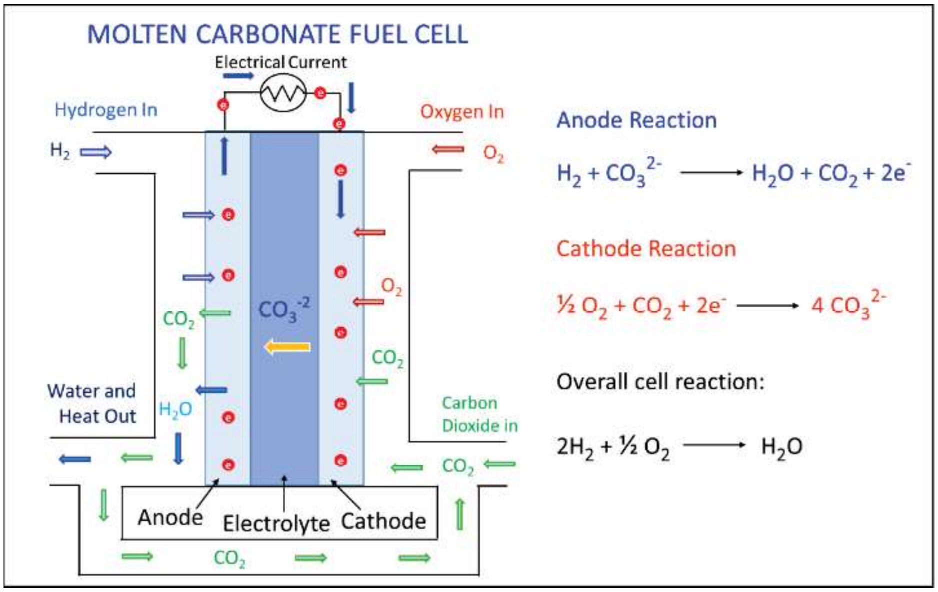

Figure 1.3: Schematic representation of a molten carbonate fuel cell (MCFC).

The major advantages of MCFCs include their high efficiency of 50–60 %, suitability of cheap nickel electrodes for providing sufficient activity, the high operating temperature of these cells limits damage from the carbon monoxide poisoning of the cells and waste heat can also be recycled to make additional electricity.[14,15] The primary disadvantage of current MCFC technology is durability. High operating temperatures and the use of corrosive electrolytes accelerates component breakdown and cell life.

Phosphoric acid fuel cells (PAFCs)

The phosphoric acid fuel cells (PAFCs) is considered the "first generation" of modern fuel cells and it is most widely used. In PAFCs, a highly concentrated (> 95%) phosphoric acid (H_3PO_4) solution is used as electrolyte. The electrolyte is often immobilized in a porous silicon carbide (SiC) matrix by capillary action and porous carbon electrodes containing a platinum catalyst is used as anode and cathode. The operating range of PAFCs is about 150–250 °C due to the low ionic conductivity of H_3PO_4 at low temperatures.[16] At the anode, hydrogen oxidized and splits into protons and electrons. The protons are transferred through the electrolyte, whereas the electrons pass through the external electrical circuit. On the cathode side, the redox reaction between positive hydrogen ions, electrons and oxygen gas results in water formation, illustrated in Figure 1.4.

The main advantage of PAFCs is their capacity to generate electricity and separate the useful heat at the same time. The process of combined heat and power (CHP) production is termed as cogeneration. PAFCs are more than 85% efficient when used for the co-generation of electricity and heat but they are less efficient at generating electricity alone (37%–42%).[17] The drawback of PAFC is its high cost of manufacture due to the much higher loadings of expensive platinum catalyst than other types of fuel cells and the catalyst are easily "poisoned" by carbon monoxide because carbon monoxide binds to the platinum catalyst at the anode, decreasing the fuel cell's efficiency.

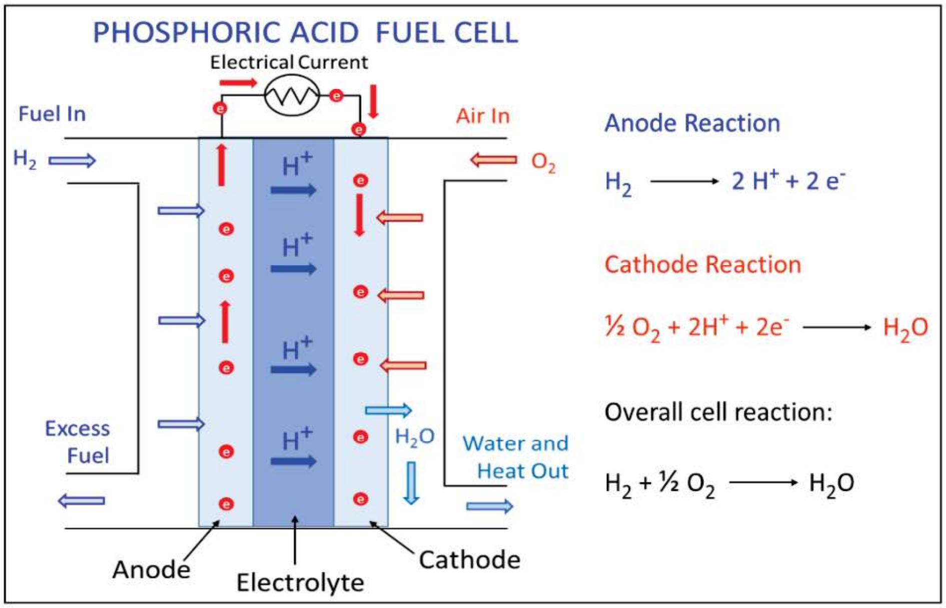

Figure 1.4: Schematic representation of a phosphoric acid fuel cell (PAFC).

Solid oxide fuel cell (SOFC)

Solid oxide fuel cells (SOFCs) are best suited for large-scale stationary power generators. A SOFC uses solid oxide as electrolyte. The most commonly used electrolyte for SOFCs is dense yttria stabilized zirconia (YSZ), a crystal structure of zirconium dioxide (ZrO_2) with the addition of yttrium oxide (Y_2O_3), due to its high chemical and thermal stability and good ionic conductivity. The SOFCs can produce electricity in the range of 600 - 1000 °C. At the cathode, the oxygen is reduced to oxygen ions (O^{2-}), which diffuse into the electrolyte material and migrate to the anode. At the anode side the oxygen ions react with the fuel, generally hydrogen and carbon monoxide, and produce water and carbon dioxide, as well as heat and electricity,[18,19] as shown in Figure 1.5.

The main advantages of the SOFC is that they can be operated at high efficiency of 50–60% and a separate reformer is not required to extract hydrogen from the fuel due to its internal reforming capability. This system can provide high-quality waste heat for (i) cogeneration applications and (ii) bottoming cycles, utilizing conventional steam turbines for additional electricity generation, and hence, CHP operation increases the fuel efficiency by up to 80 %.

The SOFC systems have demonstrated minimal air pollutant emissions and low greenhouse gas emissions, but some drawbacks, such as their high cost, very long start-up and cooling-down times, as well as sensitivity to sulphur and other contaminants.[20]

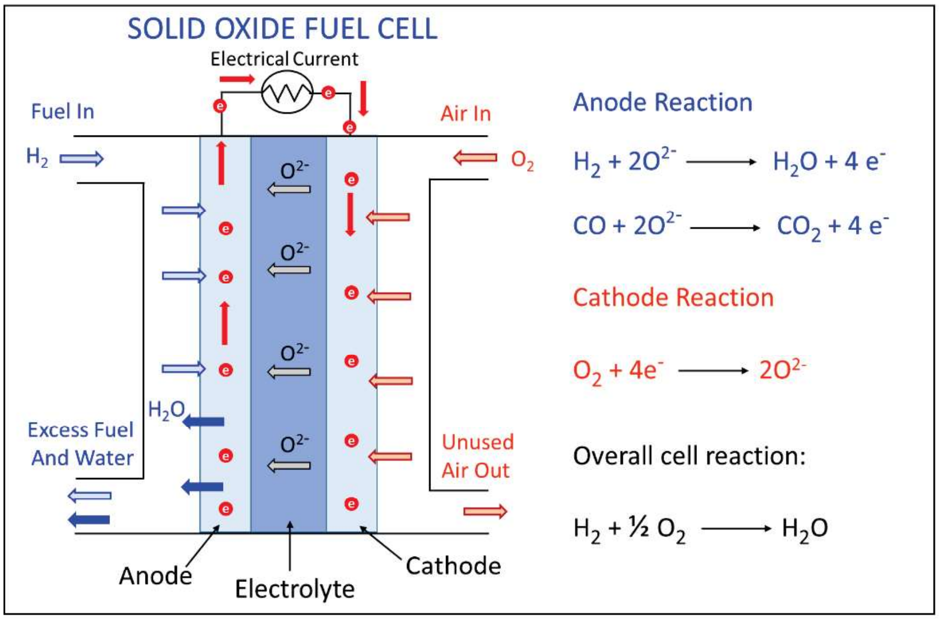

Figure 1.5: Schematic representation of a solid oxide fuel cell (SOFC).

Polymer electrolyte membrane fuel cells (PEMFCs):

Polymer electrolyte membrane fuel cells also known as polymer electrolyte fuel cells (PEFCs) or proton exchange membrane fuel cells (PEMFCs), the subject of this work, use a proton conducting polymer membrane as electrolyte. The idea of using an organic cation exchange membrane as a solid electrolyte in a fuel cell is given by Grubb in 1959.[21] At present, the PEMFC is the most promising candidate system of all fuel cell systems in terms of the mode of operation and applications. As shown in Figure 1.6, PEMFC consists of a polymeric proton-conductive membrane sandwiched between an anode and a cathode. Hydrogen is fed into the anode side where it is dissociated into its primary constituents, protons and electrons (Eq. 1.1) at the catalyst (Pt) layer. The protons subsequently migrate through the membrane from the anode to the cathode side, while the electrons go through the electrically conductive electrodes to the outside circuit and return to the cathode. At the cathode, the electrons react with the protons from the anode side and with the oxygen (Eq. 1.2). Water is produced in this electrochemical reaction and is removed from the cell by a flow of excess oxygen.[22] The electrochemical reactions that occur at both electrodes are as follows:

Anode reaction: $H_2 \longrightarrow 2H^+ + 2e^-$ … (1.1)

Cathode reaction: $\frac{1}{2} O_2 + 2 H^+ + 2e^- \longrightarrow H_2O$ … (1.2)

Overall cell reaction: $H_2 + \frac{1}{2} O_2 \longrightarrow H_2O$ + electric energy + Heat … (1.3)

Compared to other types of fuel cells, PEMFCs present several advantages. They are compact, lightweight and they generate high-power density with large current density. PEMFCs constituted with an electrolyte working at low temperature allowing rapid start-up (less warm-up time) in cold temperatures. Compared to thermal engines, vehicles integrating PEMFCs have ultra-low or zero emissions of environmental pollutants (CO, NO, VOCs, and SO_x). PEMFCs are particularly suitable for use in passenger vehicles, such as cars and buses.

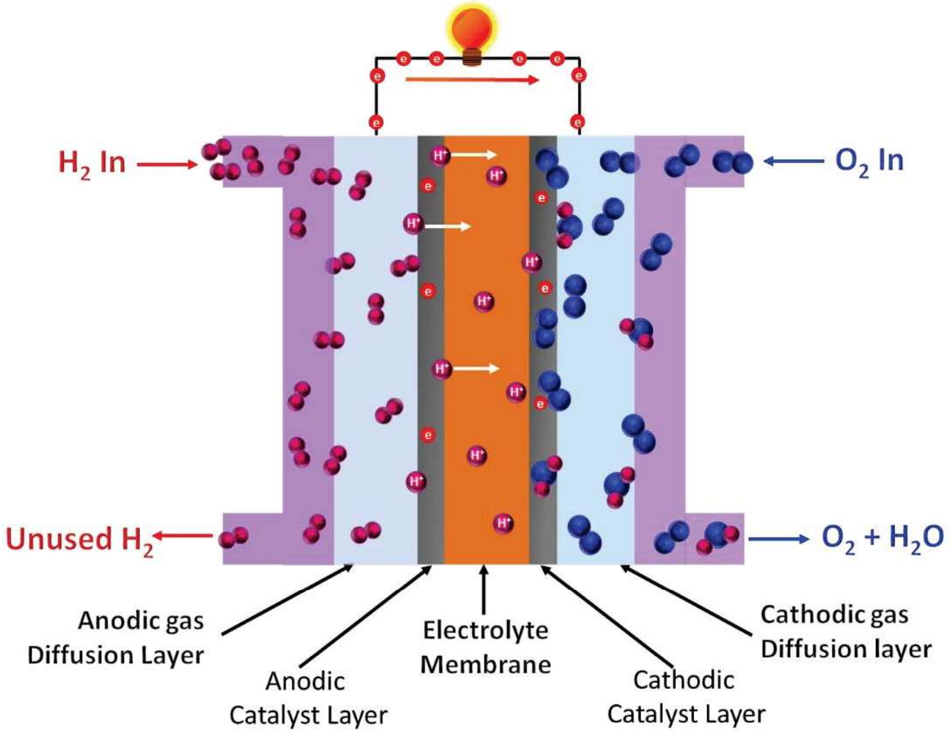

Figure 1.6: Schematic representation of a polymer electrolyte membrane fuel cell (PEMFC).

There are two major limitations of the PEMFCs, (i) the high cost of the existing perfluorinated ionomer membrane, which used as electrolyte in PEMFCs and (ii) an expensive noble-metal catalyst (typically platinum) that is used for hydrogen's oxidation generating electrons and protons. The presence of CO in the fuel gas, CO poisoning, degrades PEMFC performance by its preferential adsorption on the platinum surface and blocking the active sites. This necessitates employing extra catalytic converter for the carbon monoxide in the fuel gas that is derived using a reformer to generate hydrogen from hydrocarbon fuel.

Direct Methanol fuel cell (DMFC):

DMFC is the fuel cell that is similar to PEMFC, except that it uses methanol as the fuel directly on the anode instead of hydrogen or hydrogen-rich gas. Methanol and water react electrochemically (methanol being oxidized) at the anode to produce carbon dioxide, protons and electrons as shown in Eq. 1.4. The electrons are transported through an external circuit to the cathode while the protons migrate through the polymer electrolyte membrane to the cathode. In the cathode catalyst layer, oxygen from the ambient air reacts with the electrons and protons and generates water (Eq. 1.5).[23] The overall cell reaction, as shown in Eq. 1.6, is therefore the reaction of methanol and oxygen to produce water and carbon dioxide.

The reaction mechanism for a DMFC at anode, cathode and overall are as:

Anode reaction: $CH_3OH + H_2O \longrightarrow 6H^+ + 6e^- + CO_2$ … (1.4)

Cathode reaction: $1.5\ O_2 + 6\ H^+ + 6e^- \longrightarrow 3\ H_2O$ … (1.5)

Overall reaction: $CH_3OH + 1.5\ O_2 \longrightarrow 2\ H_2O + CO_2$ … (1.6)

The advantages of DMFC are, it uses a liquid methanol fuel, which is easily stored and transported and simplifies the fuel cell system. DMFC is often used to provide power for portable fuel cell applications such as cell phones or laptop computers.

There are two technical challenges for DMFC technologies: (1) High methanol crossover (10^{-6} mol $cm^{-2}s^{-1}$) through the existing perfluorinated ionomer membrane that are directly oxidized by oxygen on the positive electrode and severely reduces cell voltage, current density and fuel utilization, and hence cell performance. (2) Insufficient activity of the anode catalyst, and thus high over-potential loss (about 350 mV) for DMFC compared with that for PEMFC (60 mV). Slow anode kinetics due to methanol crossover reduce the power density of DMFC about 3 to 4 fold in comparison with a hydrogen fuel cell.[24]

1.1.4 Components of Proton Exchange Membrane Fuel Cells

The main components of a PEMFC are as follows:

(1) The ion exchange membrane
(2) The porous electrodes, which is composed of active catalyst layer
(3) Gas diffusion layer (GDL)
(4) Bipolar plates that delivers the fuel and oxidant to the reactive sites on both sides.
(5) Current collector
(6) End plates.

The schematic representation of the PEMFC components is shown in Figure 1.7.

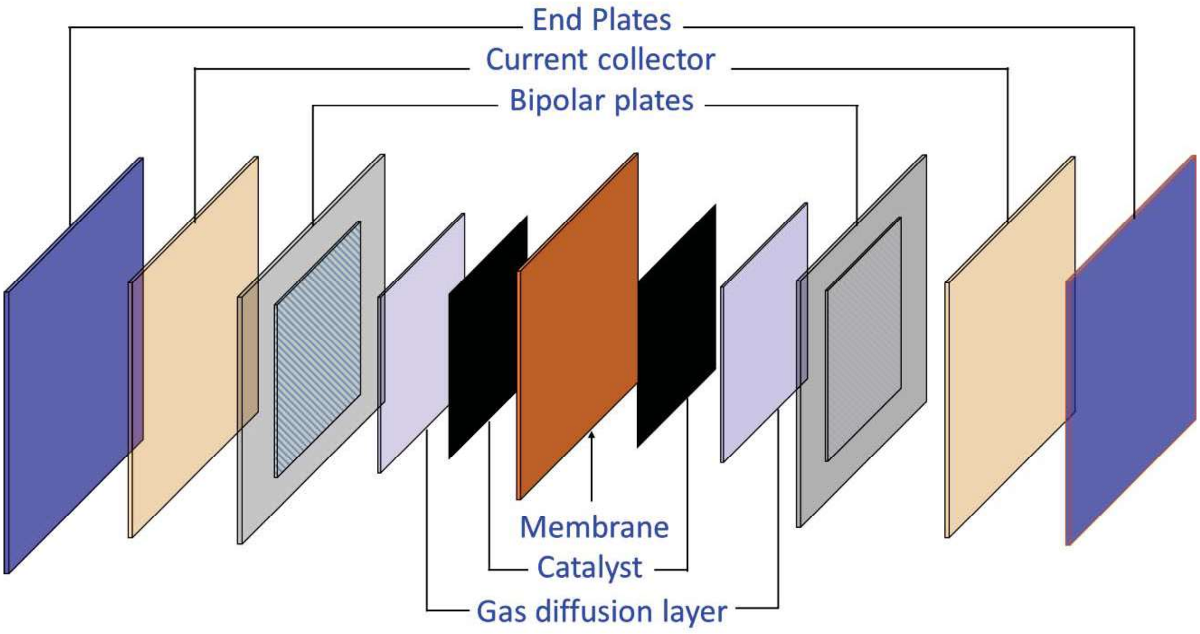

Figure 1.7: Main components of PEMFC.

Membrane

Proton exchange membrane (PEM) is the core component of the PEMFCs. A PEM functions as (i) a conductor for protons from anode to cathode; (ii) a separator to prevent mixing of reactants; (iii) an electrical insulator to drive electrons through an external path to the cathode; and (iv) a structural framework to support the electrocatalysts in the case of catalyst-coated membrane (CCM)).[25]

The membrane materials that designed to work in PEMFCs should meet the following requirements: (i) high ionic conductivity; (ii) low fuel permeability; (iii) good thermal and hydrolytic stability; (iv) excellent electrochemical stability in an aggressive environment; (v) substantial morphological and dimensional stability; (vi) outstanding mechanical properties in both the dry and hydrated states; (vii) sufficient water uptake and moderate swelling; (viii) suppressed water transport through diffusion and electroosmosis; (ix) easy fabrication to form the membrane electrode assembly (MEA), and finally, more importantly from a practical point of view, (x) a competitive low-cost and sufficient long-term durability.[26] The detail of these properties and their effect on cell performance etc. will be discussed later.

Catalyst layer

The hydrogen oxidation reaction (HOR) and the oxygen reduction reaction (ORR) require catalysts to achieve useful reaction rates. A layer of catalyst is coated on both sides of the membrane - one functions as cathode and another as anode. The best catalysts are platinum (Pt) and its alloys with certain transition metals. Conventional catalyst layers include nanometer-sized particles of platinum dispersed on a high-surface-area carbon support. The support has several functions. It helps the Pt to form nanoparticles during the formation process. It acts as an anchor for the Pt nanoparticles through some chemical–physical interactions, so that the Pt nanoparticles are less likely to grow in size during use. It also allows electrons to transport among Pt nanoparticles and throughout the catalyst layer. It may also alter the activity of the supported catalysts. The widely used catalyst is Pt supported on carbon (Pt/C), such as Pt/Vulcan XC-72.

This supported platinum catalyst is mixed with an ion-conducting polymer (ionomer) and coated on GDLs. The GDLs are hot pressed on to the membrane. In the other method, the catalyst is first coated on polymeric substance and then transferred to the membrane surface by hot pressing whereby it binds with the membrane to form (MEA). On the anode side, the platinum catalyst enables hydrogen molecules to be split into protons and electrons. On the cathode side, the platinum catalyst enables oxygen reduction by reacting with the protons generated by the anode, producing water. The ionomer mixed into the catalyst layers allows the protons to travel through these layers and reach up to the Pt particle where the reaction takes place. H_2 oxidation proceeds faster than O_2 reduction, and thus it requires less of a catalyst. With pure H_2 as the reactant, a Pt loading of 0.05 mg cm^{-2} is enough, while the catalyst loading for O_2 reduction is typically several times higher.[27]

Gas Diffusion Layer (GDL)

A layer between the catalyst layer and bipolar plates is called a gas diffusion layer. Although it does not directly participate in the electrochemical reactions, a gas diffusion layer in PEMFCs has several important functions:

- It provides a pathway for reactant gases from the flow field channels to the catalyst layer, allowing them access to the entire active area (not just to those adjacent to the channels).
- It provides a pathway for product water from the catalyst layer to the flow field channels.
- It electrically connects the catalyst layer to the bipolar plate, allowing the electrons to complete the electrical circuit.

- It also serves to conduct heat generated in the electrochemical reactions in the catalyst layer to the bipolar plate, which has means for heat removal
- It provides mechanical support to the MEA, preventing it from sagging into the flow field channels.

The required properties of the gas diffusion layer are:

- It must be sufficiently porous to allow flow of both reactant gases and product water
- It must be both electrically and thermally conductive.
- Because the catalyst layer is made of discrete small particles, the pores of the gas diffusion layer facing the catalyst layer must not be too big.
- It must be sufficiently rigid to support the MEA. However, it must have some flexibility to bend/compress under applied pressure to maintain good electrical contact with bipolar plates.

The requirements of a GDL are best met by carbon fiber based materials such as carbon fiber papers and woven carbon fabrics or cloths.

Bipolar Plate

Bipolar plates provide the structural integrity to the stack, along with gas distribution and heat dissipation. The flow field grooves within the plate referred as the ‘channel’ that helps in the uniform distribution of the reactant gasses to the electrode surface. Flow channels are typically rectangular in cross-section, but there are many different channel arrangements available e.g. Pin flow fields, Parallel/straight flow, Serpentine flow fields and dead-ended flow fields etc. The bipolar plates have several functions in a fuel cell. Their required properties follow from their functions are:

- They connect cells electrically in series—therefore they must be electrically conductive.

- They separate the gases in adjacent cells—therefore, they must be impermeable to H_2 and O_2.
- They provide structural support for the stack—therefore, they must have adequate strength, yet they must be lightweight.
- They conduct heat from active cells to the cooling cells or conduits— therefore, they must be thermally conductive.
- They typically house the flow field channels—therefore, they must be conformable.

Since the fuel cell environment is corrosive, the plate also needs to be of high corrosion resistance. Potential materials for plates include metals and graphite. Except for the corrosion resistance, a metal meets all the other requirements. In addition, a thin metal plate can be manufactured by stamping with all the needed features made in one-step, increasing the manufacturing rate and lowing the cost. Widely investigated metal plates include stainless steel, aluminum, nickel, and titanium.

Current collector

The plates, in-between the bipolar plates and the end plates, where the electrons are passed onto an external circuit, called the current collector. Current collectors in contact with the outer surface of the plates enable the measurement of the current and the voltage. The plates are typically made of graphite materials with high corrosion resistance. If metallic materials are used for making the plates, they must be coated by a corrosion resistant material such as gold or metal nitride. The end plates are insulated from the current collectors by the use of insulating materials.

End Plates

The individual components of a fuel cell stack, namely MEAs, gas diffusion layers, and bipolar plates, is held together by filter press arrangement with sufficient contact pressure to prevent leaking of the reactants between the layers and to minimize the contact resistance between those layers. This is accomplished by sandwiching the stacked components between the two end plates connected with several tie-rods around the perimeter or in some cases through the middle. The end plate must be mechanically sturdy enough to support the fuel cell stack, and be able to uniformly distribute the compression forces to all of the major surfaces of each fuel cell of the fuel cell limited compared to having separate bipolar and end plates. Some considerations when selecting the appropriate end plate material are:

- High compressive strength
- Vibration and shock resistance
- Stability over the required temperature range
- Low-cost
- Mechanical stability (providing support for the stack)

The materials that commonly used as end plate are Graphite, Stainless steel, Aluminum, Titanium, Nickel, Metal foams, PVC, Polycarbonate, Polyethylene, Various other polymers etc.

1.1.5 Fuel Cell Thermodynamics and Electrochemistry

The electrochemical reactions in fuel cells happen simultaneously on both sides of the membrane—the anode and the cathode. The basic fuel cell reactions are:

At the anode: $H_2 \longrightarrow 2H^+ + 2e^-$ … (1.7)

At the cathode: $\frac{1}{2} O_2 + 2H^+ + 2e^- \longrightarrow H_2O$ … (1.8)

Overall reaction: $H_2 + \frac{1}{2} O_2 \longrightarrow H_2O$ … (1.9)

The overall fuel cell reaction (given in Eq. 1.9), is exactly same as the reaction of hydrogen combustion.[1] That is an exothermic process, which means that there is energy released in the process:

$$H_2 + \tfrac{1}{2} O_2 \longrightarrow H_2O + \text{heat} \quad \text{… (1.10)}$$

The heat (or enthalpy) of a chemical reaction is the difference between the heats of formation of products and reactants. For Eq. 1.10 the enthalpy of reaction is:

$$\square_r H = \square_f H\ (H_2O) - \square_f H\ (H_2) - ½\ \square_f H\ (O_2) = -286 \text{ kJ/mol} \quad \dots (1.11)$$

Since the heat of formation of liquid water is -286 kJ mol^{-1} (at 25□C) and heat of formation of elements is by definition equal to zero.

The enthalpy of hydrogen combustion reaction is also called the hydrogen's heating value. The heating value is classified on final state of the water produced during the cumbstion. If liquid water is produced then it is known as Hydrogen’s higher heating value (HHV) and is 286 kJ and if water vapors is produced then it is known as the hydrogen's lower heating value (LHV) and is 241 kJ . Hydrogen heating value is used as a measure of energy input in a fuel cell. This is the maximum amount of (thermal) energy that may be extracted from combustion of hydrogen. However, in case of fuel cell electricity is produced directly from the electrochemical combustion of the hydrogen. There are some irreversible losses in energy conversion due to creation of entropy.[28] The portion of the reaction enthalpy that can be converted to electricity corresponds to Gibbs free energy, ΔG, as shown below:

$$\square G = \square H - T\square S \quad \dots (1.12)$$

The values of □G, □H and □S at 25□C are given in Table 1.1

Table 1.1: Enthalpies, entropies and Gibbs free energy for hydrogen oxidation process (at 25°C).

	ΔH ($kJmol^{-1}$)	ΔS ($kJmol^{-1} K^{-1}$)	ΔG ($kJmol^{-1}$)
$H_2 + ½ O_2 \rightarrow H_2O$ (l)	-286.02	-0.1633	-237.34
$H_2 + ½ O_2 \rightarrow H_2O$ (g)	-241.98	-0.0444	-228.74

For a fuel cell, the work is obtained from the transport of electrons across a potential difference. In general, electrical work is a product of charge and potential and described by the relation:

$W = q\ E$ … (1.13)

Where E is the potential (Volts) and q is the charge (coulombs/mol).

The total charge transferred in a fuel cell reaction per mole of hydrogen consumed (q) is expressed as Eq. 1.14:

$q = n\ N_{Avg}\ q_{el} = n\ F$ … (1.14)

Where, n is the number of electrons transferred that is equal to 2 for hydrogen fuel cells, N_{Avg} is the Avagadro number (6.022×10^{23}), q_{el} is the charge of an electron (1.602×10^{-19} coloumbs/electron) and F is the Faraday's constant (96485 coloumbs/mol.electron).

So the electrical work can be calculated as (Eq. 1.15):

$W = n\ F\ E$ … (1.15)

The work is represented by the Gibbs free energy due to the electrochemical reaction:

$W = -\Delta G$ i.e., $-\Delta G = n\ F\ E$

So the cell voltage of the system can be calculated as (Eq. 1.16) when pure hydrogen and oxygen gases were fed at standard conditions.

$$E = -\frac{\Delta G}{nF} = \frac{237.34\ (kJ/mol)}{2\ (electron) \times 96485\ (C/mol\ electron)} = 1.23\ V \qquad \ldots (1.16)$$

The efficiency of any energy conversion device is defined as the ratio between useful energy output and energy input. In case of a fuel cell, the useful energy output is the electrical energy produced, and since the cell operates <100°C the water produced in the liquid state, therefore, the energy input is hydrogen's HHV. Assuming that all of the Gibbs free energy is converted into electrical energy, the maximum possible (theoretical) efficiency of a fuel cell is:

$\eta = \Delta G/\Delta H = 237.34/286.02 = 83\%$ … (1.17)

If hydrogen's LHV is used to express the fuel cell efficiency then the maximum theoretical fuel cell efficiency would be:

$\eta = \Delta G/\Delta H_{LHV} = 228.74/241.98 = 94.5\%$ … (1.18)

The actual fuel cell potential (V_{cell}), and the actual efficiency are lower than the theoretical ones due to various losses (ΔV_{loss}) associated with kinetics and dynamics of the processes, reactants and the products. The actual fuel cell potential given by Eq. 1.19 where E is the reversible open circuit voltage (OCV):

$V_{cell} = E - \Delta V_{loss}$ … (1.19)

For the actual operation of a PEMFC the potential is decreased from its ideal value because of several irreversible losses.[27] These losses are referred to as;

(i) Activation- related losses (ΔV_{act})

(ii) Ohmic losses and (ΔV_{ohm})

(iii) Mass transport related losses (ΔV_{conc})

Cell voltage can be interpreted in terms of these losses such as:

$V_{cell} = E - (\Delta V_{act} + \Delta V_{ohm} + \Delta V_{conc})$ … (1.20)

A typical polarization curve; which represents the cell voltage-current relationship for the ideal and actual conditions are given in Figure 1.8.

- Region of **activation polarization** can be seen at low current densities. Activation polarization means that part of the generated energy is lost in order to raise the reaction rate of electrode reactions due to necessity to overcome activation energies of the reactions. These losses depends on reactions, electrocatalyst material and reactant activities. ΔV_{act} can be written according to the Butler-Volmer Equation (Eq. 1.21);

$$\Delta V_{act} = \frac{RT}{\alpha F}\ln\left(\frac{i}{i_0}\right) \quad \ldots (1.21)$$

where, R is the gas constant, T is temperature, α is transfer coefficient, i is current density and i_o is exchange current density.

Activation losses can also be defined as Tafel Equation (Eq. 1.22):

$$\Delta V_{act} = a + b \log (i_0) \qquad \ldots (1.22)$$

$a = -2.3\frac{RT}{\alpha F}\log(i_0)$ and $b = 2.3\frac{RT}{\alpha F}$, Term b is called the Tafel slope.

- Region of **Ohmic polarization** can be found in the middle-section of the voltage-current density curve. At intermediate current densities, the cell potential drops linearly with current as a result of ohmic losses. These losses are caused by ionic resistance in electrolyte, electronic resistance in electrodes and in other electrically conductive fuel cell components. Therefore, it is clear that these losses depend on material selection. ΔV_{ohm} can be expressed by Ohm's law (Eq. 1.23)

$$\Delta V_{ohm} = i\, R_c \qquad \ldots (1.23)$$

where R_c is the total internal resistance.

- Region of concentration polarization is also called mass transport related losses is observed at high current densities. The transport of the fuel/oxidising gas to the surface of electrodes becomes the major limiting factor and concentration gradients are formed in the system. As consequence the cell voltage, rapidly drops in accordance with the surface concentration of fuel/oxidising gas on the electrodes. Eventually the surface concentration of fuel/oxidising gas become zero, this corresponds to zero cell voltage. ΔV_{conc} can be written according to the Nernst Equation (Eq. 1.24)

$$\Delta V_{conc} = \frac{RT}{nF}\ln\left(\frac{i_L}{i_L - i}\right) \qquad \ldots (1.24)$$

where i_L is the limiting current density.

Then Eq. 1.20 is rewritten as Eq 1.25

$$V_{cell} = E - \frac{RT}{\alpha F}\ln\left(\frac{i}{i_0}\right) - i r_c - \frac{RT}{nF}\ln\left(\frac{i_L}{i_L - i}\right) \qquad \ldots (1.25)$$

Additionally to the mentioned dominant losses there is also crossover losses which can be significant for low temperature fuel cells. Although, the electrolyte is practically impermeable to reactant gases, some small amount of hydrogen can diffuse from anode to the cathode. However, the rate of hydrogen permeation is several orders of magnitude lower than hydrogen consumption rate, therefore, these losses may appear insignificant in fuel cell operation. At open circuit voltage (OCV) these losses may have an effect on cell potential due to the high concentration of hydrogen on the membrane surface and this may lead to a drop on OCV.

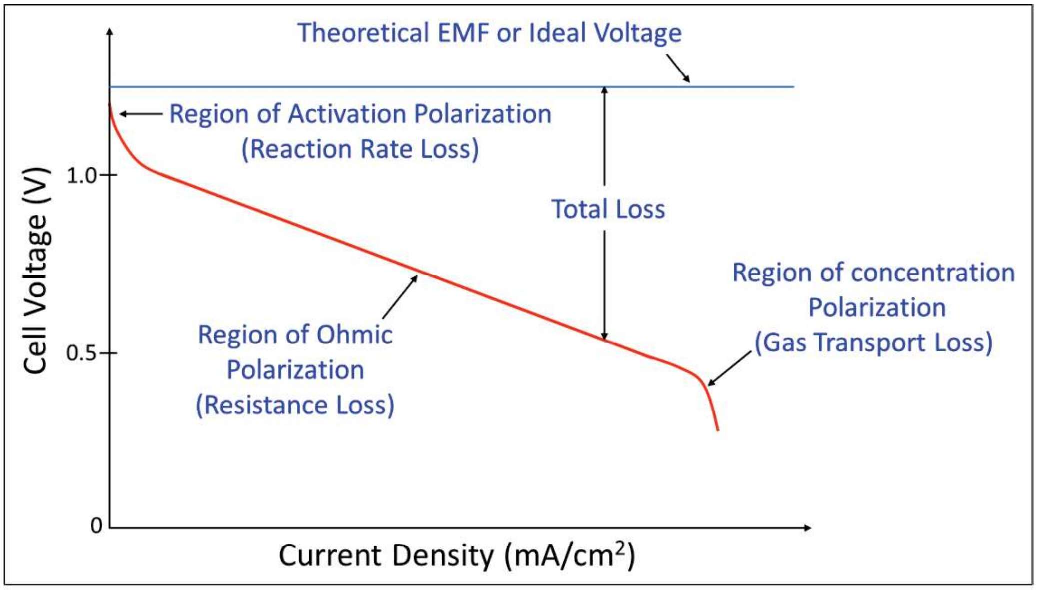

Figure 1.8: Typical polarization curve for fuel cell with significant losses.

1.2 Solid polymer electrolyte/proton exchange membrane

Proton exchange membranes (PEMs) are a key component in PEMFCs and an area of active research in commercial, government, academic institutions and the subject of this research work. In this section, the review of PEM materials is divided into two sections. The first part covers the most important properties of a membrane. The latter part provide the literature review of existing PEM materials for fuel cell application from both academic and industrial research facilities.

1.2.1 PEM Properties and Structure–Property Relationships

In order to perform effectively within a PEMFC, a membrane should possess:

- high proton conductivity
- be impermeable to gases (specifically oxygen) and/or fuel (e.g., methanol)
- achieve balanced water transport
- possess high thermo mechanical and chemical stability to fuel cell conditions and
- be an electrical insulator

Understanding how all of these properties affect the membrane performance in fuel cell is crucial not only to an understanding of PEMs in general but also to obtaining more effective methods for developing new PEM materials. Ideally, a membrane will have excellent performance in all of these areas. However, it is often found that PEMs will generally perform well in some of these areas while performing only adequately or even poorly in others. This section will present separate overviews for each of these properties as well as observed relationships between the chemical and morphological structures of the membranes.

1.2.1.1 Proton conductivity

Proton conductivity is fundamental for proton exchange membrane fuel cells and is usually the first characteristic considered when evaluating membranes for potential fuel cell use. Resistive loss in the fuel cell is proportional to the ionic resistance of the membrane and high conductivity is essential for the required performance especially at high current density.[29] This parameter is intimately connected with both acid and water content of the membrane and is affected by the strength of the acid, the chemical structure and morphology of the membrane, and temperature. Proton conductivity (σ_{H+}) is directly proportional to the activity (A_{H+}) and mobility (μ_{H+}) of the proton via the Nernst-Einstein relationship for the ionic system.

$\sigma_{H^+} = F . A_{H^+} . \mu_{H^+}$ ……… (1.26)

where, F is the faraday constant.

In PEM, the activity (A_{H+}) depends on proton concentration and degree of dissociation of the ionic group. The mobility of protons (μ_{H+}) is affected by factors, such as the proximity of acid-bearing groups, the nature of anions, and the tortuosity of the proton conduction pathway. Therefore, the proton conductivity is largely influenced by the water content vis-à-vis proton concentration. With higher proton concentration, water content increases due to the increased osmotic pressure, this in turn leads to a complete (higher degree of) dissociation of the acid groups, as well as the formation of hydrophilic well connected channels. These results in the increase in the effective proton mobility, in turn the proton conductivity thus increases.

Proton conduction mechanisms in proton exchange membranes

In order to understand the relationship between the proton conductivity, water uptake and morphology of the ion exchange membranes, it is essential to understand the proton conduction mechanism in the ion exchange membrane. Transport of protons in solid polymer electrolytes occurs through water-swollen, hydrophilic channels that form because of nanophase separation of the hydrophilic (acid-bearing functionality) and hydrophobic segments of the polymer. At a molecular level, the proton transport in hydrated polymeric matrices is in general described on the basis of three mechanisms: (A) “proton hopping” or “Grotthus mechanism” (B) “diffusion mechanism” or “vehicular mechanism” (C) Surface mechanism [30], illustrated in Figure 1.9.[30]

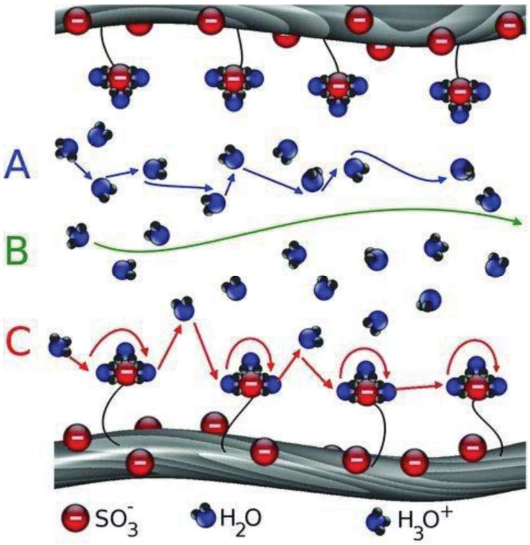

Figure 1.9: Schematic illustration of different modes of proton conduction in a solid polymer electrolyte where A = Grotthus; B = vehicular; and C = surface mechanisms.

Grotthuss or hopping mechanism: In the Grotthuss or hopping mechanism Protons can be perceived as "tunneling" through bulk solution**.** The proton transport occurs via the "passing" of protons from one water molecule to the next by the formation and breaking of O–H bonds, with the main proton carriers being $H_5O_2^+$ and $H_9O_4^+$. The produced proton by oxidation of hydrogen in anode adheres to water molecule than the provisional hydronium ion is formed and one different proton from same hydronium ion hops on the other water molecule. In this mechanism, ionic clusters were swelled in presence of water and formed the percolation mechanism for proton transfer. The simple scheme of the hopping mechanism has been shown in Figure 1.9 A.

Vehicular mechanism: The second mechanism is a vehicular mechanism. It is analogous to the molecular diffusion: i.e., the proton moves as a water-solvated species (e.g., H_3O^+, $H_5O_2^+$, and $H_9O_4^+$). In this mechanism, hydrated proton (H_3O^+, $H_5O_2^+$ and $H_9O_4^+$) diffuses through the aqueous medium in response to the electrochemical difference. In vehicular mechanism, the water connected protons ($H^+(H_2O)_x$) in the result of the electro-osmotic drag carry the one or more molecules of water through the membrane and itself are transferred with them, shown in

Figure 1.9 B. The major function of the formation of the vehicular mechanism is the existence of the free volumes within polymeric chains in proton exchange membrane, which allow the transfer of the hydrated protons through the membrane.

Surface mechanism: The bound nature of the counter anion ($-SO_3^-$ in the case of sulfonic acid-based polymer electrolytes) also presents a third mode for proton transport, namely, surface transport. In the surface transport mechanism, the protons are transported between the adjacent $-SO_3^-$ groups located on the wall of the hydrophilic channel through a series of hops between the $-SO_3^-$ group and nearby water molecules, shown in Figure 1.9 C. This model of transport has a high activation energy.[31]

In systems with relatively high water contents, it is likely that vehicular and Grotthus mechanisms predominate. However, as water content diminishes, the ratio of surface to bulk water decreases, and the surface mechanism becomes increasingly important.[32]

1.2.1.2 Water content

Water plays a vital role in ion exchange membranes. It has a strong influence upon proton conductivity, membranes mechanical strength, form stability etc. on increasing the proton concentration in the membrane, water content increases due to the increased osmotic pressure. The increasing water content in the membrane leads to:

- A complete (higher degree of) dissociation of the acid groups,
- Formation of hydrophilic well-connected channels.
- Increase in the effective proton mobility within the membrane,

This results in the increase in proton conductivity of the membrane. The conductivity increases with the water content up to a point. As the water content increases further, the concentration of protons is diminished and the conductivity is decreased.

Water content of a PEM is commonly described in terms of water uptake (weight% increase for PEM from dry to wet state) and the ratio of moles of water to the moles of acidic group (□). These were determined as per Eq. 1.27 and Eq. 1.28 respectively:

(i) Weight percentage of water in the membrane samples, which is calculated as per Eq. 1.27.

$$\%\,\text{Water Uptake} \;\square\; \frac{(\text{Wt. of wet membrane - Wt of dry membrane})}{\text{Wt of dry membrane}} \square 100 \qquad \dots (1.27)$$

(ii) Ratio of moles of water to the moles of acidic group

$$\lambda = \frac{Moles\ of\ H_2O}{Moles\ of\ SO_3H} \qquad \dots (1.28)$$

$$\lambda = \left(\frac{\text{water uptake}}{18.01}\right)\left(\frac{10}{\text{IEC}}\right) \qquad \dots (1.29)$$

The nature of the water present within a PEM can also have an effect upon its performance during PEMFC operation. At $\lambda > 6$, water exists in the three forms: free water, loosely bound water, and nonfreezable water. Free water has been defined as water that shows the same physical properties (e.g. diffusion coefficient, dielectric constant, and freezing point) as bulk water. Freezable bound water freezes at a temperature below 0°C. Non-freezing bound water is strongly bound to the polymer chain and has been suggested to play the role of a plasticizer.[33] The amount of each of these types of water has been linked to properties such as methanol permeability, electro-osmotic drag, and conductivity.[34]

1.2.1.3 Morphology

One of the most important properties of a PEM is its ability to provide an ionic path for protons to travel from the anode to the cathode. In the case of the majority of PEMs, water-saturated channels are believed to form due to the phase separation of the normally hydrophobic polymer backbone from the hydrophilic, bound sulfonic acid groups. Proton conduction is thought to occur through these channels, mediated by the ionic groups (e.g. sulfonic acid) and in conjunction with water, as discussed in proton conduction mechanisms. The connectivity and the effective mean-free path for protons increase the proton conductivity compare to the tortuous conduction pathway, with a series of dead ends; In fact, Kreuer has previously invoked these concepts of smaller conduction channels and dead ends in order to explain the lower proton mobility in Sulfonated Poly(ether ether ketone) (SPEEK) compared to Nafion.[35]

The distance between acid groups also plays a role in the mobility of protons. As the proton bearing, positively charged species (e.g., H_3O^+, $H_2O_5^+$ and/or $H_4O_9^+$ ions) are transported between the negatively charged, tethered – SO_3^- groups, it may be expected that it will be more difficult for a proton to be transported over the larger distances between – SO_3^- in comparison to the shorter distances between – SO_3^- groups. Therefore, the ‘‘effective’’ proton mobility, greatly depends on the membranes morphology like tortuosity and spatial proximity of neighboring acid groups.

1.2.1. Water Transport

Water is carried into the fuel cell via the humidified H_2/O_2 gas streams entering the gas diffusion electrodes. Combination of water vapor and liquid water passes through each electrode to the electrode/electrolyte interface. Water crossing this interface assists in the hydration of the electrolyte membrane. An additional source of water involves oxygen reduction occurring at the cathode. The transport of water through a PEM consists of a number of different modes. These are schematically illustrated in Figure 1.10. The net water flux through the PEM is a combination of electro-osmotic drag (EOD) and diffusion. EOD is due to the water of hydration that are transported through the membrane as the protons move from anode to cathode, and it is defined by the EOD coefficient, □$_{\text{drag}}$. In addition to water that can diffuse in the same direction, back diffusion of water to the anode is also possible due to the water gradient that occurs with an accumulation of water at the cathode and dehydration at the anode due to EOD. As these processes affect the water content gradient of the membrane, they also have a strong effect upon proton conductivity, which is highly dependent upon water content in sulfonic acid-based PEMs. The EOD coefficient, $\square_{drag}$, is the ratio of the water flux through the membrane to the proton flux in the absence of a water concentration gradient. As $\square_{drag}$ increases with increasing current density during PEMFC operation, the level of dehydration increases at the anode and normally exceeds the ability of the PEM to use back diffusion to the anode to achieve balanced water content in the membrane. In addition, an accumulation of water at the cathode leads to flooding and concomitant mass transport losses in the PEMFC due to the reduced diffusion rate of O_2 reaching the cathode.

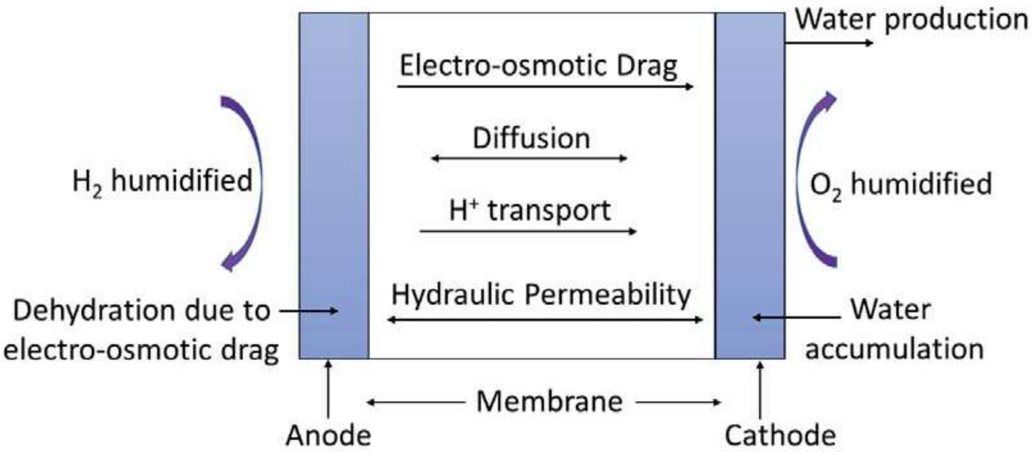

Figure 1.10: Modes of water transport in an operating H_2/O_2 PEMFC.

1.2.1.□ □h□r□o □ □h□□□□l □rop□r□□□□□□ □h□□ □□l □□□□l□y o□□□M□

The stability of membranes against thermo mechanical and chemical stresses is an important factor in determining both their short and long-term performance. Transport and chemical properties of membranes affect the fuel cell performance, while the lifetime of a fuel cell is mostly dependent on the thermo mechanical and chemical stability of the membrane. Thermo mechanical and chemical degradation of a membrane will result in a loss of conductivity, as well as mixing of anode and cathode reactant gases.

Mechanical Properties

Understanding the mechanical properties of the membrane is essential to produce high quality membranes with good durability and long lifetimes under typical fuel cell operating conditions. Previous work showed that the membrane's mechanical damage includes membrane cracks, tears, punctures, and pinholes as a result of uneven stress or other mechanical factors, and is often the main cause of early failures, especially for very thin membranes. The membrane must have good mechanical resistance to stretching and shear in hydrated and dry states. The swelling of the membrane, that is to say, the size variation related to water absorption, should not be too large to minimize shear stresses both in the hydrated and in the dry state. The swelling of the membrane must be controlled to avoid mechanical stress at the electrode/electrolyte interfaces during the cycling of the membrane. In particular, the presence of stresses at these interfaces increases Ohmic losses and reduces the performance of the system with time and cycling. The mechanical properties of the membrane should be tuned because, during MEA assembly, the membrane is pressed onto the electrodes with a clamping force of up to several bars. This operation is necessary to limit Ohmic losses.

Generally, it is the lifetime of the PEM that determines the life of the PEMFC. Thinner membranes, although they increase performance efficiency and proton conductivity, have a lower physical strength and higher gas permeability, allowing more gas crossover, which accelerates degradation. The technology for solid polymer electrolytic membranes calls for the thinnest film that is electrochemically stable. Generally, to get a good compromise between mechanical strength, gas permeability and ionic strength, the membrane thickness varies from 25–150 □m.[36]

Chemical stability:

Chemical stability of PEM is one of the vital property requirement for fuel cell application. It is generally believed that H_2O_2 and its intermediates generated during oxygen reduction and the chemical combination of H_2 and O_2, reduce the lifetime of PEMs by attacking both end-groups and side chains of membrane polyelectrolyte, but there are still controversies in their degradation mechanism and model. There are two different opinions, one group suggest that, the crossover of O_2 from the cathode to the anode through the PEM and formation of $HO_2^{\cdot}$ at the surface of the anode catalyst.[37] On the contrary, other group thought that the formation of $HO\cdot$ and $HO_2\cdot$ radicals due to the reaction of H_2O_2 (which is an intermediate of the two-electron reduction of O_2 at the cathode) with trace metal ions.[38] These radicals have a strong oxidizing power and may attack and destroy the molecular structure of PEMs. Sulfonated aromatic polymers degraded according to two possible mechanisms when oxidized by radicals: the degradation of the polymer main chain and the detachment of the sulfonic acid groups. The former results in stability and lifetime issues for the PEM, whereas the latter results in a decrease in the performance of the PEMFCs.[39]

Fenton's reagent, a mixture of hydrogen peroxide and a ferrous salt, which leads to the formation of hydroxyl radicals, according to Eqs. 1.30 to 1.33, is usually used for accelerated aging tests to evaluate the oxidative resistance of membrane. However, the corresponding experimental conditions are not yet uniform, for example, the concentration of H_2O_2 ranges from 3 to 30 %, the test temperature is from 25 to 80 °C, and the concentration of ferrous salt is from 2 to 30 ppm.[39]

$$H_2O_2 + Fe^{2+} \rightarrow HO^{\bullet} + HO^{-} + Fe^{3+} \qquad \ldots (1.30)$$

$$HO^{\bullet} + Fe^{2+} \rightarrow HO^{-} + Fe^{3+} \qquad \ldots (1.31)$$

$$HO^{\bullet} + H_2O_2 \rightarrow H_2O + HOO^{\bullet} \qquad \ldots (1.32)$$

$$HOO^{\bullet} + H_2O_2 \rightarrow H_2O + HO^{\bullet} + O_2 \qquad \ldots (1.33)$$

1.2.1. Oxygen Permeability and Methanol Crossover

Oxygen Permeability

The membrane serves as both ion conduction medium and reactant separator in a fuel cell. It is well known that the reactant gases crossover from either electrode side to the other results in "chemical short-circuiting" and the decrease in current efficiency. The permeation processes through membranes are governed by the solubility and diffusion of the permeating solute in the membrane at any given temperatures and conditions. The solubility of the solute in polymeric membranes is dependent on the chemical nature of the solute and of the corresponding membrane, while the diffusion is determined largely by the morphology of the membrane and the properties of the solute. The resulting permeation rate is then determined by a complex interplay between the properties of the system, including the morphology of the polymer, restrictions on the ability of the polymer to swell, and the chemical properties of the solute and polymer, such as hydrophilicity or hydrophobicity. It has already been recognized that gases dissolve in both the hydrophobic and the swollen hydrophilic domain, whereas most of the gas transport occurs within the swollen hydrophilic domain.[40,41]

Methanol Crossover

Sluggish methanol (MeOH) oxidation reaction kinetics and MeOH crossover through the membrane are the two major technical hurdles for DMFC technology. Generally, MeOH crossover in the fuel cell may be defined as the phenomenon of MeOH permeating from the anode compartment through the membrane to the cathode compartment. The issue of MeOH crossover in DMFC would result not only in fuel loss but also in an increase in air demand and in a decrease of the cell efficiency due to the reactions and depolarization of permeated MeOH with oxygen at the cathode. Also, the excessive permeation of water to the cathode in liquid feed DMFCs associated with MeOH crossover leads to serious water accumulation on the cathode, necessitating high air flows to alleviate flooding effects. MeOH is transported through the membrane by two modes: diffusion and electro-osmotic drag.[42,43] When MeOH comes in contact with the membrane, it diffuses through the membrane from anode to cathode, and is also dragged along with the hydrated protons under the influence of current flowing across the cell. Therefore, a correlation between the MeOH diffusion coefficient and proton conductivity is observed. The diffusive mode of MeOH transport dominates when the cell is idle, whereas the electro-osmotic drag dominates when the cell is operating, which means that current is flowing across the cell. The MeOH crossover rate is closely related to several factors, including membrane structure and morphology, membrane thickness, membrane acid content, and the cell operating parameters, such as temperature and MeOH feed concentration.

1.2.2 A literature review: Polymer electrolyte membranes for fuel cell application

1.2.2.1 Early Developments

The concept of using ion exchange membranes as electrolytes was first reported by General Electric (GE) in 1955. The idea of using organic cation exchange membranes as solid electrolytes was first described by William Thomas Grubb and Lee Niedrach in 1959.[44] The first PEMFC used in the operational system by the National Aeronautics and Space Administration (NASA) on their first 'Gemini' manned space vehicles. At that time extremely expensive materials were used and the fuel cells required very pure hydrogen and oxygen. The polymer membranes used as electrolytes were based on poly(styrene sulfonic acid).[45] However, these membranes exhibited brittleness in the dry state and were later replaced with cross-linked polystyrene-divinylbenzene sulfonic acid membranes. This material also lacked stability and underwent degradation and suffered other problems. Also, the main problem encountered with these membranes was that proton conductivity was not sufficiently high to reach a power density even as low as 100 mW cm^{-2}. In 1967, DuPont introduced a novel fluorinated polymer based on a polytetrafluoroethylene (PTFE) structure with the trademark Nafion™; this was a real breakthrough in membrane developments for PEM fuel cells. Nafion possessed inherent chemical, thermal, and oxidative stability and it displaced the unstable polystyrene sulfonic acid membranes. At this early stage of development, the most improved membranes showed lifetimes of up to 3,000 h at low current densities and temperatures of 50 ° C.[46]

Membrane materials used for the PEM fuel cell application can be broadly classified as:

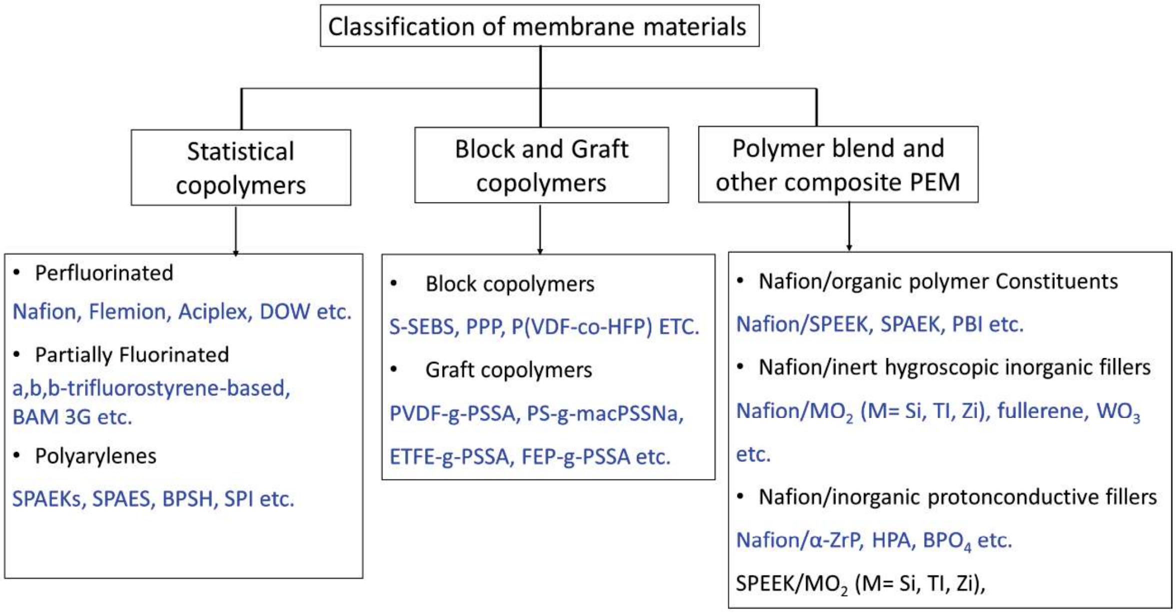

Figure 1.11: Classification of membrane materials.

1.2.2.2 Perfluorinated Membranes

The most successful PEMs to date for the PEMFCs are based on perfluorosulfonic acid (PFSA) ionomers. These membranes have been used in portable, stationary, and automotive commercial applications of PEMFC technology. In addition to providing an attractive combination of performance and reliability, these membranes demonstrated high durability. Perfluorinated PEM is a copolymer of tetrafluoroethylene and sulfonyl fluoride vinyl ether and has a semi-crystalline structure. The PFSA ionomer membranes have unique structure that comprises three domains:

- The PTFE linear backbone that gives the membranes long-term stability in oxidative or reductive conditions and good mechanical strength and structural integrity.
- Side chains of perfluorinated vinyl ether.

- The terminal sulfonic acid moieties –$SO_3^- H^+$ that are highly hydrophilic and gives the membranes desirable proton conductivity when fully hydrated.

Various PFSA polymers have been developed based on the structure of Nafion. These structures vary mainly in monomer repeatability, side chain composition, and length. The general chemical structure of PFSA is given in Figure 1.12. The values of x, y, m and n can be varied to produce material at different equivalent weights (EWs) and pendent side chain lengths. The commercial membranes are listed together with the structure parameters, equivalence weight, and the thickness range in Table 1.2. The equivalent weight being the number of grams of polymer per mole of fixed SO_3 site.[47] The acid capacity of the membranes, typically ranges from 0.67 to 1.25 miliequilivalents per gram, corresponding to 1500 to 800 EW.[48] Nafion membranes (EW ~ 1,100 g/mol) are the most widely used and studied of all the perfluorinated PEMs. Membranes with chemical structures similar to Nafion have been developed, including Flemion, which has a very similar structure to that of Nafion but with lower EW (~1,000 g/mol) and Aciplex (EW ~ 1,000–1,200). Both alternative membranes are said to exhibit similar fuel cell performance to that of Nafion.[47] The Dow Chemical Company manufactured a similar membrane with shorter side chains, which was shown to attain a power density more than double that of Nafion. Due to the higher cost of the Dow monomer in comparison to its Nafion analogue, work on this particular system was halted.

Other companies also developed PFSA membranes based on modifications on the polymers presented in Table 1.2. Examples are Gore with the development of a PTFE stabilized ionomer membrane, also known as the Gore-Select® membrane. Solvay Solexis introduced Hyflon® based on the technology developed by Dow Chemical. The company 3M developed a new polymer with a similar structure but a longer side chain ($n = 4$). Fumatec introduced the perfluorinated fumapem®F membrane based on the fumion® ionomer. Besides all new developments and new products, Nafion® is still the most described PFSA in case of fuel cell application and characterization and is generally taken as reference material in case of PEM development.

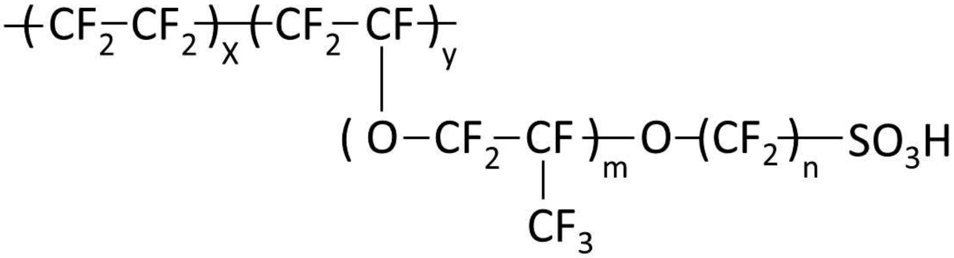

Figure 1.12: General chemical structure of perfluorosulfonic acid.

Table 1.2: Commercial perfluorosulfonic acid membranes (the indication of m, n, x and y are as given in Figure 1.12)

Structure parameter	**Trade name and type**	**Equivalent weight**	**Thickness (□m)**
m =1, n =2, x= 5-13.5, y = 1	Dupont		
	Nafion 120	1200	260
	Nafion 117	1100	175
	Nafion 115	1100	125
	Nafion 112	1100	80
m =0, 1, n =1–5	Asashi Glass		
	Flemion –T	1000	120
	Flemion –S	1000	80
	Flemion -R	1000	50
m =0, n =2–5, x = 1.5–14	Asashi Chemicals		
	Aciplex -S	1000-1200	25-100
m =0, n = 2, x= 3.6–10	Dow Chemical		
	Dow	800	125

Limitations/shortcomings of PFSA membranes:

- High cost resulting from the complicated manufacturing process required.
- Conductivity loss at higher temperatures (above 80°C) or low humidity (below 80% RH),
- High fuel (methanol) cross over.
- Poor mechanical and dimensional stability at high temperature due to its low glass transition temperature (T_g) (80–120°C) (i.e., a structural change from an amorphous plastic state to a more brittle one) that also severely limits their usefulness.
- Environmental friendliness issue due to the fluorinated polymer, in particular in the case of the mass production and disposal of the membranes.

To overcome these disadvantages, considerable efforts have been devoted to modification of conventional polymers or new alternative membranes. There have been no new PFSA membranes synthesized, but many modified conventional PFSA membranes were reported in the last several years. Various different approaches for the modification of PFSA membranes have been explored, including (i) physical or chemical treatment; (ii) reinforcement by porous support materials; and (iii) addition of organic or inorganic compounds.[25]

Various other approaches have been considered to develop new alternative membranes. The first approach includes involves direct sulfonation of non-fluorinated polymer backbones such as polystyrene, polyphosphazene, polyphenylene oxide, polysulfone, polyethersulfone, polyether ether ketone, polybenzimidazole, and polyamides. The challenge in this approach is to achieve sufficient sulfonation for high proton conductivity in the membranes without the polymer becoming soluble. The third approach involves sulfonation of pendent aromatic rings attached to a variety of copolymer (grafted) films obtained by chemical, plasma, thermal, or radiochemical graft copolymerization of styrene monomer.

1.2.2.3 Partially fluorinated

The most studied partially fluorinated ionomers are based on poly(□,□,□-trifluorostyrene) (TFS) and copolymers. The preparation of the TFS monomer was first carried out in 1949 by Cohen et al.[49] A few years later, the TFS monomer was successfully homopolymerized under radical conditions.[50] Hodgdon has investigated the sulphonation of poly(α,β,β-trifluorostyrene) with an applicability to fuel cells..[51] Moreover, Ballard Advanced Materials Corporation developed sulphonated α,β,β-trifluorostyrene membranes under the trade name BAM1G and BAM2G (Ballard Advanced Materials 1st and 2nd Generation, respectively). The longevity of these partially fluorinated membranes were limited to approximately 500 h under practical fuel cell operating conditions.[47] Based on previous work, Ballard provided a novel family of sulphonated copolymers of α,β,β-trifluorostyrene and its analogues, such as m-trifluoromethyl-α,β,β-trifluorostyrene, p-sulphonyl fluoride-α,β,β-trifluorostyrene or p-fluoro-α,β,β-trifluorostyrene – a group of materials referred to as BAM3G (Ballard Advanced Material 3rd Generation).[52] BAM3G membranes exhibited performances superior to the Nafion® and Dow® membranes. The main disadvantages of these membrane are, the complicated production process for the α,β,β-trifluorostyrene monomer and the difficult post sulphonation procedures.[53] Furthermore, the Ballard Company decided to investigate the potential of phosphonic acid-based PEMs. They presented a preparation of phosphonated α,β,β-trifluorostyrene polymers, their characterization, and indications of their fuel cell performance capabilities. The sulphonated materials showed outstanding performance in both oxygen and air conditions, while the phosphonic acid-type membranes showed excellent performance only in the oxygen fuel cells. The BAM membranes showed good stability, and conductivity values ranging from $5□10^{-2}$ to $9□10^{-2}$ S cm^{-1}.

Another strategy used for the synthesis of partially fluorinated ionomer membranes via radiation grafting. There are three steps involved during the preparation procedure: the preirradiation of the base matrix by ionizing radiation, the grafting of a monomer onto the matrix, and the sulfonation of the grafted membrane. The common base fluoropolymer films used for the preparation of radiation-grafted membranes include polytetrafluoroethylene (PTFE),[54-56] poly(tetrafluoroethylene-*co*-hexafluoropropylene) (FEP),[57-59] poly(tetrafluoroethylene)-co-perfluorinated alkyl vinyl ethers) (PFA),[60,61] poly(vinylidene fluoride) (PVDF)[62] etc. The grafting can be initiated by high-energy radiation, e.g., γ-rays, electron-beam and swift heavy ions. Binary monomers of styrene/divinylbenzene (DVB) have been widely used as the graft components.[63] These proton-conducting membranes showed good performance in PEMFCs. A major disadvantage of these membranes is the limited oxidative stability of the styrene and divinylbenzene graft chains due to the presence of the tertiary C-H bonds.[53]

1.2.2. Polyarylene Hydrocarbon Polymer Based Membranes

The challenge is to produce a cheaper material that can satisfy the requirements for the fuel cell application. Some sacrifice in material lifetime with acceptable mechanical properties, provide commercially realistic costs.[21] Good electrochemical properties over a wide temperature range may help the early marketing of PEFCs. Presently, one of the most promising routes to high-performance proton conducting polymer electrolyte membranes is the use of hydrocarbon polymers for polymer backbones. There are many advantages of hydrocarbon polymers that have made them particularly attractive:[21,64]

- Hydrocarbon polymers are cheaper than perfluorinated ionomers, and many kinds of materials are commercially available or can be synthesized with relatively cheap monomers.
- Hydrocarbon polymers containing polar groups have high water uptakes over a wide temperature range, and the absorbed water is restricted to the polar groups of polymer chains.

- Decomposition of hydrocarbon polymers can be suppressed to some extent by proper molecular design.
- Hydrocarbon polymers are easily recycled by conventional methods.
- Many hydrocarbon polymers have high thermal and mechanical stabilities; they can maintain their mechanical properties over a wide temperature range.

During the last two decades, extensive efforts have been made to develop alternative hydrocarbon-based polymer electrolyte membranes to overcome the drawbacks of the current widely used perfluorosulfonic acid ionomer membrane e.g. Nafion. Many hydrocarbon polymers such as polystyrene,[65,66] polybenzimidazole,[67-70] polyphosphazene,[38,71-73] Poly(phenylquinoxaline),[74-77] poly (ether sulfone),[78-80] poly (ether ether ketone),[81-85] and polyimides[86-89] have been developed for fuel cells.

Polystyrene-based membranes

Polystyrene-sulphonic acid (PSSA) (Figure 1.13 (A)) membranes are the oldest commercial hydrocarbon polymer-based materials and their evolution began in 1955 by General Electric.[90] They tested the first polystyrene membranes for PEMFCs and later it was used to produce the operational PEM fuel cells that were first ever employed in one of the Gemini programme space flights organized by NASA. The system, however, exhibited low power density, a short lifetime and low mechanical strength. In the practical fuel cell operating conditions, Reactive intermediates, mainly hydroxyl radicals (HO·) formed that react with PSSA via abstraction of the labile tertiary α-protons of the polymeric chain leading to the formation of a benzyl radical and follow-up chain scission and polymer degradation.[91,92] this degradation, resulting in interrupted regularity in the membrane structure and affect the lifetime of the fuel cell system.[93]

Polybenzimidazole-based membranes

Another frequently mentioned polymer for various types of fuel cell operations specially for high temperature fuel cell is poly(benzimidazole) (PBI)-based membranes. The PBI has aromatic backbone, which gives excellent thermal stability with a glass transition temperature of 430ºC along with high mechanical strength and good chemical inertness. Fully aromatic PBIs are polybenzimidazoles out of which □□□-type poly[2,2'-(□-phenylene)-5,50-bisbenzimidazole]) (□PBI) (Figure 1.13 (B)) and the □□□-type poly[2,2'-(□-phenylene)-5,50-bisbenzimidazole]) (□PBI) are popoular among them. Such kind of PBIs are mainly synthesized by the polycondesation reaction between aromatic amines and aromatic acids (or their derivatives) and self-condensation involving 3,4-diamino acids. The PBI is not a proton conducting polymer by itself and cannot be used as PEM. To ensure proton conductivity, Savinell et al. presented polybenzimidazole impregnated with phosphoric acid (PA).[67-70] So far, such polymers doped with H_3PO_4 are one of the most attractive alternatives to Nafion for high temperature polymer electrolyte membrane fuel cells. The PBI/H_3PO_4 membrane was found to exhibit low gas permeability, excellent oxidative and thermal stability, and good flexibility at temperatures up to 200–230 °C. The properties of such doped membranes and their application in PEM fuel cells and in cells using hydrocarbons and methanol as fuels have been systematically studied by Wang et. al. [70,94-96] and others.[97-100]

In another attempt, PBI is modified by sulfonation to make it an intrinsic proton conductor. This treatment leads to a significant increase in the conductivity. Staiti et al.[101], for the first time presented the synthesis and characterization of sulfonated PBI based membrane. Membranes consisting of sulfonated poly(benzimidazole) showed low proton conductivity values, which is probably due to a strong interaction between protons and nitrogen atoms of the imidazolium ring in poly(benzimidazole). The strong interaction between the basic nitrogen and sulfonic acid groups in sPBI induced crystallinity, making the semi-crystalline polymer insoluble in common aprotic solvents. An extensive review of PBI membranes together with possible modifications for fuel cell applications is given by Li and Jensen.[46]

Polyimides-based membranes

Polyimides represent yet another plausible alternative to the PFSA membranes due to their excellent thermal stability, high mechanical strength, good film-forming ability and significant chemical resistance. The aromatic polyimides are compounds containing an imide heterocyclic structure in their backbone. Polyimides can be sulfonated, thereby improving the overall intrinsic proton conductivity and hydrophilicity of these membranes and thus, sulphonated polyimides (SPIs) (Figure 1.13 (C)) have been developed as promising candidates for PEMFCs.[86] The use of polyimide membranes in fuel cell applications was first presented by Faure et al.[88] N. Cornet et al. have synthesized a number of sulfonated polyimides based on 4,4'-diamino-biphenyl 2,2' disulphonic acid (BDSA), 4,4'-oxydianiline (ODA), 4,4'-oxydiphthalic acid (OPDA) and 1,4,5,8-naphthalene tetracarboxylic dianhydride (DNTA) polymers.[87,89,102] They have studied the membrane's electrochemical and structural properties and performance in fuel cell. Zhang and co-workers have synthesized many covalently cross-linked SPI membranes for fuel cell application.[102]

Polyphosphazene-based membranes

Polyphosphazenes are an alternative class of polymers for proton exchange membranes. They are unique hybrid polymers, which contain a backbone of alternate nitrogen and phosphorous atoms with two organic, inorganic or organoetallic side groups attached to each phosphorus atom, shown in Figure 1.13 (D). The polymers are of interest to many research groups because of the opportunities they provide for structural diversification via the introduction of a vast range of side groups, which allows obtaining an unprecedented and largely controlled variety of desirable properties. Polyphosphazenes have several advantages over established hydrocarbon based polymers. One of their prime attributes is the thermal and chemical stability of the polymer backbone, both phosphorus and nitrogen are in their highest oxidation states resulting in a high degree of thermo-oxidative stability. The first attempt to develop the polyphosphazene solid electrolyte took place in 1984 and was published by Blonsky and Shiver.[71] It was Allcock et al. who reported the first synthesis of polyphosphazenes with sulphonic groups (S-PPZs) which would be a proton-conducting material for fuel cell applications.[72] Pintauro and co-workers synthesized many S-PPZs based membranes and studied their electrochemical properties.[73,103] Guo et al.[38,104] described the sulfonation of poly(bis(3-methylphenoxy)phosphazene) and obtained promising results for DMFC.

Poly(phenylquinoxaline)s -based membranes

Poly(phenylquinoxaline)s (PPQs) are a class of high-temperature/high-performance thermoplastics that have many desirable properties such as high glass transition temperatures, low dielectric constants, high chemical resistance, excellent mechanical properties, and high thermooxidative stability. These properties make these polymers a suitable candidate for the development of PEMs for fuel cell. The pendant phenyl groups improve the solubility and processing characteristics of these polymers, shown in Figure 1.13 (E)). Since the first synthesis of conventional PPQs, which were prepared from bis(o-diamine) and bis(α-diketone) monomers, extensive research has been carried out in their synthesis and characterization.[74,105-107] Kopitzke and coworkers reported a “soak-and-bake” method for the development of a sulfonated PPQ (sPPQ) film suitable for low temperature fuel cell applications.[75,77]

Ballard Advanced Materials also attempted to produce sulfonated PPQ membranes for use as low temperature, direct methanol PEM fuel cells. The first series of polymers investigated were based on sulfonated PPQs prepared via the self-polymerization of 4-(6-fluoro-3-phenylquinoxalin-2-yl)phenol in m-cresol, followed by soaking the resulting membranes in chlorosulfonic acid. This first generation of Ballard PPQ membranes, termed

“BAM-1G”, were evaluated as single cells with an active area of 50 cm^2 operating on hydrogen and air (H_2:Air = 42:24 psig) at 70 °C.[75] The BAM-1G membrane was shown to have good mechanical properties and promising initial fuel cell performance, similar to that of Nafion® 117. Furthermore, BAM-1G was shown to have good polarization curve performance. The major disadvantage of this membrane, however, was extremely short lifetime.

Poly (aryl ether sulfones)-based membrane

Poly(aryl ether)-type polymers (PAEs) are a class of high-performance engineering thermoplastics known for their excellent combination of chemical stability, physical and mechanical properties. Many kinds of PAEs containing ketone, sulfone, and nitrile groups have gained significant importance to develop conductive ionomers. In the field of proton conductive membranes for fuel cells, poly(arylene ether ketone)s and poly(arylene ether sulfones) are the most intensively studied non-fluorinated polymers. Poly(arylene ether sulfones) (PESs) are thermoplastics having excellent thermal and mechanical properties, durability under highly acidic conditions, and relatively low manufacturing cost. The basic repeat units in this family of polymers consisting of phenyl rings separated by alternate ether and sulfone ($-SO_2-$) linkages, shown in Figure 1.13 (F). Modification of poly(arylene ether sulfones) by addition of sulfonic acid using various reagents has been investigated extensively. This is extensively reviewed by Kerres.[53,108] Poly(arylene ether ketone)s, the other type of poly(arylene ethers), is in the focus of this thesis and is, therefore, discussed separately and more profoundly in the following section.

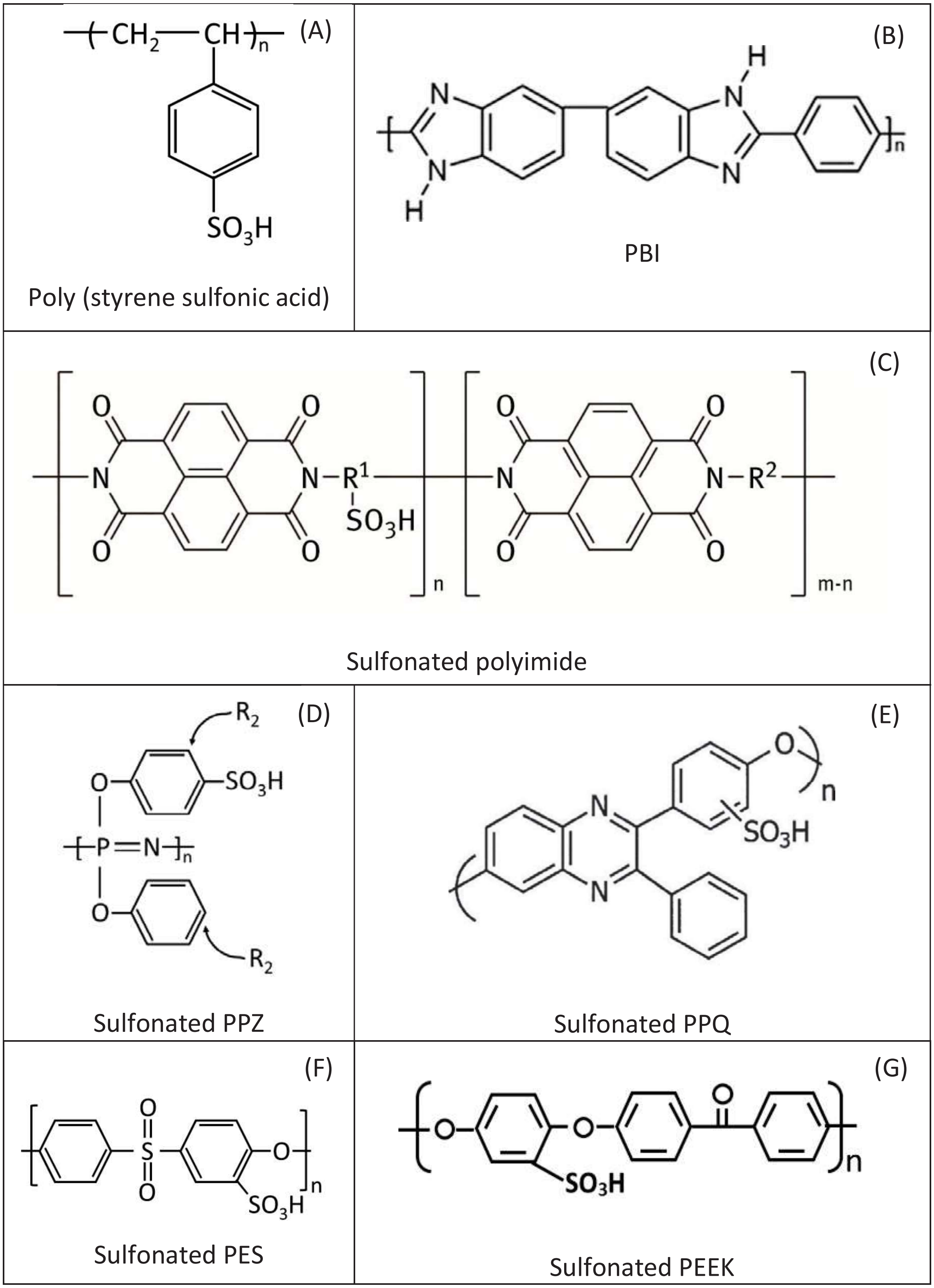

Figure 1.13: Chemical structure of polymer electrolyte membranes based on hydrocarbon polymers.

A number of other hydrocarbon polymer-based ionomeric membranes containing aryl-groups in the polymer backbone have been proposed for usage as proton exchange membranes. Their stability features and relatively low costs make them very attractive. Poly(phenylene oxide) is a promising polymer type, because of the diversity in reactions to modify the polymer structure. The best known sulfonated poly(substituted-phenylene oxide)s are sulfonated poly(2,6-dimethyl-1,4-phenylene oxide) (sPPO),[109] and poly(2,6-diphenyl-4-phenylene oxide) known as Ballard Advanced Materials, BAM2G membrane. Another polymer type in this series is poly(phenylene sulfide) , which becomes water soluble when the sulfonation degree is > 30%.[110] Rikukawa and co-workers prepared sulfonated poly(4-phenoxybenzoyl-1,4-phenylene, Poly-X 2000) (SPPBP) by post-sulfonation reactions of corresponding parent polymers. They found that SPPBP, which has pendant side chains between polymer main chain and sulfonic acid groups, showed higher and more stable proton conductivity than SPEEK.[76]

Due to the volume of work in the field of polymeric fuel cell membranes, it will go too far to describe all (co)polymers which have been synthesized and functionalized and of which membranes were prepared for testing the fuel cell characteristics. Various authors have composed extensive reviews where non-fluorinated ionomers for fuel cells are described.[21,25,26,36,53,64,110-115] From this point, the focus of this thesis lies on the sulfonated poly(arylene ether ketone)s, its structure variations and their modifications.

1.3 Poly (aryl ether ketone)

The poly(aryl ether ketone)s (PAEKs)-based membranes are one of the most promising alternatives for PEMs because of their availability, processability, excellent thermal and chemical stability, good mechanical properties, and low cost.[25] The (PAEKs) are a family of polyarylenes linked through varying sequences of ether (E) and ketone (K) units. The PAEK polymer family includes poly(ether ketone)s (PEKs), poly(ether ketone ketone)s (PEKKs), poly(ether ether ketone)s (PEEKs), poly(ether ether ketone ketone)s (PEEKKs) and poly(ether ketone ether ketone ketone)s (PEKEKKs). Among all PAEKs, The poly(ether ether ketone) [poly(oxy-1,4-phenylene-oxy-1,4-phenylene-carbonyl-1,4-phenylene)] polymer is most readily available commercially and has probably been more broadly and extensively studied in recent years than any other non-fluorinated system, with contributions from Kreuer, Kerres, Bauer, Rozière, and their co-workers and others. It is a promising alternative to PEMs due to their wide range of advantages such as good mechanical properties, outstanding thermal and chemical stability, facile processability, high availability and also low cost. The aromatic rings support various electrophilic or nucleophilic modifications. A number of studies have been done on this polymer ranging from modeling of the microstructure, proton transport properties, application in low- and medium-temperature PEMFC and DMFC, and as a component of polymer blend and hybrid inorganic-organic membranes.

1.3.1 Sulfonated poly (ether ether ketone)

The PEEK polymer is an aromatic, high performance, semi crystalline polymer with extremely good thermal stability, chemical resistance and mechanical properties. The PEEK polymer, itself is not a proton conducting polymer and cannot be used as a PEM. The most common way to modify PEEK for application as a PEM is to employ sulfonation method. Sulfonation is an electrophilic substitution reaction where a sulfonating agent reacts on the aromatic rings and their protons are substituted by sulfonic acid group. Two different synthetic approaches have been reported for the introduction of sulfonic acid groups; (i) post sulfonation of PEEK, (ii) direct copolymerization of sulfonated monomers. Post-sulfonation is attractive because of the availability of inexpensive commercial high molecular weight (MW) thermoplastic starting materials as well as relatively simple reaction procedures, enabling the process to be readily scaled up. Whereas the sulfonated monomers are less available because it is not easy to control the substitution sites of the small-MW compound in the sulfonation process and to purify the sulfonated monomers.[46]

Various sulfonating agents, such as concentrated sulfuric acid, fuming sulfuric acid and chlorosulfonic acid, can be used for sulfonation. Fuming sulfuric acid and chlorosulfonic acid are much stronger sulfonating agents than concentrated sulfuric acid, resulting in less controllable sulfonation reactions accompanied by side reactions. Here, the reaction site selectively occurs on the electron-rich site of benzene rings, such as the ortho-position to the electron donating groups. Electron-withdrawing groups deactivate benzene rings to electrophilic sulfonation. The presence of adjacent ortho-directing ether groups confers highest reactivity to the four equivalent sites on the hydroquinone unit situated between the ether segments. Therefore, O-phenyl-O units are preferentially sulfonated, whereas O-phenyl-CO groups remain unsulfonated due to the electron-withdrawing nature of the carbonyl group,[64] shown in Figure 1.14. The sulfonation rate of PEEK in concentrated sulfuric acid can be controlled by changing the reaction time, temperature, and acid concentration. A kinetic study on these parameters was done by Huang et al., who also reported that the sulfonation of PEEK is a second-order reaction.[116] The sulfonation of PEEK is generally expressed in the terms of the degree of sulfonation (DS) which defines as the ratio of sulfonated segments to the total amount of segments present in the polymer. To achieve a high proton conductivity (similar to nafion) a high DS is required. However, the mechanical and dimensional properties of SPEEK tend to deteriorate progressively with increasing degree of sulfonation[117] and membranes are vulnerable to radical attacks and degradation processes.

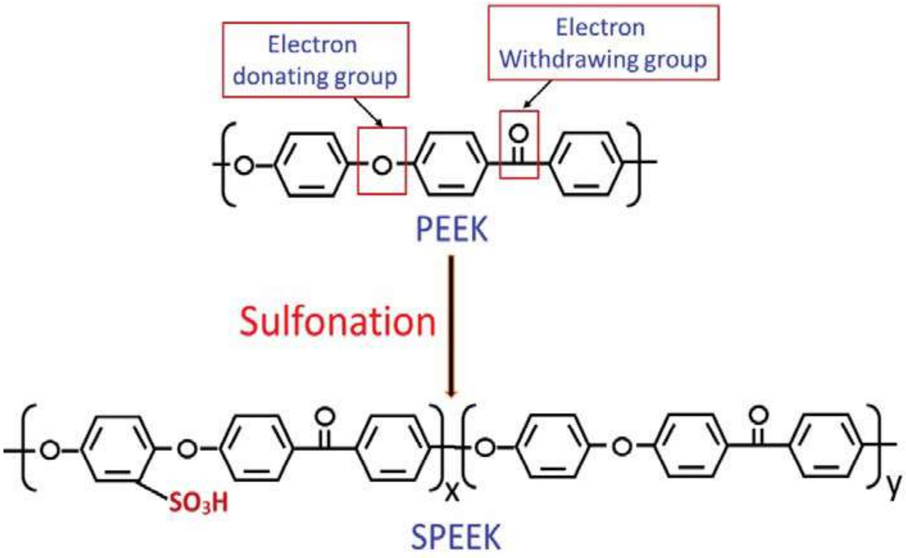

Figure 1.14: Sulfonation of poly(ether ether ketone) (PEEK).

A fundamental work was carried out by Kreuer.[35] Who made a comparison between the morphology of Nafion® and sulfonated PEEKK based on a network model. It was found, that the transport properties and morphological stability between both systems are distinctly different. Sulfonated polymers generally have lower proton conductivities and higher dimensional swelling compared to PFSAs For a given ion exchange capacity (IEC), because of their lower acidity, lower hydrophobicity of polymer backbone, and weaker phase separation between hydrophilic and hydrophobic moieties, resulting in less effective micro phase separated morphology for water channel formation [35]. This is schematically represented in Figure 1.15. Generally the Hydrophilic domains facilitate ion, liquid, or gas transport, whereas hydrophobic domains impart mechanical, chemical, or thermal stabilities. The effective formation of well-connected water structures for rapid proton conduction has been achieved by the polymer architecture (such as random copolymer, block copolymer, grafted copolymer, and densely sulfonated or clustered copolymer),[118-121] introducing Cross-linking units,[122,123] and inorganic/organic materials[124-126] into polymers.

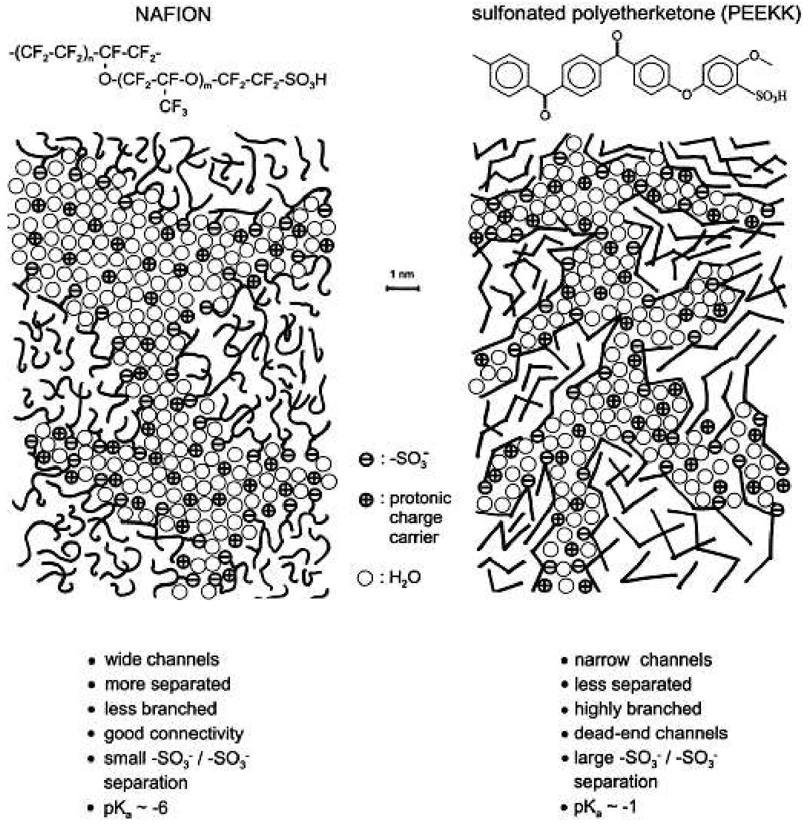

Figure 1.15: Schematic representation of the microstructures of NAFION and a sulfonated PEEKK

1.3.2 Modified poly(ether ether ketone) based membranes

In order to improve the thermal, mechanical properties and chemical stability along with a good conductivity, many modifications have been carried out, like cross-linking[39,127], blending with other polymers[128,129], an addition of inorganic moieties[130,131] etc. A number of different types of inorganic fillers such as hygroscopic oxides, surface modified oxides, zeolites, inorganic proton conductors and so on have been reported in literature. In this section a literature review of some of the modification approaches used for the properties improvement of SPEEK polymer is given in detail.

Blending

Polymer blending method have been widely used to improve the chemical and mechanical stabilities of the SPEEK polymer-based membrane. Wu et al. reported on polymer blends of

SPEEK with poly(ethersulfone) (PES),[78] poly(amide imide) (PAI),[132] and poly(vinylpyrrolidone) (PVP)[133]. This was done with the purpose to stabilize the SPEEK structure. There was a specific interaction between SPEEK and PES, which lead to the non-linear behavior in the water uptake, proton conductivity and methanol permeability. The sPEEK/PES blend membranes showed moderate proton conductivity, lower methanol permeability, water and solvent uptake compare to the pristine SPEEK. On the other hand, the water uptake of SPEEK was significantly reduced by blending with PAI. However, the adsorption of the blend membrane in concentrated methanol solution remained high. In the case of SPEEK/PVP, membranes there was an acid-base interaction occurs on the sulfonic acid group and on the tertiary amide group reduced methanol uptake and to decrease methanol permeability while maintaining high proton conductivity. In literature, various reports are available on SPEEK/PBI blend membranes.[134-137] These membranes show as a main benefit the low methanol crossover. Nevertheless, some drawbacks are present in this kind of blended membranes such as reduced water uptake and, particularly, inhomogeneity of the blend owing to the poor solubility of PBI. These membranes also present poor conductivity. Pasupathi et al.[134] reported on the SPEEK/PBI acid-base polymer blend. These membranes were studied with DMFC tests and their performance was found to be considerably better than that of commercial Nafion®117 membranes. These polymer blends were found to be extremely stable under DMFC operating conditions up to 60 °C. SPEEK with different sulfonation degrees were blended with various PVA contents by Yang.[138] PVA exhibits high methanol resistance and the large quantities of hydroxyl groups in PVA might interact with sulfonic acid groups of SPEEK. The uptake of blend membranes in water increased with the increasing PVA content, while the absorption of blend membranes in methanol solution showed a decrease upon the PVA content, which can minimize the swelling ratio of electrolyte membrane in DMFC applications. The sPEEK/PVP polymer blends showed acid-base interactions. sPEEK with a sulfonation degree of 69% blended with PVP showed decreasing proton conductivity with increasing amount of PVP. The water and methanol uptake showed best values when the PVP content was between 20% and 30%. DMFC tests with a SPEEK/PVP membrane (ratio of 4) showed better performance than Nafion®. An extensive review about ionomer blend with various interactions, e.g., covalently cross-linking, hydrogen-bridge and acid-base interactions, is given by Kerres.[139]

Cross-linking

Cross-linking is an effective and simple method of improving the chemical and mechanical stabilities of the polymer membrane. Moreover, polymer morphology is also transformed during the cross-linking process. In literature, various cross-linking methods have been suggested by different research groups[53,83,140-144], Cross-linking of sulfonated aromatic hydrocarbons can be achieved through bridging the reactive sulfonic acid group available in the polymer. The bridging can be brought about either by inter-chain self-condensation or through cross-linker involving sulfonic acid groups. The first reported cross-linking of SPEEK was carried out using suitable aromatic or aliphatic amines and formation of imide linkages, which are acidic and supposed to participate in proton transfer and thus contributing to proton conductivity of the polymer [140,141]. Kerres et. al.[53,143,144] have carried out extensive studies on the development of covalently and ionically cross-linked sulfonated polyarylenes and reported that the covalent cross-linking enhanced the thermal stability, however, the final product was brittle. Ionically cross-linked membranes were prepared by blending the acidic ionomers with basic (aminated) polymers in binary and ternary compounds. Another method of cross-linking of SPEEK through intra/interchain condensation of sulfonic acid functionalities, that is initiated simply by appropriate thermal treatment, was introduced by the authors of a US patent.[145] This method was further implemented by Mikhailenko. et al., using simple polyatomic alcohols (ethylene glycol, glycerol), as cross-linker in different solvent/solvent pairs [83]. Other groups also studied the effect of cross-linking on membrane properties by using different aliphatic, cyclic and aromatic diols.[146,147] Cross-linker structure also affects the morphology of the membrane, the aliphatic cross-linker induces hydrophilic clusters that are smaller and more connected than the aromatic cross-linkers.[148]

SPEEK/HPAs hybrid membranes

The incorporation of solid heteropolyacids (HPA) into partially sulfonated PEEK polymeric matrix constitutes a fruitful approach to enhance the SPEEKs proton conductivity. Zaidi et al.[81] prepared a series of composite membranes by incorporation of tungstophosphoric acid, its disodium salt and molybdophosphoric acid into partially sulfonated PEEK polymer. These membranes exhibited a rather high conductivity of 10^{-2} S cm^{-1} at ambient temperature and up to a maximum of about 10^{-1} S cm^{-1} above 100°C. They also reported the higher T_g of composite membranes than the pristine SPEEK membranes with a thermal stability up to around 250°C. The only drawback of HPAs, is its high solubility in water or polar solvents, owing to their low surface areas (5 to 8 m^2 g^{-1}). The high solubility leads to leaching of these acids from the membrane and deteriorates the overall performance of the fuel cell.[149] To overcome this drawback two different methods have been used. HPA's are either embedded in support materials such as inorganic oxides that have a high surface area (e.g. ZrO_2, TiO_2, SiO_2, Al_2O_3), or their protons are exchanged with other cations such as Cs^+, NH_4^+, Rb^+ and Ti^+.[150] A drawback to this technique is the resulting large size of the heteropoly salt particle, which decreases the conductivity, and possibly reduces the thermal stability of the composite.[151] A series of work has been reported by different research groups to synthesize SPEEK-heteropoly acid,[152] SPEEK and modified heteropoly acid composite membranes.[153-155] Dogan et al.[156] prepared composite membranes based on Cesium salt of tungstophosphoric acid (Cs-TPA) and SPEEK with two sulfonation degrees (DS), 60 and 70% have been used and examined both the effects of Cs-TPA in SPEEK membranes as functions of sulfonation degrees of SPEEK and the content of Cs-TPA. These membranes showed low methanol, water vapor, and hydrogen permeability, promising proton conductivity value, improved chemical stability, thermal properties and hydrolytic stability. S.Y. Oh et al. synthesized various composite membranes based on Cs^+-substituted heteropoly acids (Cs-HPAs) and SPEEK for application in fuel cells. These membranes showed improved proton conductivity and fuel cell performance.[155] composite membranes based on SPEEK and tungstosilicic acid loading on silica-alumina mixtures with various compositions was prepared by Ismail et al. Promising results in terms of selectivity of proton conductivity to methanol permeability were obtained with high HPA loading and high silica content in the inorganic composition.[157]

SPEEK/MO_2 (M = Si, Ti, Zr) membranes:

Among the various organic/inorganic composite membranes, the hygroscopic oxides, such as SiO_2, TiO_2 and ZrO_2 based composite membranes were most thoroughly studied. Oxides of Si, Zr, and Ti were doped in SPEEK membranes to reduce their swelling and fuel crossover.[158-166] Nunes et al.[158] synthesized various composite membranes based on SiO_2, TIO_2 and ZrO_2 in SPEK and SPEEK polymers by in situ hydrolysis of different alkoxides of Si, Ti and Zr. They reported that ZrO_2 modified SPEEK membrane with a 60-fold reduction of the methanol flux, with a conductivity reduced a 13-fold. However, organically modified SiO_2 nanocomposite membrane showed a 40-fold reduction in water permeability without any deterioration in proton conductivity. Incorporation of ZrO_2 in SPEEK (87% degree of sulfonation) enabled suitable PEMs for DMFC applications.[159] In general, incorporation of inorganic oxides into reduces proton conductivity, swelling and fuel permeability, due to interconnected inorganic network formation.[160] I. Colicchio et al.[161] prepared SPEEK–silica nanocomposite membranes by conversion of polyethoxysilane (PEOS) into silica via water free sol–gel method. The conversion of PEOS into silica during membrane formation induces changes in the hydrophobic–hydrophilic phase separation of the pure ionomer, influencing morphology and proton mobility. Addition of nonconductive inorganic fillers deteriorates the proton conductivity, but at 90% RH the proton conductivity of these composite membranes was higher than the pristine ionomer. Nanocomposite PEMs with low polyethoxysilane content (10 and 20 wt%) are more stable upon successive heating/cooling measuring cycles, and less dependent on membrane hydration than for the pristine membrane. Sol-gel derived silica additives (silica and functionalized silica)-SPEEK-nanocomposite membranes (with 5% and 10% silica loading) exhibited low water uptake, improved proton conductivity (0.05 S cm^{-1} at 80°C and 75% RH) and reasonable PEMFC performance at 80 °C and 75% and 50% RH.[162] TiO_2 has also been used as a filler to alter the transport properties of SPEEK membranes, using either a basic catalyst (pyridine) or a chelating agent (2,4-pentandione) to control the inorganic network features in the SPEEK matrix.[163] Sol–gel derived SPEEK-TiO_2 hybrid membranes (with varied nano-sized TiO_2 content) showed improvement in water uptake and its retention along with reduction in methanol permeability.[164]

Various other inorganic additives have been used by different research groups to modify the properties of SPEEK polymer-based membranes. Chang et al.[167] Prepared SPEEK based composite polymer membranes by embedding layered silicates, laponite and montmorillonite (MMT) into SPEEK membranes for fuel-cell applications. They found a reduction in swelling and methanol permeability. These membranes showed better performance in H_2/O_2 fuel cell tests than the pure SPEEK membrane but were inferior to Nafion. In addition to laponite and MMT, Karthikeyan also investigated magadiite.[168] Composite system with laponite and magadiite showed similar methanol behavior and proton conductivity. Gaowen et al. added organically modified MMT to SPEEK with a DS of 65%. They reported that SPEEK intercalated into MMT and that the organic modification of MMT is a necessary step to incorporate nanosized MMT in the SPEEK matrix. In these membranes, the reduction in methanol permeability was more pronounced than the decrease in proton conductivity. Gosalawit et al.[169] synthesized nanocomposite membranes by the incorporation of sulfonated MMT (SMMT) into SPEEK. They reported that the nanocomposite membranes form stability, as well as the mechanical stability increases with the SMMT loading. The proton conductivity of the hybrid membranes with SMMT was significantly higher than the membranes with nonsulfonated MMT. The methanol permeation remained low, resulting in DMFC performance remarkably better than Nafion® and pure SPEEK. Erce et al.[170] prepared zeolite based SPEEK nanocomposites with various silica/alumina compositions. The proton conductivity of the composite membrane consisting of zeolite beta fillers into SPEEK was a factor of two higher than the plain SPEEK membrane. The composite membranes could further be stabilized by blending SPEEK with SPES, resulting in better fuel cell performance. Zirconium phosphate (ZrP) is another inorganic modifier which has been extensively used by different research groups to improve the SPEEK polymer properties. Tchicaya-Bouckary et al.[171] described the in situ precipitation of Zirconium phosphate (ZrP) in SPEEK membranes. A composite membrane with 25% loading was compared to SPEEK and both membranes showed similar proton conductivity and fuel cell tests results. Composite membranes with various zirconium phosphate and zirconia combined composition were described by Nunes et al.[158] It was shown that the zirconia present in the polymer matrix had an amorphous structure leading to a well-associated network. A good balance of high conductivity and low water and methanol permeability was possible with a mixed zirconia-zirconium phosphate inorganic phase.[172] Tripathi et al.[173] studied zeolite-ZrP incorporated inorganic system in a SPEEK matrix. These additives improved the thermal, mechanical strength, oxidative and dimensional stabilities along with water retention capacity of the membranes. With an increasing amount of ZrP, the methanol permeability was reduced and the proton conductivity increased. The properties of differently modified SPEEK membranes are given in Table 1.3, particularly those used in fuel cells (H_2/O_2 and methanol) operating at low/medium temperature.

Table 1.3: Properties of derivative, composite/hybrid and cross-linked, SPEEK based membranes for fuel cell application: literature references are given in the last column.

Membrane	**SPEEK DS (%)**	**W.U. (%) 25 °C**	**MeOH permeability [cm^2/s] (25°C)**	**Conductivity [S/cm]**		**Casting Solvent**	**Ref.**
				25 °C	**80 °C**		
SPEEK/PBI (5%)	82	35	5□10^{-7}	4.6□10^{-2}	8□10^{-2}	DMAc	136
SPEEK/PBI (20%)	36	13	0.3□10^{-7}	1□10^{-2}	2.2□10^{-2}	DMAc	136
S-PEEK/PANI	44.5	92	2.1□10^{-7}	-	1.8□10^{-3} [a]	DMF	82
S-PEEK/WC	82	-	1.9□10^{-6}	-	2.5□10^{-2} [b]	DMF	174
S-PEEK/WC	99	17	-	-	5.4□10^{-2}	DMF	175
S-PEEK/WC	90	21	-	-	2.5□10^{-2} [a]	DMF	176
SPEEK/TPA (60%)	70	64		3.5□10^{-3}	1.7□10^{-2} [a]	DMAc	81
SPEEK/MPA (60%)	70	94		3.1□10^{-3}	1.1□10^{-2} [a]	DMAc	81
SPEEK/NaTPA	70	143		2.9□10^{-3}	1.5□10^{-2} [a]	DMAc	81
SPEEK/BPO$_4$ (20%)	72	74		5.1□10^{-3}	3.8□10^{-2}	DMAc	84
SPEEK/BPO$_4$ (40%)	72	116		6.1□10^{-3}	4.5□10^{-2}	DMAc	84
SPEEK/SiO$_2$ (10%)	64			3.1□10^{-3} [d]	5.7□10^{-3}	DMAc	161
SPEEK/TiO$_2$ (5%)	90				5.8□10^{-2} [c]	DMAc	177
SPEEK/TiO$_2$ (8%)	100	61.5	5.87□10^{-7}		9.6□10^{-2}	NMP	164
SPEEK/ZrO$_2$ (7.5%)	87	5		70□10^{-3}		DMSO	159
SPEEK/ZrO$_2$ (10%)	65	35		17□10^{-3}	2.8□10^{-2}	DMAc	165
SPEEK/CeO$_2$ (2.5%)	65	27				DMAc	178
SPEEK/silica/PWA (77.7/20.2/2.1)	64			3□10^{-2}	5□10^{-2}	DMAc	154
SPEEK/Cs-TPA (10%)	60	30	4.7□10^{-7}		13□10^{-2}	DMAc	156
SPEEK/ Cs-TPA	65	40			2.6□10^{-3}	DMAc	155
SPEEK/TPA/MCM-41 (70/15/15)	55		2.81□10^{-8}	2.7□10^{-3}		DMAc	179

a = 100°C, b = 115°C, c = 120°C, d = 40°C

1.4 Motivation and need of the present research work

The rising global energy demand and the environmental impact of conventional energy sources pose serious challenges to human health, energy security, environmental protection and the sustainability for natural resources. There is a need of reliable green technologies for the sustainable development of society. Hydrogen and Fuel cells are an integral part of the clean energy portfolio; Hydrogen as an energy carrier and fuel cell as a system for energy conversion or power generation with zero emission. PEMFCs are potentially one of the best candidates to replace conventional internal combustion engines in automobiles, stationary power and batteries in portable electronic devices because of their high power density and efficiency, low operating temperature and fast start-up. In the last few decades, much effort has been devoted to development of PEMFCs, and significant advancement has been achieved. However, their commercialization has not yet been achieved and the major problem is the prohibitive cost and durability of the component materials (membrane electrolyte, bipolar plate and Pt electro catalyst). The membrane presently used in PEMFCs have some shortcomings like high cost, performance loss at higher temperatures (above 80°C) or low humidity (below 80% RH), high fuel cross over etc. which impede the large scale commercialization of PEMFCs. There is, however, a great demand for non-fluorinated alternative membranes in terms of lower production cost, environmental friendliness, and high-temperature operation. Over the past few decades, a variety of approaches have been suggested to develop an alternative proton exchange membrane at lower cost with good electrochemical and mechanical properties by using hydrocarbon polymers. Among the numerous hydrocarbon polymers, sulfonated poly(ether ether ketone) (SPEEK) is a good candidate on account of its low cost, high glass transition temperature and high proton conductivity, which depend on their degree of sulfonation (DS). SPEEK membranes with high DS exhibit high proton conductivity and ion exchange capacity value (IEC). Moreover, the large number of sulfonic acid groups also result in poor mechanical and dimensional stability, which is unfavorable for fuel cell applications. A number of methods reported in the literature to modify the SPEEK polymer to get a membrane with good stability as well as conductivity, yet it is a challenging issue for the researchers. Although, extensive studies have been carried out on SPEEK-based membranes, only a very few studies are available that report the membrane performance in fuel cell.

Keeping in view the necessity of development of a low cost proton exchange membrane with good electrochemical and mechanical properties for application in PEMFCs, a different approaches has been adopted in this work to synthesize SPEEK polymer based membranes.

1.5 Objective of the thesis

The Objective of the present work is to develop SPEEK polymer-based membranes which have desirable properties for fuel cell application. In SPEEK polymer based membranes, to get a high conductivity as well as good dimensional and mechanical stability is a great challenge because the ion channels in the SPEEK membranes are tortuous, discontinuous and narrow due to the poor microphase separation structure caused by the rigid polymer backbone of PEEK and the short pendent groups. In the present work, three novel methods have been used to increase the conductivity of the SPEEK polymer based membrane and control water uptake to improve the mechanical and dimensional properties of the membranes.

(i) Our first approach was to crosslink highly sulfonated SPEEK polymer with a suitable aliphatic cross linker to modify the microphase separation structure within the membrane. A method of crosslinking of SPEEK through the condensation of sulfonic acid functionalities with poly atomic alcohols (ethylene glycol, glycerol etc.), by appropriate thermal treatment has been reported in literature. We have used this method of crosslinking and Poly ethylene glycol (PEG) as cross-linked to bring the hydrophilic moieties closer to each other and a well-connected hydrophilic channel formation within the membrane. The idea behind this work is to increase the polymer chain mobility and degree of freedom during the membrane formation by crosslinking with aliphatic polymer which will facilitate the hydrophilic/hydrophobic phase separation similar to perflurosulfonic acid membranes. In this work we have used different molecular weight of PEG crosslinker and investigated the optimum chain length of the crosslinker, that gives the maximum water cluster formation and efficient ion channel formation for ion transfer in the membrane.

(ii) It is known that the increase in the number of ionogenic groups (ion exchange capacity) of a hydrophobic polymer would render it highly hydrophilic and leads to gel formation. The large inorganic groups does not suffer such a drawback of swelling. PWA is one of the candidate that has high ionic conductivity as well as the thermal stability. In the second method we have used PEG as crosslinker and PWA as an inorganic additive to improve the electrochemical and mechanical properties of SPEEK. The idea behind this work is to further increase the membrane's conductivity by blending PWA within the membrane and there may by good retention of PWA in the membrane due to hydrogen bond formation between PEG and PWA. Therefore, the increase in the conductivity of the membrane without increasing the swelling is one of the methods that is explored in this work.

(iii) In the third method our main focus was to increase the dimensional stability and water retention in the membrane. The idea behind this work is to use a hybrid method i.e. crosslinking along with inorganic additive to form an organic-inorganic IPN structure. In previous works it was reported that the MO_2 (M= Si, Ti and Zr) based composite membranes have good water retention properties. In this work we have used a novel method to synthesize MO_2 within the membrane where PEG acts as a good dispersant to homogeneously distribute the MO_2 particles without agglomeration as well as a crosslinker.

1.6 Outline of the thesis

This thesis is divided into six chapters. The first chapter titled "**Introduction"** deals with topics like (i) brief introduction of fuel cell and different types of fuel cells, Emphasis is given to the PEMFC and their components. (ii) thermodynamics and electrochemictry of fuel cell. (iii) A thorough literature survey of different types of proton exchange membranes i.e. fluorinated, partially fluorinated, hydrocarbon polymer based etc. (iv) About SPEEK and its different modification methods, (v) need and motivation of the present research work and (vi) objective of the thesis.

The second chapter titled "**Instrumental techniques"** deals with the instrumental techniques used to investigate the electrochemical, mechanical, structural, thermal and morphological properties of solid polymer electrolyte membranes. The working principle of all the techniques is briefly mentioned in this chapter. These techniques includes electrochemical Impedance spectroscopy (EIS), Fourier Transform Infrared Spectroscopy (FTIR), Universal testing machine (UTM), Thermo gravimetric analysis (TGA), Field Emission Scanning Electron Microscopy (FESEM) - Energy Dispersive X-ray (EDX), Atomic force microscopy (AFM), Small Angle X-ray scattering (SAXS).

The third chapter titled **"Synthesis and Characterization of SPEEK and SPEEK-PEG Cross-linked Membranes"** focusses on the synthesis and characterizations of SPEEK and SPEEK-PEG cross-linked membranes. In this work, a series of cross-linked membranes have been synthesized using six different molecular weights of poly ethylene glycol (PEG) [200, 400, 600, 3000, 6000, 10,000 Da] as cross-linkers to investigate the effect of cross-linker chain length on membrane morphology and properties. Membrane topography and morphology were investigated using AFM and SAXS, which showed that there was formation of cluster like structure, and that hydrophilic-hydrophobic phase separation occurs after cross-linking that makes the membranes mechanically stronger and reduces its swelling in water at higher temperature. Membrane properties were found to be strongly dependent on the cross-linker chain length. PEG-400 and PEG-600 cross-linked membrane gave desirable properties in terms of overall membrane performance such as proton conductivity (0.095 S cm^{-1}), mechanical strength, and membrane durability etc. These two membranes (SPEEK-PEG-400 and SPEEK-PEG-600) performance was studied in H_2/O_2 fuel cell. To explore its utilization in the methanol fuel cell, the methanol permeability of the SPEEK-PEG 400 membrane was evaluated and compared with Nafion, which showed lower permeability than Nafion up to 55°C.

In the fourth chapter titled “**Effect of Phosphotungstic Acid Blending on Properties and Performance of Sulfonated Poly(ether ether ketone)-Poly(ethylene glycol) Cross-linked Membranes”** the effect of phosphotungstic acid (PWA) blending in sulfonated poly(ether ether ketone) (SPEEK) and poly(ethylene glycol) (PEG) cross-linked membrane is investigated in terms of electrochemical and mechanical properties. PWA is a good inorganic modifier because of its unique properties like high conductivity, thermal stability, high selectivity and non-corrosive nature.A series of SPEEK-PEG-PWA membranes were fabricated where PEG-600 was used as an interpenetrating polymer network (IPN) type cross-linker and PWA as an inorganic additive. PWA weight percentage was varied from 0% to 50%. All the membranes were equilibrated with water at room temperature (27ºC) and elevated temperature (60ºC) and their properties were investigated. SEM with EDX studies were used to ascertain the tungsten concentration remaining in the membrane after treatment in water at higher temperature. A systematic decrease in the tungsten concentration was observed with the increase in the initial tungsten percentage. Membranes blended with 10% PWA showed the best properties among all, i.e., highest conductivity (0.11 S cm^{-1}), mechanical strength and chemical stability. Membranes with 10% tungsten and without tungsten were studied in H_2/O_2 fuel cell. The membrane blended with 10wt% PWA gave 33% higher power density than the membrane without PWA.

The fifth chapter titled “**Synthesis and Characterization of Cross-linked Sulfonated poly(ether ether ketone)-poly(ethylene glycol) /MO$_2$ (M=Si, Ti and Zr) Organic-Inorganic Nanocomposite Membrane”** deals with synthesis, characterization and performance studies of organic–inorganic nano-composite membranes. In this study, a series of SPEEK-PEG/MO$_2$ (M=Si, Ti and Zr) membranes were fabricated where, PEG-400 is used as an (IPN)-type cross-linker as well as dispersant to homogeneously distribute silica/titania/zirconia nanoparticles in the membrane, which are synthesized by in-situ sol-gel method. The synergistic effect of cross-linking and inorganic additive on the membrane’s electrochemical and mechanical properties, and fuel cell performance were investigated. Experimental results revealed that nanocomposite membranes have better properties than pristine SPEEK-PEG membranes, e.g., conductivity, form stability, mechanical strength, thermal and oxidative stability etc. FE-SEM and AFM images showed that the SiO$_2$, TiO$_2$ and ZrO$_2$ particles are distributed homogeneously without aggregation. The EDX mapping images of silicon, titanium and zirconium also supported the FE-SEM images and the elemental map’s spectrum revealed the complete conversion of precursor to silica, titania and zirconia. The nanocomposite membranes with optimum amount of MO$_2$ showed good form stability in water for up to 80 °C, whereas membrane samples without nanoparticles showed excessive swelling beyond 60 °C in water. This chapter is divided into three parts to discuss the results/outcomes of all the three MO$_2$ (Si, Ti and Zr) different types of nanocomposite membranes separately.

In the Sixth and last chapter titled **“Conclusions, Implications and Future Perspectives”,** the results of the entire work carried out as a part of the thesis, have been summarized. The chapter brings out the achievements and the novel scientific understandings emerging out of this work, which are in line with the objectives targeted. This chapter also discuss the possible future extensions of the work.

CHAPTER-2

Instrumental techniques

2.1 Introduction

The understanding of synthesized membranes properties is essential before their performance analysis in a fuel cell. Various membranes properties e.g. membranes conductivity, mechanical stability, thermal stability, morphological characterizations etc. were investigated by using different experimental techniques. Various techniques were employed for the characterization of membrane properties, such as: Impedance spectroscopy (IS) for membranes conductivity measurement; Fourier-transform infrared spectroscopy (FTIR) for identification of molecular components and structure; universal testing machine (UTM) for mechanical properties study, thermogravimetry (TGA) for thermal stability study, scanning electron microscopy (SEM) and atomic force microscopy (AFM) for the membranes surface morphology and topography analysis, Small angle X-ray scattering (SAXS) for the analysis of the bulk morphology; Energy dispersive x-ray spectroscopy (EDX) for the elemental analysis. The basic working principle of all the instruments is briefly described in this chapter.

2.2 Impedance spectroscopy (IS)

Impedance spectroscopy (IS) is a powerful technique to study the electrical properties of materials and their interfaces (i.e., electrode-electrolyte interfaces). Impedance Spectroscopy is also called AC Impedance or Electrochemical Impedance Spectroscopy (EIS) and is used to investigate the dynamics of bound or mobile charge in the bulk or interfacial regions of any kind of solid or liquid material: ionic, semiconducting, mixed electronic–ionic, and even insulators (dielectrics). It utilizes the modeling of the electrochemical system into the electrical circuit of resistances, capacitances, or other electrical components.[180,181]

Theory:

We know that like resistance, the impedance is a measure of the ability of a system to impede the flow of electrical current (electron or ions). However, the impedance can deal with time or frequency dependent phenomena, unlike resistance. The resistance is the ratio of voltage to current, similarly, the impedance is also the ratio of time dependent voltage to time-dependent current. Electrochemical impedance is usually measured by applying an AC potential over a broad range of frequencies to an electrochemical cell and then measuring the current through the cell. Typically, the applied potential (V) is a sinusoidal wave waveform that varies with time (t), defined as:

$$V_t = V_0 Sin\,(\omega t) \qquad \dots (2.1)$$

Where V_t is the potential at time t, V_o is the amplitude of the signal (maximum voltage intensity) and ω is the radial frequency.

The relationship between radial frequency ω (expressed in radians/second) and frequency f (expressed in Hertz (1/sec)).

$$\omega = 2\pi f \qquad \dots (2.2)$$

The response signal I_t is a sinusoidal waveform with a phase difference (ϕ) and has different amplitude, I_0:

$$I_t = I_0 Sin(\omega t + \phi) \qquad \dots (2.3)$$

where I_o is the maximum current intensity and ϕ is the phase angle between the applied voltage and response current waveforms. The electrical impedance parameter, Z(ω), which defines the ratio between the applied voltage and the resulting electric current, Z(ω)= V(t)/I(t) is expressed as Eq. 2.4.

$$Z\,(\omega) = \frac{V_0 Sin\,(\omega t)}{I_0 Sin\,(\omega t + \phi)} = Z_0 \frac{Sin\,(\omega t)}{Sin\,(\omega t + \phi)} \qquad \dots (2.4)$$

With Euler's relationship, shown in Eq. 2.5;

$$\exp\,(j\phi) = Cos\,\phi + jSin\,\phi \qquad \dots (2.5)$$

The impedance is then represented as a complex number (Eq. 2.6).

$$Z_\omega = Z_0(Cos\phi + jSin\phi) = Z_{real} + j\,Z_{imag} \qquad \dots (2.6)$$

Where Z_{real} and Z_{imag} are the real and imaginary parts of the electrical impedance data, respectively.

Data Presentation

The expression for Z(ω) is composed of a real and an imaginary part. If the real part is plotted on the X-axis and the imaginary part is plotted on the Y-axis of a chart, we get a "Nyquist Plot". The Nyquist plot for a typical RC circuit is given in Figure 2.1(A). Notice that in this plot the Y-axis is negative and that each point on the Nyquist Plot is the impedance at a particular frequency. On the Nyquist plot the impedance can be represented as a vector of length |Z|. The angle between this vector and the X-axis is commonly called the "phase angle" is (ϕ). One major shortcoming of the "Nyquist plot" is, the frequency at any point cannot be determined from the plot. The semicircle is characteristic of a single "time constant". Electrochemical Impedance plots often contain several time constants. Often only a portion of one or more of their semicircles is seen.

Another popular presentation method is the "Bode plot". The impedance is plotted with log frequency on the X-axis and both the absolute values of the impedance ($Z = Z_0$) and phase shift on the Y-axis. The Bode plot for the RC circuit is shown in Figure 2.1(B). Unlike the Nyquist plot, the Bode plot explicitly shows frequency information.

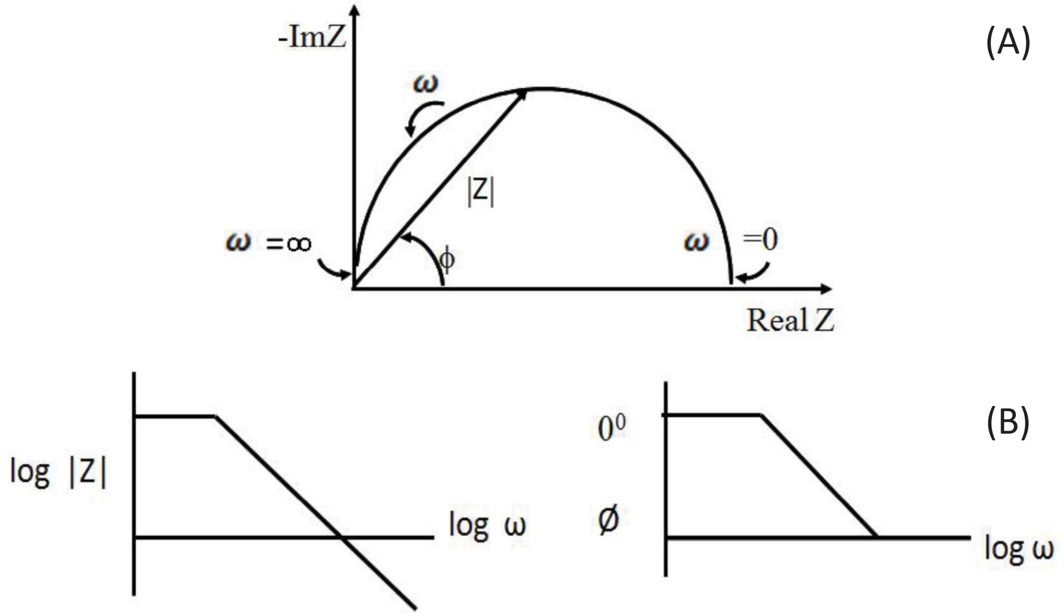

Figure 2.1: (A) Nyquist and (B) Bode plot representation of a typical RC circuit.

Equivalent circuit elements

EIS data is commonly analyzed by fitting it to an equivalent electrical circuit model. Most of the circuit elements in the model are common electrical elements such as resistors, capacitors, and inductors. The circuit elements used to model the system, and their current-voltage characteristics and impedances are given in Table 2.1:

Table 2.1: Common electrical elements□

Component	Symbol	Current Vs. Voltage	Impedance
Resistor		$V = I\square\square$	$Z_{\square} = \square$
Capacitor	 □	$I = C\frac{\square V}{\square t}$	$Z_C = \frac{1}{j\omega C} = \square\frac{j}{\omega C}$
Inductor	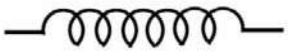	$V = \square\frac{\square I}{\square t}$	$Z_{\square} = j\omega\square$

Under steady-state conditions ($\square V\square t\square\square$), the current through the resistor is proportional to the applied voltage, the capacitor is equivalent to an open circuit, and the inductor is equivalent to a short circuit. When elements are in series, the current flowing through them is the same, and the overall voltage is the sum of voltages across individual elements. When elements are in parallel, the voltage is the same for all elements, and the overall current is the sum of current flowing through each element. Impedance contributions are additive in series and inverse additive in parallel.

The impedance of a resistor is independent of frequency and has no imaginary component. With only a real impedance component, the current through a resistor stays in phase with the voltage across the resistor. The impedance of an inductor increases as frequency increases. Inductors have only an imaginary impedance component. As a result, the current through an inductor is phase-shifted -90 degrees with respect to the voltage. The impedance versus frequency behavior of a capacitor is opposite to that of an inductor. A capacitor's impedance decreases with increase in frequency. Capacitors also have only an imaginary impedance component. The current through a capacitor is phase shifted +90 degrees with respect to the voltage.[182]

From the electrical impedance spectroscopy (EIS) outputs, an impedance graph (imaginary part versus real part) can be plotted and thus information regarding an expected equivalent circuit can be extracted. Figure 2.2 shows a typical example of EIS graphs and equivalent circuits. The real and imaginary parts of the impedance are associated with the existence of resistor and capacitor, which are in- and out-of-phases with the applied AC signal, respectively.[183]

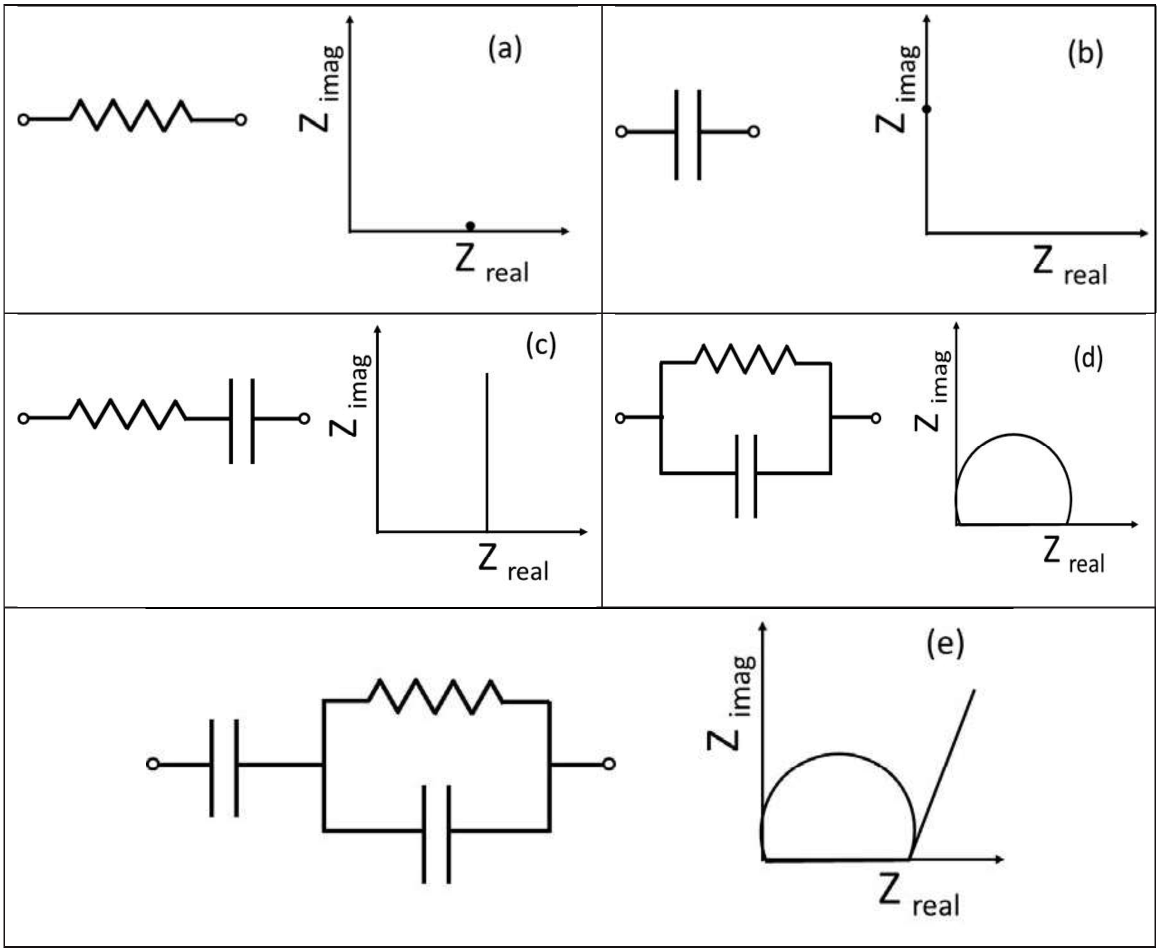

Figure 2.2: Cole-Cole plots and their equivalent circuits for (a) a pure resistor, (b) a pure capacitor, (c) a capacitor and a resistor in series, (d) a capacitor and a resistor in the parallel combination, and (e) a leaky system

A typical Impedance plot of a solid polymer electrolyte consists of the high-frequency distorted semicircle representing the parallel combination of bulk resistance and capacitance, which could be due to the bulk conductivity of the solid polymer electrolytes, and the low-frequency inclined spike like (nonvertical) region attributed to the ion diffusion in the polymer electrolyte. The low-frequency tail indicates the capacitive nature of the interface and the absence of electronic conductivity, while the distorted semicircle is representative of grain boundary effects in the sample.[184,185]

In the present study, the proton conductivity of the synthesized membranes were measured by using Novo control Alpha-ATB impedance analyzer having pseudo 4 probe impedance test interface (where $V_{High}I_{High}$ terminals are shorted $V_{Low}I_{Low}$), is connected to two Pt wire electrodes (diameter 900 microns each) 15 mm apart (schematic of the impedance analyzer is given in Appendix). The instrument was checked using standard load (100E) before the measurement. The conductivity of the samples was calculated using the relation $\sigma = d/RA$, where d and A are the distance between the electrodes and the cross-sectional area of the membrane respectively, and R is the resistance derived, from the frequency-interval (10^7 to 10^5 Hz) using Bode plot.

2.3 Fourier Transform Infrared spectroscopy (FTIR)

Infrared spectroscopy is one of the most powerful analytical techniques for the identification, characterization, and quantification of structural features in a material. When IR radiation passes through a sample, some radiation is absorbed by the sample and some transmitted. The resulting signal at the detector is a spectrum representing the molecular ‘fingerprint’ of the sample. The usefulness of infrared spectroscopy arises because different chemical structures (molecules) produce different spectral fingerprints. The infrared region of the spectrum encompasses radiation with wave numbers ranging from about 12,800 to 10 cm^{-1} or wavelengths from 0.78 to 1000 μm. From the instrumentation and application point of view, the infrared region has been subdivided into near IR region (overtone region), mid IR region (vibration rotation region) and far IR region (rotation region). The techniques and the applications of methods based upon the three infrared spectral regions differ considerably. The various bands can be interpreted according to the characteristics functional groups present in the compound.[186]

Generally, two types of IR Instrumentation are used to obtain infrared spectra:

- Dispersive spectrophotometers, which use a monochromator to produce an infrared spectrum one resolution element at a time.
- Michelson interferometers, which use a moving mirror to create an interference pattern, or interferogram, from which all resolution elements are determined simultaneously.

A schematic diagram of the essential components of a FT spectrometer based on Michelson interferometer is shown in Figure 2.3. It consists of two perpendicular mirrors; one of which is a stationary mirror and other a movable mirror which can be displaced perpendicularly to the fixed mirror at a constant velocity. Between these two mirrors a beam splitter is set at 45° from the initial position of the movable mirror. A parallel beam of radiation from an infrared source is passed to the mirrors through the beam splitter. The beam splitter reflects about half of the beam to the fixed mirror, which reflects it back to the beam splitter and transmits the other half to the movable mirror, which reflects it back to the beam splitter. The returning beams are again split and mixed about half going back to source and half passing through the sample compartment. The composition of the beam splitter depends on the spectral region of interest. For example in the mid-infrared region (4000-400 cm^{-1}), a beam splitter of germanium coated on KBr plate (substrate) is often used. Germanium reflects the radiation while KBr transmits most of the desirable radiation. In the far infrared region, germanium coated on CsI (800-200 cm^{-1}) or germanium coated on Mylar (polyethylene terephthalete) (650-10 cm^{-1}) are used as beam splitters. A thin film of the beam splitter material is coated on an optically flat substrate.

The return beams from both the mirrors along the same path length as their incident path are recombined into a single beam at the beam splitter. The path length of one of the return beams is changed in order to create phase difference to cause an interference pattern. The recombined radiation is then directed through the sample and focused on to the detector. The detector measures the amount of energy at discrete intervals of mirror movement. The design of the Michelson interferometer is such as to make measurement in any infrared region possible by simply changing the beam splitter and the detector.[187]

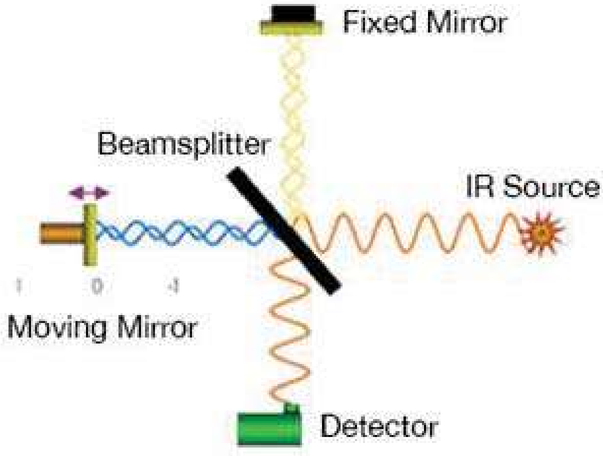

Figure 2.3: Schematic diagram of FTIR

ADVANTAGES OF FOURIER TRANSFORM TECHNIQUE

The main advantages of FT spectroscopy are the greater ease and speed of measurement. The entire spectrum can be recorded within a few seconds using sophisticated computers. Recent developments in FT Infrared spectrometers have thus led to higher resolution, total wavelength coverage, higher accuracy in frequency and intensity measurements. It can also be used in the characterization of all kinds of samples. In FT method, all the source energy passes through the instrument and the resolving power is constant over the entire spectrum. The signal to noise ratio is also improved.

There are four major sampling techniques in FTIR:

- Transmission
- Attenuated Total Reflection (ATR)
- Specular Reflection
- Diffuse Reflectance

Each technique has strengths and weaknesses, which motivate their use for specific samples. An ATR technique is most suitable of the polymer membrane samples analysis.

ATR: In ATR-FTIR spectroscopy the infrared light travels through an Internal Reflection Element (IRE) which is optically dense crystal with a high refractive index (e.g. Ge, Si, ZnSe, ZnS etc.). To measure an ATR-FTIR spectrum, the sample needs to be put in close contact with the IRE as depicted in Figure 2.4. The incident infrared light travels through the IRE, bouncing on the interface between IRE and sample. As a result, the light will be partially transmitted and partially reflected. On changing the incident angle of the light with the IRE total internal reflection can be achieved, all light is confined within the crystal. However, the electromagnetic field of the light extends from the interface into the sample medium. This field extension is called the evanescent wave, which can be absorbed by the sample. Due to the absorption, the initial infrared beam attenuates and a transmission spectrum of the sample can be recorded. The experiments described in this paper were all performed using a multi-bounce trapezoidal ZnSe IRE with an angle of incidence of 45°C. The penetration depth of the light depends on the refractive indices of the IRE (n_1) and sample (n_2), wavelength (λ) and the angle of incidence (θ) according to Eq. 2.7.[188]

$$d_p = \frac{\lambda}{2\pi n_1 (\sin^2 \theta - (n_2/n_1)^2)^{1/2}} \quad \ldots (2.7)$$

Generally, most spectrometers calculate an ATR-absorbance spectrum normalizing for the penetration depth (which proportional to the wavelength) according to:

$$\text{[illegible]} = -\log\left(\frac{\text{[illegible]}}{\text{[illegible]}_0}\right)\frac{\text{[illegible]}\, n \tan \text{[illegible]}}{\text{[illegible]}} \qquad \ldots (2.8)$$

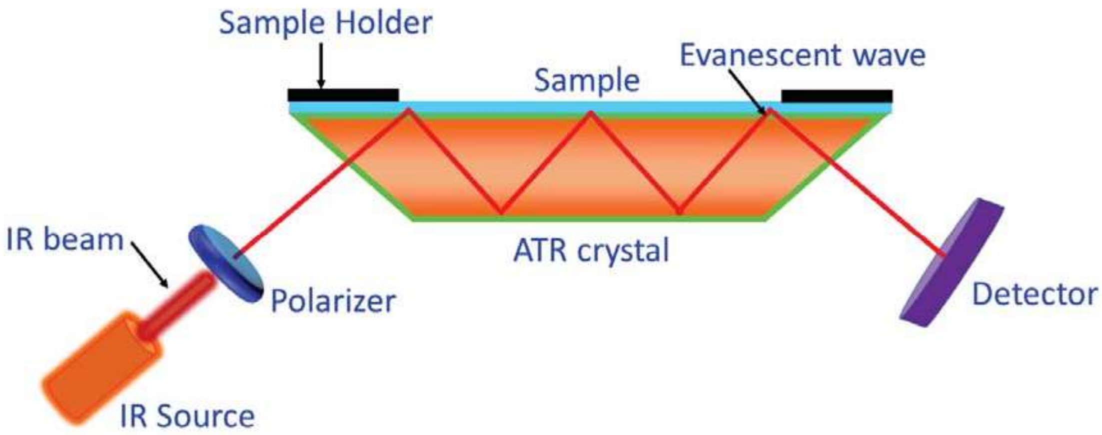

Figure 2.4: Schematic representation of ATR principle.

Advantages of ATR mode analysis:

- Minimal sample preparation—place the sample on the crystal and collect data.
- Fast and easy cleanup—simply remove the sample and clean the surface of the crystal.
- Analysis of samples in their natural states—no need to heat, press into pellets, or grind in order to collect spectra.
- Excellent for thick or strongly absorbing samples—ideal for difficult samples like black rubber

In the present work, the FTIR spectra of the synthesized membranes were collected in ATR mode. A Bruker, Vertex 70 spectrometer using software OPUS, VERSION 6 was used for the measurement. The spectra were recorded in the range of 400-4000 cm^{-1}. The membrane sample was pressed on a ZnSe crystal using a screw type device attached to the crystal mount. About 100 scan average was taken for each spectrum.

2.4 Field-emission Scanning Electron Microscopy - Energy Dispersive Spectroscopy (FESEM-EDS)

The Field Emission Scanning Electron Microscope (FESEM) is a type of electron microscope that produces images of a sample by scanning the surface with a focused beam of electrons. The electrons interact with atoms in the sample, producing various signals that contain information about the sample's surface morphology and chemical composition. The electron beam is scanned in a raster scan pattern, and the beam's position is combined with the detected signal to produce an image. FESEM can achieve resolution better than 1 nanometer.

Interaction of Electron with Samples: When a focused beam of electrons hits the sample surface, they penetrat into it for some distance (about 1 μm) before hitting another particle. These incident electrons are greatly scattered resulting in elastic and inelastic scattering inside the sample forming a region (teardrop-shaped) called as interaction volume. Elastic scattering results in BSEs (backscattered electrons) whereas inelastic scattering produces SEs (secondary electrons), Auger electrons and X-rays.[189] Figure 2.5, shows the interaction of electron beam with a specimen surface and signal emission. The resulted electrons are recorded at their respective detectors. Out of all the emitted signals, SE and BSEs are the most widely used ones and are explained below. The three signals that provide the greatest amount of information in SEM are the secondary electrons, backscattered electrons, and X-rays.

Back scattered electrons: Incident electrons that are elastically scattered through an angle of more than 90° are called backscattered electrons (BSE) and yield a useful signal for imaging the sample. These electrons have approximately the same energy as that of the primary ones and are easy to record. The fraction of beam electrons backscattered in this way varies strongly with the atomic number Z of the scattering atoms but does not change much with changes in incident energy. BSE images show atomic number contrast. The images formed using the BSEs provide information about the compositional differences, specimen topography, crystal orientation and grain boundaries.

Secondary electrons: These electrons are produced when an incident electron excites a weekly bonded outer shell electron (in conductors) or a valence electron (in semiconductors and insulators). During this process, the electrons from the specimen receive kinetic energy from the incident electrons and start moving towards the surface. Mostly, the SEs are emitted by the atoms near the specimen surface. Moreover, the number of SEs is greater than the incident electrons due to the multiple scattering events, which subsequently increase the signal level. Therefore with SE mode, the spatial resolution in an image is high. The images formed using the SEs provide surface topography and morphology with good resolution.[190]

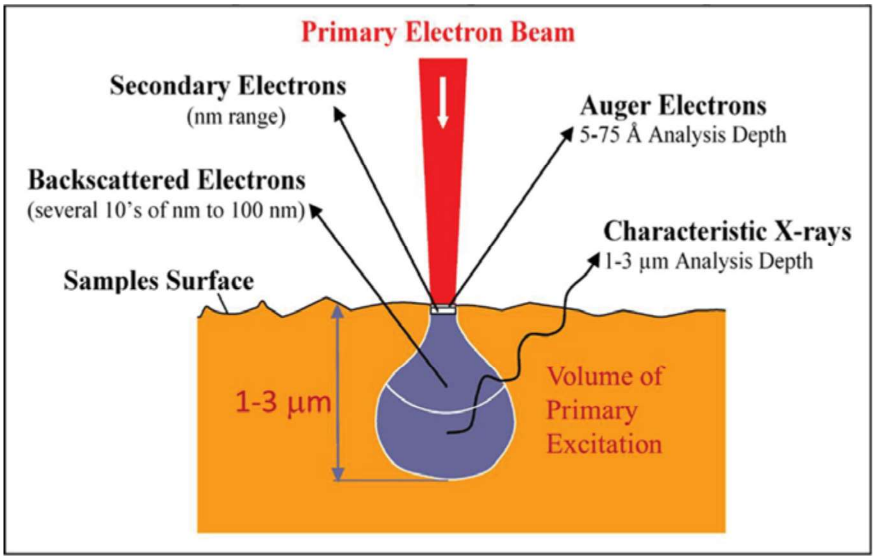

Figure 2.5: Interaction volume and signal emission

X-ray: Another class of signals produced by the interaction of the primary electron beam with the specimen is characteristic x-rays. The analysis of characteristic x-rays to provide chemical information is the most widely used microanalytical technique in the SEM. When a primary electron (from the beam) strikes an atom of the sample, it ejects an electron originally positioned in an inner shell (K shell), an outer shell electron may fall into the inner shell to reestablish the proper charge balance in its orbitals following an ionization event. In doing so, this high-energy electron must release some of its energy in the form of X-rays. As a consequence, the energy released (expressed in eV) is exactly equal to the energy difference between the two levels, shown in Figure 2.6. Detection and measurement of X-ray energy permits elemental analysis and is commonly referred to as Energy Dispersive X-ray Spectroscopy (EDS or EDX or EDXA). EDS can provide rapid qualitative, or with adequate calibration standards, quantitative analysis of elemental composition with a sampling depth of 1–2 microns. X-rays may also be used to form maps or line profiles, showing the elemental distribution in a specimen surface.[191]

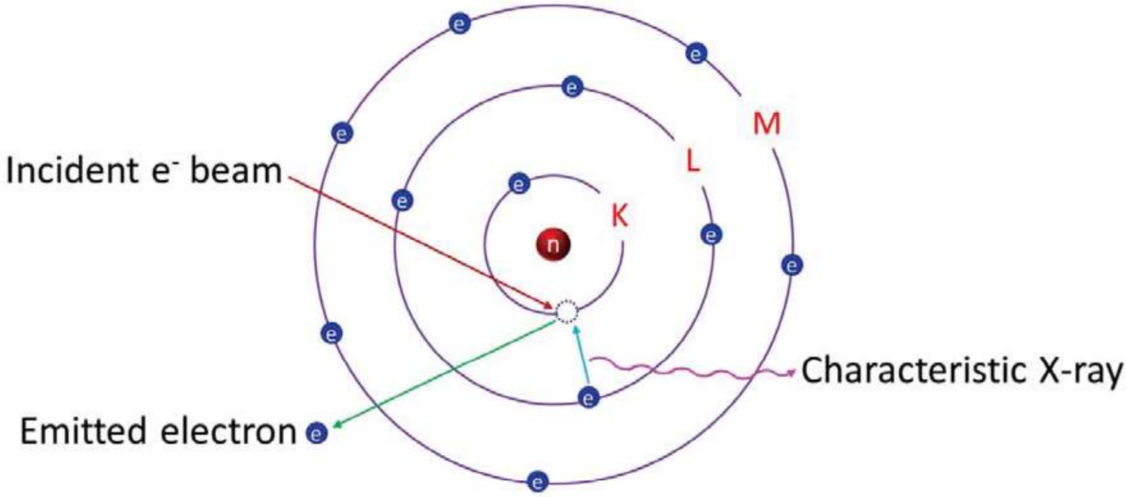

Figure 2.6: Schematic description of the characteristic X-ray formation

FESEM components

The basic architecture along with the major components of a FESEM is shown in the Figure 2.7. All these components perform different roles in generating the electron micrographs. The main components are described below:

a) Source of electrons (Electron gun):

In standard electron microscopes, electrons are mostly generated by heating a tungsten filament by means of a current to a temperature of about 2800°C. Sometimes electrons are produced by a crystal of lanthanum hexaboride (LaB_6) that is mounted on a tungsten filament. In a field emission (FE) scanning electron microscope, no heating but a so-called "cold" source is employed. An extremely thin and sharp tungsten needle (tip diameter 10^{-7} – 10^{-8} m) functions as a cathode in front of a primary and secondary anode. The voltage between the cathode and anode is in the order of magnitude of 0.5 to 30 KV. The electron beam produced by the FE source is about 1000 times smaller than in a standard microscope and therefore the image quality is markedly better. As field emission necessitates an extreme vacuum (10^{-8} Torr) in the column of the microscope, a device is present that regularly decontaminates the electron source by a current flash. In contrast to a conventional tungsten filament, a FE tip last theoretically for a lifetime provided the vacuum is maintained stable.

b) Column with lenses and apertures

The electron beam is focused by the electromagnetic lenses (condenser lens, scan coils, stigmator coils and objective lens) and the apertures in the column to a tiny sharp spot.

Electromagnetic lenses: The two sets of electromagnetic lenses that are available in an electron column are the condenser lenses and the objective lenses. Condenser lenses lying above the aperture strip are mainly responsible for controlling the electron concentration and the diameter of the beam. Objectives lenses that are present under the aperture converges the incoming beam and focus it on the sample surface.

Scan coils: The two sets of scan coils that are available in the electron column are used to raster the electron beam in both horizontal and vertical directions on the sample surface. The first pair deflects the beam off the optical axis and the second pair bends the beam back on to the axis at the pivot point of the scan. Apart from scan generation, they are also used in controlling the magnification of the instrument.

The Stigmator coils: The Stigmator coils are utilized to correct irregularities in the x and y deflection of the beam and thus to obtain a perfectly round-shaped beam. When the beam is not circular, but ellipsoidal, the image looks blurred and stretched (see ALIGN X Y in the virtual FESEM).

c) Electron detectors:

In general, an SEM consists of various detectors each of which is used to collect different types of emitted electrons. The commonly used detectors are SE detector and BSE detector. Two types of SE detectors are available with the modern SEMs. The primary type is the most commonly used Everhart-Thornley detector that is fixed to the side walls of the chamber It works by attracting the emitted secondary electrons by a positive potential applied to a ring around the detector. The second type is in-lens detector that is fixed alongside the electromagnetic lens. BSE detectors are located just below the pole piece of the object lens and collect the emitted backscattered electrons.

d) Positioning platform:

A movable positioning platform is placed in the lower part of the SEM electron column and is used to load the specimen. In FESEM, the object can be moved in horizontal and vertical direction on the screen by operating the arrows in the POSITION box. In the real microscope the object can be repositioned in the chamber by means of a joystick that steers in left-right axis, or forward and backward. In addition, the object can be tilted (e.g. for stereo views), rotated and moved in Z direction (= closer or further away to the objective lens). It is mainly responsible for better positioning the sample such that it is well exposed to the electron beam.

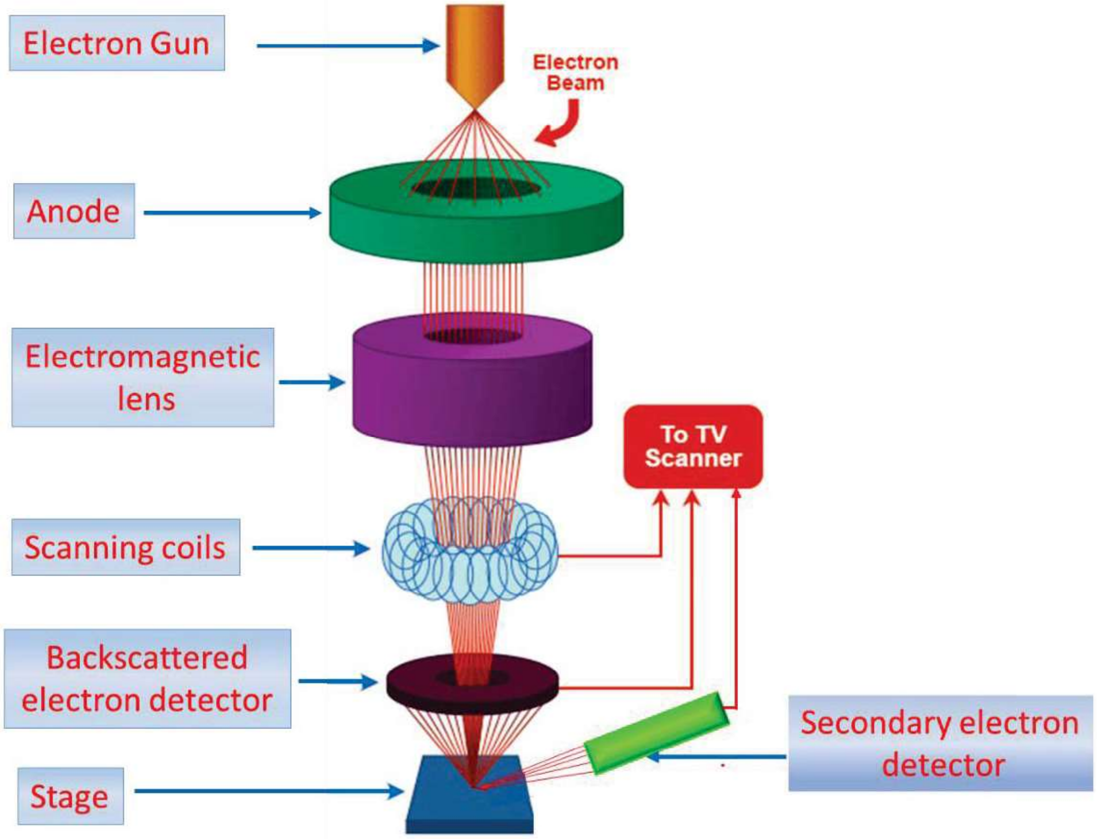

Figure 2.7: Schematic diagram of a scanning electron microscope.

Image acquisition process:

The image acquisition process starts with the beam generation. Initially, an accelerating voltage is supplied to the electron gun to produce the electrons. The electrons that are redirected by the anode traverse the electron column vertically. The series of electromagnetic lenses and apertures present in the electron column control the beam diameter and focus it on the sample surface. Finally, to acquire an image, a region on the sample surface has to be scanned by the electron beam in both horizontal and vertical directions with a great speed. This is then performed by the scan coils (one for each direction) by varying the current passing through them as a function of time. As a result of the beam interaction with sample surface, deferent signals are emitted. The resulted electrons are recorded at their respective detectors and then the gathered information is amplified, digitized and recorded as an image. As the wavelength of the electrons is much smaller than visible light, no color image can be produced using a SEM. Here an interesting fact about SEM is, unlike optical systems no lens is directly involved in image acquisition.

In the present work Auriga6553 FESEM (resolution <2.5 nm @30 KV and magnification 300 X – 500 KX) equipped with EDX spectrometer (Oxford-EDX) used for the membrane samples analysis. The spectrometer has X-Max Extreme Silicon Drift Detector (20 mm^2), having resolution of 150 eV at 20 keV. Since the polymeric membrane samples are non-conducting in nature, the samples were coated with metal layer before analysis. The samples were sputter coated with a thin layer of gold/palladium Au:Pd (60:40) in an argon atmosphere. gold-palladium alloy was coated for 100 seconds at a current of 15 mA. For the cross-section analysis the samples were fractured in liquid nitrogen and mounted vertically on a stub.

2.5 Atomic force microscopy (AFM)

Atomic force microscopy (AFM) is a versatile and powerful microscopy technique for studying the 2-D and 3-D topography of a material at the nanoscale. AFM can image all materials hard or soft, synthetic or natural (including biological structures such as cells and biomolecules) irrespective of opaqueness or conductivity. AFM images are obtained by measuring forces between a sharp probe (radius less than 10 nm) and sample surface at very short distance (0.2-10 nm probe-sample separation).[192]

Working principle

The basic components of an AFM are; the probe tip, the cantilever, the scanner, the laser, a data processor and a photodetector as shown in Figure 2.8. The probe is supported on the free end of a flexible cantilever, gently scanning the surface and records the small force between the probe and the surface. This force can be described using Hooke`s law (Eq. 2.9):

$$F = -kx \qquad \dots (2.9)$$

Where F = Force; k = Spring constant; x = Cantilever deflection.

Attractive or repulsive forces resulting from interactions between the tip and the surface will cause a positive or negative bending of the cantilever. The bending is detected by deflections in the cantilever using reflections from a laser beam. Forces involved in the tip-sample interaction affect how the probe interacts with the sample. The movement of the tip or sample in the *x*, *y*, and *z*-directions is controlled by a piezoelectric tube scanner. For typical AFM scanners, the maximum ranges are 80 µm x 80 µm in the *x*-*y* plane and 5 µm for the *z*-direction. The resulting map of the area $z = f(x, y)$ represents the topography of the sample. A photodetector measures the difference in light intensities between the upper and lower photodiodes and then converts this signal into a voltage. This method enables a computer to generate a three-dimensional map of the surface topography.

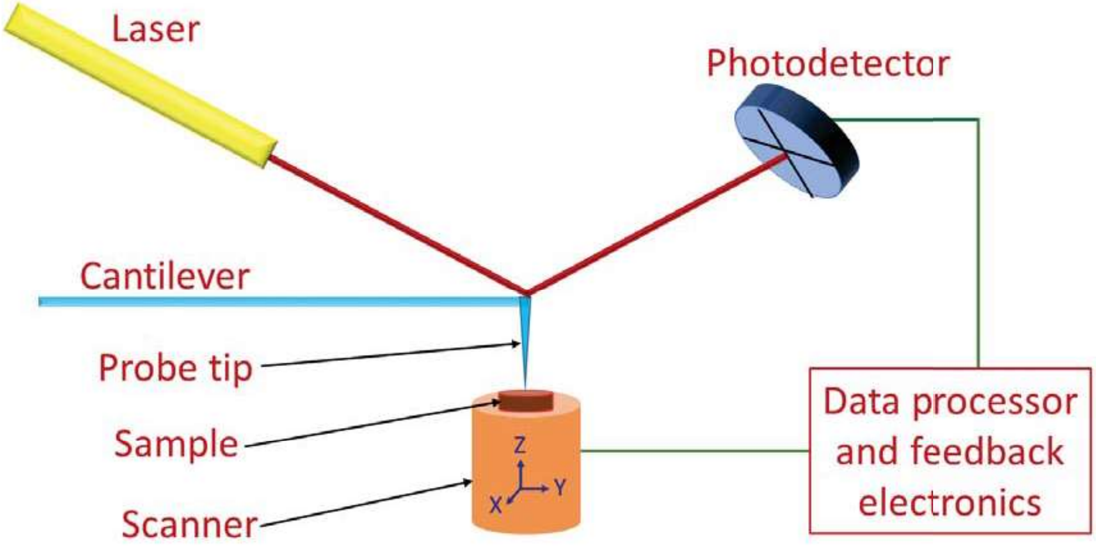

Figure 2.8: Schematics of AFM

Different AFM modes:

There are three primary imaging modes in AFM based on the force and distance between the tip and the sample: Contact mode, non-contact mode and Semi contact or intermittent contact or tapping mode (Shown in Figure 2.9). The choice of the AFM scanning mode is depends on the surface characteristics of interest and on the hardness/stickiness of the sample.[193]

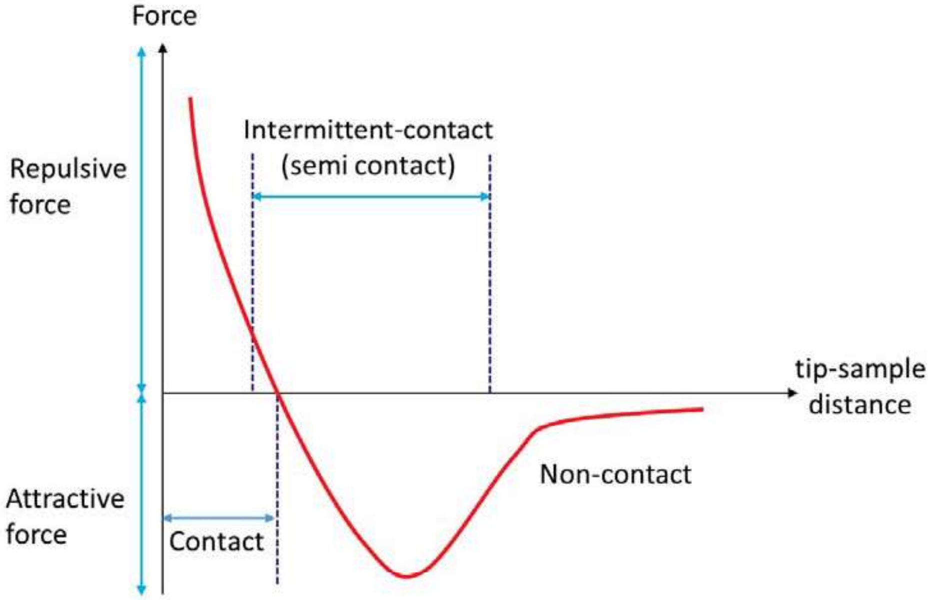

Figure 2.9: Potential energy diagram of a probe and sample.

Contact mode: In contact mode, the tip scans the sample in close contact with the surface. The probe-surface separation is less than 0.5 nm and the force on the tip is repulsive (typical value of 10^{-7} N). The forces between the probe and the sample remain constant by maintaining a constant cantilever deflection then an image of the surface is obtained. The advantages of this imaging mode are: fast scanning, well for rough samples and it can provide information about the samples physical properties e.g. elasticity, adhesion, hardness, friction, etc. It has some serious drawbacks e.g. the dragging motion of the probe tip, combined with adhesive forces between the tip and the surface, excessive force in this mode can also damage the surface or blunt the probe tip and create artifact data. This mode is useful for the hard surface but not suitable for the soft samples like polymer, thin films, biomolecules etc.

Noncontact mode: In non-contact mode, the probe does not touch the sample but oscillates above the surface of the sample during scanning. The cantilever is held 5-10 nm away from the sample surface. Attractive Van der Waals forces acting between the tip and the sample are detected, and topographic images are constructed by scanning the tip above the surface. In non-contact mode of AFM studies, stiff cantilevers are used because the soft cantilevers can be pulled into contact with the sample surface. However, the use of stiffer cantilevers reduces the change in cantilever deflection and vibrational amplitude, and thus, a sensitive detection scheme is needed. In this mode of operation, the force between the tip and the sample is several orders of magnitude lower than the force in contact mode (10^{-13} N). The advantages of this mode are soft sample can be analyzed and the lifetime of the probe is increased. The disadvantages of this mode are generally lower resolution; contaminant layer on surface can interfere with oscillation; usually, need ultra-high vacuum to have the best imaging; sensitive to external vibrations and the inherent.

Semi contact or intermittent contact or tapping mode: This mode is a key advance in AFM. This potent technique allows high-resolution topographic imaging of sample surfaces that are easily damaged (polymers, thin films), loosely hold to their substrate, or difficult to image by other AFM techniques. In semi contact scanning mode the cantilever makes intermittent contact with the surface in a resonant frequency (hundreds of KHz). The probe slightly “taps” on the sample surface during scanning, contacting the surface at the bottom of its swing. The probe-surface separation occurs in a range of 0.5 and 2 nm. The tip in contact with the surface to provide high resolution and then lifting the tip off the surface to avoid dragging the tip across the surface. Unlike contact and non-contact modes, when the tip contacts the surface, it has sufficient oscillation amplitude to overcome the tip-sample adhesion forces. Also, the surface material is not pulled sideways by shear forces since the applied force is always vertical. Another advantage of the tapping mode technique is its large, linear operating range. This makes the vertical feedback system highly stable, allowing routine reproducible sample measurements. This mode is well suited for imaging soft samples and for samples with poor surface adhesion.

Surface texture parameters and functions

The 2-D and 3-D topographic images provide information about various surface parameters, which are broadly classified as: amplitude parameters (based on overall height of the surface); Spatial parameters (based on direction of the plane or wavelength direction); Hybrid parameters (based on both the height direction and the direction of the plane) and Functional parameters (based on special functioning properties like bearing, sealing and lubricant retaining capabilities). Among various surface parameters, the amplitude parameter is most widely used for a material surface analysis and gives an idea about the surface roughness of the material. Roughness is often described as closely spaced irregularities or with terms like ‘uneven’, ‘coarse in texture’, ‘broken by prominences’ etc. It is quantified by the vertical spacing of a real surface from its ideal form. If these spacing is large, the surface is rough; if they are small the surface is smooth.[194,195]

Roughness Parameters

A number of standard parameters are used to describe surface roughness of a samples. Such as:

Average roughness (Ra): Average roughness is the arithmetic mean of the absolute values of the height of the surface profile Z(x), which is describe in Eq. 2.10.

$$R_a = \frac{1}{L}\int_0^L \left| Z(x) \right| dx \qquad \ldots (2.10)$$

Where Z(x) is the function that describes the surface profile analyzed in terms of height (Z) and position (x) of the sample over the evaluation length "L".

The average roughness, is just the mean absolute profile, making no distinction between peaks and valleys, thus it can be the same for surfaces with roughness profile very different.

Root mean square roughness (R_q): Root mean square (RMS) roughness is the square root of the sum of the squares of the individual heights and depths from the mean line. It is describe in Eq. 2.11.

$$R_q = \sqrt{\frac{1}{L}\int_0^L \left|Z^2(x)\right| dx} \qquad \ldots (2.11)$$

The R_q is more sensitive to peaks and valleys than the average roughness due to the squaring of the amplitude in its calculation.

Maximum Profile Peak height (R_p), Maximum Profile valley depth (R_v) and Maximum height of the Profile (R_T): The Maximum Profile Peak Height (Rp) is the measure of the highest peak around the surface profile from the baseline. Likewise, the Maximum Profile Valley Depth (Rv) is the measure of the deepest valley across the surface profile analyzed from the baseline. We can write:

$$R_p = \left|\max Z(x)\right| \qquad \text{For} \quad 0 \leq x \leq L$$

$$R_V = \left|\min Z(x)\right| \qquad \text{For} \quad 0 \leq x \geq L$$

Thus, the Maximum Height of the Profile (R_T) can be defined as the vertical distance between the deepest valley and highest peak.

$R_T = R_P + R_V$

These parameters are useful when trying to find some very sharp peak, which could affect any application of the sample, a scratch or an unusual crack on the material.

Ten point average roughness (R_Z): The ten point average roughness (R_Z) defined by ISO system, is the arithmetic mean of the five highest peaks added to the five deepest valleys over the evaluation length measured, which is mathematically represented as Eq. 2.12.

$$R_Z = \frac{1}{n}\left[\sum_{i=1}^{n} P_i + \sum_{i=1}^{n} V_i\right] \qquad \ldots (2.12)$$

Where P_i and V_i represent the height of the ith peak and depth of the ith valley respectively. n is the number of samples along the assessment length.

In the present work, a NT-MDT atomic force microscope with Solver NEXT SPM controller and Nova Px software was used to study the surface topography of the membrane samples in semi contact mode. A NSG10 series cantilever, made up of N-type single crystal silicon of 95 ± 5 μm length and 30 ± 5 μm width, a resonant frequency of 220-250 kHz, and a spring constant of 12 N m^{-1} was used for probing. Topographic and phase images were acquired with resolution of 256 points per line.

2.6 Small angle X-ray scattering (SAXS)

Small-angle X-ray scattering (SAXS) is a technique to probe micro-inhomogeneity (in the nanometer range) in a sample matrix. The interaction of X-ray with inhomogeneity in matter can cause a small deviation of the radiation from its incident direction, called small-angle X-ray scattering. It involves measurement of elastically scattered X-rays (wavelength 0.1 - 0.2 nm) at very small angles (typically 0.1 - 10°)[196]. This is a nondestructive technique, which provides information about the shape and size of different nanostructured materials (particles, lamellae, fractals etc.), distances between scatterers in partially ordered materials, pore sizes etc. The technique requires only a minimum of sample preparation. It can be broadly used for the characterization of metals, colloids, oil, polymers, cement, plastics, proteins, foods and pharmaceuticals in fundamental research as well as in quality control.

Principle of SAXS

There are two main interactions of X-rays with matter: absorption and scattering. If X-rays hit a material, a fraction will pass through the sample, a fraction will be absorbed and transformed into other forms of energy (heat, fluorescence radiation, etc.) and a fraction will be scattered into other directions of propagation. The scattering behavior depends on:

- The atoms inside the sample will scatter the incident radiation into all directions, which gives a background radiation that is almost constant at small angles.
- The particles (i.e., clusters of atoms) inside the sample will produce additional scattering (so-called excess scattering) which is due to the fact that the particles are made of a different material or density (to give contrast) and are in the size-range of the X-ray wavelength.

By measuring the angle-dependent distribution of the scattered radiation (intensity), it is possible to draw conclusions about the average particle structure. The scattering intensity (or amplitude) is a function of scattering angle (2θ) or scattering vector (q). The scattering vector is defined as the difference between the incident and scattered wave vector K_i and K_s. As a wave vectors K_i and K_s are proportional to the linear momentum of the scattered and incident photon respectively ($p = hK$, h denotes the Plank constant), the scattering vector $q=K_s - K_i$ denotes the momentum transfer vector. Figure 2.10 is a schematic representation of a SAXS experimental setup. The scattering vector can be described as $q = |q| = 4\pi \sin(\theta)/\lambda$, 2θ is the scattering angle.[197]

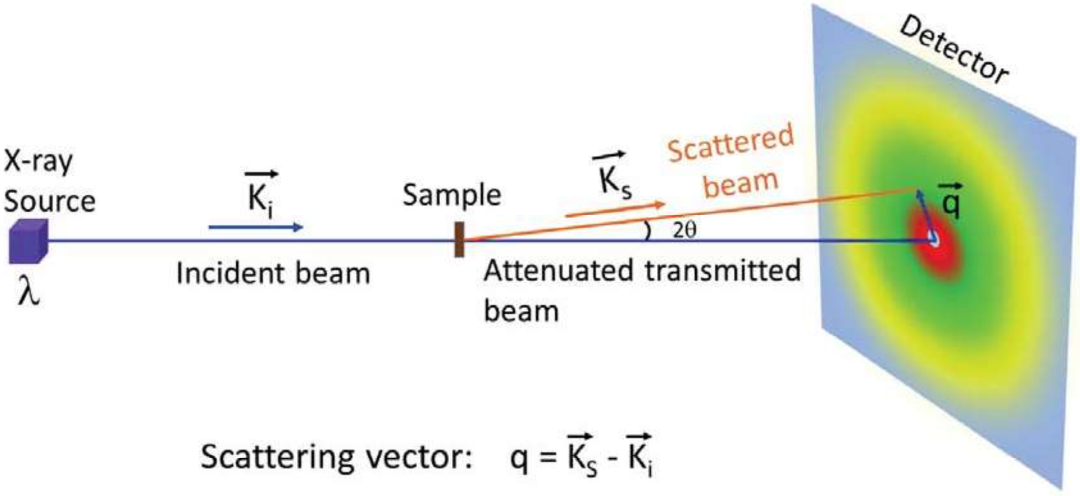

Figure 2.10: Schematic representation of the experimental setup for a SAXS experiment and representation of the scattering vector (q) on the detector surface.

Laboratory Based SAXS Instrument

A typical laboratory based SAXS experimental setup consists of: X-ray source, monochromator, a collimation system, a sample holder, a beam stop and a detection system, shown in Figure 2.11. The source irradiates the sample, and the detector measures the radiation coming from the sample in a certain range of angles. Because 2θ is small, large sample to detector distance is maintained to improve the angular resolution. The collimation system makes the beam narrow and defines the zero-angle position. Most available X-ray sources produce divergent beams that is overcome by making beam parallel by a multilayer parabolic mirror (Gobble mirror) in conjunction with slit collimation. In SAXS, the non-scattered beam that merely travels through the sample must be blocked without blocking the closely adjacent scattered radiation. The beam stop prevents the intensive incident beam hitting the detector, which would overshadow the relatively weak scattering of the sample and would even destroy some of the detectors.[198]

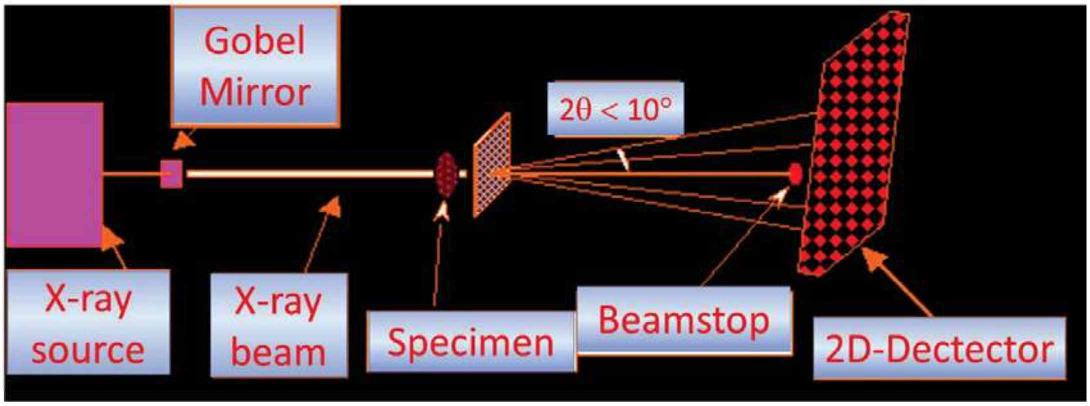

Figure 2.11: A schematic of typical SAXS instrument

Laboratory based SAXS instruments can be divided into two main groups based on collimator design:

(i) Point Collimation Instruments: Point collimation instruments have pinholes that shape the X-ray beam to a small circular or elliptical spot that illuminates the sample. Thus, the scattering is centro-symmetric about the primary X-ray beam and the scattering pattern in the detection plane consists of circles around the primary beam. Owing to the small illuminated sample volume and the loss of incident beam intensity in the collimation process, the scattered intensity is small and therefore the measurement time is in the order of hours or days in case of very weak scatterers. If focusing optics like bent mirrors or bent monochromatic crystals or collimating and monochromatic optics like multilayers are used, measurement time can be greatly reduced. Point collimation geometry allows one to investigate non-isotropic systems such as fibers, sheared liquids.

(ii) Line Collimation Instrument: Line collimation instruments confine the beam only in one dimension so that the beam profile is a long but narrow line. The illuminated sample volume is much larger compared to that in point-collimation and the scattered intensity at the same flux density is proportionally larger. Thus measurement time with line-collimation SAXS instruments is much shorter compared to point-collimation and in the range of minutes. A disadvantage is that the recorded pattern is essentially an integrated superposition (a selfconvolution) of many pinhole patterns. The resulting smearing can be easily removed using model-free algorithms or deconvolution methods based on Fourier transformation, but only if the system is isotropic. Line collimation is of great benefit for any isotropic nanostructured materials, e.g., proteins, surfactants, particle dispersion and emulsions.

The present experiments have been carried out with a laboratory-based SAXS instrument with CuK_{α} as probing radiation (wavelength 1.54 Å). Sample to detector distance has been kept 107 cm. The samples were covered both sides by 25 micrometer thick polyimide films to avoid either water uptake or water evaporation during the scattering measurements.

2.7 Universal testing machine (UTM)

A Universal testing machine (UTM) is used to study the mechanical properties i.e. the behavior of a material under stress e.g. tensile strength, elongation, stiffness, brittleness, hardness etc.

Working principle:

A UTM consists of one or two vertical load bearing columns on which are mounted a fixed base horizontal plate and a moveable horizontal crosshead on top. The movable crosshead is attached to a rotating ball screw in order to drive a load-bearing crosshead up and down. An electrical motor powers a series of pulleys and gears which turn the screw, creating the crosshead motion. A membrane sample piece is gripped at both ends in the jaws of UTM, which slowly exerts an axial pull so that the sample is stretched until it breaks. A load cell in series with the grip measures the force applied to the specimen, which can be displayed on a digital display or a PC. An extensometer is automatically recorded the change in gauge length during the test. Once the machine is started, it begins to apply an increasing load on the specimen. Throughout the tests, the control system and its associated software record the load and extension or compression of the specimen. The data obtained from the tensile tests describes many mechanical features of the polymer. Figure 2.12 shows a typical stress-strain curve for a thermoplastic polymer, and Table 2.2 describes the features of a stress-strain curve.[199]

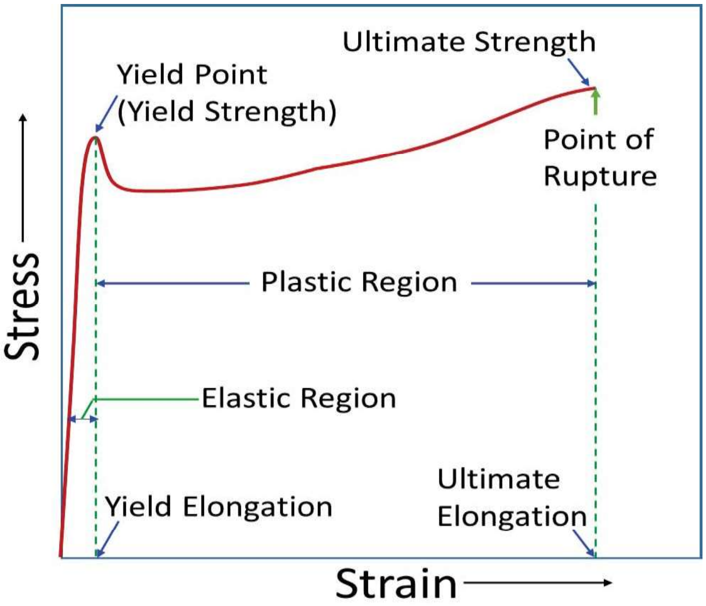

Figure 2.12: Typical stress-strain curve of a thermoplastic polymer

Table 2.2: Definition of terms on a stress-strain curve

Definition	Description
Yield Point (strength)	Yield point is the first point (load) at which the specimen yields. This is when the specimen's cross-sectional area begins to decrease. This is called necking.
Modulus of Elasticity	The ratio of stress to strain within the elastic region of the stress-strain curve.
Yield Elongation	The strain at the yield point
Elastic Region	The portion of the curve before the yield point
Plastic Region	The portion of the curve after the yield point
Ultimate (tensile) strength	The maximum stress that a membrane samples can withstand before breaking.
Ultimate elongation	The total elongation just before fracture.

Deformation Behavior

There are two main deformation regions in a stress-strain curve; elastic and plastic deformation. Figure 2.13 shows the characteristic stress-strain behavior for an amorphous polymer. It is characterized by a linear elastic region, a yielding followed by a drop in stress, a formation of a neck, a drawing of the neck, an increase in stress due to the straightening of polymer chain, and finally fracture. The elastic deformation in these polymers is the result of two mechanisms. An applied stress causes the covalent bonds within the chain to stretch and distort, allowing the chains to elongate elastically. When the stress is removed, recovery from this distortion is almost instantaneous. In addition, entire segments of the polymer chains may be distorted. In this case, when a stress is applied and then removed, the chains move back to their original position over a period of time. This time can range from a few seconds to a few months. This time-dependent behavior is viscoelastic and contributes to the non-linearity of elastic behavior when the stress is removed.[200,201]

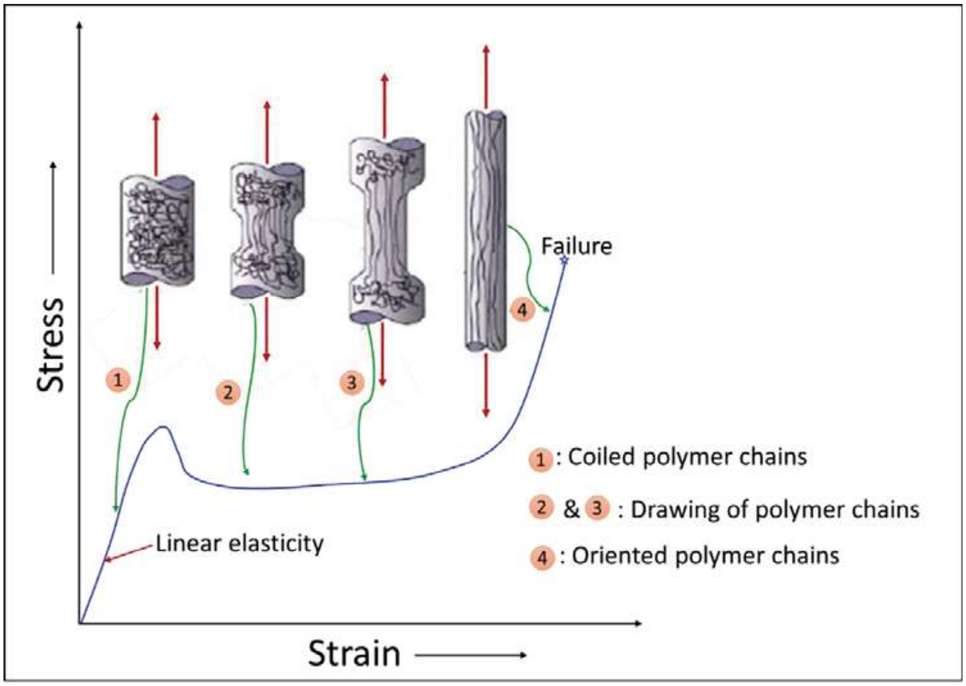

Figure 2.13: Deformation behavior of thermoplastic polymers during tensile testing

Thermoplastic polymers exhibit non-isochoric behavior during tensile and compression testing as well as particular deformations like local necking (tension) or buckling (compression). Semi-crystalline thermoplastic polymers show a particular behavior in uniaxial tensile testing. After reaching the initial yield point local necking occurs followed by a cold-drawing plateau, which is associated with the propagation of the neck at the expense of the undrawn regions (Figure 2.13). The neck propagation is caused by orientation of the originally coiled polymer chains along the stress direction. After necking is completed along the entire specimen strain-hardening occurs until rupture of the specimen at high strains. In uniaxial compression testing of thermoplastic polymers an irregular buckling of the specimen can occur. In both tension and compression, non-isochoric behavior of the polymers during plastic deformation becomes apparent.

In this work, uniaxial tensile testing of membrane samples was performed with a Universal testing machine (make HEMETEK LRX Plus) having maximum load of 5 KN, a single column with a crosshead travel range of 735 mm (29 inches). A NEXYGEN^{TM} plus software is used for the data analysis.

2.8 Thermo gravimetric Analyzer (TGA)

The Thermogravimetric Analyzer (TGA) is an essential laboratory tool used for material characterization. Thermogravimetric (TG) is a method of thermal analysis in which the mass changes of a material are measured as a function of increasing temperature (with constant heating rate), or as a function of time (with constant temperature and/or constant mass loss). Changes in the mass of a sample due to various thermal events (desorption, absorption, sublimation, vaporization, oxidation, reduction and decomposition) are studied while the sample is subjected to a program of change in temperature. Therefore, it is used in the various properties analysis of a material,[202,203] such as:

- Purity and thermal stability.

- Decomposition of inorganic and organic compounds.
- Determining the composition of the mixture.
- Reaction kinetics studies.
- Oxidative and reductive stability.
- Determining moisture, volatile and ash contents.
- Desolvation, sublimation, vaporizations, sorption, desorption, chemisorptions etc.

There are three different types of TG analysis are available:

- **Isothermal or Static**: In this case, the sample is maintained at a constant temperature for a period of time during which a change in weight is recorded.
- **Quasi-static:** In this technique, the sample is heated to a constant weight at each of a series of increasing temperature.
- **Dynamic:** In this type of analysis, the sample is subjected to condition of a continuous increase in temperature at a constant heating rate, i.e., usually linear with time.

Instrumentation of thermogravimetry:

The instrument used in thermogravimetry (TG) is called a thermobalance, shown in Figure 2.14. It consists of several basic components in order to provide the flexibility necessary for the production of useful analytical data in the form of TGA Curve.

Basic components of a typical thermobalance are given below:

i) Balance
ii) Furnace: a heating device
iii) Unit for temperature measurement and control (Programmer)
iv) Recorder: an automatic recording unit for the mass and temperature changes.

Balance: The basic requirements of a Balance are accuracy, sensitivity, reproducibility and capacity. There are two types of balances, null point and deflection type.

- Null type balance, which is more widely used, is consists of a sensor which detects the deviation from the null point and restores the balance to its null point by means of a restoring force.
- Deflection balance, which converts the deflection of balance beam into a suitable mass by means of photographic recording or recording electrical signals or using an electro-chemical device.

The different balances used in TG instruments are having measuring range from 0.0001 mg to 1 g depending on sample containers used.

Furnace

The furnace and control system is designed in such a way that to produce linear heating at over the whole working temperature range of the furnace and to maintain any fixed temperature. A wide temperature range generally -150 °C to 2000 °C of furnaces is used in different instruments depending on the models. The range of furnace is basically depends on the types of heating elements are used.

Temperature Measurement and Control

Temperature measurement and regulation is done with the help of thermocouples. The chromel–alumel thermocouple is often used for temperature up to 1100 °C whereas Pt/(Pt–10% Rh) is employed for temperature up to 1750 °C. The temperature may be controlled or varied using a program controller with two thermocouple arrangement, the signal from one actuates the control system whilst the second thermocouple is used to record the temperature.

Recorder

The recording unit makes use of a microprocessor, which allows for digital data acquisition and processing using a personal computer.

The whole balance system is housed in an inert atmosphere. There is a control mechanism to regulate the flow of inert gas to provide inert atmosphere and water to cool the furnace. The temperature sensor of furnace is linked to the programmer to control heating rates, etc. The balance output and thermocouple signal may be fed to recorder to record the TG Curve.

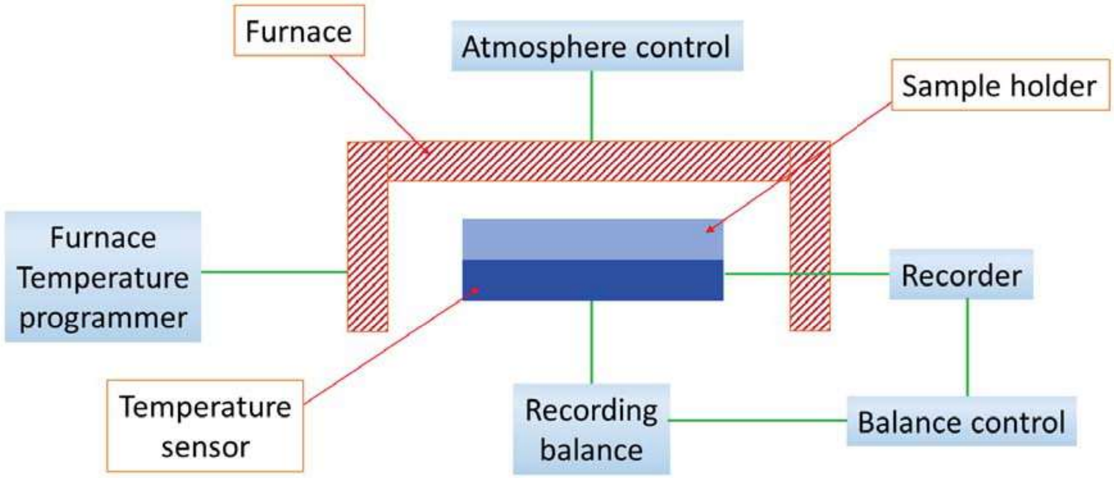

Figure 2.14: Block Diagram of a Thermobalance.

In this work, the thermal stability of the membrane samples was evaluated by thermo-gravimetric (TG) analysis in a nitrogen atmosphere using METTLER TOLEADO TGA analyzer. The TGA analyzer has a temperature range from RT to 1100 °C, Weighing accuracy of 0.005% and Weighing precision of 0.0025%. Alumina crucible having size 6*4.5 mm is used for the TG measurement. STAR^{e} Software used for the TG analysis. The heating rate of 10 °C min^{-1} was maintained and the thermogram was recorded in the temperature range from 50 °C to 700 °C. Samples were weighed accurately in the range of 8 to 10 mg and used for recording TG traces.

CHAPTER-3

[illegible]
[illegible]
[illegible]

3.1 Introduction

The membranes based on PEEK, have been found promising candidate due to their good thermo-mechanical and chemical stability with benefits of lower cost.[39,85] However, SPEEK shows lower conductivity compared to PFSA membranes owing to its rigid structure that limits movement of protons.[35] In order to increase conductivity, a higher degree of sulfonation (>80%) is required, and this, in turn, reduces mechanical and form stability of SPEEK substantially. In order to improve mechanical properties and form stability, many modifications have been carried out, like cross-linking,[39,127] blending with other polymers,[128,129] an addition of inorganic particles[130,131] etc.

Cross-linking method is a simple and effective way to achieve the desired properties including proton conductivity and mechanical/chemical stability of the membrane. Cross-linking of SPEEK can be conveniently achieved through bridging the reactive sulfonic acid functions by appropriate moieties. A series of studies has been carried out by different research groups on the development of covalently and ionically cross-linked polyarylenes [53,143,144,204,205], and the advantages and disadvantages of such efforts have been elaborated. Another method of cross-linking of SPEEK through intra/interchain condensation of sulfonic acid functionalities, that is initiated simply by appropriate thermal treatment, was introduced by the authors of a US patent.[145] This method was further implemented by Mikhailenko. et al., using simple polyatomic alcohols (ethylene glycol, glycerol), as cross-linker in different solvent/solvent pairs.[83] The present chapter describe the synthesis and characterization of SPEEK and SPEEK-PEG cross-linked membranes. Here PEG is used as a cross-linker and the method used for cross-linking is same as described by Mikhailenko. et al. A series of SPEEK-PEG cross-linked membranes have been synthesized on varying the molecular weight of PEG and studied the effect of cross-linker chain length on membranes properties. Various properties of all the membranes have been characterized including the proton conductivity, water uptake, mechanical strength, thermal stability etc. and the membranes which showed the appropriate properties have been analyzed in fuel cell to investigate the utility of membranes.

In the present study, six different molecular weight of PEG (molecular weight 200, 400, 600, 3000, 6000, and 10000 Da) [PEG-200, PEG-400, PEG-600, PEG-3000, PEG-6000 and PEG-10000] are used to investigate the effect of cross-linker chain length on membrane properties and morphology. The influence of cross-linked chain length will be discussed in detail in terms of water sorption, proton conductivity and cluster size etc.

3.2 Experimental

3.2.1 Materials

Poly(ether ether ketone) (PEEK) purchased from Gharda chemicals (MW >200000 Da.). Poly(ethylene glycol) of different molecular weights were purchased from Fluka Biochemicals. They are designated (MW range given in brackets) as namely PEG-200 (190-210 Da), PEG-400 (380-420 Da), PEG-600 (570-630 Da), PEG-3000 (2700-3300 Da), PEG-6000 (5000-7000 Da) and PEG-10000 (8500-11500 Da). Sufuric acid, Ethanol were purchased from SD Fine chemicals and were of analytical reagent (AR) grade.

3.2.2 Synthesis of sulfonated poly (ether ether ketone)

In the present study the PEEK polymer used was in the form of beads. The PEEK beads was dried overnight at 120°C before sulfonation. The sulfonation of PEEK was carried out by dissolving the PEEK beads in sulphuric acid and methane sulfonic acid. Methane sulfonic acid (15% and 30% by $v\ v^{-1}$) was added as diluent to control the rate of sulfonation and to achieve homogeneous sulfonation. PEEK beads (20 g) were dissolved in 200 mL of the reacting solvent using a mechanical shaker at room temperature for different length of time (24 hrs. to 144 hrs.). The sulfonated solution was poured on ice cold water with vigorous agitation for precipitation and the precipitate was washed several time with distilled water to remove the excesses acid till pH >6, followed by drying in an air draft oven at 120°C till constant weight.

3.2.3 Synthesis of SPEEK-PEG cross-linked membrane

Membrane preparation was carried out by solution casting method. SPEEK having IEC of 2.0 meq g^{-1} has been used for membrane preparation. SPEEK was dissolved in water:ethanol (1:1) mixture at 60 °C to prepare 5 wt% solution. Here, for the polymer (SPEEK) dissolution, water:ethanol (1:1) mixture was used as solvent because the cross-linking of SPEEK with polyols does not occur in the presence of dimethyl acetamide (DMAc), dimethyl sulfoxide (DMSO) and N-methyl-2-pyrrolidone (NMP) solvents, as these solvents compete with diol molecules for interaction with $-SO_3H$ which prevents the cross-linking of SPEEK. Whereas, ethanol/water mixed solvent gives the better result. PEG of specific MW (200, 400, 600, 3000, 6000, and 10000 Da) was weighed separately in a calculated amount in sample bottles and the polymer (SPEEK) solution was then added with vigorous stirring. The mixture was stirred for 5 hrs at room temperature to prepare homogenous solution. Membranes were prepared using varying amount PEG of a specific MW, i.e., 20 %, 33% and 40%. It was observed that the membranes without cross-linker and up to 20% cross-linker results into the brittle membranes, whereas 33% of PEG gave the better property. Therefore 33% PEG was used for membrane preparation. The mixture (SPEEK and PEG) after homogenization was casted in a petri dish followed by solvent evaporation under IR lamp for 8 hrs, the casting temperature was kept at 60 °C by adjusting the height of the IR lamp. Finally, the cast membranes were heat treated in an air draft oven at different temperatures for definite time period i.e. at 80 °C for 2 hrs., 100 °C for 2 hrs., 130 °C for 16 hrs. After the scheduled heat treatment the membranes changed their color and solubility. A membrane image before and after cross-linking is shown in Figure 3.1. The membranes became blackish brown after cross-linking and were insoluble in hot water (at 80 °C for 24 h) or in a mixture of ethanol:water [50:50]. The membranes were designated as SPEEK-PEG-200, SPEEK-PEG-400, SPEEK-PEG-600, SPEEK-PEG-3000, SPEEK-PEG-

6000 and SPEEK-PEG-10000 according to their cross-linker (PEG) molecular weight. The thickness of all the membranes were in the rage of 200-250 microns.

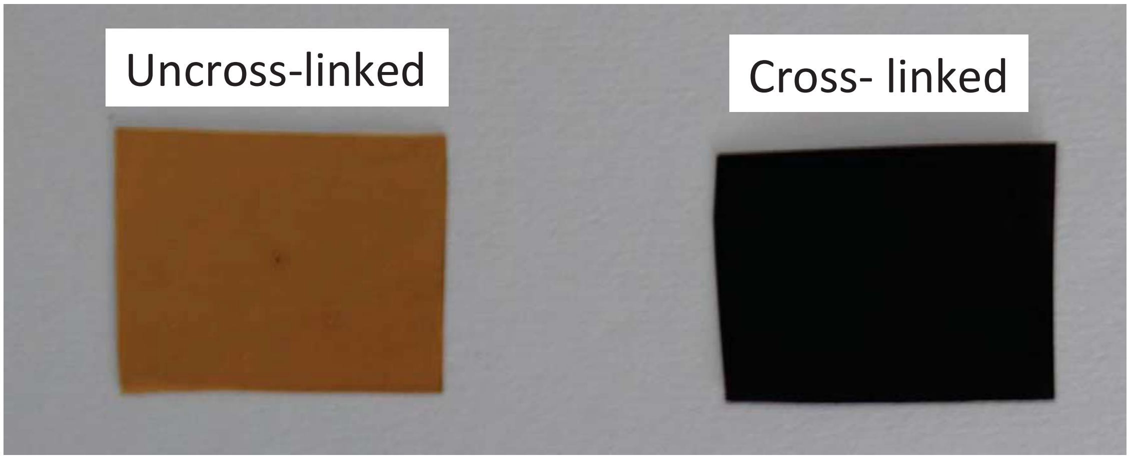

Figure 3.1: A SPEEK-PEG membrane image before and after cross-linking.

3.3 Characterization

3.3.1 Ion exchange capacity (IEC)

The ion-exchange capacity (IEC) of PEMs is a crucial parameter, which effects almost all other membrane's properties. Its determination is therefore an important step in characterizing an ion-exchange membrane. The ion-exchange capacity is a measure of the number of fixed charges per unit weight of dry polymer/membrane. It is usually expressed in milli-equivalents per gram dry polymer/membrane. In the present work, IEC provides an indication of the concentration or number density of sulfonic acid groups present in SPEEK polymer and membranes, which are responsible for conduction of protons and thus is an indirect and reliable approximation of the proton conductivity. The IECs of the polymer (SPEEK) and cross-linked membranes (SPEEK-PEG) were measured using the titration method. The samples in $-SO_3H$ form were immersed in 1M NaCl solution with constant stirring for 24 h in order to release the H^+ ions. Then, the acid solution was titrated against 0.01 M NaOH solution. The IEC was determined by using Eq. 3.1.

$$\mathrm{IEC}(\text{mequivalents} \cdot \mathrm{g}^{-1} \text{ of dry membrane}) = \frac{\text{NaOH consumed (ml)} \times \text{molarity of NaOH}}{\text{Weight of dry membrane}} \quad \text{... 3.1}$$

3.3.2 Degree of sulfonation (DS)

Degree of sulfonation (DS) is defines as the ratio of sulfonated segments to the total amount of segments present in the polymer. The degree of sulfonation of a polymer can be calculated using Eq. 3.2.[206]

$$DS = \frac{M_P \times IEC}{\{1000 - (M_F \times IEC)\}} \quad \text{... 3.2}$$

Where M_P is the molecular weight (g mmol^{-1}) of the nonfunctional polymer (PEEK) repeat unit and M_F is the molecular weight (g mmol^{-1}) of the functional group ($-SO_3Na$).

Substituting the values of M_P and M_F in Eq. 3.2, the DS of SPEEK can be calculated by using Eq. 3.3.

$$DS = \frac{288 \times IEC}{\{1000 - (103 \times IEC)\}} \quad \text{... 3.3}$$

If the DS is assumed to be 100%, then the IEC of the SPEEK would be 2.56 meq g^{-1}, which is the maximum sulfonic acid content that permitted for substitution.

3.3.3 ATR-FTIR Characterization of SPEEK and SPEEK-PEG cross-linked membrane

The SPEEK polymer as well as SPEEK-PEG cross-linked membranes were characterized by (ATR-FTIR). A Bruker, Vertex 70 spectrometer using software OPUS, VERSION 6 was used for the measurement. The spectra were recorded in the range of 400-4000 cm^{-1}. The membrane sample were pressed on a ZnSe crystal using a screw type device attached to the crystal mount. About 100 scan average was taken for each spectra.

3.3.4 Electrochemical characterization of membranes

The membrane conductivity was measured using Novocontrol Alpha-ATB impedance analyser having 4 wire impedance test interface that is connected to two Pt wire electrodes (diameter 900 microns each) 15 mm apart. The instrument was checked using standard load (100E) as well as Nafion-117 sample that was pre-treated in 1:1 HNO_3 and boiled in distilled water for 1 hr, this sample gave a conductivity of 0.1 S cm^{-1}. The membrane samples were cut in strips of 6 mm width and average thickness was taken by measuring at several places. The conductivity measurements were carried out at 27 °C with relative humidity of 50%. The conductivity of the sample measured in the longitudinal direction was calculated using the relation $\sigma = d/RA$, where d and A are the distance between the electrodes and the cross-sectional area of the membrane respectively, and R is the resistance derived from the frequency-interval (10E7 to 10E5 *Hz*) using Bode plot.

3.3.5 Water Uptake measurement of cross-linked membranes

Water uptake by membranes was measured in two different conditions, after equilibrating in water (i) at room temperature (27 °C) for 48 hrs, (ii) at elevated temperature (60 °C) for 1 hrs. Membrane pieces (2 cm^2) were cut from all the samples and kept at room temperature and 60 °C in distilled water thereafter the weight of membranes were measured in wet condition. Dry weight of the same was measured by drying the sample in an air draft oven at 110 °C till constant weight. The water uptake was calculated using Eq. 3.4.

$$\%\,\text{Water Uptake} = \frac{(\text{Wt. of wet membrane - Wt of dry membrane})}{\text{Wt of dry membrane}} \times 100 \qquad \text{... 3.4}$$

3.3.6 Membranes morphological characterization by Small Angle X-ray Scattering

The membranes morphological characterization was done by SAXS measurement. The membrane samples were treated in water at room temperature and 60°C prior to the experiments and were covered both sides by 25 micrometer thick polyimide films to avoid either water uptake or water evaporation during the scattering measurements.

Radial averaging of the raw experimental data was performed to obtain the scattering intensity (□□□□) within a wave vector transfer ($q= 4\pi\, Sin(\theta)/\lambda$, and $d=2\pi/q$) where λ represents the wavelength and 2θ represents the scattering angle range corresponding to q value of 0.1 nm^{-1} to 2.5 nm^{-1}). The scattering data were corrected for sample absorption. In order to analyze the scattering profiles, interacting polydisperse spherical particle model is adopted. The scattering intensity $I_{Mem}(q)$, under local monodisperse approximation[207] is represented as

$$I_{Mem}(q) = C_1\left(\int_0^{\infty} P_{Cluster}(q,R)R^6 D_{Cluster}(R)S(q,R)dR\right) \quad \text{… 3.5}$$

where, the term $P_{Cluster}(q,R)$ represents the form factor of the water cluster.

$$P_{Cluster}(q,R) = 9\frac{(\sin(qR) - qR\cos(qR))^2}{(qR)^6} \quad \text{… 3.6}$$

$D_{Cluster}(R)$ represents the size distribution of the water cluster, i.e., $D_{Cluster}(R)dR$ indicates the probability of having radius of water cluster between R to $R+dR$. In present case, standard lognormal distribution is considered, as given by the following equation.

$$D_{Mem}(R) = \frac{1}{\sqrt{2\pi\sigma^2 R^2}}\exp\left[-\frac{[\ln(R/R_{med})]^2}{2\sigma^2}\right] \quad \text{… 3.7}$$

R_{med} denotes the median radius and σ denotes the polydispersity index of the distribution being obtained by fitting the SAXS profiles. The term R□ comes from the square of the volume of the cluster with radius R□C□ is the scale factor, independent of q, and depends on the scattering contrast and number density of the clusters. *S(q*□*R)* is the hard sphere structure factor[208] and represents the spatial correlation among the clusters. *S(q)* provides the information about the local volume fraction (*f*) of the clusters. In order to take care the scattering contribution in low q (<1 nm^{-1}), an extra contribution for the un-correlated structure was considered and is represented by Debye, Anderson and Brumberger Model.[209]

$$I_{Large}(q) = C_2\left(\frac{1}{\left(1+q^2\xi^2\right)^2}\right) \qquad \dots 3.8$$

Total scattering intensity was assumed to be the cumulative contribution of $I_1(q)$ and $I_2(q)$.

$$\therefore I(q) = I_1(q) + I_2(q) \qquad \dots 3.9$$

Eq. 3.9 was fitted to the experimental data using a non-linear least square method, in order to estimate the unknown parameters.

3.3.7 Topographical characterization of SPEEK and SPEEK-PEG membranes by Atomic Force Microscope studies

The surface topography of the membrane was studied using NT-MDT atomic force microscope with Solver NEXT SPM controller. The topography characterization of SPEEK and SPEEK-PEG membrane samples was carried out in hydrated and non hydrated conditions. Wet samples were allowed to rest in air for 5 min to evaporate the top layer of water. Measurements were carried out in semi contact mode and an area of 20 µm X 20 µm is scanned for the topography.

3.3.8 Mechanical Strength characterization

Universal testing machine (make HEMETEK LRX Plus) was used for the measurement of mechanical strength of the membranes. Each sample was treated in water at room temperature (27 °C) and cut into 3 strips of width about 6 mm. Each strip was clamped in the machine where the distance between the clamps was kept 50 mm and tensile strength and % elongation at break were measured. Care was taken to ensure that the samples were in wet condition. Similarly another set samples were treated in water at 60 °C and after cooling the measurement was repeated at room temperature. All the measurements were carried out at 27 °C with 50% relative humidity. A load cell of 1 kN and extension rate of 100 mm min^{-1} were used for these measurements.

3.3.9 Thermal stability characterization of SPEEK and SPEEK-PEG membranes

Thermal stability of the sulfonated polymers and membranes were evaluated by thermo-gravimetric (TG) analysis in nitrogen atmosphere using METTLER TOLEADO TGA analyzer. The heating rate of 10 °C min^{-1} was maintained and the Thermogram was recorded in the temperature range from 50 °C to 800 °C. About 8-10 mg of sample was weighed accurately and used for recording TG traces.

3.3.10 Membrane performance study in PEMFC

The membranes performance in the fuel cell was carried out in a single cell having active electrode area of 25 cm^2. The membrane electrode assemblies (MEA) were prepared using a commercially available electrode having 20% Pt on Vulcan CR72 (Pt loading: 0.5 $mgcm^{-2}$). The MEA was prepared along with membrane preparation unlike the commonly used hot press method.[210,211] The hot press method uses Nafion solution that helps in increasing three phase contact as well as binding of the electrode with the membrane. However, in the present case the the electrodes were coated with the same polymer solution that was used for respective membrane synthesis. The membranes were assembled with electrode before curing process, at this stage the electrodes and the membranes were bonded. The whole MEA assembly was then cured in line with the procedure described in the synthesis of SPEEK-PEG membranes. The image of cured MEA given in Figure 3.2.

Figure 3.2: A MEA image used in fuel cell analysis.

The cured MEA was sandwiched between two graphite plates with serpentine flow field and two gold-coated copper plates as a current collector in a single fuel cell setup. Plate-type heaters were inserted in between the current collectors and end plates to control the cell temperature. The cell temperature was measured at the graphite plate using a digital thermometer. During the cell test, H_2 (50 ml min^{-1}) and O_2 (100 ml min^{-1}) was passed through a heated bubble type gas humidifier. The humidifier temperature was kept 5°C above the cell operating temperature. The MEA was first operated at 30°C and the polarization curve was recorded after performing 10 on-off cycles of 30 min each with MEA operated at maximum power density. In the next step, the temperature was increased to 40°C and polarization curve was recorded after 10 cycles. After that, the temperature was increased to 50°C and polarization curve was recorded after 10 cycles The MEA was finally pre-conditioned by operating the cell at 60°C. The cell was operated under the condition of open circuit voltage (OCV) for 10 min followed by operating at 300 mA cm^{-2} for 30 min, and at the end of it polarization curve was recorded. The activation was carried out for 16 h till a constant polarization curve that did not change during the next cycles was obtained. The fuel cell measurements then were carried at 60°C.

3.3.11 Methanol Permeability Measurement

The Methanol permeability across the membranes was determined by using in-house developed two-compartment diffusion cell made of Perspex, shown in Figure 3.3. The cell containing solutions A and B in two identical compartments separated by the test membranes was utilized for permeability tests. The membranes were placed between the two compartments by a screw clamp. Solution A is 2 M methanol and solution B is deionized water. Both compartments were stirred during the permeation experiments. The membrane was equilibrated in 2 M methanol for 24 hrs initially and thereafter at the measurement temperature for 1 hr and washed with water before measurement. The samples are collected from the DM water compartment (solution B) at regular interval of time and analyzed for total organic carbon (TOC) using TOC analyzer (make ANATOC). The TOC method was standardized by using known methanol standards, the correlation factor for the measured and the calculated amount of methanol was 1.018, therefore this method is used for the determination of methanol concentration in the compartment B. The methanol permeability is determined using the following equation.[212]

$$\square_{\square} = \frac{\square\square_{\square}}{\square\square} = \frac{\square}{\square_{\square}}\left[\frac{\square\square}{\square}\right]\left(\square_{\square} - \square_{\square}\right) \qquad \ldots 3.10$$

Where, k_B is the methanol flux through the membrane, D is diffusion coefficient, H is partition coefficient, L is membrane thickness, C_A and C_B is concentration of methanol in compartment A and B respectively.

Equation (5) is rearranged to give the permeability P (defined as permeability P =D·H)

$$P = (D \times H) = \frac{k_B \times V_B \times L}{A \times (C_A - C_B)} = \frac{(mol/cm^3 s) \times (cm^3) \times (cm)}{(cm^2) \times (mol/cm^3)} = \frac{cm^2}{s} \quad \text{... 3.11}$$

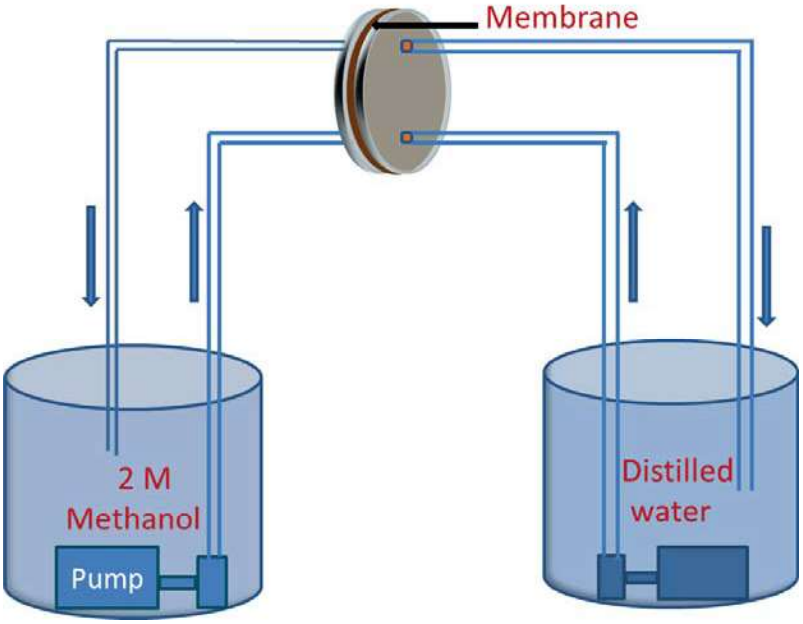

Figure 3.3: Experimental setup for methanol permeability measurement.

3.4 Results & Discussion

3.4.1 Sulfonation of PEEK and Characterization of SPEEK

Concentrated sulphuric acid is commonly used for sulfonation of PEEK. In the present study the PEEK used was in the form of beads. Initially it was observed that the use of sulphuric acid resulted in the heterogeneous sulfonation. The beads took 24 hrs to get dissolved in order to form a homogeneous solution. The polymer chains that dissolve in the initial stages of dissolution get highly sulfonated whereas polymer that dissolve at the end gets less sulfonated.

The highly sulfonated polymer fraction dissolve in water during the precipitation process resulting in the lower yield (<80%) of sulfonated polymer. This heterogeneity in sulfonation was reduced by the use of methanesulfonic acid (MSA) which is a solvent for PEEK. The MSA acts as a diluent and controls rate of sulfonation especially in the initial stages of dissolution. The complete dissolution of the PEEK bead in the sulphuric acid and MSA mixture takes 8 hrs and yields polymers with more homogeneous sulfonation. The SPEEK yield obtained by this method, was more than 95%. The two concentrations of MSA investigated are namely 15% and 30%. The IEC values of SPEEK as a function of sulfonation reaction time is plotted in the Figure 3.4.

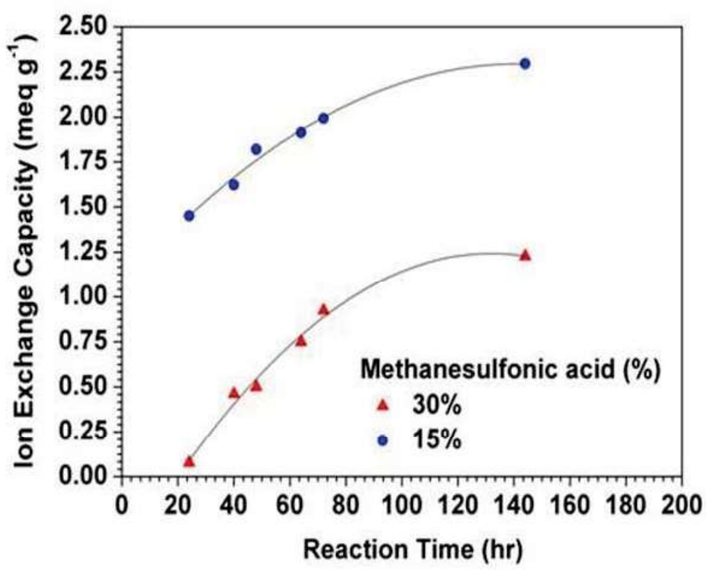

Figure 3.4: Ion exchange capacity of SPEEK polymer with sulfonation time at two different concentrations of Methanesulfonic acid.

The IEC increases steadily with time of sulfonation reaction. The higher amount of diluent (30% MSA) results in lower sulfonation and lower IEC. The 15% MSA is found to be optimal and yields polymer with maximum IEC of 2.3 meq g^{-1} (in dry in H^{+} form). The sulfonated polymer at this IEC which have 90% DS being in gel form and prone to dissolution during precipitation and washing, however, the SPEEK polymer with IEC of 2 meq g^{-1} and

72.5% DS (reaction time 72 hrs) did not dissolve during precipitation and washing and therefore used in the present experiments.

3.4.2 Structural characterization of SPEEK and SPEEK-PEG cross-linked membrane

The sulfonation was also confirmed by ATR-FTIR spectroscopy. The spectral range from 850 to 1100 cm^{-1} gives the characteristic peak of sulfonation and cross-linking of sulfonic acid groups with PEG. The two characteristic peaks of -SO_3H groups at 1020 and 1079 cm^{-1} Figure 3.5 were observed for SPEEK membrane, which are assigned to the symmetric and asymmetric stretching vibration modes of O=S=O, respectively.[127] The cross-linking of SPEEK with PEG was confirmed by the shifting of symmetric stretching peak of -SO_3H group from 1020 cm^{-1} to 1024 cm^{-1} after cross-linking.

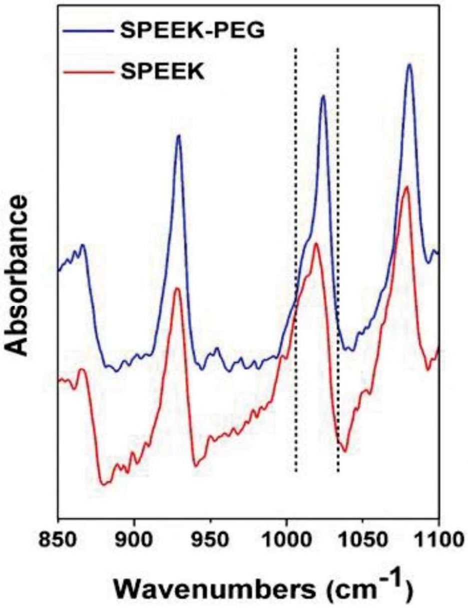

Figure 3.5: ATR-FTIR spectra of SPEEK and SPEEK-PEG cross-linked membranes.

3.4.3 Electrochemical and morphological properties of SPEEK-PEG cross-linked membranes

In the present study, cross-linker of six different molecular weights were used to investigate the effect of chain length of cross-linker on membrane properties and morphology. All the membranes were characterized after equilibrating in water at room temperature and elevated temperature (60 °C) which could be encountered by membrane in electrochemical device like fuel cell. It was observed that there is a significant change in properties of the membranes on increasing the equilibration temperature. The conductivity and water uptake of the cross-linked membranes equilibrated in water at room temperature for 48 hrs are in the range of 0.062-0.072 S cm^{-1} (± 0.005 S cm^{-1} maximum) and that for the membranes equilibrated at high temperature in the range of 0.07-0.095 S cm^{-1}. The corresponding water uptake for the room temperature equilibrated membranes is 50-60% and for the high temperature equilibrated membranes are in the range of 80-120% as shown in Figure 3.6.

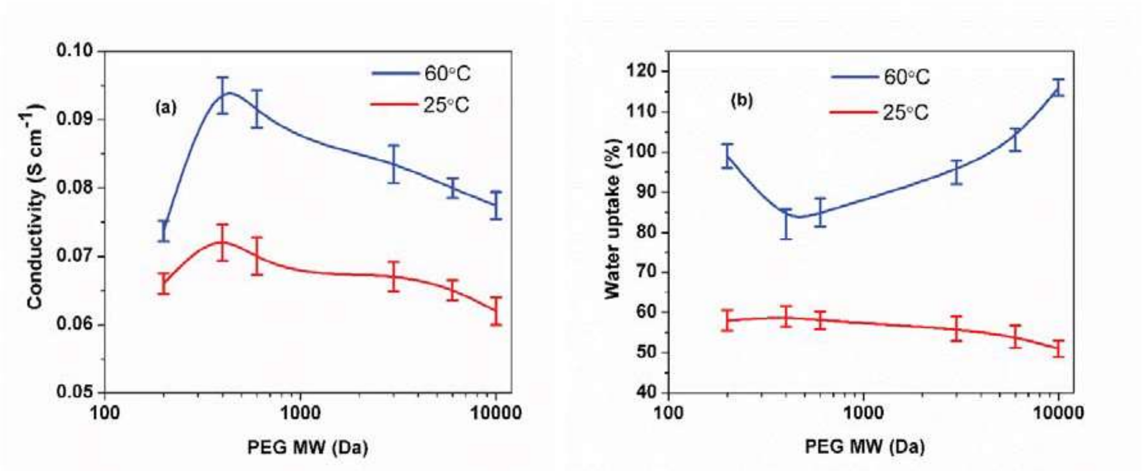

Figure 3.6: Variation of (a) conductivity and (b) water uptake as a function of molecular weight of cross-linker (PEG) for the room temperature (25 °C) and elevated temperature (60 °C) equilibrated membranes.

It is seen that, the cross-linker chain length/molecular weight does not have any significant effect on conductivity or water uptake for room temperature treated membrane, whereas the conductivity and water uptake increased after treatment in water at elevated temperature (60 °C) and the cross-linker chain length also shows a pronounce effect. This may be due to the expansion of the membrane is controlled by cross-linked chain length. It is seen clearly in Figure 3(a) that the conductivity sharply increases at

PEG-400 remains constant till PEG-600 and then decreases monotonically as a function of MW of PEG. On the other hand, water uptake is lowest in the membrane cross-linked with PEG-400 and the trend is opposite to that of conductivity Figure 3(b).

The proton conductivity of ion exchange membranes mainly depends on the IEC, water uptake and membrane morphology. After cross-linking, membranes IEC was reduced by approximately 0.2 meq g^{-1} (from 2 to 1.8 meq g^{-1}) and all the membranes have nearly equal IEC (1.8-1.85 meq g^{-1}), i.e., there is no significant effect if cross-linker chain length on IEC of the membranes.

The high proton conductivity of the SPEEK-PEG membranes treated at higher temperature could be explained by water uptake and membrane morphology. Generally, proton transport in PEMs can occur by three mechanisms; (i) surface mechanism, (ii) Grotthus mechanism, (iii) vehicular mechanism; depending on the water environment. In the surface mechanism, the protons are transported between the adjacent $-SO_3^-$ groups located on the wall of the hydrophilic channel through a series of hops between the $-SO_3^-$ group and nearby water molecules. In the bulk water region of the hydrophilic channels, proton transfer occurs by two complementary mechanisms: the Grotthuss mechanism and the vehicular mechanism. The former involves the breaking and making of hydrogen bonds between proton-donating hydronium ions (i.e. $H_5O_2^+$ or $H_9O_4^+$) and proton-accepting water molecules; and molecular reorientation. The latter occurs by the movement of proton-water aggregates, in a process similar to molecular diffusion [30]. The overall proton conductivity is the sum of the contributions from the three mechanisms. As the water uptake increased from room temperature to 60 °C the H^+ diffusion becomes fast and conductivity increased.

The morphology of the membrane was examined by AFM. Two types of membranes, namely SPEEK and SPEEK-PEG-400 cross-linked membranes in dry and wet state were studied to investigate the effect of cross-linking on the membrane morphology and are shown in Figure 3.7. The SPEEK membrane shows (Figure 3.7 (A)) smooth surface structure owing to homogeneous distribution of the sulfonic acid groups results in poor phase separation. In contrast, a distinct phase separation is observed for SPEEK-PEG-400 cross-linked membrane in Figure 3.7(C). The separation into a hydrophilic and a hydrophobic domain is less pronounced in SPEEK membrane due to less hydrophobic and more rigid aromatic chains that have lower mobility and degree of freedom during the membrane formation process. On the other hand, in SPEEK-PEG cross-linked membrane there is well-defined micro-phase separation of hydrophilic and hydrophobic regions due the incorporation of flexible cross-linker into rigid polymer chains. It facilitates the movement of the polymer chains during the membrane formation and reorganization of the polymer chains, thereby changing membrane morphology and phase separation occurs. The structure of both the membranes in the wet state shows smoother surface as compared to the membrane in the dry state. That could be due to the hydrophilic region would collapse in the dry state forming a rough surface structures which expand and form a smooth surface on the absorption of water (Figure 3.7 C1 and D1). A well-defined polymer morphology improved the electrochemical performance and the more interconnected hydrophilic domains that facilitate ion transport.

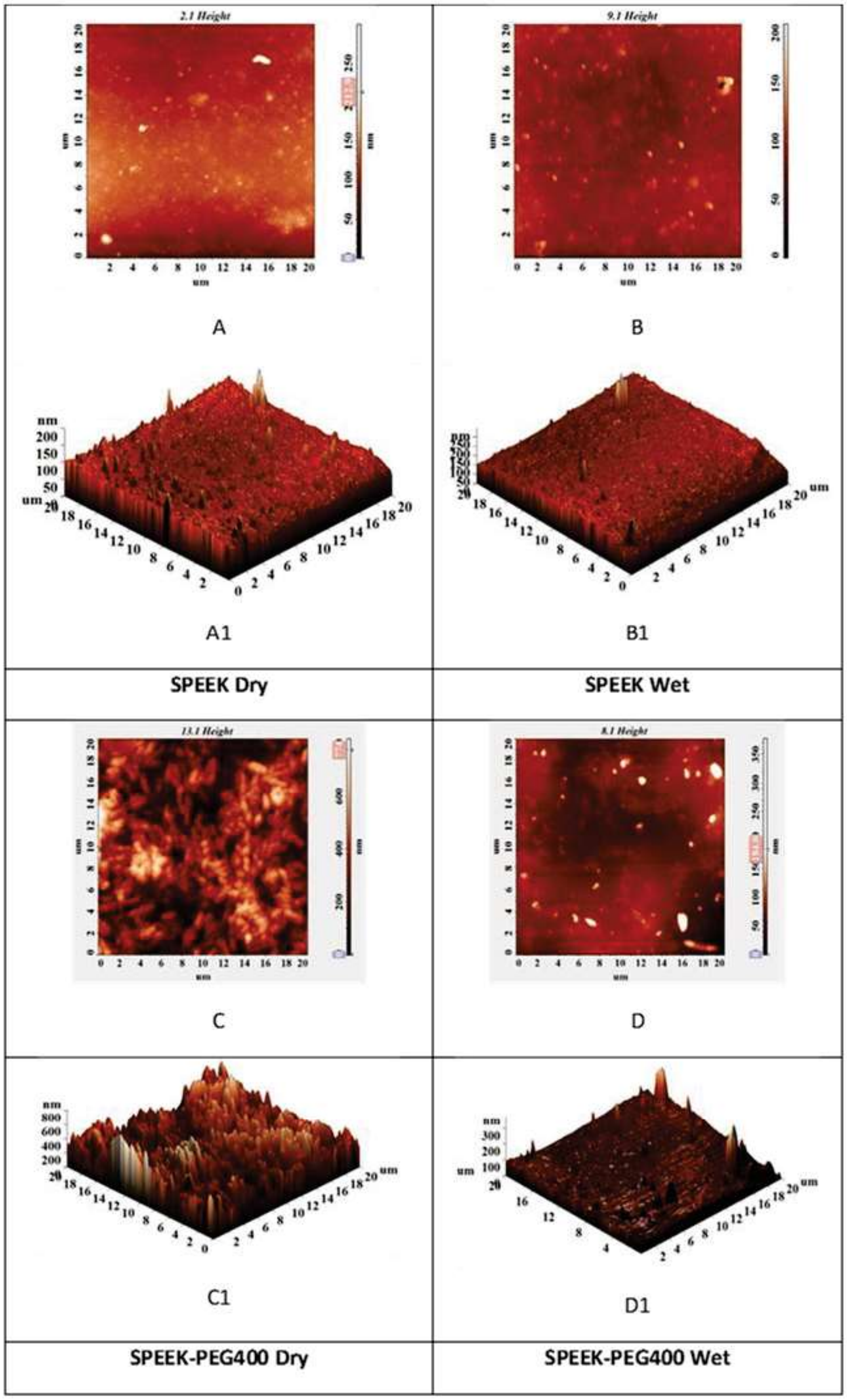

Figure 3.7: AFM Images of SPEEK and cross-linked SPEEK-PEG in dry and wet state A & B shows SPEEK Dry and SPEEK Wet membrane top surface and the A1 & B1 is the 3D view. Similarly C and D shows top surface of SPEEK-PEG-400 dry and wet membrane with their corresponding 3D view shown in C1 and D1.

While the AFM measurements provided information about the surface morphology of the membranes, SAXS measurements were useful in investigating the bulk morphology of the membranes and it is commonly used to study the morphology of ionomer membranes. The characteristic separation length between the ion-rich domains, i.e., the ionic clusters, is observed in the terms of the position, q value, and width of the so-called ionomer peak.[213] Gierke et al. calculated the size of the ionic clusters in Nafion®, and found that the sizes were smaller than the characteristic separation length deduced from the ionomer peak position.[214] The morphology of the Nafion membrane during swelling, as well as under dry conditions, has previously been thoroughly studied by SAXS.[215] In addition, the sulfonated poly(ether ether ketone)s have been investigated by several groups using SAXS measurements.[216-219]

Small angle X-ray scattering studies of SPEEK-PEG-400 that is equilibrated in water at room temperature and at 60 °C were carried out and compared with Nafion-117 (Figure 3.8). The shoulder-like profile similar to Nafion was pronounced for all the membranes which implied the presence of a nano-scale periodic structure, i.e., a phase separated structure in SPEEK-PEG membrane, this is consistent with the AFM result. The SPEEK-PEG-400 membrane treated at room temperature shows a weak broad peak at q value of 1.8 nm^{-1} (d=3.5 nm) whereas the membrane treated at 60 °C the peak shifts at lower q value of 0.8 nm^{-1} (d=7.9 nm) with higher intensity. The maxima in case of Nafion-117 is observed at q value of 1.2 nm^{-1} (d=5.2).

The interparticle model [220] can be employed to understand the existence of the two temperature regions (for example, membrane treated in water at room temperature and 60 °C) in Figure 3.8. According to this model, the Bragg spacing is a measure of the center-to-center distance in the ionic clusters. Going from the room temperature state to the state of being equilibrated in water at 60 °C, we may assume that there is a cluster combination occurs. The first absorbed water may cause several neighboring small clusters to aggregate to form bigger clusters and as the temperature is increased up to 60 °C, the size of the cluster increases and the increase in the center-to-center distance between the clusters. The inter cluster distance (d value) increases from 3.5 to 7.9 nm for membranes treated at room temperature and at 60 °C respectively. A reorganization may occur to give even larger clusters. In addition, water may penetrate into the organic part and plasticize the polymer chain, increasing the flexibility of the polymer backbone and facilitating the reorganization of the clusters. Adjacent clusters may combine to form even larger ones and the number of $-SO_3H$ groups per cluster would increases in order to keep the specific surface constant and consequently the total number of clusters decrease.

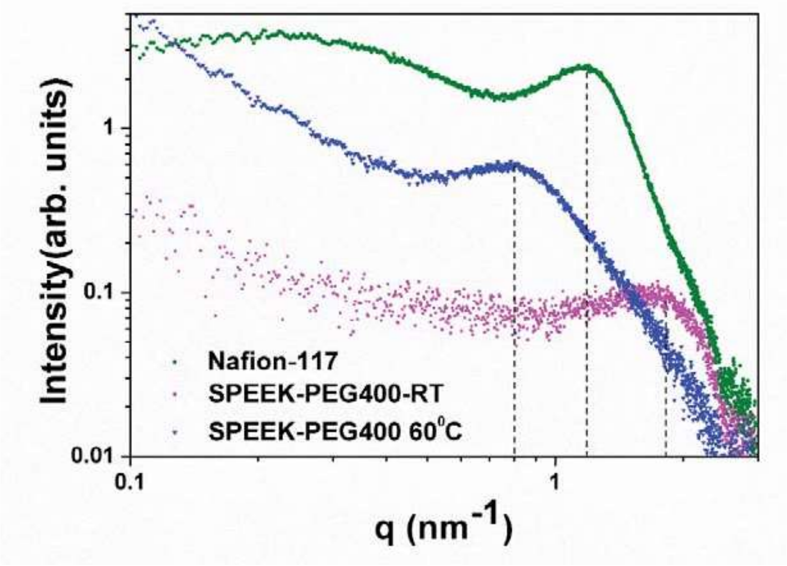

Figure 3.8: Comparison of the SAXS profiles of Nafion and SPEEK-PEG-400 cross-linked membrane after equilibrating in water at room temperature and 60 °C.

The AFM and SAXS profiles give an idea of the membrane morphology after cross-linking i.e. there is formation of hydrophilic-hydrophobic phase separation and cluster like structure. These clusters overlap on absorption of water and facilitate channel formation where the vehicular diffusion of protons contribute to high proton mobility resulting in increased membrane conductivity after treatment at higher temperature.

To investigate the effect of cross-linker chain length on membrane conductivity and water uptake which is shown Figure 3.6, the SAXS profiles of all six membranes were further fitted using a hard sphere model which gives the mean cluster diameter and its fraction, a distribution of the size was calculated using Eq. 3.7 and shown in Figure 3.9 (a). It is clearly seen that there is a significant difference in the size distribution with change in the chain length/molecular weight of the cross-linker. The variation in the peak intensity with molecular weight of PEG is clearly visible in the Figure 3.9 (a). The difference in cluster size with chain length of cross-linker is also shown in Figure 3.9 (b). The maximum peak intensity, which is direct representation of the maximum number of clusters of a particular size (R+dR) and size of the cluster at maximum intensity ($R_{Cluster}$) is plotted in Figure 3.10 along with the conductivity for all the membranes. Here the conductivity curve is same as plotted in Figure 3.6 for 60 °C treated membranes. All the curves are fitted logarithmically in two regions i.e. from 200-400 Da and 400-10000 Da. As seen in Figure 3.10, the $R_{Cluster}$ value at maximum intensity has inverse correlation with the conductivity whereas the intensity has direct correlation with the membrane conductivity. At the MW of PEG-400, cluster size is lower whereas the number of clusters are higher and also conductivity is higher. On the other hand, at MW of PEG 200 and 10000 Da, cluster sizes are higher, number of clusters are lower and the conductivity is also lower (Figure 3.10). The higher number of clusters would lead to lower inter cluster distance leading to cluster overlaps and channel formation, also the channel connectivity probability would increase leading to increase in conductivity. Lesser number of clusters would decrease the cluster overlap and lesser number of channel formation thereby decreasing conductivity. This implies that larger number of small sized clusters results in higher conductivity than larger size small number of clusters.

In all the characterizations, the membranes properties e.g. conductivity, water uptake, cluster intensity and cluster size have shown two distinct regions from 200 to 400 Da and 600 to 10000 Da. For lower chain length/molecular weight (<400 Da), the number of –OH groups are higher for same percentage of PEG (33%). This results in the absorption of more water molecule at higher temperature and reduce the H$^+$ concentration. Similar results were observed for lower molecular weight cross-linker, e.g., ethylene glycol, i.e. water uptake of 2100% at 80 °C,[83] The higher water uptake would also result in merger of clusters thereby increasing the cluster size and reducing the cluster intensity.

For higher chain length i.e. above 600 Da the conductivity decreased logarithmically with MW, the decrease in conductivity could be due to the entanglement of polymer chains that makes tortuous path and hindered the H$^+$ movement and the other possibility is the formation larger size cluster which uptake more water at higher temperature equilibration (Figure 3.6) and H$^+$ concentration reduced. Thus PEG-400 has the optimum chain length that gives highest conductivity and lowest water uptake.

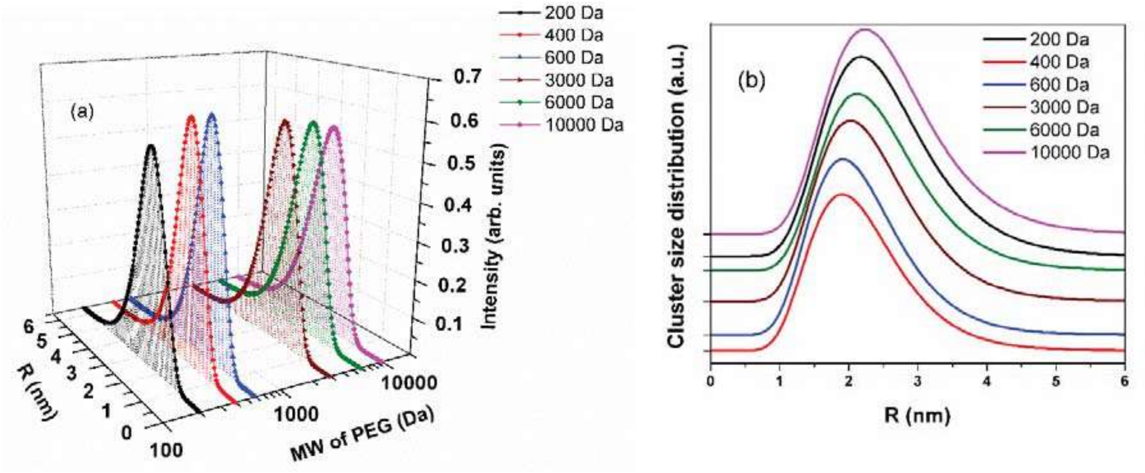

Figure 3.9: Cluster size distribution of SPEEK-PEG membranes for different molecular weight of PEG (a) 3D and (b) 2D plots.

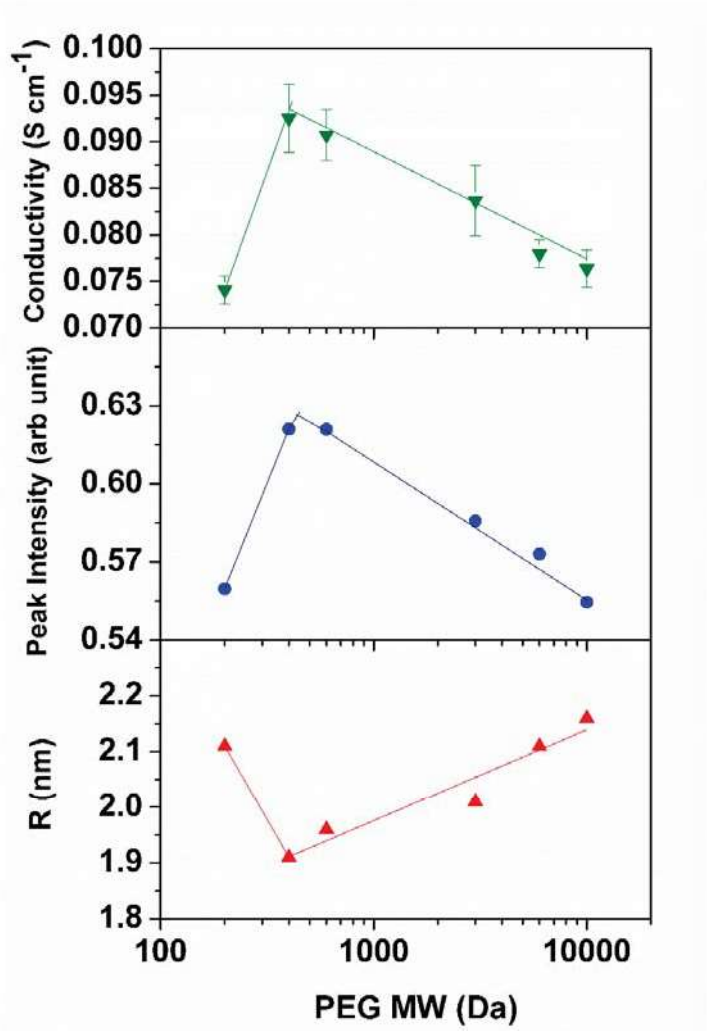

Figure 3.10: Variation of cluster radius, peak intensity with PEG molecular weight and comparing the trend with corresponding conductivity of the membrane.

3.4.4 Mechanical Properties of SPEEK-PEG cross-linked membranes

Mechanical properties are greatly influenced by water uptake and membrane morphology. Figure 3.11 shows the stress-strain curve of two types of SPEEK-PEG membranes, SPEEK-PEG-400 (highest conductivity) and SPEEK-PEG-10000 (lowest conductivity) treated at room temperature (27 °C) and elevated temperature (60 °C) in water along with Nafion.

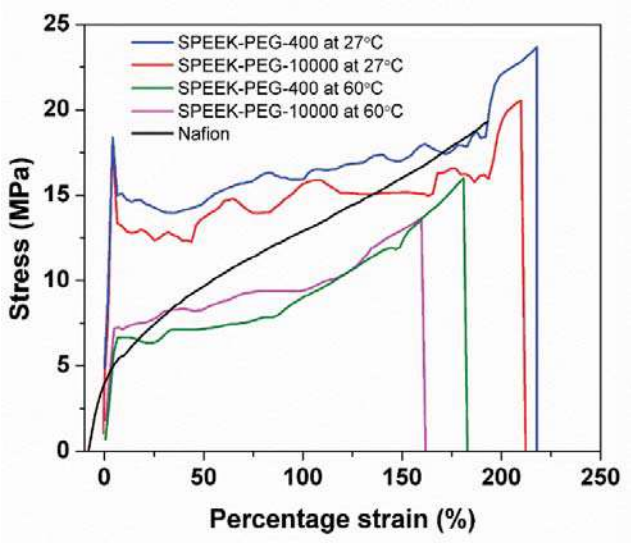

Figure 3.11: Stress-strain curve of membrane treated at 27 °C and at 60 °C.

There is a marked difference between the mechanical properties of the membranes treated at room temperature and elevated temperature. The stress-strain curve for membrane samples treated at 60 °C is smother without necking at the yield point compare to the samples treated at room temperature (27 °C) which indicated that the membrane has softened. Membranes treated at room temperature have very high Young's modulus, e.g., SPEEK-PEG-400 has Young's modulus of 543 MPa, which is reduced after treatment at 60 °C to 280.5. This indicates that the room temperature treated membrane are very stiff and after treatment of membrane in water at 60 °C modifies the membrane structure to a great extent and improvement in the membrane elasticity is observed. The treated membrane stress-strain behavior resembles that of the Nafion, which has Young's modulus of 26 MPa. The increased water uptake, increases the mobility of the polymer chain resulting in decrease in the Young's modulus and stiffness.

Room temperature treated membrane's the tensile strength is in the range of 20 to 25 MPa and the percentage elongation in the range of 205 to 225%, whereas for the 60 °C treated samples the tensile strength and percentage elongation reduced to 10 to 15 MPa and 150 to 190% respectively. With increased water uptake the intermolecular force between the polymer chains decreased leading to increased chain mobility and decreased tensile strength.

3.4.5 Thermal stability of SPEEK and SPEEK-PEG membrane

Thermal stability of membranes is a very important parameter in order to operate the membrane at higher temperatures. Figure 3.12 shows TGA traces of SPEEK having different IEC, PEG-400 and cross-linked SPEEK-PEG-400 membrane. The PEEK and PEG showed one step degradation whereas SPEEK and SPEEK-PEG cross-linked membranes showed three step degradation. The three degradation temperature are below 200 °C, between 200 °C and 450 °C and between 450 °C and 800 °C.

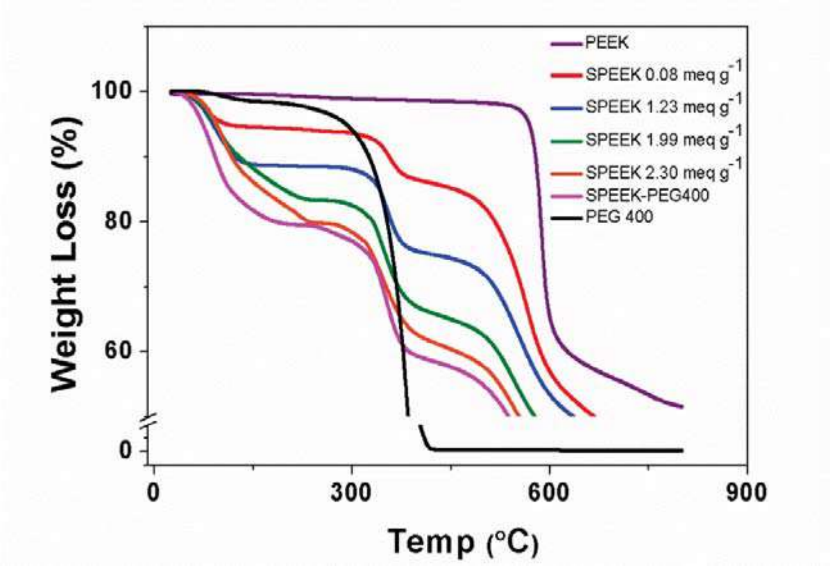

Figure 3.12: Thermo gravimetric analysis of SPEEK of different IEC and SPEEK cross-linked with PEG-400.

The first weight loss is seen below 200 °C and is due to the loss of free and bound water. The TGA traces of SPEEK sulfonated to different extent shows variation in the % mass loss between degradation temperatures of 300-400 °C. The % mass loss increases with increase in the degree of sulfonation. This indicates that the mass loss is due to the degradation of the sulfonic acid groups. The similar results are seen in the SPEEK-PEG-400 cross-linked membrane where the degradation of sulfonic acid begins at 350 °C, and the PEG also degrades beyond 300 °C. Mass loss in the 500-800 °C region is associated with the complete polymer degradation. Therefore, SPEEK-PEG membranes can be used for temperatures up to 300 °C in the dry state.

3.4.6 Membrane performance analysis in PEMFC

As seen from the above discussions, the membranes properties are strongly dependent on the chain length of the cross-linkers. The membranes cross-linked with PEG-400 and PEG-600, gave desirable properties in terms of overall membrane performance such as proton conductivity, mechanical strength, and membrane durability etc. In order to understand the membranes performance in fuel cell, MEAs were prepared by using two membranes SPEEK-PEG-400 and SPEEK-PEG-600 membranes. The MEAs performance tests were carried out from 30 °C to 60 °C and the polarization and power density curves as a function of current density are plotted in Figure 3.13. At all temperatures, it is observed that both the MEAs shows approximately similar performance. The maximum power density, current density and voltage at various temperatures for both the membranes are given in table Table 3.1 As seen in Figure 3.13 (a) and (b), at 60 °C the SPEEK-PEG-400 membrane showed the maximum power density of 183.04 mW cm^{-2} at 440 mA cm^{-2} and at 0.416 V. On the other hand, SPEEK-PEG-600 membrane showed the maximum power density of 170.52 mW cm^{-2} at 420 mA cm^{-2} and at 0.406 V, i.e. approximately similar performance of both the membranes in fuel cell.

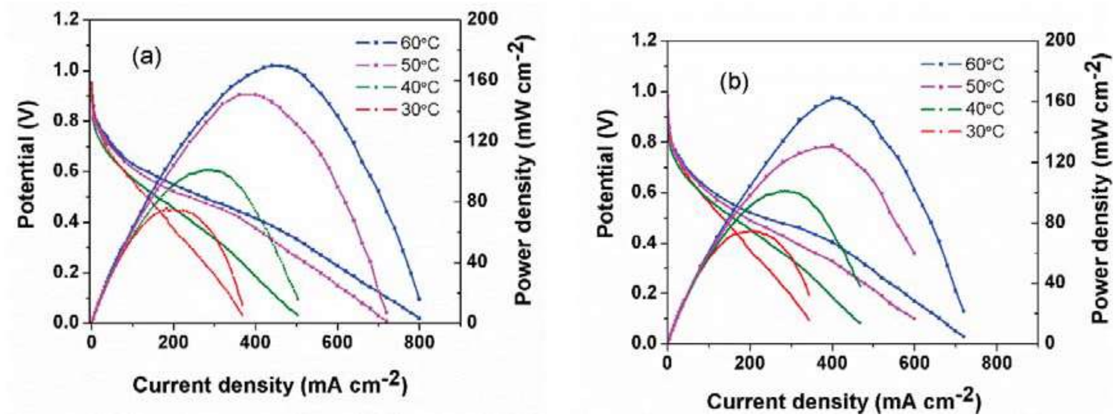

Figure 3.13: Fuel cell performance of (a) SPEEK-PEG-400 and (b) SPEEK-PEG-600 cross-linked membranes at various temperatures.

Table 3.1: The maximum power density, current density and voltage at various temperatures of SPEEK-PEG-400 and SPEEK-PEG-600 cross-linked membranes.

Sample name	Temperature (°C)	Current density (mA cm^{-1})	Voltage (V)	Power density (mW cm^{-1})
SPEEK-PEG-400	30	216	0.342	73.87
	40	292	0.346	101.03
	50	380	0.389	147.82
	60	440	0.416	183.04
SPEEK-PEG-600	30	208	0.357	74.25
	40	284	0.356	101.10
	50	400	0.358	143.20
	60	420	0.406	170.52

3.4.7 Methanol Permeability analysis

Among all the cross-linked membranes in this study, the SPEEK-PEG-400 showed the best properties in terms of conductivity, mechanical strength, % elongation etc. and therefore was used to study the methanol permeability. The study was carried out in order to compare with Nafion-117 and to explore its utilization in the methanol fuel cell.

Concentration of methanol permeated through SPEEK-PEG-400 membrane as function of time was measured at three different temperatures (25, 40 and 55 °C) and plotted in Figure 3.14. The methanol concentration increases linearly with time. The concentration increases steeply as with the increase in temperature. The methanol concentration at a given temperature is seen to be lower than that of Nafion at the same temperature. The slope of the curves in Figure 3.14 gives the rate of change of methanol concentration with time (k_B) (By using Eq. 3.10).

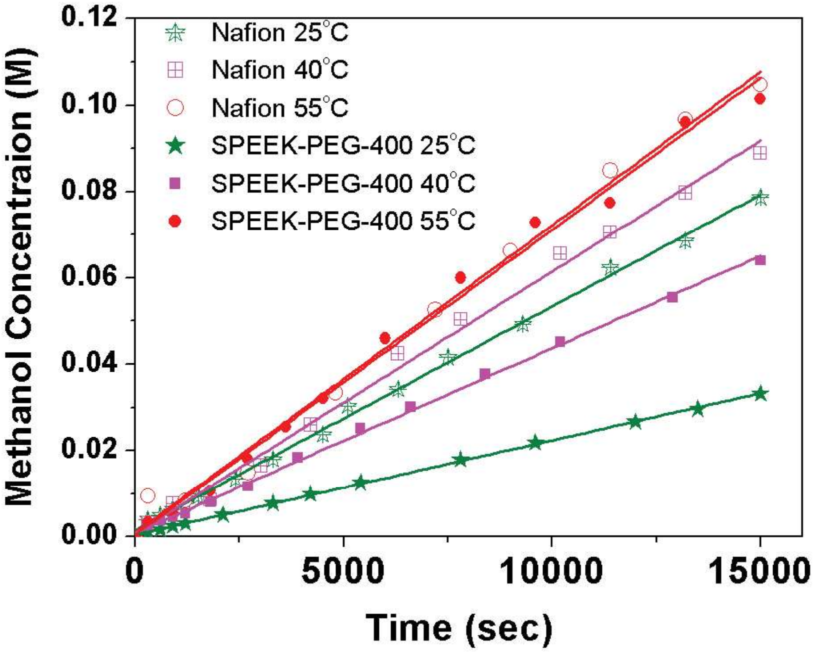

Figure 3.14: Methanol concentration in solution B as a function of time.

The methanol permeability through SPEEK-PEG-400 and Nafion-117 membranes is calculated using equation 3.11 and plotted in Figure 3.15. The permeability increases linearly with temperature for both the membranes. It is clearly seen that the SPEEK-PEG-400 membrane has lower methanol permeability than that of the Nafion 117. Therefore, this is membrane can be used alternative to Nafion-117 for direct methanol fuel cells up to 55 °C.

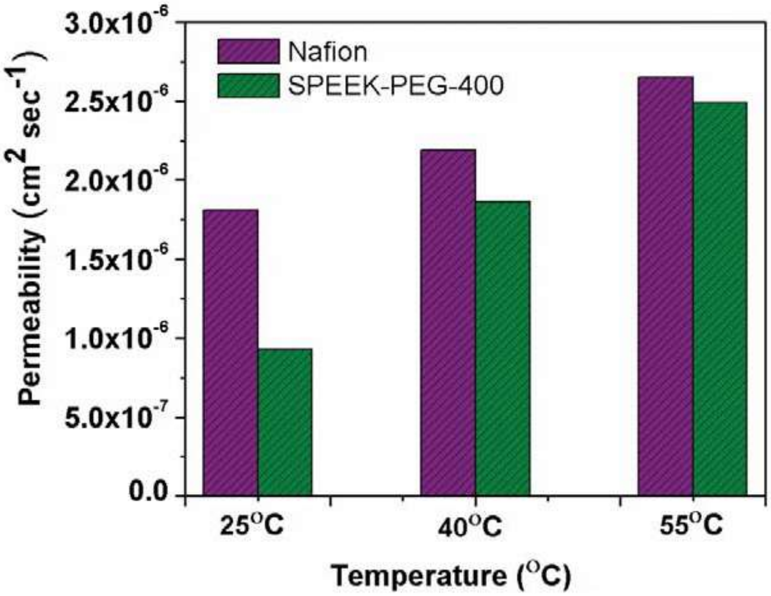

Figure 3.15: Methanol permeability of Nafion and SPEEK-PEG-400 membranes at various temperatures.

3.5 Conclusions

In this study, SPEEK-PEG cross-linked membranes have been prepared by using six different molecular weight of PEG (200-10000 Da) and the effect of the cross-linker chain length on membrane properties and morphology were investigated. AFM and SAXS studies confirm the phase separation (hydrophilic/hydrophobic) and cluster like structure formation after cross-linking. The properties of membranes were evaluated after equilibrating in water at room temperature (27 °C) and elevated temperature (60 °C) for fuel cell application. These membranes have shown good form stability up to 60 °C and proton conductivity in the range of 0.070-0.095 S cm^{-1}. Highest conductivity obtained is with PEG-400 and PEG-600 of 0.095 S cm^{-1}, which is similar to that of the commercially available perflurosulfonic acid membranes. The high conductivity is a consequence of the optimum chain length of PEG required for formation of cluster structure in the membrane. These membranes have shown good mechanical properties after treatment in water at room temperature (20 to 25 MPa) and elevated temperature (10 to 15 MPa). All the membranes were found to be thermally stable up to 300

°C and can be used for high temperature applications. SPEEK-PEG-400 and SPEEK-PEG-600 cross-linked membranes performance ware studied in PEMFC upto 60 °C. The methanol permeability of SPEEK-PEG-400 membrane was found to be lower than Nafion membrane. These membrane having conductivity similar to Nafion will be suitable for many Fuel cell/electrochemical applications.

4.1 Introduction

The earlier research efforts on the improvement on the polymer electrolytes reveal that the most commonly used processes is the addition of inorganic moieties. The Combination of organic material's properties (conductivity, flexibility, processability etc.) and inorganic material's properties (chemical and thermal stability, decrease of fuel permeability, increase water retention etc.) showed improved results. Various inorganic materials have been used extensively for SPEEK composite membrane fabrication were, e.g., inorganic oxides MO_2 (M= Ti, Zr, Si), clays, Zeolites, heteropoly acids (HPA) etc.[24,177,221-225] Heteropoly acids are one of the good inorganic modifier because of their unique properties like high conductivity, thermal stability, high selectivity and non-corrosive nature (with few exceptions).[226] Among the various heteropolyacids, phosphotungstic (PWA) and phosphomolibdic (PMA) acids, in their 29-water molecules hydrate form ($H_3PW_{12}O_{40}.29H_2O$ and $H_3PMo_{12}O_{40}$ $.29H_2O$) are characterized by high protonic conductivity, i.e, 0.17 and 0.l8 $Ohm^{-1}cm^{-1}$, respectively.[227] Such high ionic conductivity properties together with the lower cost make heteropolyacids very attractive for fuel cells.

In the previous chapter, we have seen that the SPEEK polymer properties are significantly improved by using PEG as cross-linker. PEG of molecular weight 400 Da and 600 Da (PEG-400 and PEG-600) showed the appropriate chain length for better hydrophilic/hydrophobic phase separation and best electrochemical and mechanical properties. The aim of the present work was to modify the properties of highly sulfonated SPEEK polymer based membrane by using a hybrid method (cross-linking along with the addition of inorganic additive). In this context, SPEEK-PEG-PWA membranes were fabricated where PEG-600 is used as an IPN type cross linker and PWA as an inorganic additive.

In this study, a series of composite cross-linked membranes have been synthesized by varying the weight percentage of PWA (5% to 50%) in the SPEEK-PEG-PWA composite-cross-linked membranes and investigated the optimum weight percentage of PWA. The influence of PWA blending has been discussed in terms of membranes conductivity, water uptake, chemical and mechanical stability and in fuel cell performance. The retention of PWA in the membrane samples have been discussed in detail by using EDX profile of Tungsten in the membrane samples.

4.2 Heteropoly acids

Heteropoly acids are part of a large class of polyoxometalates (POMs) and are composed of a metal such as tungsten, molybdenum or vanadium; oxygen; an element from the p-block of the periodic table, such as silicon, phosphorous or arsenic and acidic hydrogen atoms. Heteropoly acids are one of the good inorganic modifier because of their unique properties like high conductivity, thermal stability, high selectivity and non-corrosive nature (with few exceptions)[226]. Solid HPA's have a discrete ionic structure, comprising of fairly mobile heteropoly anions and counter-cations (H^+, H_3O^+, $H_5O_2^+$, etc.), unlike the network structure of zeolites and metal oxides. This unique structure exhibit high proton mobility and a "pseudo-liquid phase"[228,229]. Keggin and Wells–Dawson are two important structures of the HPAs. The HPA having Keggin structure were the most stable and more easily available; Keggin anions which typically represented by the formula $XM_{12}O_{40}^{x-8}$ as shown in Fig. 1[230],where X is the central atom (Si^{4+} , P^{5+}, etc.), x is its oxidation state, and M is the metal ion (Mo^{6+} or W^{6+} etc.) also called addenda atoms. The Keggin unit of HPA has twelve MO_6 octahedra surrounding the central XO_4 tetrahedron. The Keggin unit has four types of oxygen atoms in it: four oxygen atoms of the central XO_4tetrahedron (O_c), twelve oxygen atoms that bridge the M atoms not sharing a central oxygen atom (corner-sharing, O_{b2}), twelve oxygen atoms that bridge two M atoms sharing the same central oxygen atom (edge-sharing, O_{b1}), and twelve terminal oxygen atoms (O_t) associated with a single M atom.[231]

There are two kinds of protons in the HPA crystals. One is the dissociated, hydrated proton that is combined with the HPA anion; the other is the unhydrated proton that is located on the bridging oxygen in the HPA anion. Because the dissociated protons have good mobility, the HPA crystals have some characteristics of a 'pseudo liquid phase'. They are, in effect, superionic protonic conductors and are promising solid electrolytes.[232]

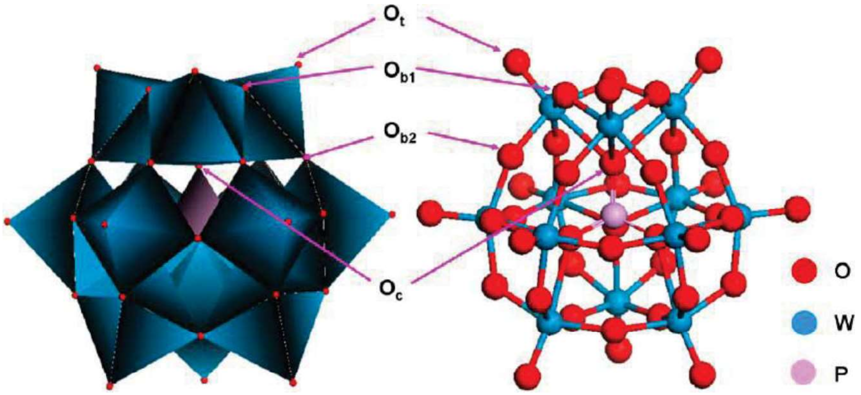

Figure 4.1: The Keggin structure of anion of PWA ($PW_{12}O_{40}^{3-}$): Ot, Ob1, Ob2, and Oc labeled the four types of oxygen in the structure. (Reprinted with permission from Zhou et. al, J. Am. Chem. Soc., 136 (2014) 4954-4964. Copyright 2014 American Chemical Society 224

4.3 Experimental

4.3.1 Materials

PEEK was purchased from Gharda chemicals (MW >200000 Da.), PEG of molecular weight of 600 Da (PEG-600) purchased from Fluka Biochemicals, sulfuric acid, Ethanol purchased from SD Fine chemicals (SDFCL) and are of analytical reagent (AR) grade. Tungustophosphoric acid purchased from SDFine Chemicals Limited. Ethanol was distilled before use.

4.3.2 Synthesis of cross-linked SPEEK-PEG and composite cross-linked SPEEK-PEG-PWA membranes

The membrane was prepared by solution casting method. SPEEK having ion exchange capacity of 2 meq g^{-1} was dissolved in ethanol:water mixture (50:50) to make 5% (W/V) solution. PEG (33.3 wt% of SPEEK) of molecular weight 600 Da (PEG-600) was weighted separately and

SPEEK solution was added to it. The required weight percentage of PWA (0, 5, 10, 20, 30, 40 and 50 %) was added to the SPEEK-PEG solution for preparation of desired composite membranes. The solution was stirred for 5 hrs at 50°C for homogeneous mixing and partial evaporation of the solvent. The mixed solution was cast in a petri dish and dried under infrared (IR) lamp for 6 hrs. The dried membranes were cured in an air draft oven at different temperature for definite time intervals, i.e., at 80°C for 2 hrs, 100°C for 2 hrs, and finally at 130°C for 16 hrs to cross-link SPEEK and PEG. The membranes were equilibrated in distilled water for 48 hrs at room temperature (27°C) before characterization. The thickness of the wet membranes was in the range of 200 to 250 microns.

4.4 Characterization of membranes

4.4.1 Structural characterizations by ATR-FTIR

The membranes, as well as SPEEK and PWA were characterized by ATR-FTIR. The details about the instrument is given in section 2.3.

4.4.2 Leaching study of PWA by Energy Dispersive X-ray (EDX) spectroscopy

The leaching study of PWA from the membrane at 60°C in water was characterized by measuring the weight percentage of tungsten retained in the samples using EDX method. Dry membrane samples were fractured in liquid nitrogen and mounted vertically on a stub, these samples were then vacuum sputtered with a thin layer of Au:Pd prior to SEM examination. The cross-section morphologies of the membranes were examined with a Camscan CS3200 scanning electron microscope (SEM) equipped with energy-dispersive X-ray (EDX) spectrometer (ENCA 250).

4.4.3 Topographical characterization of SPEEK-PEG and SPEEK-PEG-PWA membranes

The surface topography of the membrane was studied using NT-MDT atomic force microscope with Solver NEXT SPM controller and Nova Px software and operated at semi contact mode. A NSG10 series cantilever, made up of N-type single crystal silicon of 95 ± 5 □m length and 30 ± 5 □m width, a resonant frequency of 220-250 kHz, and a spring constant of 12 N m^{-1} was used for probing. Topographic and phase images were acquired with resolution of 256 points per line. The freshly prepared membranes were kept at room temperature and 50% relative humidity for two days before the measurements.

4.4.4 Water Uptake memsurment of SPEEK-PEG and SPEEK-PEG-PWA membranes

Water uptake by membranes were measured in two different conditions, after equilibrating in water at room temperature (27°C) for 48 hrs and at 60°C for different time intervals. Membrane pieces (2 cm^2) were cut from all the samples and kept at 60°C in distilled water for different time intervals (1h, 4hrs, 8hrs and 12hrs). Membrane weight was measured in wet condition by wiping out excess water over the samples, and in dry condition after drying the sample in an air draft oven at 110°C till constant weight. The water uptake was calculated using Eq. 1.27

4.4.5 Conductivity measurement of SPEEK-PEG and SPEEK-PEG-PWA membranes

The membrane conductivity was measured using Novo control Alpha-ATB impedance analyzer having 4 wire impedance test interface that is connected to two Pt wire electrodes (diameter 900 microns each) 15 mm apart. The instrument was checked using standard load (100E) as well as Nafion-117 sample that was pre-treated in 1:1 HNO_3 and boiled in DM water for 1 hr, this sample gave a conductivity of 0.1 Scm^{-1}. The conductivity measurements were carried out at 27°C with relative humidity of 50%. The conductivity of the sample measured in the longitudinal direction. The conductivity was calculated using the relation $\sigma = d/RA$, where d and A are the distance between the electrodes and the cross-sectional area of the membrane respectively, and R is the measured resistance, from the frequency-interval (10E6 to 10E4 Hz) of Bode plot.

4.4.6 Mechanical Properties Characterization of SPEEK-PEG and SPEEK-PEG-PWA membranes

Universal testing machine (make HEMETEK LRX Plus) was used for the measurement of the mechanical strength of the membranes. Each sample was treated in water at room temperature (27°C) and cut into 3 strips of width about 6 mm. Each strip was clamped in the machine where the distance between the clamps was kept 50 mm and tensile strength and % elongation at break were measured. Similarly, another set samples were treated in water at 60°C and after cooling the measurement was repeated at room temperature. All the measurements were carried out at 27°C with 50% relative humidity. Care was taken to ensure that the samples were in wet condition. A load cell of 1 KN and extension rate of 100 mm min^{-1} were used for these measurements.

4.4.7 Oxidative stability study of SPEEK-PEG and SPEEK-PEG-PWA membranes

The oxidative stability of membranes under PEMFC operating conditions is essential due to the formation of hydroxyl ($HO^{\cdot}$) and hydroperoxy ($HOO^{\cdot}$) radicals. These radicals have a strong oxidizing power and may attack and destroy the molecular structure of PEMs. The oxidative stability of the membranes was investigated by measuring the weight loss by the membranes after immersion in Fenton's reagent (3% H_2O_2 containing 2 ppm $FeSO_4$) at 27°C for 48 hrs and at 60°C for 6 hrs. The Membrane pieces (2 cm^2) were dried and weighed before and after the Fenton test to evaluate % weight loss.

4.4.8 Thermal stability characterization of SPEEK-PEG and SPEEK-PEG-PWA membranes

The thermal stability of the membranes was evaluated by thermo-gravimetric (TG) analysis in a nitrogen atmosphere using METTLER TOLEADO TGA analyzer. The heating rate of 10°C min^{-1} was maintained and the thermogram was recorded in the temperature range from 50°C to

600°C. Samples were weighed accurately in the range of 8 to 10 mg and used for recording TG traces.

4.4.9 Membrane performance study in PEMFC

The membranes performance in the fuel cell was carried out in a single cell having active electrode area of 25 cm^2. The membrane electrode assemblies (MEA) were prepared using a commercially available electrode having 20% Pt on Vulcan CR72 (Pt loading :0.5 mg cm^{-2}). The MEA was prepared along with membrane preparation unlike the commonly used hot press method.[210,211] The hot press method uses Nafion solution that helps in increasing three phase contact as well as binding of the electrode with the membrane. However, in the present case, the membrane is cross-linked and thereafter bonding with the electrode having dissimilar material like Nafion would require additional parametric studies which are out of scope of the present studies. Therefore, the electrodes were coated with the same polymer solution that was used for respective membrane synthesis (SPEEK-PEG or SPEEK-PEG-10%PWA). The membranes were assembled with electrode before curing process, at this stage the electrodes and the membranes were bonded. The whole MEA assembly was then cured in line with the procedure described in the synthesis of SPEEK-PEG-PWA membranes.

The cured MEA was sandwiched between two graphite plates with serpentine flow field and two gold-coated copper plates as a current collector in a single fuel cell setup. Plate-type heaters were inserted in between the current collectors and end plates to control the cell temperature. The cell temperature was measured at the graphite plate using a digital thermometer. During the cell test, H_2 (50 ml min^{-1}) and O_2 (100 ml min^{-1}) was passed through a heated bubble type gas humidifier. The humidifier temperature was kept 5°C above the cell operating temperature. The MEA was first operated at 25°C and the polarization curve was recorded after performing 10 on-off cycles of 30 min each with MEA operated at maximum power density. In the next step, the temperature was increased to 40°C and polarization curve was recorded after 10 cycles. The MEA was finally pre-conditioned by operating the cell at 60°C. The cell was operated under the condition of open circuit voltage (OCV) for 10 min followed by operating at 300 mA cm^{-2} for 30 min, and at the end of it polarization curve was recorded. The activation was carried out for 16 h till a constant polarization curve that did not change during the next cycles was obtained. The fuel cell measurements then were carried at 60°C.

4.5 Results & discussion

SPEEK having IEC of 2 meq g^{-1} was used for membrane synthesis. The degree of sulfonation calculated[206] from IEC is about 72% and the polymer exhibits high swelling characteristics and forms brittle membranes that are prone to cracking in dry condition. Cross-linking with PEG results in flexible membranes with increased mechanical strength and reduced swelling in water. This membrane had good dimensional stability up to 60°C in water. The cross-linking decreases the number of sulfonic acid groups (from 2 meq g^{-1} to 1.8 meq g^{-1}) available for proton transfer in the membrane, however, the SPEEK-PEG membrane displays conductivity of 0.06 Scm^{-1} at room temperature and 0.09 Scm^{-1} after treating the membrane at 60°C in water which is comparable with commercial perfluorosulfonic acid membranes. The conductivity was further enhanced by the addition of PWA (that has free H^+) in the composite cross-linked membranes (SPEEK-PEG-PWA) that were synthesized by addition of varying weight percentage of PWA. PWA distribution in membrane samples was estimated from tungsten distribution profile across the membrane cross-section using Energy Dispersive X-ray technique. The distribution of PWA was found to be uniform across the membrane. The PWA interaction with the polymer matrix was studied using Attenuated Total Reflectance Fourier Transform Infrared Spectroscopy (ATR-FTIR).

4.5.1 Structural properties analysis of SPEEK, PWA and membranes

The ATR-FTIR spectra of sulfonated polyether ether ketone (SPEEK), cross-linked SPEEK-PEG, composite cross-linked SPEEK-PEG-PWA (10% and 50%) membranes and pure PWA, are shown in Figure 4.2. The spectral band between 850 -1100 cm^{-1} gives an idea of the interaction between sulfonic group, PEG, and PWA. The sulfonation of PEEK was confirmed by the two characteristic peaks of -SO_3H groups at 1020 and 1079 cm^{-1}, which are assigned to the symmetric and asymmetric stretching vibration modes of O=S=O, respectively[127]. The cross-linking of SPEEK with PEG was confirmed by the shifting of symmetric stretching peak of the -SO_3H group from 1020 cm^{-1} to 1024 cm^{-1}.

To understand the infrared spectra of the PWA incorporated membranes, requires the understanding of the pure PWA vibrational modes. It is reported that the PWA bands are generally localized according to their structures.[233] In the primary structure (Keggin structure, $H_3PW_{12}O_{40}$), protons interact exclusively with the bridging oxygen because of the greater basicity of the bridging oxygen (O_b), W–O_b–W, and not with the terminal oxygen (O_t) (W=O_t) as shown by quantum chemical calculations[233] and NMR analysis.[234] In the hydrated form of the heteropolyacids, the terminal oxygen atoms of the anions associates with the $H_5O_2^+$ bridges to generate a secondary structure ($H_3PW_{12}O_{40}\cdot 6H_2O$), the evidence of this is established from the X-ray and neutron diffraction studies. As per the data reported for the characteristics peaks of different vibrational modes of $H_3PW_{12}O_{40}$ and $H_3PW_{12}O_{40}.6H_2O$ are at 1088 or 1065, 1007, 899, 814 or 744 and 1080, 980, 887, 795[235] and these were assigned to the stretching vibration of P–O, W=O_t, W–O_c–W and W–O_e–W respectively. The interaction of the terminal oxygen with the protonated water dimer in the secondary structure leads to shifting of the vibrational band of the terminal oxygen in the primary structure from 1007 to 980 cm^{-1}. Contrary to this, the bridging oxygen in the secondary structure forms a hydrogen bond leading to red shift for the symmetric stretching band of corner-shared octahedra, W–O_c–W (from 887 to 899 cm^{-1})

and for symmetric stretching band of edge-shared octahedra, W–O_e–W (from 895 to 914 cm^{-1}). The shift of central tetrahedron P–O band, due to the broad characteristics of the band corresponding to the primary structure cannot be clearly defined.

There was a negligible effect on the band shift with increase in concentration of PWA in the composite membranes. It is interesting to note that the terminal oxygen band for the composite membranes shift towards the higher wavenumber compared to the secondary structure of the PWA, whereas the wavenumber of the bridging oxygen bands in the composite membranes are same as the pure PWA, i.e., the terminal oxygen band at 973 cm^{-1} in pure PWA is shifted to 979cm^{-1} in the composite membranes and the bridging oxygen bands are at 899 and 814 cm^{-1}. The P–O stretching band at 1074 cm^{-1} and asymmetric vibrational mode of O=S=O of the sulfonic group in SPEEK shows a single peak in the composite membrane with a shoulder. These results clearly demonstrate that only the terminal oxygen of the PWAs interact within the composite, the sulfonic group's bands are not affected by introducing PWA in the composite membrane so the interaction of the terminal oxygen atom of PWA is probably with the –OH group of PEG in connection with protonated water molecules.

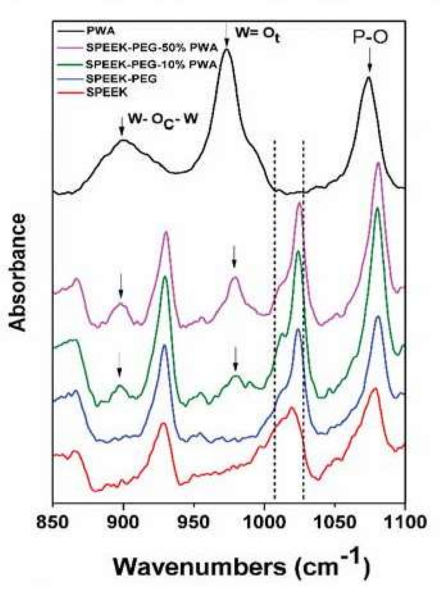

Figure 4.2: FTIR spectra of SPEEK, SPEEK-PEG cross-linked membrane, pure PWA and SPEEK-PEG-PWA composite membranes.

4.5.2 PWA retention analysis within the membrane

The leaching of PWA from the membrane samples were studied by determination of the weight percentage of tungsten in the membrane samples equilibrated in water at 27°C for 48 hrs and at 60°C for 8 hrs using EDX method. Line profile of the weight percentage of tungsten was plotted against the membrane thickness in Figure 4.3. It is clearly seen from Figure 4.3 that the tungsten is distributed uniformly throughout the thickness of the membrane, there is no precipitation of tungsten/PWA to the bottom of the membrane during the solution casting of the membrane. The results showed that the extent of leaching of PWA through the membrane when treated at 60°C for 8 hrs increased in a non-linear fashion with increasing %PWA. With 5% PWA blended membrane sample, the tungsten percentage decreased from 4.5% to 2.2%. Similarly, for 10%, 20%, 30%, 40% and 50% PWA, it decreased from 8% to 6%, 14% to 11%, 17.5% to 13%, 21% to 5% and 27.5% to 3% respectively.

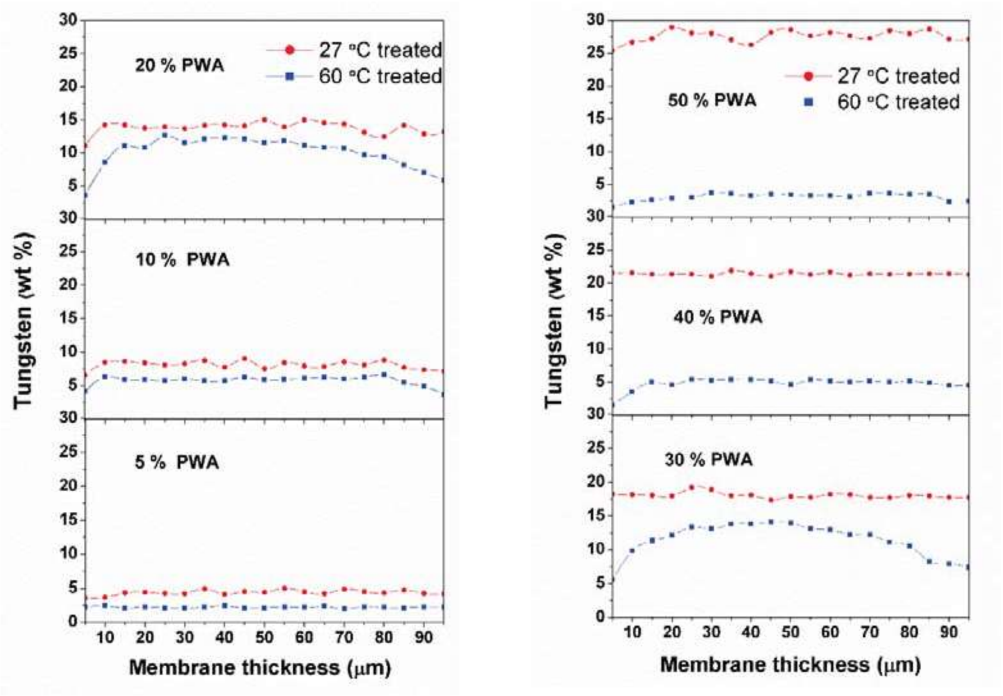

Figure 4.3: EDX line profile of tungsten weight percentage across the membrane thickness for membranes treated at 60°C for 8 hrs.

At lower concentrations, the leaching of PWA was found to be lower as compared to the high concentration of PWA (40-50%) where the final amount retained in the membrane was lower than that for the membrane with 10% PWA. This indicates that not only the concentration factor affect the leaching kinetics but also there must be a contribution from the structural factor. At higher concentration of PWA, water ingression in the polymer network increases. This, in turn, increases the free volume in the polymer network leading to an increase in polymer chain mobility that results in the more open microstructure. The open microstructure further facilitates higher rate of diffusion resulting in very low PWA retention in the membrane. Careful analysis of leaching profile has led to insight of diffusion of the PWA out of the membrane. PWA leaching was greatly dependent on the structure of the membrane. As seen in the Figure 4.3, change in the curvature of weight percentage profile of tungsten after treatment at 60°C for all the samples was evident. In 5% and 10% PWA blended samples, the tungsten profile was almost flat except at the edges as the concentration of tungsten near the membrane surface falls as expected. The amount of water was 133%, at this level the membrane structure was more compact and there was a high resistance for the tungsten diffusion. The water uptake for 20% and 30% PWA blended samples was about 170 and 221% respectively, indicating slightly more open structure, which was corroborated by the curvature of the leaching profile of the tungsten for these concentrations. The leaching of tungsten from the surface was more pronounced indicating decreased resistance for it's diffusion. At still higher concentrations (40 and 50% of PWA) the final tungsten concentration was very low indicating that the rate of diffusion was very fast. In addition, the tungsten concentration at the membrane edge and in the bulk were the same, that indicating very less resistance for its diffusion, this proves that there is absolute open microstructure. It is also important to note that whenever such a highly open microstructure exists it is possible that the onset of leaching of tungsten (PWA) may start much before the membrane swells completely. The first layer of PWA leached out leaves an open water filled channel through which the next PWA molecule diffuses out.

These membranes were further treated at 60°C in water up to 50 hrs and it was observed that the amount of tungsten was same in 5 and 10% PWA blended membranes and no further leaching occurred, however, membranes with higher PWA blended undergoes further leaching and the membrane blended with 50% PWA got converted in to a gel form leading to difficulty in handling/characterization of the membrane. This microstructural change alters the membrane properties like conductivity, mechanical properties etc.

4.5.3 Topographical study of SPEEK-PEG and SPEEK-PEG-10%PWA membranes

The AFM phase images (2D and 3D) of SPEEK-PEG and SPEEK-PEG-10%PWA are given in Figure 4.4 (A) and Figure 4.4 (B) respectively. The light regions are generally due to the softer domains, which represent the hydrophilic regions, whereas the dark regions are due to the hydrophobic regions[236]. In both the images, the hydrophilic and hydrophobic regions are well connected. The connectivity and size of the hydrophilic region control the conductivity of the membrane. As seen in Figure 4.4 (A) and (B), the hydrophilic and hydrophobic regions are slightly broader in SPEEK-PEG-10%PWA (Figure 4.4 (B)) compare to the SPEEK-PEG membrane (Figure 4.4 (A)), may be due to the addition of PWA which is a hydrophilic moiety and goes towards the hydrophilic region and make it broader. The 3D images showed that the surface roughness of the composite membrane is also slightly higher than the pristine SPEEK-PEG membrane. For better comparison of surface variation, the roughness parameters are given in Table 4.1. Where R_q, R_a, and R_{max} represent the root mean square roughness, average roughness and maximum roughness respectively.

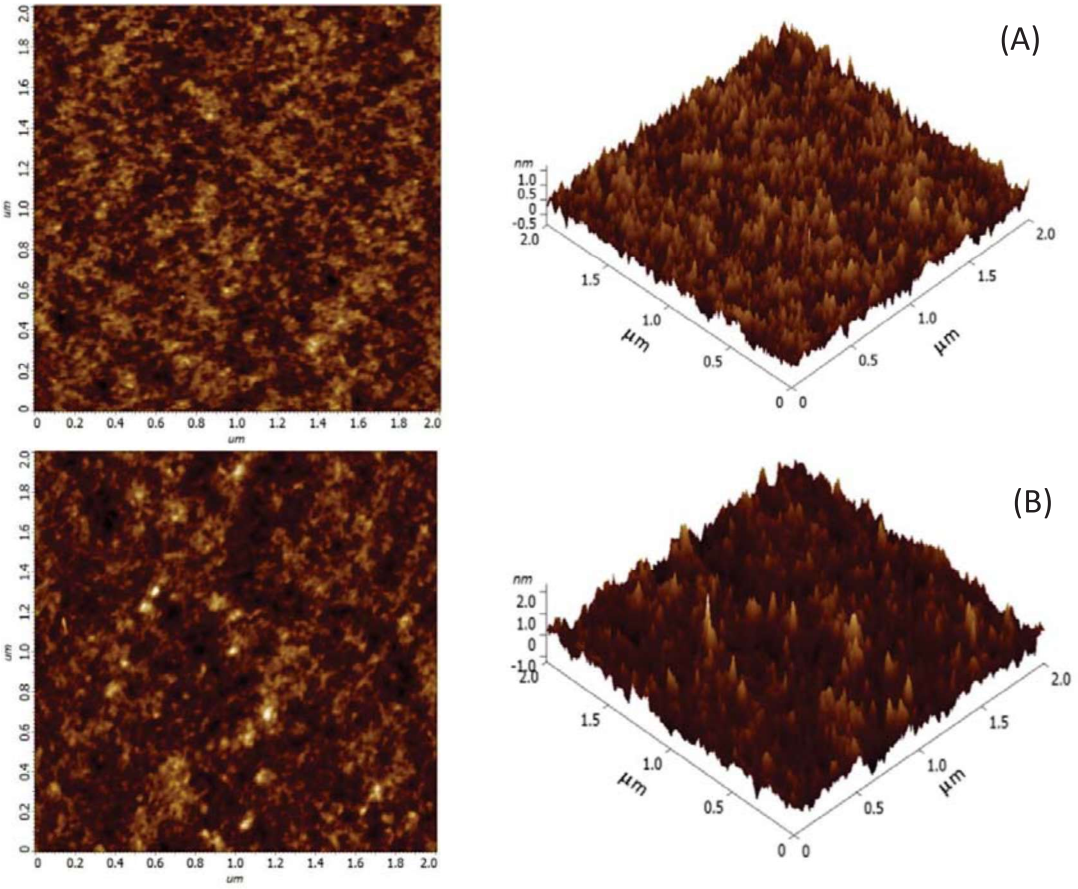

Figure 4.4: 2D and 3D AFM images of (A) SPEEK-PEG (B) SPEEK-PEG-10%PWA.

Table 4.1: Surface roughness parameters of SPEEK-PEG cross-linked and SPEEK-PEG-10%PWA composite membrane obtained from 2 µm × 2 µm AFM images.

Sample Name	R_q (nm)	R_a (nm)	R_{max} (nm)
SPEEK-PEG	0.204	0.163	1.184
SPEEK-PEG-10%PWA	0.335	0.261	2.413

4.5.4 Conductivity and Water Uptake analysis of SPEEK-PEG and SPEEK-PEG-PWA membranes

Proton Conductivity is an important property of ion exchange membrane to use in fuel cell. The proton conductivity is largely influenced by the water content vis-à-vis proton concentration. With higher proton concentration, water content increases due to the increased osmotic pressure, this in turn leads to a complete (higher degree of) dissociation of the acid groups, as well as the formation of hydrophilic well connected channels. This results in the increase in the effective proton mobility, in turn the proton conductivity thus increases[30].

The conductivity and water uptake with respect to weight percent of PWA (0 to 50%) blended in the samples are plotted in Figure 4.5. Proton conductivity and water uptake of the cross-linked SPEEK-PEG and composite cross-linked SPEEK-PEG-PWA membranes equilibrated in water at 27°C for 48 hrs and at 60°C for different time intervals (1, 4, 8 and 12 hrs) is plotted in Figure 4.5 (a) and (b). As seen in the Figure 4.5(a, b), at room temperature the conductivity and water uptake increased linearly with the increased amount of PWA from 0% to 50%. The conductivity increased from 0.062 to 0.119 Scm^{-1} whereas the water uptake increased from 46% to 59%.

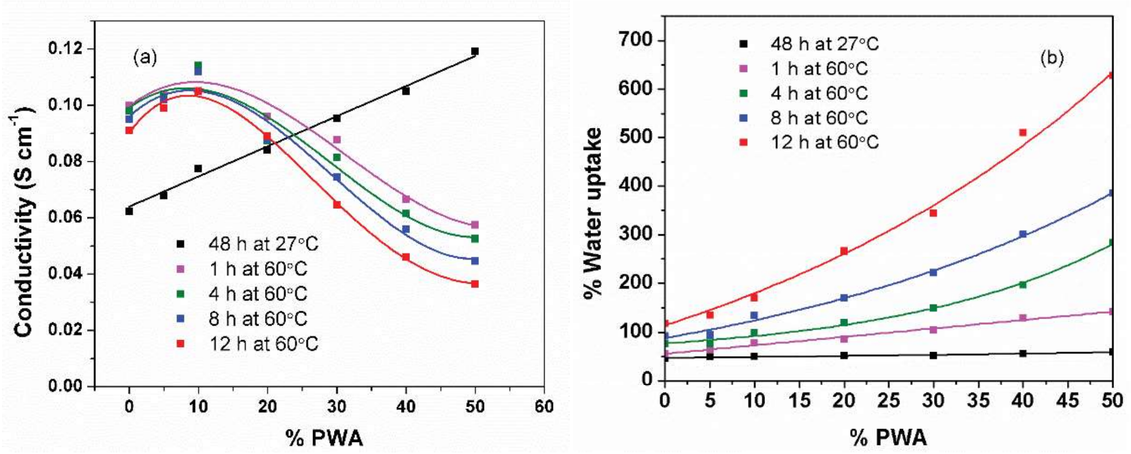

Figure 4.5: Variation of conductivity (a) and water uptake (b) as a function of blended weight % of PWA; the time in hrs indicates the membrane equilibration time in water at 27°C and 60°C.

The thermal treatment of samples at 60°C in water changed the conductivity pattern completely. The conductivity increased for membrane blended up to 10 weight % PWA, thereafter gradual decrease of conductivity was noted. The water uptake, on the other hand, increased exponentially. The two factors responsible for the decreased conductivity were, (i) increase in water uptake and (ii) leaching of PWA from the membrane sample; both these factors led to decrease in H^+ concentration.

The treatment of membranes at 60°C in water for 8 hrs, led to the increase in the conductivity of the membranes blended up to 10% PWA. At 0%, 5%, 10%, the respective increase in conductivity was from 0.062 to 0.095 S cm^{-1}, 0.065 to 0.102 S cm^{-1} and 0.077 to 0.112 S cm^{-1}, the corresponding increase in water uptake was from 46% to 91.7%, 49.2% to 93.8% and 51% to 133%. The increased conductivity with the water uptake indicates increased proton mobility through the membrane. This indicates the possible formation of the more connected hydrophilic channel even though some amount of PWA was leached out of the membrane.

A drastic increase in water uptake on thermal treatment in water was observed for samples that were initially blended with 20%, 30%, 40% and 50% PWA, resulting in decreased conductivity. This study shows that beyond 20% PWA, high amount of leaching along with large amount of water uptake results in a more open structure as inferred from SEM-EDX leaching profiles and swelling. A large amount of water uptake as well as leaching decrease the proton concentration in the membrane, both these factors negatively influence the conductivity of the membrane and thus conductivity sharply decreased beyond 20% PWA blended sample. The membrane with 10% PWA blending has optimum water uptake with low PWA leaching leading to highest conductivity even after treatment at a higher temperature (60°C) in water for the longer duration. A comparison of conductivity of HPA-based composite membrane (Nafion/HPA and SPEEK/HPA) reported in literature and the SPEEK-PEG-10%PWA is given in appendix.

4.5.5 Mechanical Properties of SPEEK-PEG and SPEEK-PEG-PWA membranes

Mechanical properties are greatly influenced by water uptake and membrane morphology. Figure 4.6 (a) and (b) shows the stress-strain curve of membranes treated at 27°C and 60°C in water respectively. Figure 4.6 (a), shows that on increasing the amount of PWA in the membrane samples the curve shifts monotonically downwards, corresponding to decreasing Young's modulus (Table 4.2), stiffness and strength, whereas the elongation at break increases. As PWA weight percentage increased from 0 to 50% in the membrane samples, the water uptake increased from 46 to 59% (Figure 4.6 (b)). The decrease in stiffness and strength is due to increase in water uptake, which acts as a plasticizer in the membrane.[237] The increase in ductility is due to the increase in the amount of inorganic additive.[238]

The tensile strength for the membranes decreased linearly with the weight percent of PWA. The membranes equilibrated in water at 27°C had higher strength than membranes treated at 60°C (Figure 4.6 (c)), which may be due to the lower water uptake at room temperature. The water uptake for samples treated at 60°C increased from 91% to 385% and tensile strength decreased from 19 MPa to 5 MPa compared to the samples treated at room temperatures (27°C) where the water uptake was 46 to 59% with decrease in tensile strength from 26 MPa to 14 MPa. With increased water uptake the intermolecular force between the polymer chains decreased leading to increased chain mobility and decreased tensile strength. The stress-strain curve for membrane samples treated at 60°C (Figure 4.6 (b)) is different to the samples treated at room temperature (27°C) i.e. the curves became smother, there is no necking at the yield point for the samples which were initially blended with more than 10% PWA etc., which indicated that the membrane has softened. The PWA leaching and water uptake increased with increasing the initial PWA blending percentage. Here, both of these effects were also seen in mechanical properties in Figure 4.6 (b).

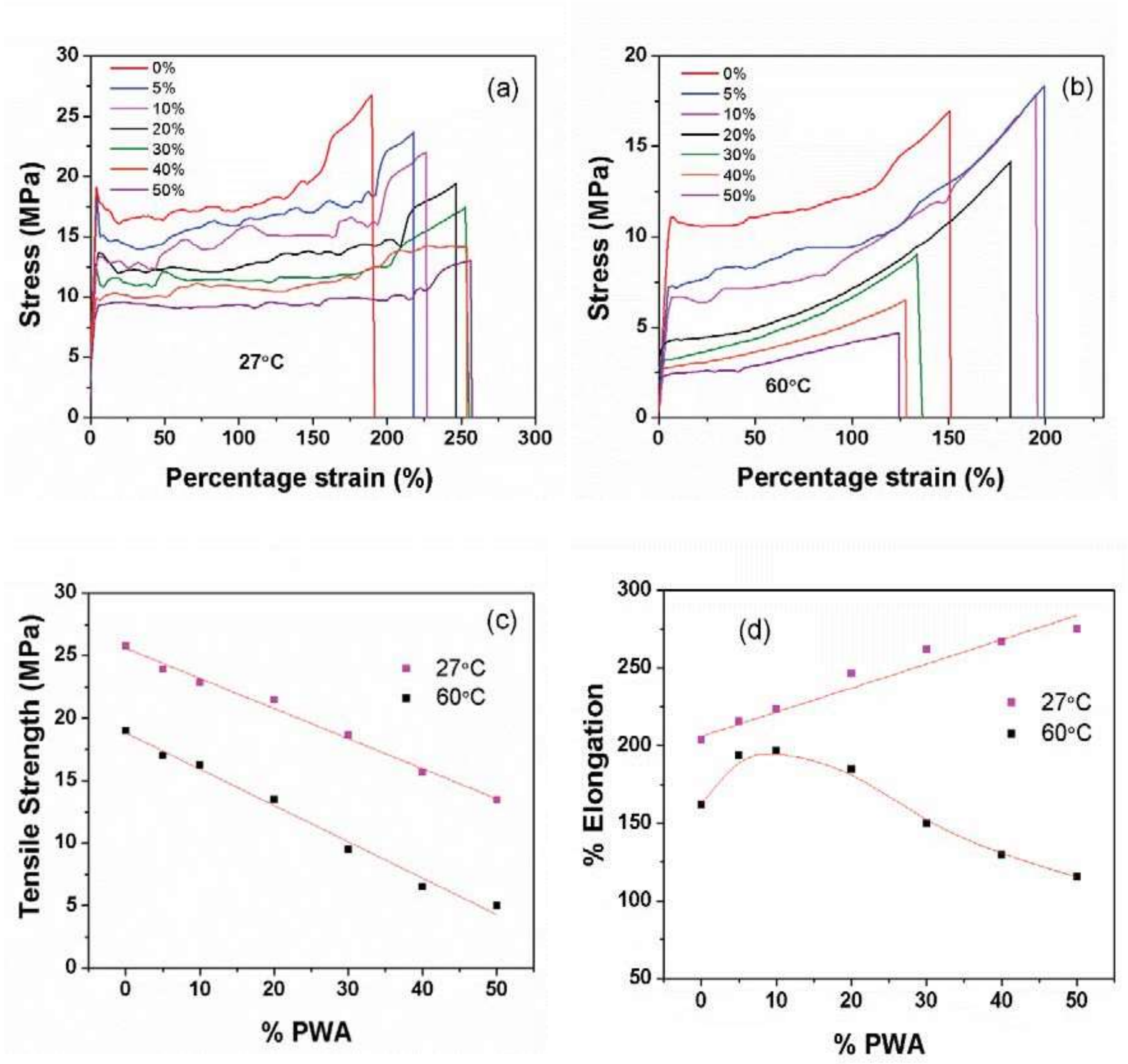

Figure 4.6: stress-strain curve of membrane (a) treated at 27°C, (b) at 60°C treated membrane (c) Tensile strength (d) percentage elongation.

The percentage elongation (Figure 4.6 (d)) showed a similar trend as that of the conductivity profile of the membranes (Figure 4.5(a)). For the room temperature treated membrane the % elongation increases linearly (from 203 to 275%) with increase in the weight % of PWA due to increase in the water uptake from 46% to 59%, where water acts as plasticizer; at the same time the increase in the mobility of the H^+ ion increased the conductivity of the membranes. For membranes treated at 60°C the % elongation increases upto 10%PWA and thereafter starts decreasing (similar to conductivity). This correlation is due to the following reason.

Table 4.2: Young's modulus of the room temperature (27°C) treated and 60°C treated membranes

Sample name	Young's modulus of the room temperature treated membrane (MPa)	Young's modulus of the membranes treated at 60°C (MPa)
SPEEK-PEG-0%PWA	604 ± 25	375 ± 12
SPEEK-PEG-5%PWA	528 ± 23	292 ± 11
SPEEK-PEG-10%PWA	400 ± 19	238 ± 8
SPEEK-PEG-20%PWA	338 ± 15	66 ± 4
SPEEK-PEG-30%PWA	300 ± 15	49 ± 4
SPEEK-PEG-40%PWA	280 ± 13	30 ± 3
SPEEK-PEG-50%PWA	252 ± 12	21 ± 2

The increase in the percentage elongation up to 10 weight % PWA blended sample is due to the increase in the water content in the membrane which act as plasticizer. However, beyond 10 weight % PWA blended membranes, the water content increases rapidly (accompanied with leaching of PWA) which increases the swelling of the membrane. In these membranes, the polymer chains are already far apart and are in a stretched form and on applying a lower stress the membranes break rather than expanding. Therefore, even though water acts as a plasticizer up to a certain extent, it does not help beyond 10% of PWA loading and thus the % elongation is decreased. Similarly the conductivity increases on increasing the water uptake by the membrane, up to 10%PWA due to the increase in H^+ mobility in the membrane and on further increasing the water uptake, it starts diluting the H^+ concentration and conductivity starts decreasing.

4.5.6 Oxidative Stability analysis of SPEEK-PEG and SPEEK-PEG-PWA membranes

Oxidative stability of the membranes was evaluated by Fenton test and the results are given in Table 4.3. The results showed marginal degradation at 27°C, however, the degradation increased after treatment at 60°C. This is due to the increased water uptake. The oxidative attack occurs mostly in or in the proximity of hydrophilic domains due to the penetration of short-lived ˙OH or ˙OOH radicals in these domains. It is noticeable that the addition of PWA (up to 10%) increased the oxidative stability of the membranes. Membrane blended with 10 weight % PWA showed higher oxidative stability compare to the more than 10 weight% PWA blended samples. This is possibly due to the lower water content of the 10 weight% PWA where the probability of ˙OH or ˙OOH radical attack is reduced. At higher weight% of PWA, the treatment at 60°C increases the water contented to a greater extent and renders the polymer more susceptive to the radical attack.[239] Therefore, degradation increased significantly beyond 10% of PWA blending.

Table 4.3: Membrane weight loss (%) after treatment in Fenton reagent at 27°C and 60°C for 6 hrs

Sample Name	**% weight loss at 27 °C**	**% weight loss at 60 °C**
SPEEK-PEG-0%PWA	0.99	25.8
SPEEK-PEG-5%PWA	0.68	19.9
SPEEK-PEG-10%PWA	0.91	20.5
SPEEK-PEG-20%PWA	0.82	40.9
SPEEK-PEG-30%PWA	0.38	42.7
SPEEK-PEG-40%PWA	0.59	46.5
SPEEK-PEG-50%PWA	0.53	52.6

4.5.7 Thermal stability of SPEEK-PEG and SPEEK-PEG-PWA membranes

Thermal stability of membranes was investigated by thermo gravimetric analysis. Figure 4.7 shows TGA traces of cross-linked SPEEK-PEG and composite cross-linked membranes SPEEK-PEG-10%PWA, SPEEK-PEG-20%PWA and SPEEK-PEG-40%PWA. All the samples showed three-step degradation. Three distinct degradation temperature steps observed were, (i) below 200°C, (ii) between 250°C and 400°C and (iii) beyond 450°C.

In the first step weight loss occurs below 200°C which was due to the loss of free and bound water. The second step, weight loss occurs between 250 to 400°C which was due to the degradation of sulfonic acid groups and in the third step, weight loss above 450°Cwasdueto the main polymer chain degradation[146]. It was observed that there was a proportional reduction in weight loss in the composite membrane on increasing the PWA weight percentage in the membrane samples, this was due to the decreasing wt% of the polymer in the composite. All the membranes are stable up to 250°C and can be used in the high-temperature fuel cells.

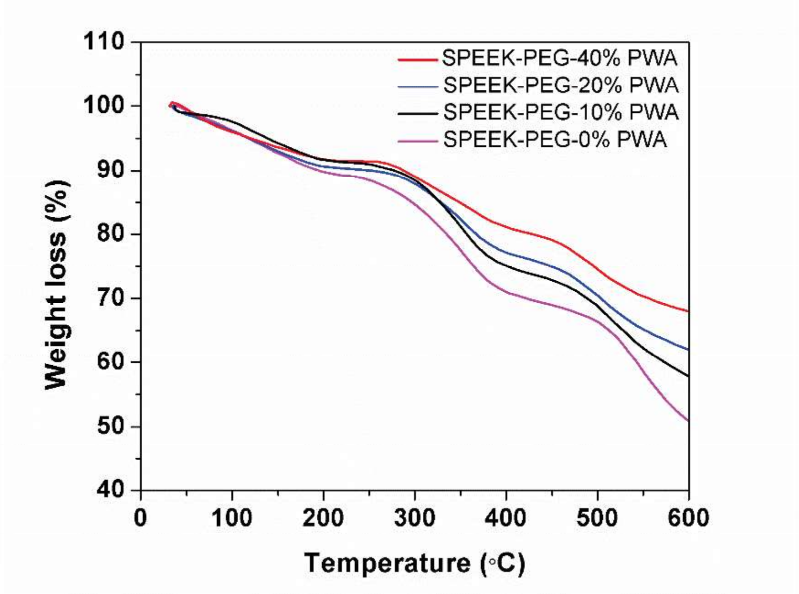

Figure 4.7: Thermo gravimetric traces for SPEEK-PEG and SPEEK-PEG-PWA membranes.

4.5.8 General discussion

Polyethylene glycol acts as cross-linker in SPEEK polymer-based membrane at appropriate thermal treatment. It forms alcohol-ether oligomers/polymers bonded to $–SO_3^-$ group generating an interpenetrating network. The PEG molecule attached to a sulfonic acid group will preferably react with another PEG molecule forming poly addition molecule having a possibility to form the free terminal –OH group. On addition of PWA which has terminal oxygen atom, interacts with the free –OH group of PEG and some amount of PWA remains within the membrane even after treatment of the membrane in water at higher temperature. The free PWA molecules which do not interact with PEG or SPEEK, leach out from the membrane after treatment in water at higher temperature and affect the membrane properties like conductivity, mechanical properties, chemical stability etc. In this work, 10 weight % PWA showed the optimum amount that interacted with the polymer molecules and enhanced the membrane properties to a significant extent. Amongst all the SPEEK-PEG-PWA composite membranes, the membrane with 10%PWA (equilibrated at 60°C) had the highest conductivity of 0.11 S cm^{-1}, high percentage elongation 190% and the tensile strength of 15 MPa. This membrane also displayed a good oxidative stability as well as PWA retention. On the other hand the samples without PWA, i.e., SPEEK-PEG had a conductivity of 0.09 S cm^{-1}, % elongation of 160% and tensile strength of 19 MPa.

4.5.9 Membranes performance analysis in PEMFC

As seen from the above discussions, the membrane properties are significantly affected by PWA blending and the membrane containing 10 weight % PWA showed the best electrochemical and mechanical properties among all composite membranes. In order to understand the effect of PWA blending on the membrane performance in fuel cell, MEAs were prepared by using two membranes SPEEK-PEG and SPEEK-PEG-10%PWA. The MEAs performance tests were carried out from 25°C to 60°C and the polarization and power density curves as a function of current density are plotted at three different temperatures; 25°C, 40°C and 60°C, given in Figure 4.8(a), (b) and (c) respectively.

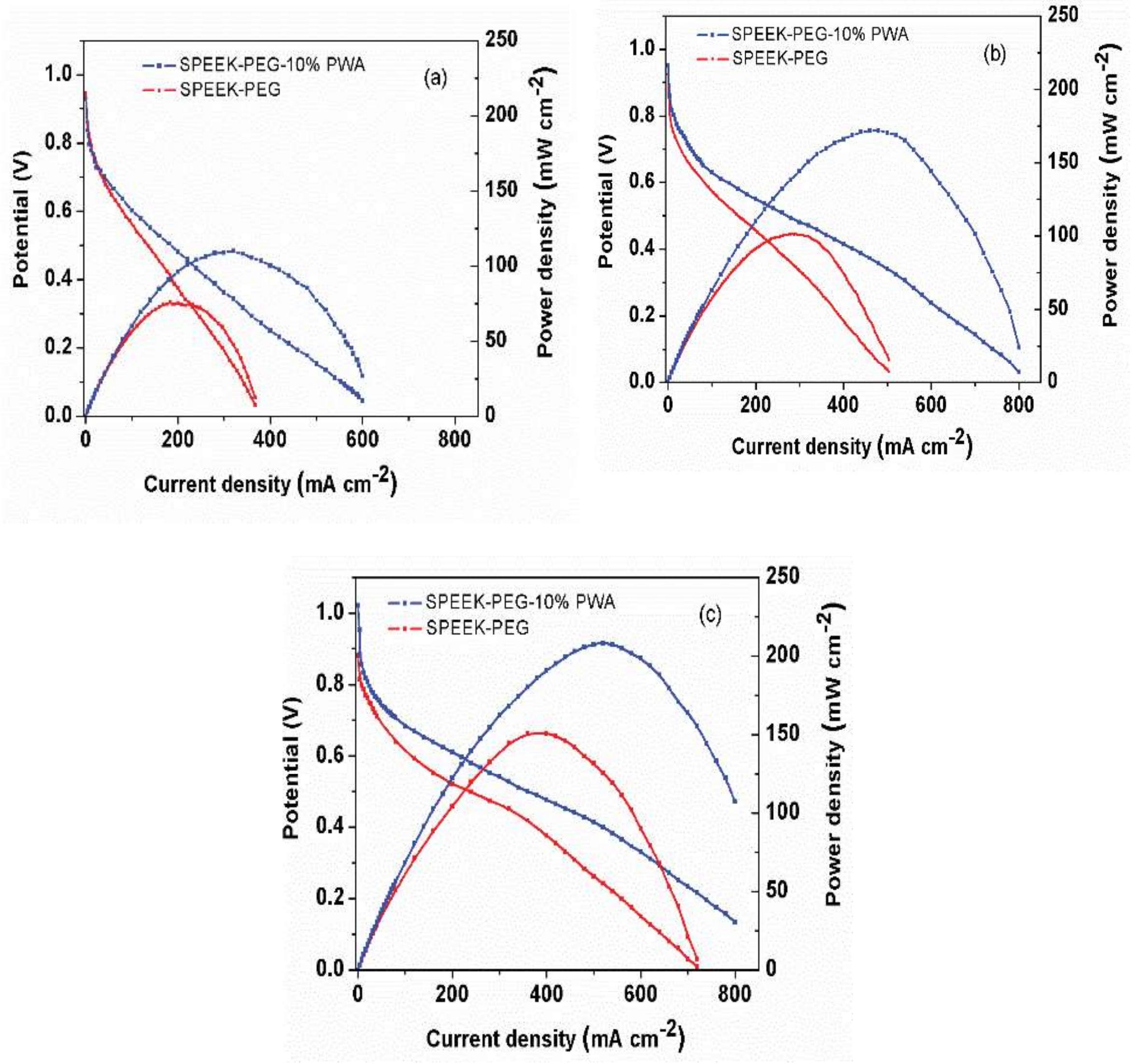

Figure 4.8 Comparison of the polarization and power density curves of SPEEK-PEG and SPEEK-PEG-10%PWA membranes at (a) 25°C (b) 40°C and (C) 60°C in H_2/O_2 fuel cell.

As seen in Figure 4.8(a), at 25°C the SPEEK-PEG membrane showed the maximum power density of 73.5 mW cm^{-2} at current density of 210 mA cm^{-2} and voltage 0.35 V which was enhanced to 112 mW cm^{-2} at 320 mA cm^{-2} and at 0.35 V for SPEEK-PEG-10%PWA membrane. Similarly in Figure 4.8 (b), at 40°C the SPEEK-PEG membrane showed the maximum power density of 106.56 mW cm^{-2} at 296 mA cm^{-2} and 0.36 V which was enhanced to 184 mW cm^{-2} at 460 mA cm^{-2} and 0.4 V for SPEEK-PEG-10%PWA membrane. Whereas in Figure 4.8 (c), at 60°C for SPEEK-PEG membrane, the maximum power density is 160 mW cm^{-2} at 400 mA cm^{-2} and at 0.4 V which was enhanced to 204 mW cm^{-2} at 520 mA cm^{-2} and at 0.42 V. These results clearly indicated that, on blending of PWA in the membrane enhanced the MEA performance in the fuel cell. At 60°C the maximum power density was increased by 33%.

MEA durability study

The durability studies of the membranes in the fuel cell were carried out by measurement of OCV during the 100 cycles for both the membranes (SPEEK-PEG and SPEEK-PEG-PWA) at 60 °C and each cycle was performed after half an hour interval. The OCV profile of both the membranes as a function of number of cycles is plotted in Figure 4.9.

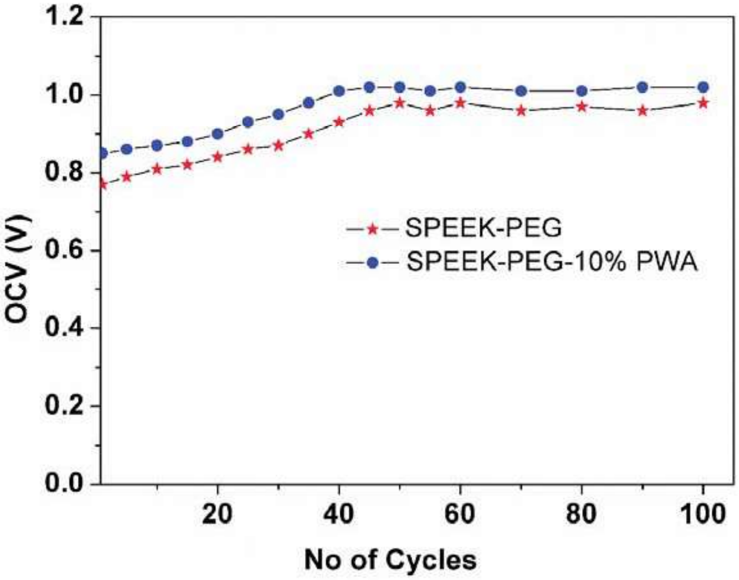

Figure 4.9: Change in OCV with number of cycles performed in H_2/O_2 fuel cell using SPEEK-PEG and SPEEK-PEG-10%PWA membranes

The OCV for both the membranes increased during the first 40 cycles attributed to the activation of the MEA assembly, thereafter the OCV remained constant and there was no significant decrease in OCV for 100 cycles. SPEEK-PEG membrane showed slightly lower values of OCV, i.e., 0.95 V (~0.07V less) than of SPEEK-PEG-10%PWA, which showed OCV of 1.02 V. The OCV for SPEEK-PEG-10%PWA increased from 0.85 V to 1.02 V at the end of 50 cycles and it remained constant till 100 cycles.

4.6 Conclusion

Cross-linked SPEEK-PEG and composite cross-linked SPEEK-PEG-PWA membranes with six different weight percentage of PWA (5, 10, 20, 30, 40 and 50%) were synthesized and characterized. The cross-linking with PEG and blending with PWA was verified by FTIR spectra. The electrochemical and mechanical properties of membranes were investigated after treatment in water at room temperature (27°C) and 60°C with regard to application in electro membrane processes/ fuel cell. The room temperature equilibrated membranes showed increased conductivity with increasing PWA percentage in the membrane samples from 0.06 to 0.12 S cm^{-1}. All the membranes had good mechanical properties, i.e., the tensile strength in the range of 15 to 25 MPa and the percentage elongation in the range of 200 to 270 %. All the membranes were thermally stable up to 250°C. Leaching of PWA from the membrane samples after treatment at 60°C was studied by estimation of tungsten distribution profile across the membrane cross-section using Energy Dispersive X-ray technique. Treatment of these membranes at 60°C in water for different lengths of time changed their electrochemical properties. This was attributed to the leaching of PWA and water uptake which changed the membrane morphology.

Following the treatment of membranes at 60°C, SPEEK-PEG-10%PWA showed the highest conductivity (0.11 S cm^{-1}), high tensile strength (16 MPa) and percentage elongation (190%) among the PWA composite membranes. This membrane also showed high oxidative stability and PWA retention. Whereas membranes without PWA (0%PWA), the conductivity was 0.09 Scm^{-1}, the tensile strength was 19 MPa and percentage elongation was about 160%. The enhanced membrane properties after addition of PWA also had a significant effect on the H_2/O_2 fuel cell performance. At 60°C the cross-linked SPEEK-PEG-0%PWA membrane gave maximum power density of 153 mW cm^{-2} at 400 mA cm^{-2} and 0.4 V which was enhanced to 204 mW cm^{-2} at 520 mA cm^{-2} and 0.42 V for SPEEK-PEG-10% PWA i.e. there was about 33% increase in the maximum power density by blending 10% PWA.

In summary, SPEEK-PEG-10%PWA membrane can be used as an alternative candidate for fuel cells/electro-membrane processes. The optimum amount of addition of heteropolyacid could enhance the membrane properties to a reasonable extent. This study also showed that excess amount of such hydrophilic additive would lead to leaching of the species and lower chemical stability that in turn would affect long-term stability in the electro-chemical environment.

Chapter-5

Synthesis and Characterization of Cross-linked Sulfonated poly(ether ether ketone)-poly(ethylene glycol) / MO_2 (M=Si, Ti and Zr) Organic-Inorganic Nanocomposite Membrane

5.1 Introduction

There are various methods have been used to achieve the desired properties in a PEM for fuel cell application, like cross-linking [127,240], blending with other polymers [136], semi-interpenetrating polymer networks [148], addition of inorganic fillers etc. [241]. Incorporation of inorganic fillers into the organic polymer membranes (organic-inorganic nanocomposite/composite membranes) is an effective approach to improve the membrane properties. This is because of the combined influence of the organic and inorganic phases towards the thermal, mechanical, and chemical stability, as well as the electrochemical characteristics, in addition to the improved water retention property. During the last few decades, a number of efforts have been attempted by using different inorganic additives e.g., TiO_2, SiO_2, ZrO_2, clay, heteropolyacids, zeolites etc.[158-160,164,177,224,242,243] to increase the performance of SPEEK based membranes. Among the numerous organic-inorganic composites, polymer/hydroscopic metal oxides (TiO_2, SiO_2, ZrO_2) composites were extensively studied because of their lower cost, inferior electrical conductivity and better water retention properties etc. The homogenous distribution and minimizing the self-aggregation of inorganic additives in the polymer-inorganic composite membranes is the most important parameter that boosts the membrane properties. Among different methods of organic-inorganic composite membrane synthesis, the in situ sol-gel method is the best approach to control the particle size and distribution of the inorganic phase into the polymer network. However, there is a compatibility issue between hydrocarbon polymer and metal oxides which restricts the uniform distribution of metal oxides into the polymer matrix and the composite membrane thus become opaque with the increase in inorganic content due to the rapid agglomeration of metal oxide particles. Some research groups used synthetic surfactant e.g. urethane acrylate non-ionomer (UAN) to improve the compatibility between silica and poly(imide) and poly(styrene) based composite membranes.[244,245]

The objective of this study was to prepare organic–inorganic nano-composites in a combination of IPN type cross-linked structure to improve the electrochemical and mechanical properties of highly sulfonated SPEEK polymer based membrane. In this context, SPEEK-PEG/MO_2 (M = Si, Ti, Zr) membranes were fabricated where, PEG-400 is used as an IPN-type cross-linker as well as dispersant to homogeneously distribute MO_2 nanoparticles which are synthesized by *in-situ* sol-gel method. Polyols (PEG) are highly beneficial for controlling inorganic particle nucleation, growth and agglomeration of nanoparticles as PEG adhere on the particle surface (especially on oxides) and serve as colloidal stabilizers.[246]

In this work we have systematically investigated the effect of varying weight percentage of MO_2 content in the SPEEK-PEG/MO_2 nanocomposite membranes on different electrochemical and mechanical properties. The intermolecular structure and morphology of the SPEEK-PEG/MO_2 nanocomposite membranes were characterized by FT-IR, FESEM, AFM and EDX methods. The influence of MO_2 addition has been discussed in terms of membranes conductivity, water uptake, chemical and mechanical stability and investigated the optimum concentration of MO_2. The membranes having optimum MO_2 weight percentage, is studied in H_2/O_2 fuel cell and compared with pristine SPEEK-PEG membrane.

5.2 Sol-gel method

Sol–gel method is one of the well-established synthetic approaches to prepare novel metal oxide nanoparticles as well as mixed oxide composites. This method has potential control over the textural and surface properties of the materials. Sol–gel reactions involve two consecutive steps; (i) hydrolysis of metal alkoxides to produce hydroxyl groups, (ii) polycondensation of the hydroxyl groups to form a three-dimensional network, shown in *Figure 5.1*. The metal alkoxide precursor M(OR)n, (M is a network-forming element: Si, Ti, Zr, Al, B, etc., and R is an alkyl group (C_xH_{2x+1})) undergoes rapid hydrolysis to produce the metal hydroxide solution, followed by immediate condensation which leads to the formation of three-dimensional gels.

The sol–gel process occurs at room temperature in low molecular weight solvents. A sol is a dispersion of colloidal particles (size 1–100 nm) in a liquid, and a gel is an interconnected, rigid network with pores of sub-micrometer dimensions and polymeric chains whose average length is greater than a micron. During hydrolysis and condensation reactions, low molecular weight byproducts (alcohol or water) are generated. In the sol-gel process, the reaction of metal alkoxides and water in the presence of acid or base forms a one phase solution that goes through a solution-to-gel transition to form a rigid, two-phase system comprised of solid metal oxides and solvent filled pores. Hydrolysis and condensation is a nucleophilic substitution involving three steps: nucleophilic addition, proton transfer within the transition states, and removal of the protonated species. Hydrolysis and condensation proceeds without catalyst for non-silicate metal alkoxides, whereas acid or base catalysis is required for silicon based metal alkoxides. The structure and morphology strongly depends on the nature of a catalyst if used (pH of the reaction). Many factors influence the kinetics of hydrolysis and condensation reactions, including the water/silane ratio, catalyst, temperature, and the solvent nature.

Condensation can proceed through either alcoxolation or through oxolation. In both processes, an oxo bridge is formed between the metals (M–O–M) but the leaving group differs. During alcoxolation, two partially hydrolysed metal alkoxide molecules combine and an oxo bridge is formed between the two metals with alcohol departing as the leaving group. In oxolation two partially hydrolysed metal alkides combine to form an oxo bridge between the metal centers but water is the leaving group.

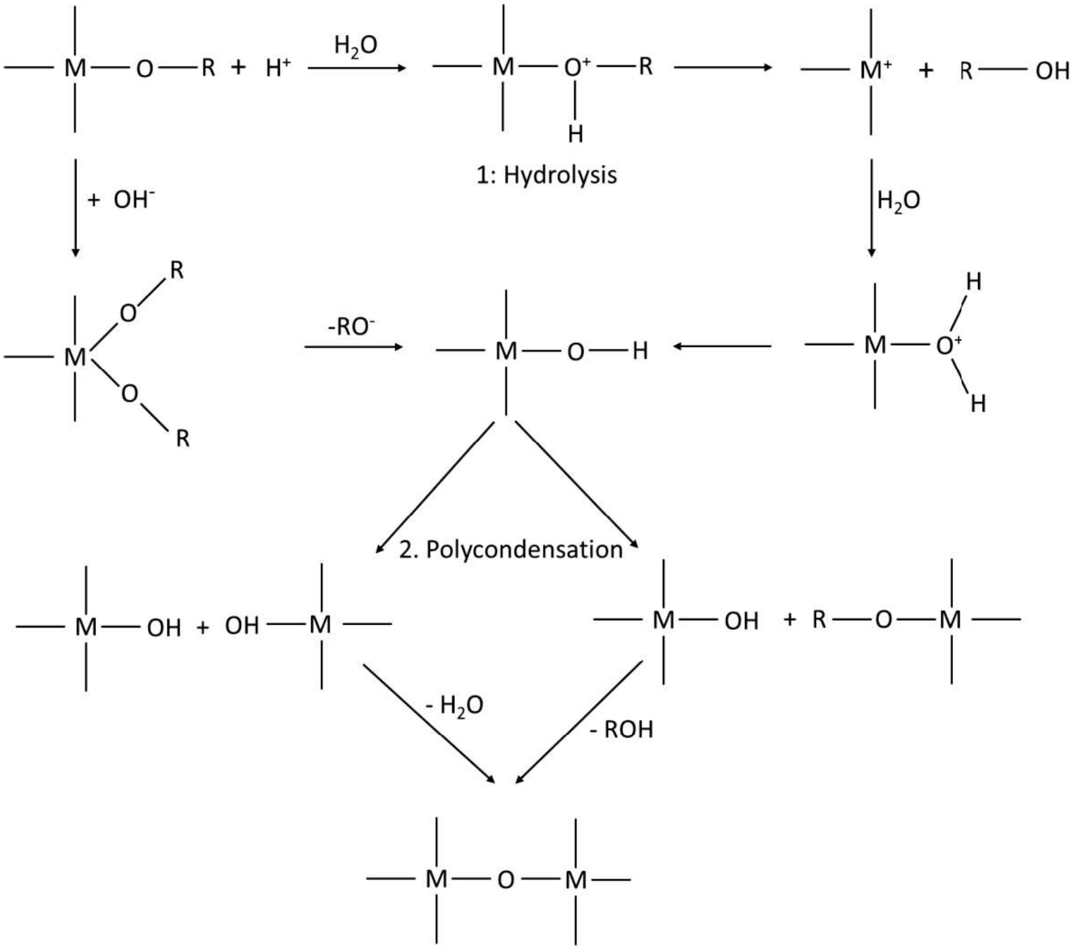

Figure 5.1: Schematic representation of the sol–gel mechanism for metal alkoxide

5.3 Experimental

5.3.1 Materials

Poly(ether ether ketone) (PEEK) purchased from Gharda chemicals (MW >200000 Da.), poly(ethylene glycol) (PEG) of molecular weight (400 Da) PEG-400 purchased from Fluka Biochemical, sulfuric acid, ethanol purchased from SD Fine chemicals (SDFCL) and are of analytical reagent (AR) grade. Tetraethyl orthosilicate (TEOS), Titanium (IV) butoxide and Zirconium (IV) butoxide purchased from sigma Aldrich. Acetyl acetone purchased from Chemical centre, Mumbai. Ethanol was distilled before use.

5.3.2 Synthesis of nanocomposite membranes

SPEEK having IEC of 2.12 meq g^{-1} was used for the synthesis of membranes. The sulfonation of PEEK was carried out as given in section 3.2.2.The membranes were prepared by solution casting method. SPEEK was dissolved in ethanol: water mixture (50:50) to make 5% (W/V) solution. PEG (33.3 wt% of SPEEK) of molecular weight 400 Da (PEG 400) was weighted separately and SPEEK solution was added to it. The mixture was stirred at room temperature for 6 hrs. Thereafter, the sol-gel method was adopted to prepare SPEEK-PEG/MO_2 composites through the hydrolysis of metal alkoxide, in this the sulfonic group of SPEEK acts as acid catalyst. The details of the all three different types (SiO_2, TiO_2 and ZrO_2) of composite membranes synthesis process are given bellow:

SPEEK-PEG/SiO_2 nanocomposite membranes synthesis:

Different amounts of TEOS (0.1 M solution in ethanol) were added (with SPEEK-PEG:SiO_2 mass ratios of 97.5:2.5, 95:5, 92.5:7.5, 90:10 and 87.5:12.5, respectively) into the polymer solution with vigorous stirring at room temperature. The resulting solution was stirred at room temperature for 10 hrs and at 60°C for 8 hrs. The mixed solutions were cast in a petri dish and dried under infrared (IR) lamp for 6 hrs. The dried membranes were cured in an air draft oven at different temperature for definite time intervals, i.e., at 80°C for 2 hrs, 100°C for 2 hrs, and finally at 140°C for 16 hrs. The content of SiO_2 in the resulting membrane was calculated assuming complete conversion of TEOS to SiO_2. The membranes are correspondingly denoted as SPP/SiO_2-2.5 (SPEEK-PEG/2.5% SiO_2), SPP/SiO_2-5 (SPEEK-PEG/5% SiO_2), SPP/SiO_2-7.5 (SPEEK-PEG/7.5% SiO_2), SPP/SiO_2-10 (SPEEK-PEG/10% SiO_2) and SPP/SiO_2-12.5 (SPEEK-PEG/12.5% SiO_2), respectively. Whereas without SiO_2 added membrane is denoted as SPP (SPEEK-PEG/0% SiO_2). All the membranes thickness were measured after equilibrating in water for 48 hrs at room temperature.

SPEEK-PEG/TiO_2 and SPEEK-PEG/ZrO_2 nanocomposite membranes synthesis:

TiO_2 and ZrO_2 networks were generated in the organic polymer solution by hydrolysis of Titanium (IV) butoxide $Ti(OBu)_4$ and Zirconium (IV) butoxide $Zr(OBu)_4$. Both alkoxides react very fast with water/moisture, therefore, Acetyl acetone (ACAC) was added as chelating agent to the solution to avoid the precipitation of the inorganic compound. The molar proportion ACAC/alkoxide, was kept 1:2, to inhibit precipitation. Different amounts of $Ti(OBu)_4$ and $Zr(OBu)_4$ (0.05 M solution in ethanol) were added (with SPEEK-PEG:TiO_2 and SPEEK-PEG:ZrO_2 mass ratios of 97.5:2.5, 95:5, 92.5:7.5 and 90:10 respectively) into the polymer solution with vigorous stirring at room temperature. The mixed solutions were cast in a petri dish and dried under infrared (IR) lamp for 6 hrs. The dried membranes were cured in an air draft oven at different temperature for definite time intervals, i.e., at 80°C for 2 hrs, 100°C for 2 hrs, and finally at 140°C for 16 hrs. The content of TiO_2 and ZrO_2 in the resulting membrane was calculated assuming complete conversion of $Ti(OBu)_4$ and $Zr(OBu)_4$ to TiO_2 and ZrO_2 . The nanocomposite membranes based on titania and zirconia are correspondingly denoted as SPP/TiO_2-2.5 (SPEEK-PEG/2.5% TiO_2), SPP/TiO_2-5 (SPEEK-PEG/5% TiO_2), SPP/TiO_2-7.5 (SPEEK-PEG/7.5% TiO_2), SPP/TiO_2-10 (SPEEK-PEG/10% TiO_2) and SPP/ZrO_2-2.5 (SPEEK-PEG/2.5% ZrO_2), SPP/ZrO_2-5 (SPEEK-PEG/5% ZrO_2), SPP/ZrO_2-7.5 (SPEEK-PEG/7.5% ZrO_2), SPP/ZrO_2-10 (SPEEK-PEG/10% ZrO_2), respectively. Whereas without TiO_2 and ZrO_2 added membrane is denoted as SPP.

5.4 Characterization of membranes

5.4.1 Morphological characterization

The morphology of the membranes has been extensively studied by two microscopic techniques: field emission scanning electron microscope (FESEM) and Atomic Force Microscope (AFM), in order to understand the correlation between microstructure and membrane properties. Whereas energy-dispersive X-ray spectroscopic (EDX) technique (attached to the FE-SEM) was used to analyze the elemental distribution of the MO_2 on the surface of the membranes. Dry membrane samples were mounted on a stub, these samples are then vacuum sputtered with a thin layer of Au:Pd prior to FE-SEM examination. The morphology of the membranes was examined with an Auriga6553 Field emission scanning electron microscope (FESEM) equipped with EDX spectrometer (Oxford-EDX). The spectrometer has X-Max Extreme Silicon Drift Detector (20 mm^2), having resolution of 150 eV at 20 keV.

The surface morphology of the membrane was studied using NT-MDT atomic force microscope with Solver NEXT SPM controller and Nova Px software and operated at semi contact mode. A NSG10 series cantilever, made up of N-type single crystal silicon of 95 ± 5 □m length and 30 ± 5 □m width, a resonant frequency of ~250 kHz, and a spring constant of 12 N/m was used for probing. The freshly prepared membranes were kept at room temperature at 50% relative humidity for two days before the measurements. Each sample was first imaged at 20 □m × 20 □m, and then three different parts were investigated in more detail at 5 □m × 5 □m and 2 □m × 2 □m; at the center, a few micrometers from the edge, and in between. A flattening correction was applied which fitted the points within each scan line with a polynomial.

5.4.2 Ion exchange capacity and degree of sulfonation

IEC is defined the content of sulfonic acid groups in 1 g of a dry polymer/membrane. It plays a crucial role in membrane properties, such as the water uptake, swelling ratio and proton conductivity. The IECs of the polymer (SPEEK), cross-linked membrane (SPP) and nanocomposite membranes (SPP/SiO_2, SPP/TiO_2 and SPP/ZrO_2) were determined by back titration method. The samples in -SO_3H form were immersed in 1M NaCl solution with constant stirring for 24 hrs in order to exchange the H^+ ions with Na^+. Then, the proton released from the membranes was titrated against 0.01 M NaOH solution. The IEC was calculated using Eq. 3.1.

5.4.3 Water Uptake measurement of nanocomposite membranes

Water uptake by the membranes was measured in the same condition in which the conductivity was measured. Five different membrane pieces (2 cm^2) were cut from each membrane sample and kept at various temperature (i.e. 30 °C, 40 °C, 50 °C, 60 °C and 80 °C) for one hour and after that membranes weight were measured by wiping out excess water over the samples. These are designated as the weight of wet membrane at each temperature. After that, all the samples were dried in an air draft oven at 110°C till there constant weight and their dry weights were measured. The water uptake was calculated using Eq. 1.27.

5.4.4 Conductivity measurement of nanocomposite membranes

The in-plane proton conductivity was measured at various temperatures (from 30 °C to 80 °C) and 100% relative humidity by using Novo control Alpha-ATB impedance analyzer having 4 wire impedance test interface that is connected to two Pt wire electrodes (diameter 900 microns each) 15 mm apart. The instrument was checked using standard load (100E) as well as Nafion-117 sample that was pre-treated in 1:1 HNO_3 and boiled in DM water for 1 hr, this sample gave a conductivity of 0.1 S cm^{-1}. Before the conductivity measurement the membrane samples were equilibrated in water for 1 hr at the temperature on which the conductivity was measured (e.g. the membranes were equilibrated at 30 °C in water for one hour and then the conductivity was measured at 30 °C, similar procedure was followed for the other temperatures). The conductivity of the samples was calculated using the relation $\sigma = d/RA$, where d and A are the distance between the electrodes and the cross-sectional area of the membrane respectively, and R is the resistance derived, from the frequency-interval (10^7 to 10^5 Hz) using Bode plot.

5.4.5 Structural characterizations of nanocomposite membranes

Owing to the high IR absorbance of these membranes, transmission studies are not possible, and FT-IR spectra were collected in attenuated total reflectance (ATR) mode. The membranes, as well as SPEEK were characterized by Attenuated Total Reflectance Fourier Transform Infrared Spectroscopy (ATR-FTIR). A Bruker, Vertex 70 spectrometer using software OPUS, VERSION 6 was used for the measurement. The spectra were recorded in the range of 400-4000 cm^{-1}. The membrane sample was pressed on a ZnSe crystal using a screw type device attached to the crystal mount. About 100 scan average was taken for each spectrum.

5.4.6 Mechanical Properties measurement of nanocomposite membranes

Uniaxial tensile testing of fully hydrated membranes was performed with a Universal testing machine (make HEMETEK LRX Plus) using a 1 kN load cell. Each sample was treated in water at room temperature (27°C) for 48 hrs before measurement. Rectangular pieces of dimension 100 mm × 6 mm were cut from all the samples and extended at a constant crosshead speed of 0.50 mm/s with a 50 mm gauge length (corresponding to a constant strain rate of 0.01 S^{-1}). The samples thickness was determined by averaging the three measurements taken at different places in the membrane pieces. All the measurements were carried out at 27 °C with 50% relative humidity. Care was taken to ensure that the samples were in wet condition. Each test was replicated at least 5 times. Three properties including Young’s modulus, tensile strength, and elongation at break were determined from strain–stress relationships.

5.4.7 Oxidative stability study of nanocomposite membranes

The oxidative stability is one of the important property evaluating the lifetime of PEMs under harsh fuel cell conditions. The oxidative stability of the membranes was investigated by measuring the weight loss by the membranes after immersion in Fenton’s reagent (3% H_2O_2

containing 2 ppm $FeSO_4$) at 27°C for 48 hrs and at 80°C for 1 hrs. The Membrane pieces (2 cm^2) were dried and weighed before and after the Fenton test to evaluate the percentage weight loss.

5.4.8 Thermal characterization of nanocomposite membranes

The thermal stability of the membranes was evaluated by thermo-gravimetric (TG) analysis in a nitrogen atmosphere using METTLER TOLEADO TGA analyzer. The heating rate of 10 °C min^{-1} was maintained and the thermogram was recorded in the temperature range from 50 °C to 700 °C. Samples were weighed accurately in the range of 8 to 10 mg and used for recording TG traces.

5.5 Nanocomposite Membranes performance study in PEMFC

The membranes performance in the fuel cell was evaluated in a single cell having active electrode area of 25 cm^2. The membrane electrode assemblies (MEA) were prepared using a commercially available electrode having 20% Pt on Vulcan CR72 (Pt loading is 0.5 mg cm^{-2}). The MEA was prepared along with membrane preparation unlike the commonly used hot press method. The electrodes were coated with the same polymer solution that was used for respective membrane synthesis. The membranes were assembled with electrode before curing process, at this stage the electrodes and the membranes were bonded. The whole MEA assembly was then cured in line with the procedure described in the synthesis of membranes.

The cured MEA was sandwiched between two graphite plates with serpentine flow field and two gold-coated copper plates as a current collector in a single fuel cell setup. Plate-type heaters were inserted in between the current collectors and end plates to control the cell temperature. The cell temperature was measured at the graphite plate using a digital thermometer. During the cell test, H_2 (50 ml min^{-1}) and O_2 (100 ml min^{-1})

was passed through a heated bubble type gas humidifier. The humidifier temperature was kept 5 °C above the cell operating temperature. The membrane performance in fuel cell was carried out from 30 °C to 60 °C. The MEA was first operated at 30 °C and the polarization curve was recorded after performing 10 on-off cycles of 30 min each with MEA operated at maximum power density. In the next step, the temperature was increased to 40 °C and 50 °C and polarization curve was recorded after 10 cycles at each temperature. The MEA was finally pre-conditioned by operating the cell at 60 °C and then measurements were carried at 60 °C.

5.6 Results & Discussion

5.6.1 PEG as IPN-type cross-linker and dispersant

Poly(ethylene glycol) act as cross-linker in SPEEK polymer-based membrane at appropriate thermal treatment. It forms alcohol-ether oligomers which bonded to $-SO_3$ group and generating an interpenetrating network.[127] It was observed that highly sulfonated SPEEK polymers (DS □ 75%) have good solubility in ethanol-water mixture and it forms a very brittle membrane after drying including a large number of cracks. As discussed in chapter 3, on addition of PEG and appropriate thermal treatment, the membrane properties are enhanced to a great extent and the resulting membranes are flexible with good mechanical strength. PEG of molecular weight 400 Da showed the appropriate chain length for better hydrophilic/hydrophobic phase separation and best electrochemical properties. Although the SPEEK-PEG cross-linked membranes showed good electrochemical and mechanical properties, their application in the fuel cell with respect to their long-term performance is limited because of excessive swelling in water at a higher temperature (□ 60 °C).

In the present work, we have used a hybrid approach (cross-linking as well as the addition of inorganic moieties) to improve the SPP cross-linked membrane properties by incorporating SiO_2, TiO_2 and ZrO_2 moieties which is synthesized in situ by sol-gel method. A series of SPP/MO_2 organic-inorganic composite membranes have been synthesized to investigate the optimum MO_2 percentage and a SPP membrane (without MO_2) has been synthesized for comparison. The nanoparticles have a strong tendency to agglomerate, due to the van der Waals interactions, electrostatic or steric stabilization is usually used to stabilize colloids by creating repulsions between the particles.[247] Electrostatic stabilization consists of the adsorption of ions on the surface of the particles with creation of the electric double layer, whereas steric stabilization can be achieved by the adsorption of large molecules such as polymers forming a dense layer around the particles. PEG acts as a surface modifier of inorganic sols and sterically stabilizes the dispersion. The chelating effect of PEG moreover, is highly beneficial for controlling particle nucleation, particle growth and agglomeration of nanoparticles as it adheres on the particle surface (especially on oxides) and serves as colloidal stabilizers.[246] PEG facilitate to form micro-micelles under aqueous conditions and the inorganic particles nucleate and grow within the micelles and form a homocentric bundle structure. It also allows MO_2 to migrate into the organic chain via hydrogen bonds and homogeneously distribute within the membrane.[248]

Due to controlled reaction conditions and appropriate heat treatment, various interactions among SPEEK, PEG and MO_2 are possible e.g. (i) condensation of -OH of PEG/MO_2 and -SO_3H of SPEEK to give sulfonic ester group (ii) self-condensation of PEG which may result in retaining free -OH groups imparting hydrophilicity to the membrane (iii) Condensation of –OH group of PEG and MO_2 (iv) IPN network formation between SPEEK, PEG and SiO_2, shown in Figure 5.2.

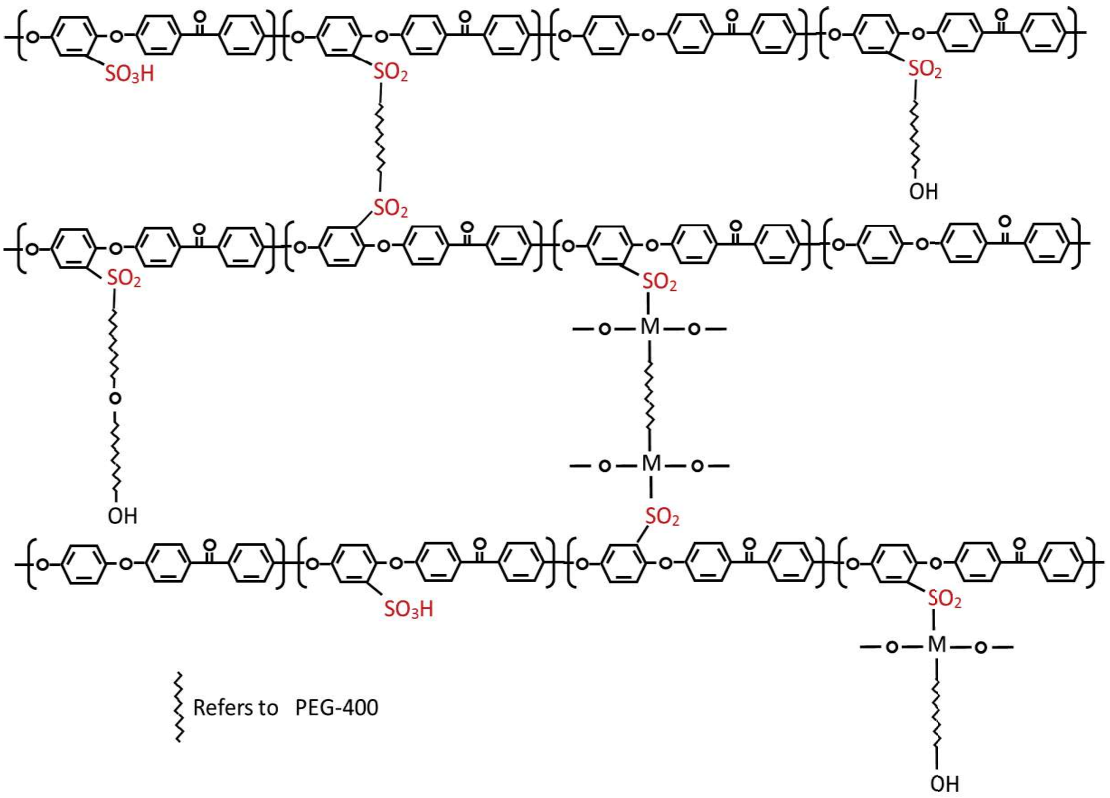

Figure 5.2: Proposed structure of nanocomposite membrane.

This section is now divided into three parts to discuss the results/outcomes of all the three different types of nanocomposite membranes separately.

5.6.2 Results and discussion of SPEEK-PEG/SiO_2 (SPP/SiO_2) nanocomposite membranes:

The details of SPP/SiO_2 nanocomposite membranes are given in Table 5.1. All the membranes thickness were measured after equilibrating in water for 48 hrs at room temperature.

5.6.2.1 Ion exchange capacity of SPP/SiO_2 membranes

IEC of the polymer/membrane represents the amount of exchangeable protons and plays an important role for water uptake and proton conductivity. The IEC and DS of SPEEK polymer that is used for membrane synthesis are 2.12 meq g^{-1} and 78% respectively. The IEC value of SPP and SPP/SiO_2 nanocomposite membranes are given in Table 5.1. It can be seen in Table 1 that, the IEC values of membranes decreased with the increasing of silica content, and were in the range of 1.81-1.63 meq g^{-1}. The reduction of IEC may be attributed to the two possible reasons; i) dilution effect of the PEG and SiO_2; since the same DS of SPEEK matrix was used here to prepare all the membranes, therefore, the sulfonic acid contents were same in all the nanocomposite membranes and on addition of PEG and SiO_2 there is decrease in sulfonic acid group per unit weight of membrane. ii) interaction between sulfonic and hydroxyl groups of PEG and SiO_2 in the membrane.

Table 5.1: Details of the SPP/SiO_2 prepared samples.

Sample designation	**SPP/SiO_2 (W/W)**	**Thickness (μm)**	**IEC meq g^{-1}**
SPP	100/0	190±10	1.81
SPP/SiO_2-2.5	97.5/2.5	200±10	1.76
SPP/SiO_2-5	95/5	210±10	1.73
SPP/SiO_2-7.5	92.5/7.5	210±10	1.70
SPP/SiO_2-10	90/10	220±10	1.66
SPP/SiO_2-12.5	87.5/12.5	220±10	1.63

□□□□2□2 Morphological study of SPP/SiO_2 membranes

The dimensions and the number of the inorganic particles in all the membranes samples were small enough to result in a transparent membrane except SPP/SiO_2-12.5 membrane, which is opaque. PEG played a key role in controlling the particle size of SiO_2 as well as the homogeneous distribution of Nano sized SiO_2 within the membrane. Figure 5.3 (A), (B) and (C), shows the FE-SEM image of SPP/SiO_2-5, SPP-SiO_2-10 and SPP-SiO_2-12.5 membranes. SiO_2 particles identified as bright dots were observed in the Si-mapping image using the energy-dispersive X-ray spectrometer (EDX) attached to the FE-SEM and shown in Figure 5.3 (a), (b) and (c). The hydrogen bond between –OH group of PEG, SiO_2 and sulfonic acid (–SO_3H) facilitated better dispersion and improved the compatibility between the organic and inorganic components. It was also observed from Figure 5.3 (A), the *in-situ* grown silica nanoparticles with average size is lower than 70 nm, are isolated from each other at low percentage of silica (5%). Whereas, upon the addition of 10% SiO_2, there is increase in the number of silica particles rather than their size and increased in the interlinking between the silica particles (Figure 5.3 (B)).

This indicates that the incorporation of PEG along with SiO_2 prevented aggregation of the SiO_2 particles and contributed to homogeneous distribution of particles within the polymer matrix. On further addition (12.5%), the SiO_2 particles start agglomerating as shown in Figure 5.3 (C). This is also supported by the Si-mapping image shown in Figure 5.3(a), (b) and (c). In Figure 5.3 (a) the Si particles are more scattered and less intense, and on increasing the SiO_2 percentage in the membrane samples the Si intensity increases and spectra becomes more dense Figure 5.3 (b) and (c).

The EDX elemental mapping of sulfur and oxygen along with silicon is given in Figure 5.4. The mapping spectra of silicon confirms that SiO_2 nanoparticles are homogeneously distributed within the nanocomposite membranes. Here, it is clearly observed that the increase in the silicon density in the membranes on increasing the SiO_2 weight percentage in the membrane samples (Figure 5.4 (a) to (c)). Whereas, the other elements (C and S) spectra are not showing significant difference because of their high percentage within the membranes.

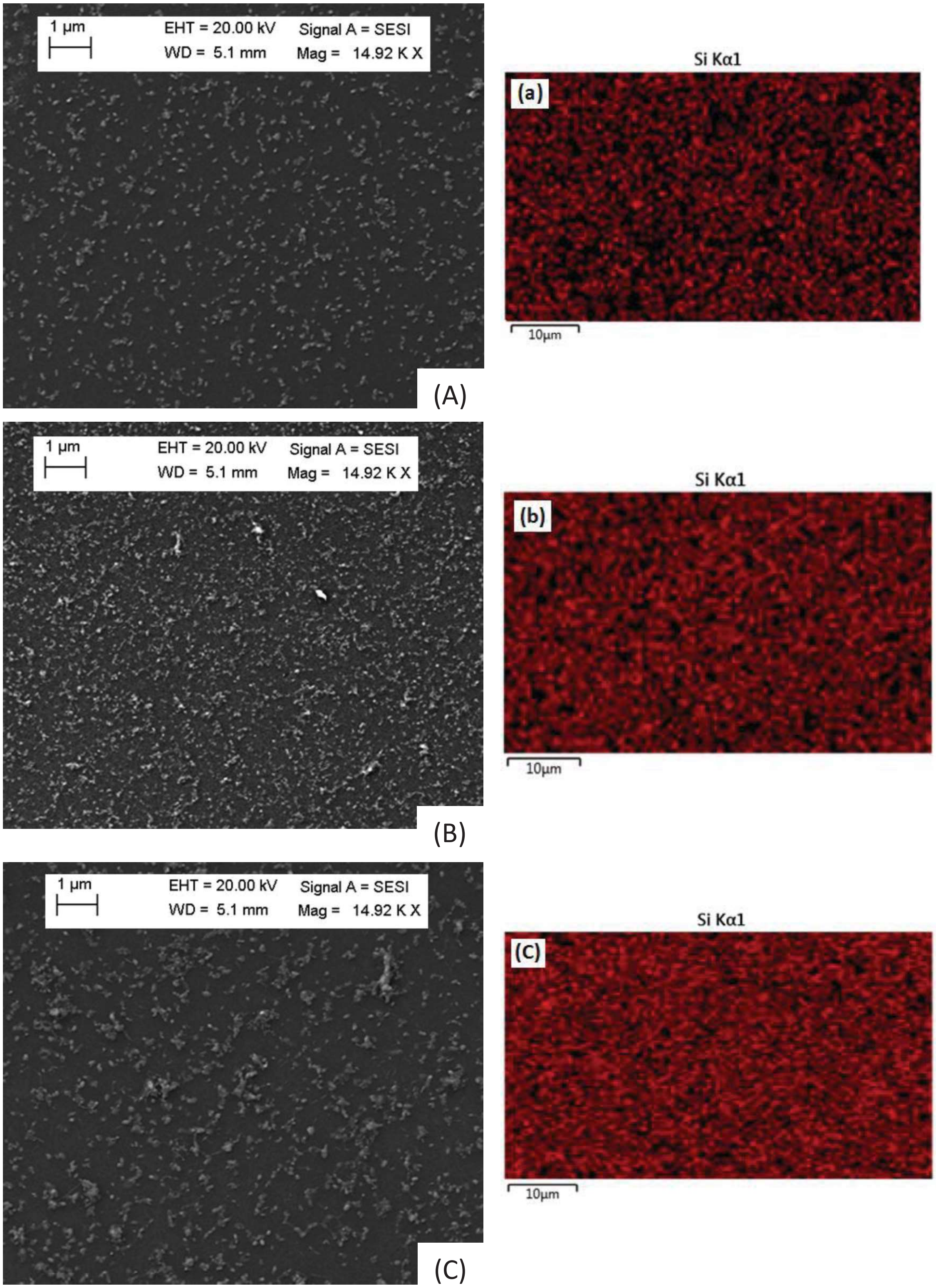

Figure 5.3: FE-SEM images of (A) SPP/SiO_2-5 and (B) SPP/SiO_2-10 (C) SPP/SiO_2-12.5 and EDX images of (a) SPP/SiO_2-5 and (b) SPP/SiO_2-10 (c) SPP/SiO_2-12.5.

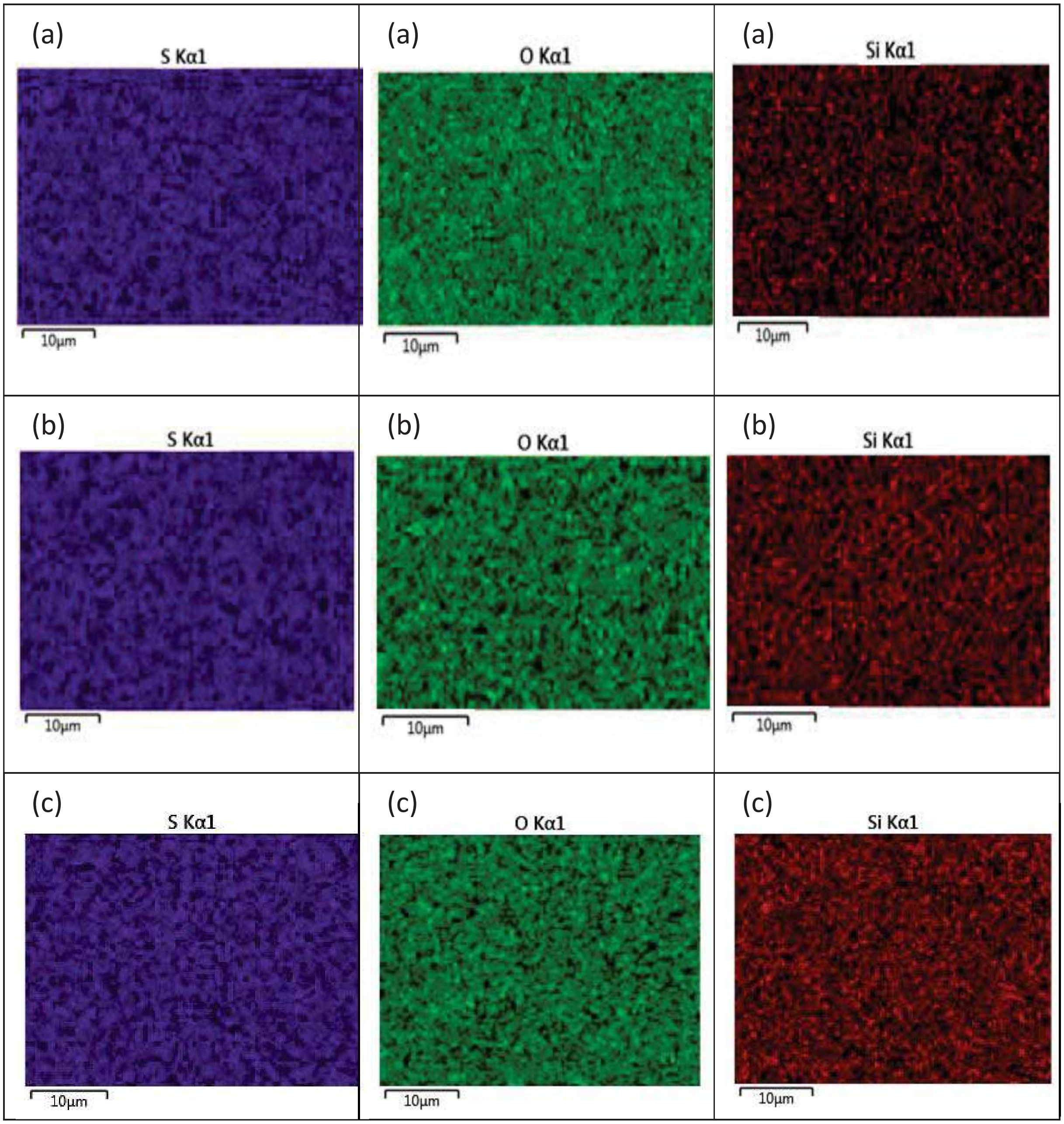

Figure 5.4: EDX elemental mapping spectra of (a) SPP/SiO$_2$-5 (b) SPP/SiO$_2$-10 and (c) SPP/SiO$_2$-12.5 membranes.

The EDX spectra of three different nanocomposite membranes (SPP/SiO$_2$-5, SPP/SiO$_2$-10 and SPP/SiO$_2$-12.5) along with SPP membrane are shown in Figure 5.5. It is seen that, the silicon peak intensity increases in the membrane samples according to the silica precursor used for the nanoparticles synthesis. The weight percentage of the silicon nanoparticles within the membranes (SPP/SiO$_2$-5, SPP/SiO$_2$-10 and SPP/SiO$_2$-12.5) was obtained from the EDX spectra of the membranes and given in Table 5.2. The calculated weight percentage of silicon and SiO_2 by assuming the complete conversion of TEOS precursor to SiO_2 are also given in the table. Here, it is clear seen that the silicon weight percentage obtained from the EDX spectra for 5% and 10% SiO_2 membrane samples are 2.3% and 4.7% respectively which is similar to the calculated silicon weight percentage (2.33 and 6.67). This shows the approximately complete conversion of precursor to SiO_2. In the case of SPP/SiO_2-12.5 membrane, the Silicon weight percentage obtained from the EDX spectra is 6.4% which is higher than the calculated weight percent of silicon i.e. 5.85%. This may be due to the agglomeration of SiO_2 particles in SPP/SiO_2-12.5 membrane.

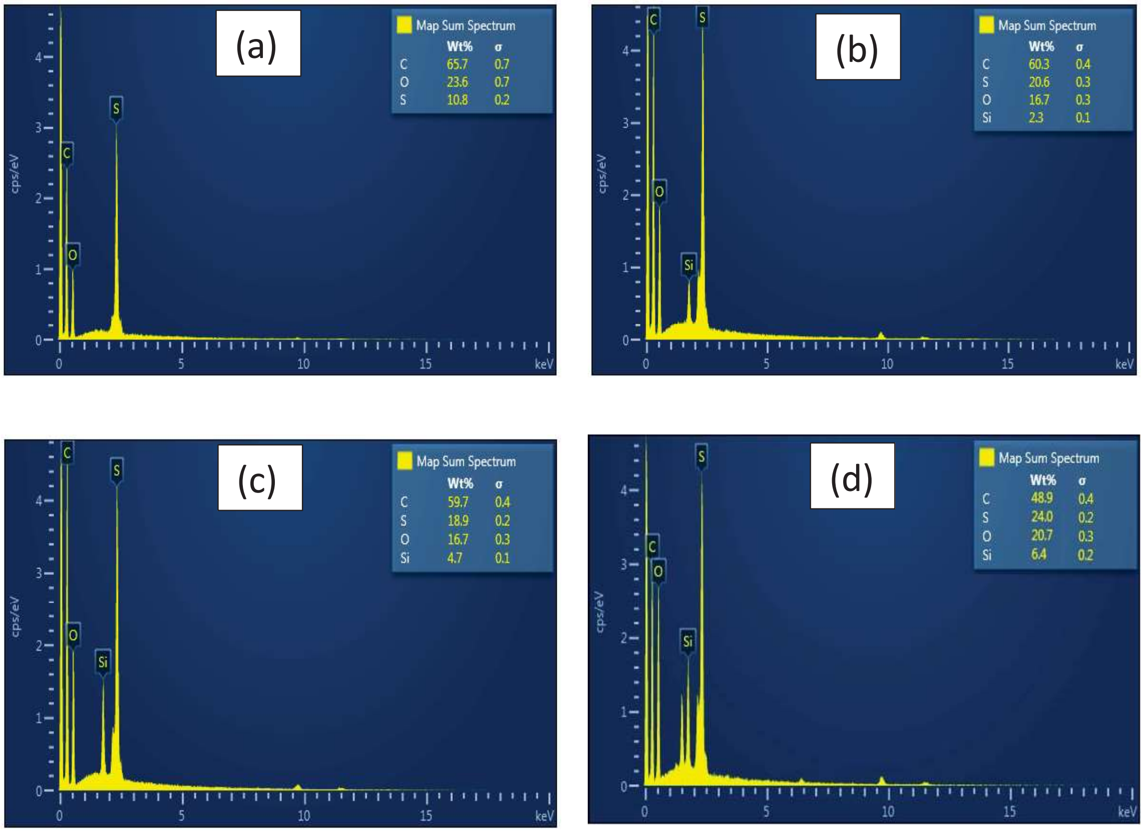

Figure 5.5: EDX spectra of (a) SPP (b) SPP/SiO_2-5 (c) SPP/SiO_2-10 and (d) SPP/SiO_2-12.5 membranes.

Table 5.2: Silicon weight percentage in the SPP/SiO_2 nanocomposite membranes

Sample name	**SiO_2 (wt %) Calculated**	**Si (wt %) Calculated**	**Si (wt %) EDX spectra**
SPP/SiO_2-5	5	2.33	2.30
SPP/SiO_2-10	10	4.67	4.7
SPP/SiO_2-12.5	12.5	5.85	6.4

Figure 5.6 shows the 2D and 3D AFM images of SPP, SPP/SiO_2-5 and SPP/SiO_2-10 membrane, supporting the FE-SEM images. As shown in Figure 5.6(a), there is regular network like structure formation in SPEEK-PEG membrane as PEG forms an IPN type structure in SPEEK-PEG membrane. Whereas in Figure 5.6 (b) and (c), there are many small dot like particles with diameters of less than 70 nm and cross-sectional heights of about 20−30 nm. Those small spherical particles are entangled chains of SiO_2 molecules. The number of spherical particles increased on increasing the SiO_2 percentage from 5% to 10% without much increase in particle diameter. The 3D images showed that the surface roughness of the membranes increases on increasing the SiO_2 percentage in the membrane. For better comparison of surface variation the roughness parameters are given in Table 5.3, where R_q, R_a and R_{max} represent the root mean square roughness, average roughness and maximum roughness respectively. It is evident from Table 5.3 the average roughness of SPEEK-PEG membrane is 0.176 nm which increased to 3.042 nm and 4.742 nm for SPP/SiO_2-5 and SPP/SiO_2-10, respectively.

Here, it is noticeable that on adding 5 wt% SiO_2 in the membrane sample, the average roughness of the membrane surface was increased from 0.176 nm to 3.042 nm i.e. the membrane roughness is increased by 2.866 nm (3.042 – 0.176), whereas on increasing the SiO_2 percentage to 10 wt% it increased to 4.742 nm i.e. only 1.7 nm (4.742- 3.042), increase in roughness on increasing the SiO_2 content form 5% to 10%. Which confirms that, the SiO_2

particle size does not increased proportionally on increasing the silica weight percentage in the membrane, only the number of particles are increased.

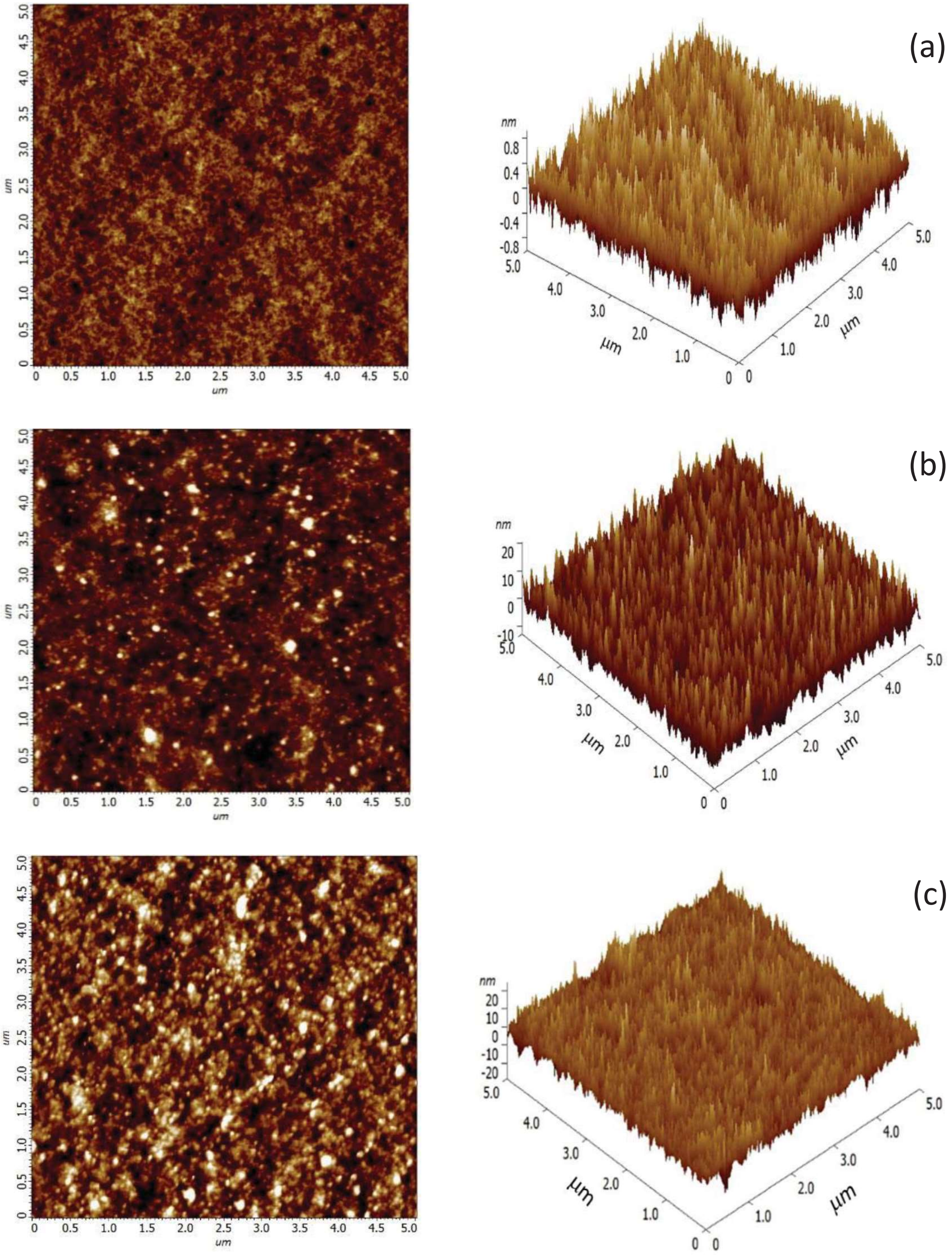

Figure 5.6: 2D and 3D AFM images of (a) SPP (b) SPP/SiO$_2$-5 and (c) SPP/SiO$_2$-10

Table 5.3: Surface roughness parameters of SPEEK-PEG cross-linked and SPEEK-PEG/SiO_2 nanocomposite membranes with two different weight percentage of SiO_2 (5% and 10%) obtained from 5 μm × 5 μm AFM images.

Sample Name	**R_q (nm)**	**R_a (nm)**	**R_{max} (nm)**
SPP	0.221	0.176	0.922
SPP/SiO_2-5	3.800	3.042	20.523
SPP/SiO_2-10	6.308	4.742	27.943

5.6.2.3 Water uptake and Proton conductivity analysis of SPP/SiO_2 membranes

In general, the proton conductivity of the ionomer membrane depends on the water uptake, number of available acid groups and their dissociation capability and morphology of the membrane. Water molecules play a vital role in ion exchange membrane e.g. dissociate the acid functionality to generate proton and facilitate proton transport i.e. act as proton carrier in the membrane. The water uptake and proton conductivity of SPP and SPP/SiO_2 nanocomposite membranes with different silica content were investigated as a function of temperature and shown in Figure 5.7 (a) and (b). Figure *5.7* (a), shows the water uptake of the SPP and SPP/SiO_2 nanocomposite membranes as a function of SiO_2 content at various temperatures (30 °C, 40 °C, 50 °C, 60 °C and 80 °C). With increasing temperature, the water uptake of SPP and SPP/ SiO_2 membranes increased due to the thermal relaxation of the polymer chains. The water uptake of the nanocomposite membranes containing silica nanoparticles is controlled by two factors (i) SPP/ SiO_2 cross-linked network structure which is hinder the chain mobility and narrow down the average distance between polymer chains that reduces the free volume capable of holding water molecules,resulting in a decrease in water uptake, (ii) high hygroscopic effect due to the unreacted silanol groups (–Si–OH), which increases the content of bound water.

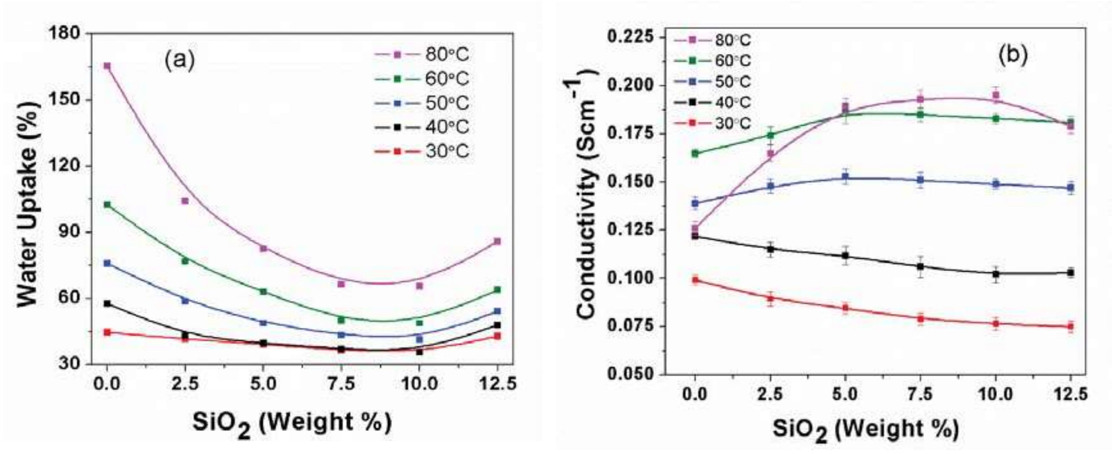

Figure 5.7: Variation of (a) water uptake and (b) conductivity as a function of SiO_2 weight percentage in the membranes at various temperatures.

As shown in Figure 5.7 (a) the water uptake of SPP/SiO_2 nanocomposite membranes is lower than the pristine SPP membrane and it exhibited a decreasing tendency with an increase in SiO_2 content up to 7.5%, after that up to 10% of SiO_2 it shows the similar values and then starts increasing. This can be explained by the fact that, up to 7.5 % of SiO_2 loading, the reduction in IEC and free volume becomes the primary affecting factor in the water uptake, 7.5% to 10% the reduction in IEC and free volume should decrease the water uptake but due to simultaneous increase in hygroscopic effect, the water uptake is almost constant, hence no specific change is observed. Whereas beyond 10 % of SiO_2 the hygroscopic effect (due to the possibility of an increase in silanol group) is the primary factor for an increase in water uptake. It is also noted that the water uptake by the membranes increases gradually by increasing the equilibrating temperature, due to the increase in polymer chain movement with temperature which facilitates the increase in free volume. Similar trends were reported in grafted silica/SPEEK nanocomposite membranes with SPEEK of 85% DS, where water uptake first decreased up to 10% of silica content and then increased on increasing the silica content in the membrane.[249]

The proton conductivity of the membrane has been measured in fully hydrated condition at various temperature (30 °C, 40 °C, 50 °C, 60 °C and 80 °C) and shown in *Figure 5.7* (b). On increasing the temperature, the conductivity of all the membranes increases up to 60 °C because of the thermal movement of H^+ and increase in water uptake increases the H^+ mobility in the membrane. Whereas, at 80 °C some of the membranes show lower conductivity than 60 °C mainly because of the large water uptake or H^+ dilution, it is evident from Figure 5.8. Water molecules per unit functional group (□) for the nanocomposite membranes are calculated by the following Eq. 1.29.

As seen in Figure 5.8, the number of water molecules per unit sulfonic group (□) in SPP membrane is increases from 13.7 to 31.6 on increasing the equilibration temperature of membrane in water from 30 °C to 60 °C which increases the H^+ mobility within the membrane. Whereas, at 80 °C, the □ value is increased to 51.0 which reduced the H^+ concentration and the conductivity goes down. Similarly, the composite membranes containing 2.5% and 12.5% SiO_2 has lower conductivity at 80 °C than 60 °C. Although the □ value in these membranes is increased up to 32.8 and 29.2 respectively at 80 °C, the decrease in conductivity may be due to the lower IEC value compared to SPP membrane and SiO_2 network structure formation which lower the H^+ movement and conductivity with some dilution effect. In 5%, 7.5% and 10% SiO_2 embedded membranes the maximum □ value at 80 °C is 26.4, 21.7 and 21.9 respectively which are optimum to increase the H^+ mobility and conductivity.

In Figure 5.7 (b), at 30 °C and 40 °C the proton conductivity trend is almost similar and the membranes conductivity reduced from 0.095 S cm^{-1} to 0.075 S cm^{-1} and 0.122 S cm^{-1} to 0.099 S cm^{-1} respectively. On increasing the silica content from 0% to 12.5%. The lowering in the proton conductivity is due to the reduced water uptake value along with the dilution effect of silica on sulfonic acid groups that reduces the ion exchange capacity. At 50 °C and 60 °C the trend is similar and the maximum conductivity is shown by SPP/SiO_2-5 membrane. The possible reason for that is below 5% SiO_2 embedded membrane the dilution of H^+ (because of large water uptake) and above 5%, the decrease in IEC, lower water uptake with more IPN type structure that hinder the H^+ movement. At 80 °C SPP/SiO_2-10 shows highest conductivity due to the optimum water uptake, effective microstructure formation and control amount of silica nanofiller (10% of the polymer) that facilitate the H^+ movement.

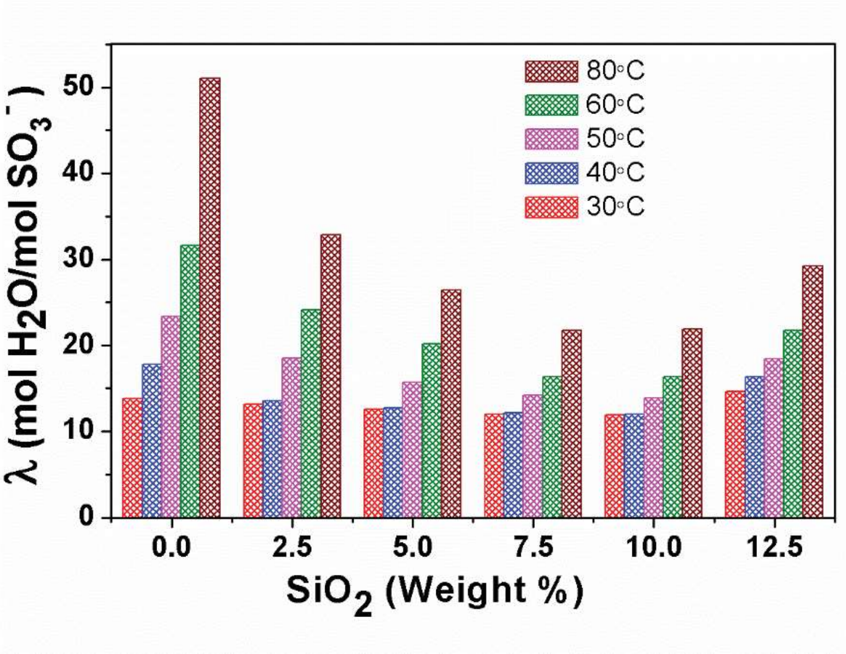

Figure 5.8: Variation of water molecules per unit functional group as a function of SiO_2 weight percentage in the membranes at various temperatures.

5.6.2.4 Structural characterizations of SPP/SiO_2 membranes

The ATR-FTIR spectra of sulfonated polyether ether ketone (SPEEK), cross-linked SPP and composite cross-linked SPP/SiO_2 with two different weight percentage of SiO_2, 5% and 10% (SPP/SiO_2-5, 10) membranes are shown in Figure 5.9. The sulfonation of PEEK was confirmed by the two characteristic peaks of -SO_3H groups at 1020 and 1079 cm^{-1}, which are assigned to the symmetric and asymmetric stretching vibration modes of O=S=O, respectively [127]. A broad peak in the range of 3200–3700 cm^{-1} appeared in the spectra of all the samples due to the O-H stretching vibration in the hydration water and O-H groups belonging to the sulfonic acid (–SO_3H) functional group into the polymer matrix, PEG and silanol (Si–OH). The presence of

PEG is observed in particular SPP and SPP/SiO$_2$ membranes at 2950-3100 cm^{-1} due to the C–H symmetric stretching bands which is absent in the spectra of SPEEK.

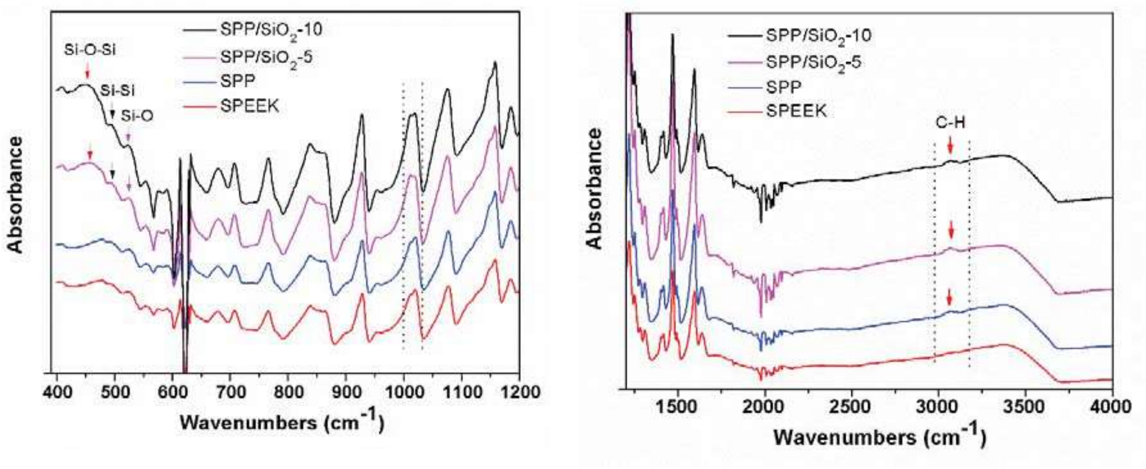

Figure 5.9: ATR-FTIR spectra of SPEEK, SPP and SPP/SiO$_2$ (5% and 10%) membranes.

In the composite membranes spectrum all the typical bands of the silica sol-gel materials are present. The band at 460 cm^{-1} is due to the bending Si–O–Si. The low intensity band at 580 cm^{-1} is attributed to siloxane rings in the silica network and the band at 948 cm^{-1} is assigned to Si–OH bond vibrations which may overlap with the C-O-C stretching band around 940 cm^{-1}.[250] The peaks at 1080 cm^{-1} is become broaden in the composite membranes due to the overlapping of asymmetric Si-O-Si stretching vibration with O=S=O band around 1079 cm^{-1} [162]. A change in the shape of the peak at 1020 cm^{-1} in the composite membranes is observed which may be due to the hydrogen bonds between the sulfonic acid (–SO$_3$H) and silanol (Si–OH) group. All the FTIR band assignments are summarized in Table 5.4.

Table 5.4: FTIR band assignments for SPEEK, SPP and SPP/SiO_2 membranes.

Wavenumber (cm^{-1})	**Vibrational modes**
1653	Carbonyl stretching
1488	Aromatic C–C vibration
1250	C-O stretching
1020,1079,1170	O=S=O stretching
1030,1080,810	Si-O-Si stretching
460	Si-O-Si bending
3700-3200	O-H stretching
1640	O-H bending
580	siloxane rings in the silica network

5.6.2.5 Mechanical Properties of SPP/SiO_2 membranes

The mechanical properties of the membrane are another important parameter for fuel cell application, which depends on many factors like water uptake, microstructure, temperature, preconditioning etc. The stress-strain curve of all the membranes is plotted in Figure 5.10 (a). The membranes first undergo reversible elastic deformation under applied stress, as shown in the initial linear part of the stress–strain curves. Subsequently, membranes persist irreversible inelastic deformation with the increased applied stress, as shown in the curvature portion of the curves. Finally, membranes reached their fracture strength, resulting in breakage. All the samples display a sharp yield point followed by neck formation with the variation in yield stress and the yield stress increases with increasing the SiO_2 content in the membranes. The stress-strain curves shows that the membranes brittleness increases on increasing the SiO_2 percentage in the membrane.

In practical operation, inelastic deformation caused by excessive stress leads to the fatigue damage of the membranes, resulting in membrane failure. For better comparison, the mechanical properties e.g. Young's modulus, tensile strength and percent elongation at break were extracted from stress-strain curves and investigated specifically. The curves monotonically shifted upward to indicate increasing tensile strength, and elongation-to-break decreases in this order.

Young's Modulus and Tensile Strength

Young's modulus provides an information of the stiffness of the material which is a measure of how much it deforms elastically per unit applied stress and calculated from the slope of initial linear portion of the stress-strain curve. The values of Young's modulus of the SPP and SPP/SiO_2 membranes are shown in Figure 5.10 (b). The Young's modulus of the SPP membrane is the lowest of all the membranes with a value of 340.78 MPa. Incorporation of SiO_2 nanoparticles exhibited an increasing trend of Young's modulus for membranes with increasing SiO_2 contents. The Young's modulus of the membranes SPP/SiO_2-2.5, SPP/SiO_2-5, SPP/SiO_2-7.5 SPP/SiO_2-10 and SPP/SiO_2-12.5 are 403.3, 426.5, 443.6, 468.2 and 528.2 MPa respectively, indicating enhanced stiffness of the composite membranes. Similar trends were reported in Nafion/SiO_2 membrane.[251] The tensile strength is a parameter to evaluate the strength of the membrane, it is the maximum stress that a membrane samples can withstand before breaking. As shown in Figure 5.10 (c), tensile strength of the SPP membrane is lowest among the investigated membranes with a value of 16.55 MPa. The tensile strength of the composite membranes increases with increasing the silica percentage in the membrane, i.e. 17.79, 18.32, 19.57, 21.27, 23.9 MPa for SPP/SiO_2-2.5, SPP/SiO_2-5, SPP/SiO_2-7.5 SPP/SiO_2-10 and SPP/SiO_2-12.5 nanocomposite membranes. The increase in stiffness and strength of the nanocomposite membranes can be explained by the incorporation of SiO_2 and their homogeneous distribution in membrane. On incorporation of SiO_2, there is increase in the formation of hydrogen bond between the OH group of PEG, SiO_2 and $-SO_3H$, that increases the stiffness and strength of the membranes. Other factor which contributes to increase in stiffness and strength is increase in cross-linking and IPN formation between the organic and inorganic moieties.

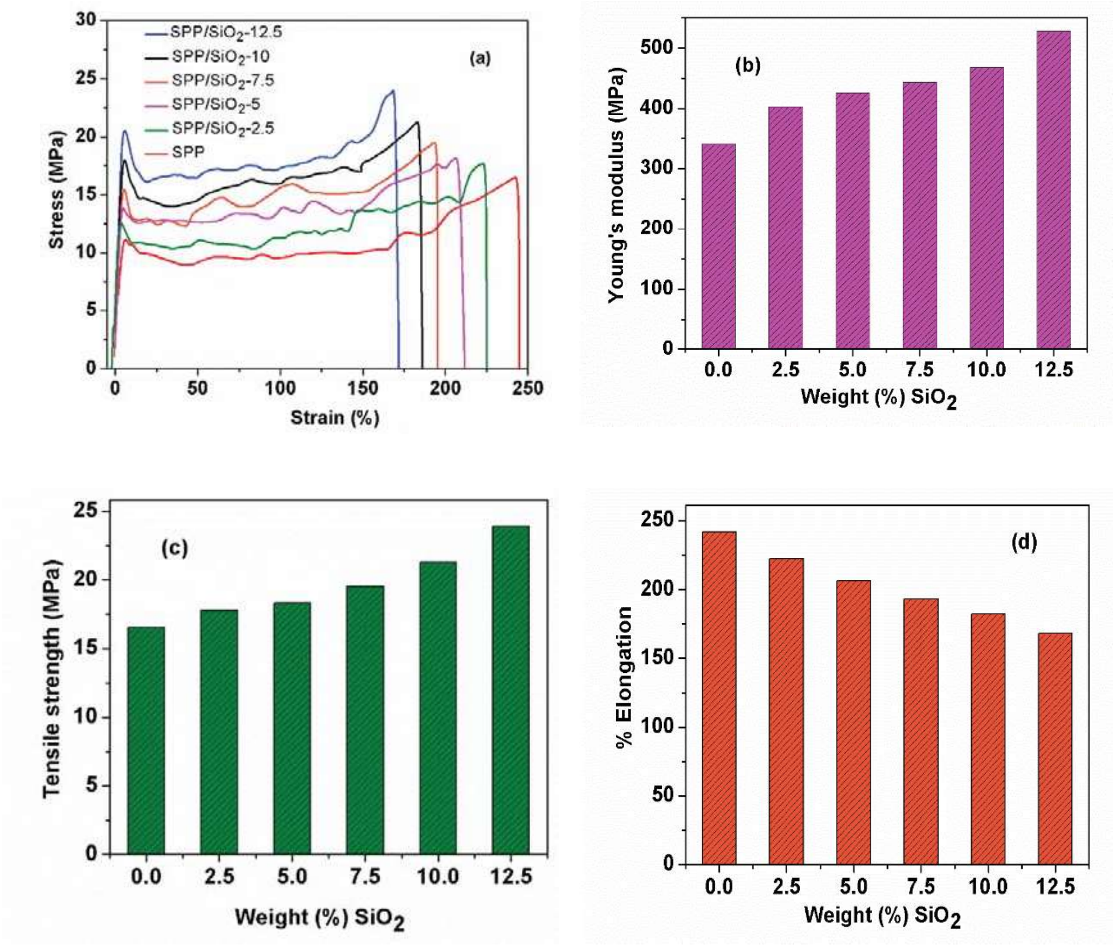

Figure 5.10: (a) stress-strain curve (b) Young's modulus (c) Tensile strength (d) percent elongation of the membranes as a function of SiO_2 weight percentage.

Percent elongation

The percentage elongation at break, corresponding to the maximum elongation of the membrane at fracture compare to the initial length. Which is calculated by the maximum length divided by the original length, gives an information of ductility of membrane. As shown in Figure 5.10 (d), the percentage elongation of the SPP membrane is 242%. The elongation of the SPP/SiO_2 nanocomposite membranes exhibited a decreasing tendency due to the increase of SiO_2 content and reached 168% for the SPP/SiO_2-12.5 membrane. the decrease in percentage elongation can be explain by two factors; (i) decrease in water uptake on increasing the SiO_2 weight percentage in the membrane which decreases the polymer chain mobility, since water act as plasticizer, (ii) due to increase in cross-linking network of SiO_2 that restricted the movement of the polymer (SPEEK and PEG) chain segments.

5.6.2.6 Oxidative stability of SPP/SiO_2 membranes

Oxidative stability of the membranes was evaluated by Fenton test and the results are given in Table 5.5. The results showed marginal degradation at 27°C, however, the degradation increased after treatment at 80°C. This is due to the increased water uptake. As shown in Table 5.5, at 80°C all of the hybrid membranes (SPP/SiO_2) showed higher oxidative stability than the pristine SPP membrane and the oxidative stability gradually increased on increasing of silica content within the membrane. The weight loss in SPP membrane is 28.8% whereas the SPP/SiO_2-12.5 membrane shows the weight reduction by 9.2%. The increase in the oxidative stability could be due to the following two reasons. Firstly, on increasing the SiO_2 percentage within the membranes, there is increase in the cross-linkable sites with IPN structure formation that reduces the water uptake at higher temperature. As the network structure formation increased, the packing density of polymer chains is also increased (reducing the free volume available for penetration of $HO^{\bullet}$ and $HO_2^{\bullet}$ radicals), which reduces the free radical attack on the polymer chain and increases the oxidative stability. Secondly, it may be due to the reinforcement effect of cross-linkage, as a polymer chain is attacked by a free radical, the dissociated molecular chain can be still attached on the polymer network by cross-linking point which increased the complete dissociation time of polymer chain under the radical attack and membrane durability.

Table 5.5: Membrane weight loss (%) after treatment in Fenton reagent at 27°C for 48 hrs and at 80°C for 1 hr.

Sample Name	% weight loss at 27 °C for 48 hrs	% weight loss at 80 °C for 1 hr
SPP	0.99	28.8
SPP/SiO$_2$-2.5	0.78	19.9
SPP/SiO$_2$-5	0.61	15.3
SPP/SiO$_2$-7.5	0.52	11.2
SPP/SiO$_2$-10	0.48	9.5
SPP/SiO$_2$-12.5	0.49	9.2

5.6.2. Thermal stability of SPP/SiO$_2$ membranes

Thermal stability of membranes was investigated by thermogravimetric analysis. Figure 5.11 shows the thermal decomposition thermograms of SPEEK, SPP and SPP/SiO$_2$ nanocomposite membranes with different SiO$_2$ (2.5%, 5%, and 10%) loading. All the samples showed three consecutive weight loss steps; (i) below 200°C, (ii) between 250°C and 400°C and (iii) beyond 450°C.

The initial weight loss occurs below 200 °C is associated with the loss of free and bound water within the membrane. The second step, weight loss occurs between 250-400 °C which was due to the decomposition of sulfonic acid groups and PEG and in the third step, weight loss above 450 °C was due to the main polymer chain degradation.[146] Again, from the Figure 5.11 it is observed that third weight loss temperature which was started at around 480 °C for pristine SPP membrane shifted slightly towards higher temperature 500 °C for the nanocomposite SPP/SiO$_2$ membranes. This may take place due to the formation of SiO$_2$ network. The TGA results revealed that all the membranes had fairly good thermal stability, where the onset of thermal decomposition of sulfonated moieties 250 °C occurred well above the low and medium temperature PEM fuel cell application. In addition, the increase in weight residues at 700 °C is nearly proportional to the mass fraction of SiO_2 introduced in the membrane which ultimately increases the thermal stability of membranes.

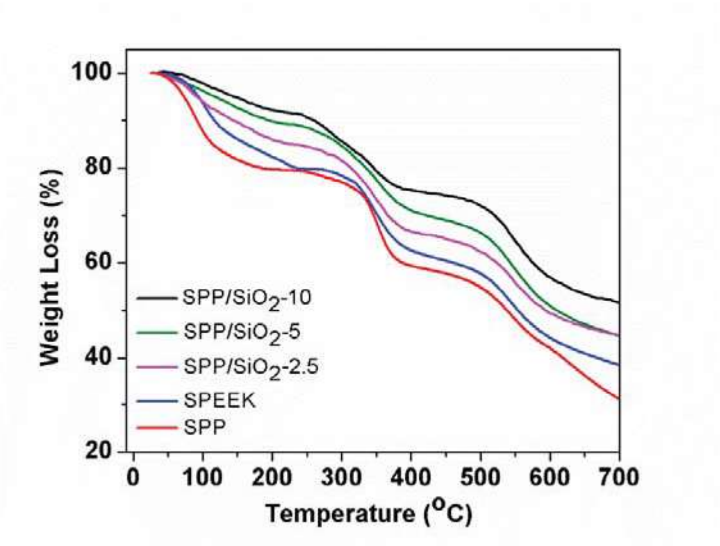

Figure 5.11: Thermo gravimetric traces of SPEEK, SPP and SPP/SiO_2-(2.5, 5, 10) membranes.

5.6.2. SPP/SiO_2 nanocomposite membrane performance study in PEM FC

As seen from the above discussions, the membrane properties are greatly affected by SiO_2 percentage in the membrane e.g. conductivity, water uptake, mechanical strength, thermal and oxidative stability etc. the membrane containing 10 wt% SiO_2 showed the highest conductivity and optimum water uptake at higher temperature (≥ 60 °C) among all the nanocomposite membranes. In order to understand the effect of SiO_2 addition on the membrane performance in fuel cell, MEAs were prepared by using two membranes SPP and SPP/SiO_2-10. The MEAs performance tests were carried out from 30 °C to 60 °C and the polarization and power density curves as a function of current density are plotted in Figure 5.12. At all temperatures, it was observed that the higher performance results for the MEA prepared by using SPP/SiO_2-10 membrane compare to SPP. The maximum power density, current density and voltage of both the membranes at various temperatures (30°C ,40°C ,50°C and 60°C) is given in Table 5.6. As seen in Table 5.6, at 60 °C the SPEEK-PEG membrane gives the maximum power density of 184 mW cm^{-2} at 460 mA cm^{-2} and at 0.4 V, which is enhanced to 378.4 mW cm^{-2} at 800 mA cm^{-2} and at 0.473 V for SPP/SiO$_2$-10 membrane. The maximum power density due to the addition of 10% of SiO$_2$ was enhance to more than twofold higher.

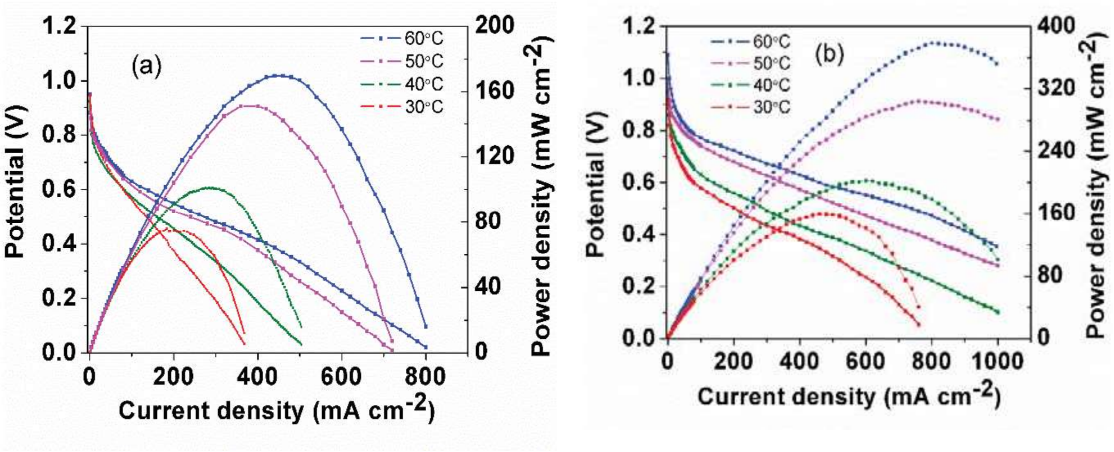

Figure 5.12: Fuel cell performance of (a) SPP and (b) SPP/SiO$_2$-10 membranes at various temperatures.

Table 5.6: The maximum power density, current density and voltage at 60°C of SPP and SPP/SiO$_2$ nanocomposite membrane.

Sample Name	Temperature (°C)	Potential (V)	Current density (mA cm^{-2})	Power density (mW cm^{-2})
SPP	30	0.33	216	71.28
	40	0.34	298	101.32
	50	0.4	340	120.00
	60	0.4	460	184.00
SPP/SiO$_2$	30	0.347	460	159.62
	40	0.351	560	196.56
	50	0.4	740	296.00
	60	0.473	800	378.40

The durability studies of the membranes in the fuel cell were carried out by measurement of OCV during the 200 cycles for both the membranes (SPP and SPP/SiO_2-10) at 60 °C and each cycle was performed after half an hour interval. The OCV profile of both the membranes as a function of number of cycles is plotted in Figure 5.13. The OCV for both the membranes increased during the first 50 cycles attributed to the activation of the MEA assembly, thereafter the OCV remained constant up to 200 cycles and there was no significant decrease in OCV for 200 cycles. SPEEK-PEG membrane showed slightly lower values of OCV, i.e., 0.98 V (~0.07V less) than of SPP/SiO_2-10, which showed OCV of 1.09 V.

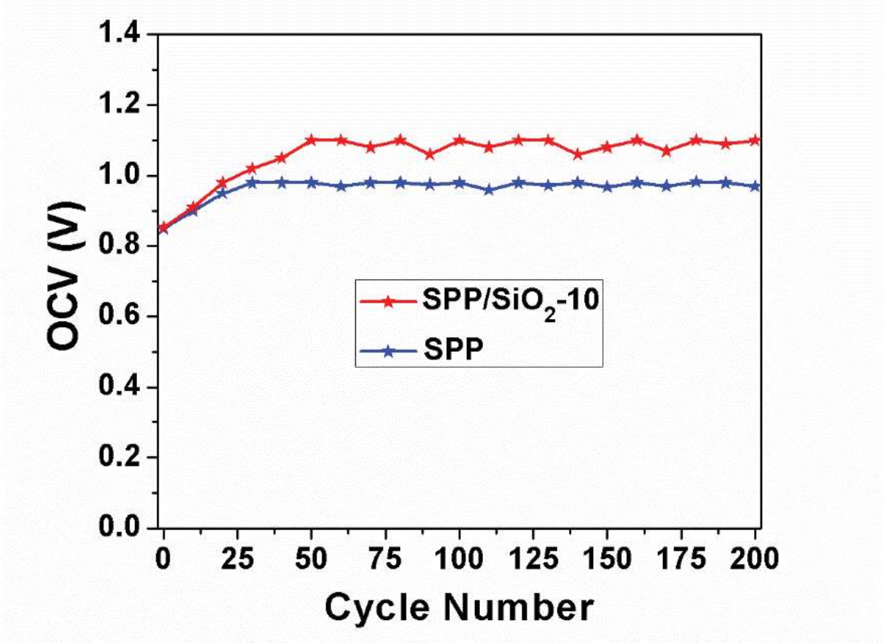

Figure 5.13: Change in OCV with number of cycles performed in H_2/O_2 fuel cell

5.6.3 Results and discussion of SPEEK-PEG/TiO_2 (SPP/TiO_2) nanocomposite membranes:

The details of SPP/TiO_2 nanocomposite membranes are given in Table 5.7 All the membranes thickness were measured after equilibrating in water for 48 hrs at room temperature.

5.6.3.1 Ion exchange capacity SPP/TiO_2 membranes

The IEC and DS of SPEEK polymer that is used for membrane synthesis are 2.12 meq g^{-1} and 78% respectively. The IEC value of SPP and SPP/TiO_2 nanocomposite membranes are given in Table 5.7. It can be seen in Table 5.7 that, the IEC values of membranes decreased with the increasing of TiO_2 weight percentage in the membranes, and were in the range of 1.81-1.69 meq g^{-1}. The reduction of IEC may be attributed to the two possible reasons; i) dilution effect of the PEG and TiO_2; since the same DS of SPEEK matrix was used here to prepare all the membranes, therefore, the sulfonic acid contents were same in all the nanocomposite membranes and on addition of PEG and TiO_2 there is decrease in sulfonic acid group per unit weight of membrane. ii) interaction between sulfonic and hydroxyl groups of PEG and TiO_2 in the membrane.

Table 5.7: Details of the SPP/TiO_2 prepared samples.

Sample designation	**SPP/TiO_2 (W/W)**	**Thickness (μm)**	**IEC meq g^{-1}**
SPP	100/0	190±10	1.81
SPP/TiO_2-2.5	97.5/2.5	200±10	1.77
SPP/TiO_2-5	95/5	210±10	1.74
SPP/TiO_2-7.5	92.5/7.5	210±10	1.71
SPP/TiO_2-10	90/10	220±10	1.69

5.6.3.2 *Morphological characterization of SPP/TiO_2 membranes*

The morphological changes in the membranes on varying the TiO_2 weight percentage in the nanocomposite membranes are explained in this section on the basis FE-SEM images, EDX spectra and elemental mapping and AFM images.

Figure 5.14 (A), (B) and (C), shows the FE-SEM image of SPP/TiO_2-2.5, SPP-TiO_2-5 and SPP-TiO_2-10 membranes. TiO_2 particles identified as bright dots were observed in the Ti-mapping images shown in Figure 5.14 (a), (b) and (c). It is observed from Figure 5.14 (A), (B) and (C), that the TiO_2 nanoparticles are evenly distributed throughout the membranes for every polymer/TiO_2 ratio. It is also observed from Figure 5.14 (A), the *in-situ* grown TiO_2 nanoparticles with average size is lower than 20 nm, are isolated from each other at low weight percentage of TiO_2 (2.5%). Whereas, upon the addition of 5% TiO_2, there is increase in the number of TiO_2 particles and the interlinking between the nanoparticles, shown in Figure 5.14(B). The average size of the nanoparticles is increased to 35 nm. On further addition (10%), the TiO_2 particles size increased and they start agglomerating as shown in Figure 5.14 (C). These figures demonstrate various facts: first, the PEG prevents nanoparticles aggregation. Second, the synthesized nanoparticles have spherical shape and even distribution and the third is, at higher weight percentage of TiO_2 (5 and 10%) the nanoparticles are well connected and form network like structure.0, which is responsible for its good form stability, mechanical strength and chemical stability that will be discussed in the coming sections.

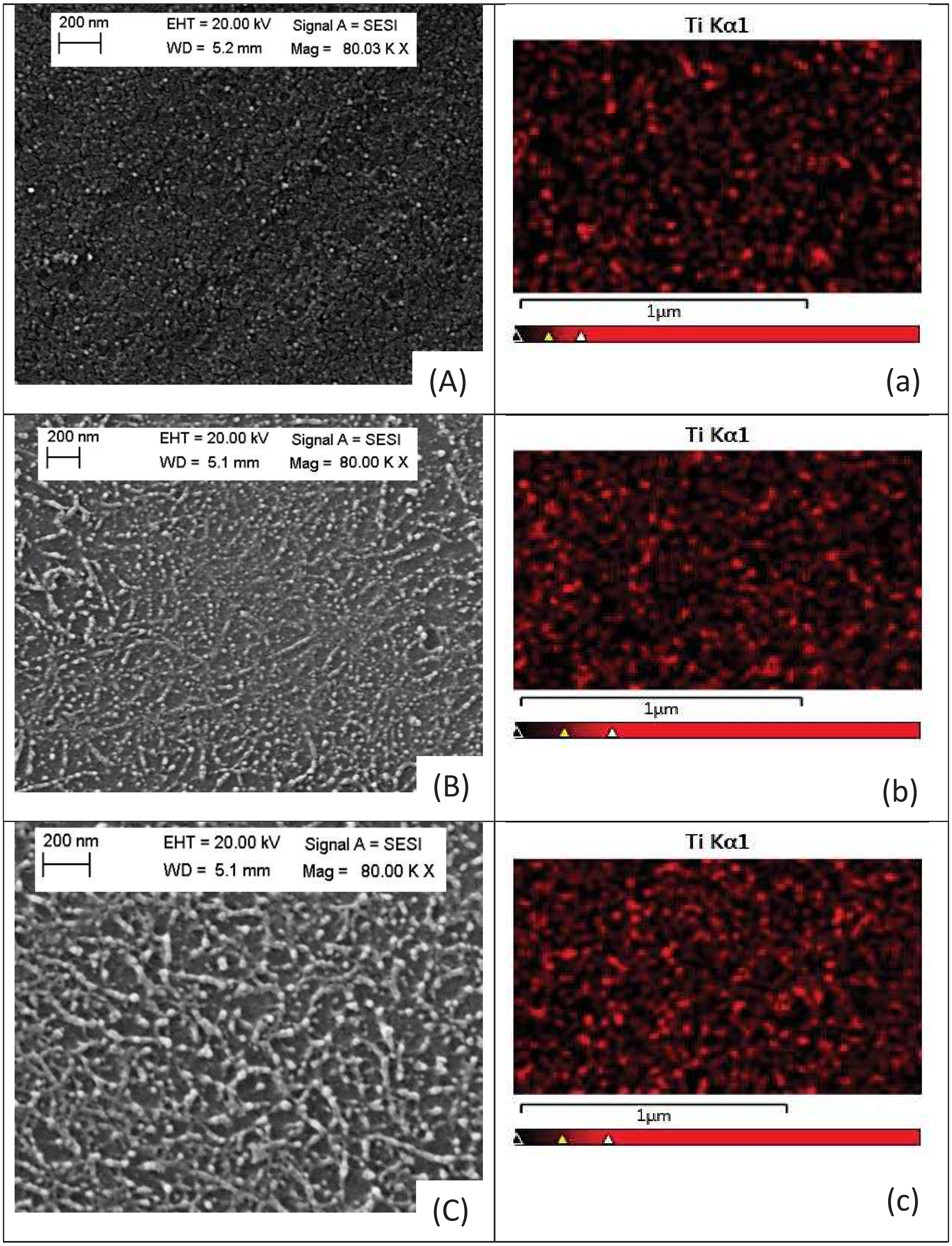

Figure 5.14: FE-SEM images of (A) SPP/TiO_2-2.5 and (B) SPP/TiO_2-5 (C) SPP/TiO_2-10 and EDX images of (a) SPP/TiO_2-2.5 and (b) SPP/TiO_2-5 (c) SPP/TiO_2-10.

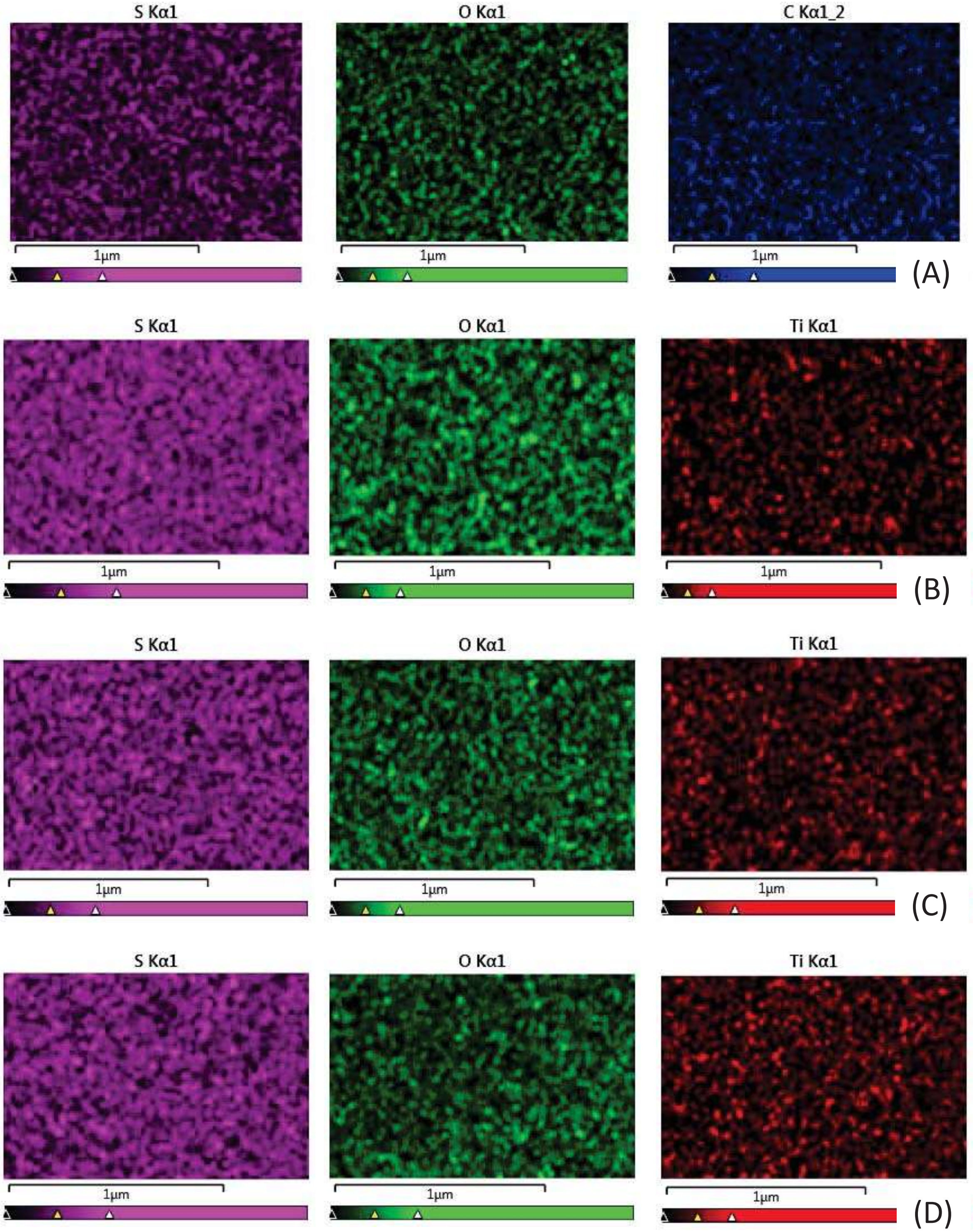

Figure 5.15: EDX elemental mapping spectra of (A) SPP (B) SPP/TiO_2-2.5 (C) SPP/TiO_2-5 and (D) SPP/TiO_2-10 membranes.

The EDX elemental mapping of sulfur and oxygen along with titanium is given in Figure 5.15. The mapping spectra of titanium confirms that TiO_2 nanoparticles are homogeneously distributed within the nanocomposite membranes. Here, it is clearly observed that the increase in the titanium density in the membranes on increasing the TiO_2 weight percentage in the membrane samples (Figure 5.15 (a) to (c)). Whereas, the other elements (C and S) spectra are not showing significant difference because of their high percentage within the membranes.

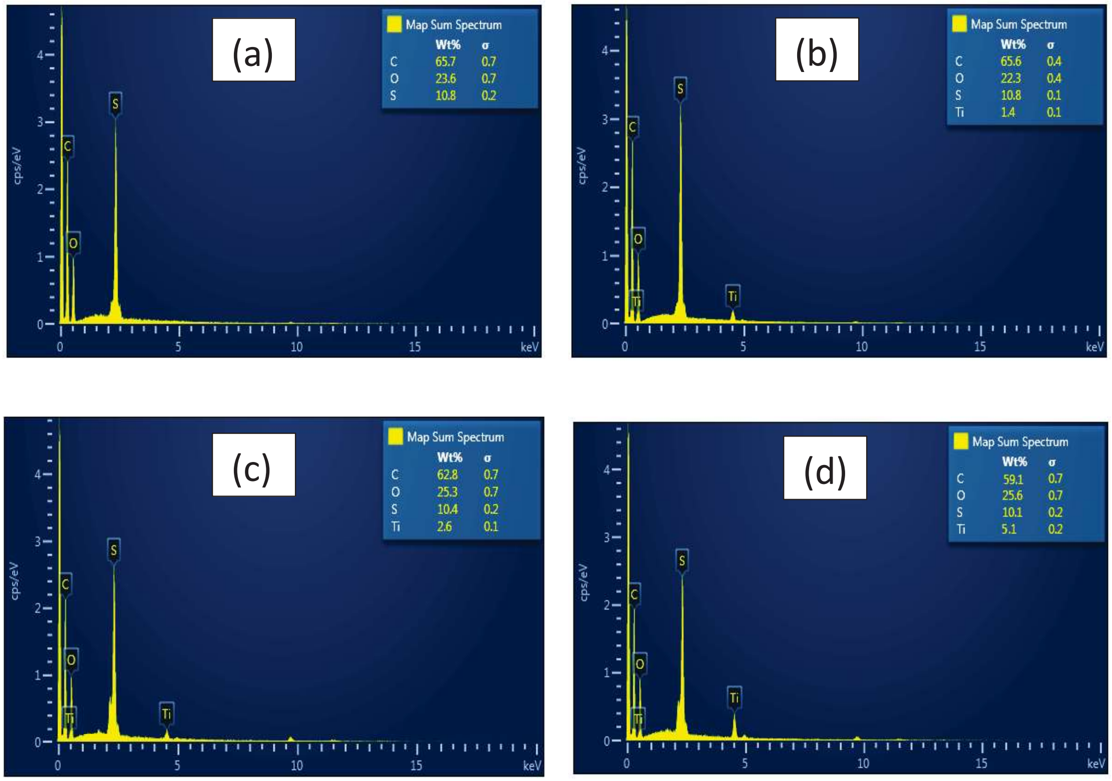

Figure 5.16: EDX spectra of (a) SPP (b) SPP/TiO_2-2.5 (c) SPP/TiO_2-5 and (d) SPP/TiO_2-10 membranes.

The EDX spectra of three different nanocomposite membranes (SPP/TiO_2-2.5, SPP/TiO_2-5 and SPP/TiO_2-10) along with SPP membrane are shown in Figure 5.16. It is seen that, the titanium peak intensity increases in the membrane samples according to the titania precursor used for the nanoparticles synthesis. The weight percentage of the titanium nanoparticles within the membranes (SPP/TiO_2-2.5, SPP/TiO_2-5 and SPP/TiO_2-10) was obtained from the EDX spectra of the membranes and given in Table 5.8. The calculated weight percentage of titanium and TiO_2 by assuming the complete conversion of $Ti(OBu)_4$ precursor to TiO_2 are also given in the Table 5.8. Here, it is clear seen that the titanium weight percentage obtained from the EDX spectra approximately similar to the calculated titanium weight percentage. This shows the approximately complete conversion of precursor to TiO_2 .The difference between the calculated weight percentages of titanium and obtained from EDX spectra is increases from lower to higher weight percentage, this may be due the some amount of precursor lost during the synthesis process.

Table 5.8: Titanium weight percentage in SPP/TiO_2 nanocomposite membranes.

Sample name	**TiO_2 (wt %) Calculated**	**Ti (wt %) Calculated**	**Ti (wt %) EDX spectra**
SPP/TiO_2-2.5	2.5	1.49	1.4
SPP/TiO_2-5	5	2.99	2.6
SPP/TiO_2-10	10	5.99	5.1

Figure 5.17 shows the 2D and 3D AFM images (2 μm × 2 μm) of SPP membrane. There is regular network like structure formation in SPEEK-PEG membrane as PEG forms an IPN type structure in SPEEK-PEG cross-linked membrane. The roughness parameters obtained from this image is given in Table 5.9.

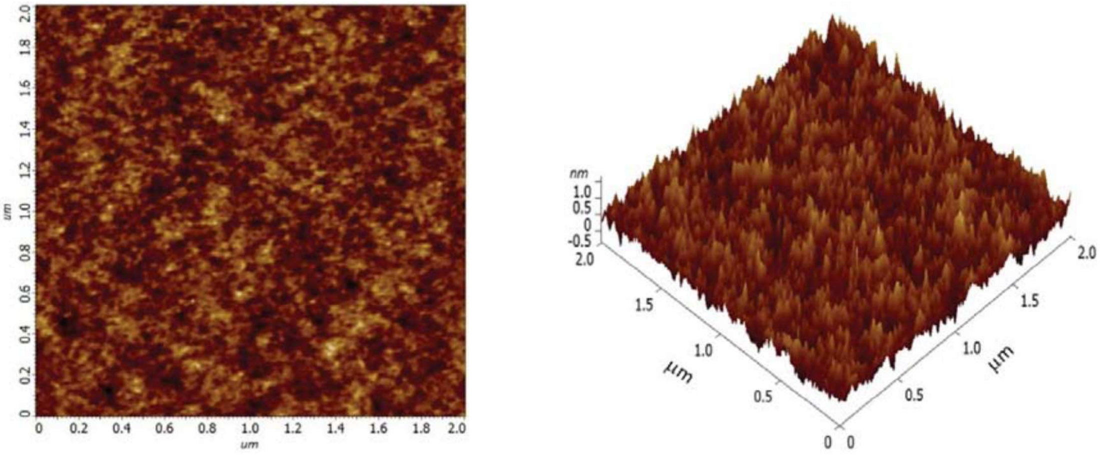

Figure 5.17: 2D and 3D AFM images (2 μm × 2 μm) of SPEEK-PEG (without nanoparticles addition) membrane.

The AFM images of SPP/TiO_2 nanocomposite membranes are given in Figure 5.18. The 2D and 3D AFM images of SPP/TiO_2-2.5, SPP/TiO_2-5 and SPP/TiO_2-10 membranes, shown in Figure 5.18 (A), (B) and (C) supported the FE-SEM images given in Figure 5.14. As shown in Figure 5.18 (a), there are many small dot like particles with diameters of less than 20 nm and cross-sectional heights of about 3 nm. These particles size and density increased on increasing the TiO_2 weight percentage in the membranes, as shown in Figure 5.18 (b) and (c), those small spherical particles are entangled chains of TiO_2 molecules. The 3D images showed that the surface roughness of the membranes increases on increasing the TiO_2 percentage in the membrane. For better comparison of surface variation the roughness parameters are given in Table 5.9, where R_q, R_a and R_{max} represent the root mean square roughness, average roughness and maximum roughness respectively.

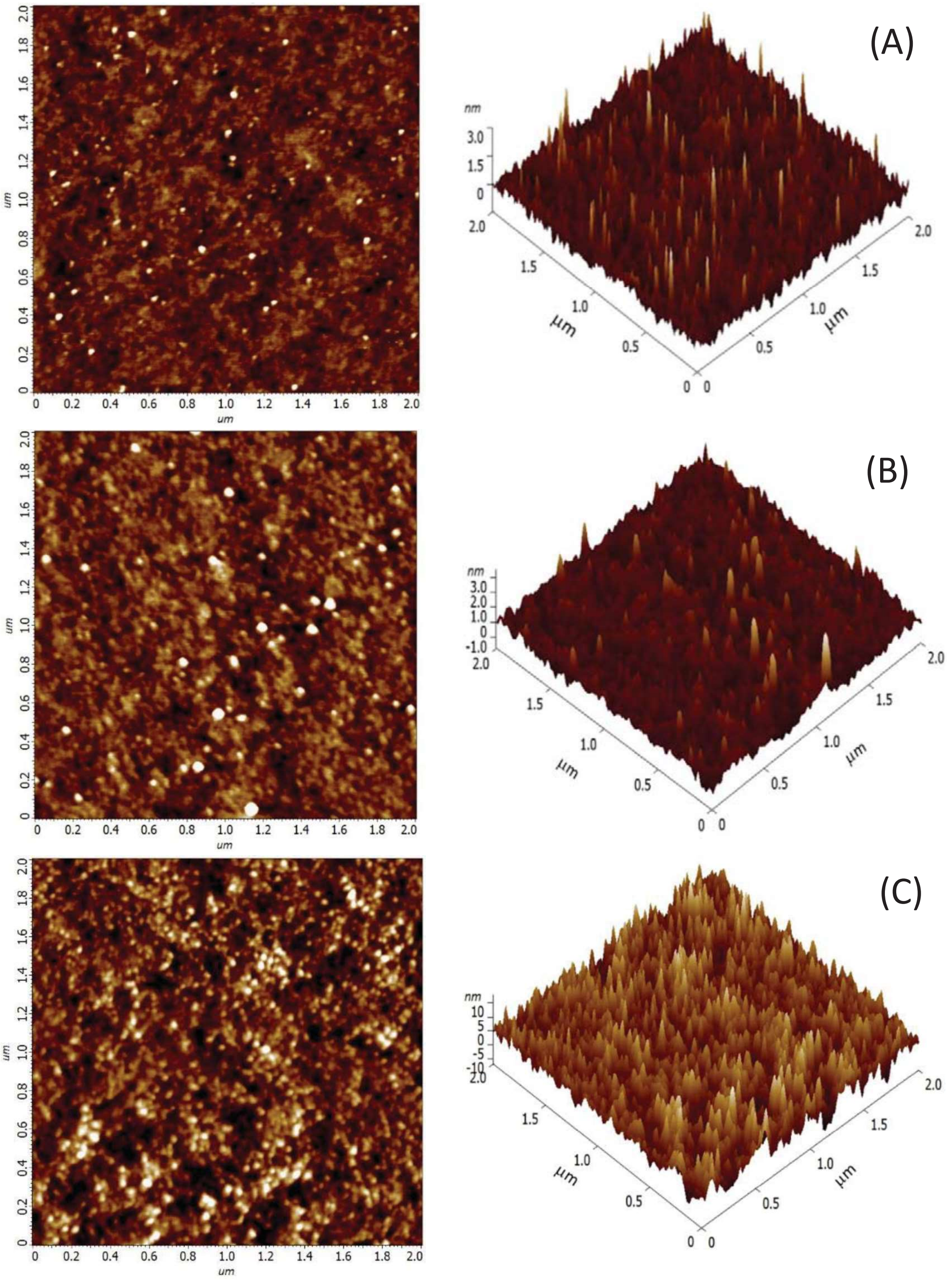

Figure 5.18: 2D and 3D AFM images of (a) SPP/TiO_2-2.5 (b) SPP/TiO_2-5 and (c) SPP/TiO_2-10 membranes.

Table 5.9: Surface roughness parameters of SPEEK-PEG cross-linked and SPEEK-PEG/TiO_2 nanocomposite membranes with three different weight percentage of TiO_2 (2.5%, 5% and 10%) obtained from 2 µm × 2 µm AFM images.

Sample Name	R_q (nm)	R_a (nm)	R_{max} (nm)
SPP	0.204	0.163	1.184
SPP/ TiO_2-2.5	0.345	0.260	3.029
SPP/TiO_2-5	0.352	0.263	3.568
SPP/TiO_2-10	2.880	2.251	13.085

5.6.3.3 *Water uptake and Proton conductivity analysis of SPP/TiO_2 nanocomposite membranes*

The water uptake and proton conductivity of SPP and SPP/TiO_2 nanocomposite membranes with different TiO_2 weight percentage were investigated as a function of temperature and shown in Figure 5.19 (a) and (b).

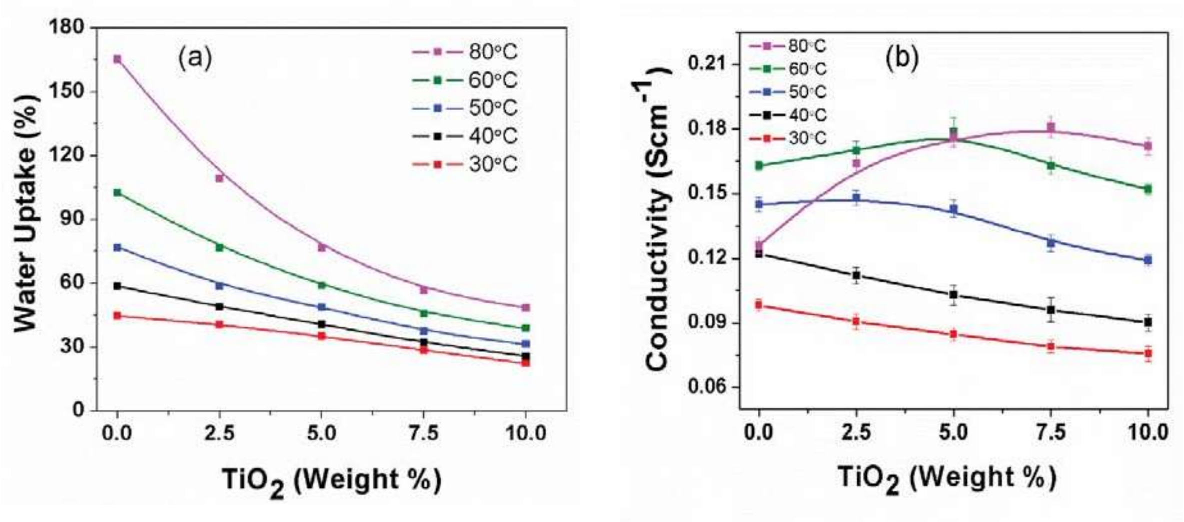

Figure 5.19: Variation of (a) water uptake and (b) conductivity as a function of TiO_2 weight percentage in the membranes at various temperatures.

Figure 5.19 (a), shows the water uptake of the SPP and SPP/TiO_2 nanocomposite membranes as a function of TiO_2 content at various temperatures (30 °C, 40 °C, 50 °C, 60 °C and 80 °C). With increasing temperature, the water uptake of SPP and SPP/ TiO_2 membranes increased due to the thermal relaxation of the polymer chains. The water uptake of the nanocomposite membranes containing TiO_2 nanoparticles is controlled by SPP/ TiO_2 cross-linked network structure which is hinder the chain mobility and narrow down the average distance between polymer chains that reduces the free volume capable of holding water molecules, resulting in a decrease in water uptake. As shown in Figure 5.19 (a) the water uptake of SPP/TiO_2 nanocomposite membranes is lower than the pristine SPP membrane and it exhibited a decreasing tendency with an increase in TiO_2 content. This can be explained by the fact that, TiO_2 loading, the reduction in IEC and free volume becomes the primary affecting factor in the water uptake. It is also noted that the water uptake by the membranes increases gradually by increasing the equilibrating temperature, due to the increase in polymer chain movement with temperature which facilitates the increase in free volume. Similar trends were reported in SPEEK/TiO_2 nanocomposite membranes with SPEEK of 57% DS, in literature. where water uptake decreased with increasing in the titania content in the membrane.[166]

The proton conductivity of the membrane has been measured in fully hydrated condition at various temperature (30 °C, 40 °C, 50 °C, 60 °C and 80 °C) and shown in Figure 5.19 (b). On increasing the temperature, the conductivity of all the membranes increases up to 60 °C because of the thermal movement of H^+ and increase in water uptake increases the H^+ mobility in the membrane. Whereas, at 80 °C some of the membranes show lower conductivity than 60 °C mainly because of the large water uptake or H^+ dilution, it is evident from Figure 5.20. Water molecules per unit functional group (λ) for the nanocomposite membranes are calculated by using Eq. 1.29.

As seen in Figure 5.20, the number of water molecules per unit sulfonic group (λ) in SPP membrane is increases from 13.7 to 31.5 on increasing the equilibration temperature of membrane in water from 30 °C to 60 °C which increases the H^+ mobility within the membrane. Whereas, at 80 °C, the λ value is increased to 50.7 which reduced the H^+ concentration and the conductivity goes down. Similarly, the composite membranes containing 2.5 weight percentage of TiO_2 (SPP/TiO_2-2.5), the λ value increased from 12.7 to 24.1 on increasing the temperature from 30 °C to 60 °C that facilitate the H^+ mobility and conductivity increased. However, at 80 °C the conductivity is lower than 60 °C, that mainly because of the high λ value i.e. 34.3. In the case of 5 weight percentage TiO_2 composite membrane (SPP/TiO_2-5), the conductivity at 60°C and 80 °C are almost equal and that because of the two reasons; (i) the increase in temperature increases the H^+ mobility (ii) The λ value increased to 24.5 which diluted the H^+ concentration. The increase in H^+ thermal mobility should increase the conductivity but simultaneously the dilution effect decreased the conductivity and therefore this membrane shows almost similar conductivity at 80 °C than 60 °C. The membranes that contain 7.5% and 10% TiO_2, showed the conductivity increased from 30°C to 80 °C and that due to the increase in thermal movement of H^+ and increase in λ value which also facilitate the H^+ mobility. The λ value for SPP/TiO_2-7.5 membrane is increased from 9.2 to 18.2 and for SPP/TiO_2-10 membrane it is increased from 7.3 to 15.8. Here it is noticeable that, at 80°C, the SPP/TiO_2-7.5 nanocomposite membrane has the highest conductivity among all, that may be due to the two possible reasons (i) In lower titania weight percentage (□ 7.5%) imbedded samples the water uptake is high the dilutes the H^+ concentration and decreased the conductivity (ii) at higher weight percentage lower IEC value and TiO_2 network structure formation which lower the H^+ movement and conductivity.

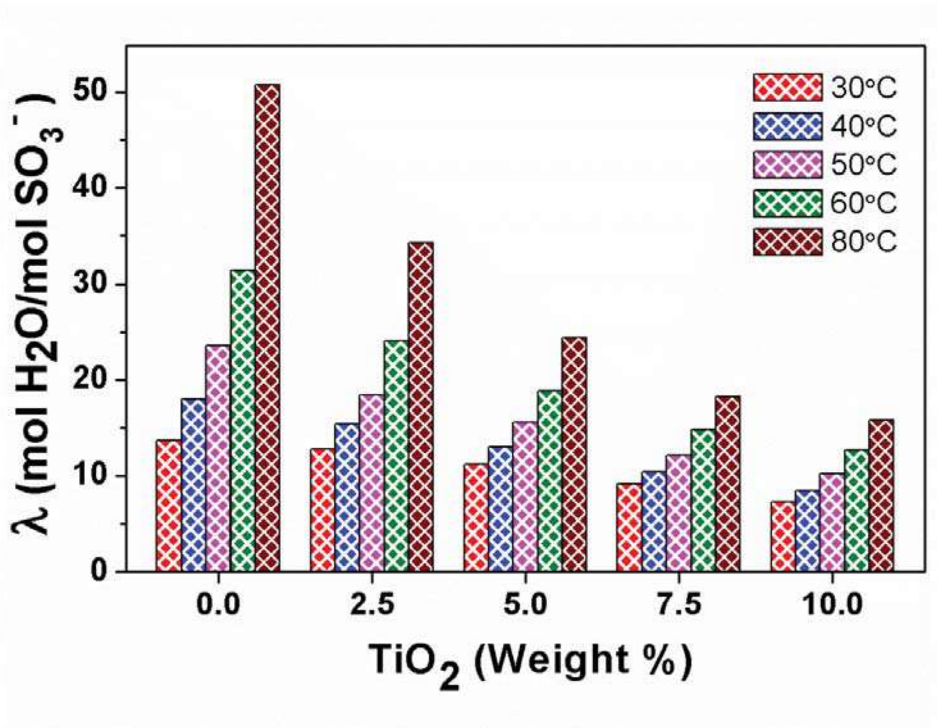

Figure 5.20: Variation of water molecules per unit functional group as a function of TiO_2 weight percentage in the membranes at various temperatures.

Structural characterization of SPP/TiO_2 nanocomposite membranes

The ATR-FTIR spectra of SPEEK, cross-linked SPP and composite cross-linked SPP/TiO_2 with two different weight percentage of TiO_2, 5% and 10% (SPP/TiO_2-5 and SPP/TiO_2-10) membranes are shown in Figure 5.21. The sulfonation of PEEK was confirmed by the two characteristic peaks of -SO_3H groups at 1020 and 1079 cm^{-1}, which are assigned to the symmetric and asymmetric stretching vibration modes of O=S=O, respectively.[127] A broad peak in the range of 3200–3700 cm^{-1} appeared in the spectra of all the samples due to the O-H stretching vibration in the hydration water and O-H groups belonging to the sulfonic acid (–SO_3H) functional group into the polymer matrix, PEG and Ti–OH. The presence of PEG is observed in particular SPP and SPP/TiO_2 membranes at 2950-3100 cm^{-1} due to the C–H symmetric stretching vibration bands which is absent in the spectra of SPEEK. The bands in the range 1500–1400 $cm^{−1}$ are due to CH, CH_2, and CH_3 bending vibration and those in 1300–

1200 cm^{-1} correspond to vibration of the methoxy group O-CH$_3$ and the alcohol group C-OH.[252]

In the composite membranes spectrum all the typical bands of the titania sol-gel materials are present. The characteristic signal for TiO$_2$ nanoparticles due to the vibration of Ti-O-Ti bond is observed around 450 cm^{-1}.[253] A change in the shape of the peak at 1020 cm^{-1} in the composite membranes is observed which may be due to the hydrogen bonds between the sulfonic acid (–SO$_3$H) and Ti–OH group. the peak at 580 cm^{-1} shows stretching vibration of Ti-O and peaks at 1400 cm^{-1} shows stretching vibrations of Ti-O-Ti which may overlap with the CH$_2$ bending vibration. All other FTIR band assignments are same as given in Table 5.4.

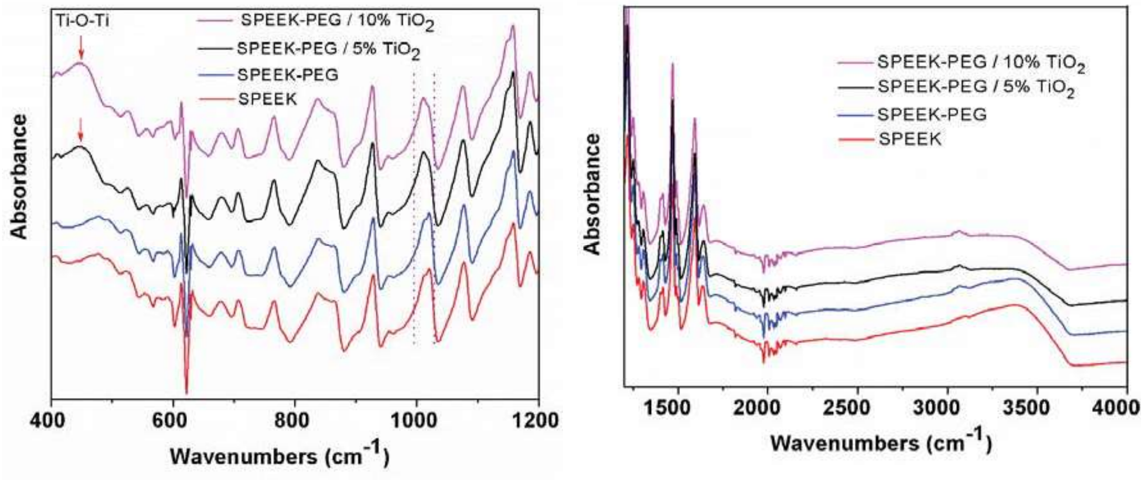

Figure 5.21: ATR-FTIR spectra of SPEEK, SPP and SPP/TiO$_2$ (5% and 10%) membranes.

Mechanical Properties of the SPP/TiO$_2$ membranes

The mechanical properties of the membrane are another important parameter for fuel cell application which depends on many factors like water uptake, microstructure, temperature, preconditioning etc. The stress-strain curve of all the membranes are plotted in Figure 5.22 (a). The membranes first undergo reversible elastic deformation under applied stress, as shown in the initial linear part of the stress–strain curves. Subsequently, membranes persist irreversible inelastic deformation with the increased applied stress, as shown in the curvature portion of the curves. Finally, membranes reached their fracture strength, resulting in breakage. All the samples display a sharp yield point followed by neck formation with the variation in yield stress and the yield stress increases with increasing the TiO_2 content in the membranes. The stress-strain curves shows that the membranes brittleness increases on increasing the TiO_2 percentage in the membrane.

In practical operation, inelastic deformation caused by excessive stress leads to the fatigue damage of the membranes, resulting in membrane failure. For better comparison, the mechanical properties e.g. Young's modulus, tensile strength and percent elongation at break were extracted from stress-strain curves and investigated specifically. The curves monotonically shifted upward to indicate increasing tensile strength, and elongation-to-break decreases in this order.

Young's Modulus and Tensile Strength

The values of Young's modulus of the SPP and SPP/TiO_2 membranes are shown in Figure 5.22 (b). The Young's modulus of the SPP membrane is the lowest of all the membranes with a value of 325.22 MPa. Incorporation of TiO_2 nanoparticles exhibited an increasing trend of Young's modulus for membranes with increasing TiO_2 contents. The Young's modulus of the membranes SPP/TiO_2-2.5, SPP/TiO_2-5, SPP/TiO_2-7.5 and SPP/TiO_2-10 are 322, 336.75, 382.33, 443.88, 543 MPa respectively, indicating enhanced stiffness of the composite membranes. Similar trends were reported in Nafion/TiO_2 membrane.[254] The tensile strength is a parameter to evaluate the strength of the membrane, it is the maximum stress that a membrane samples can withstand before breaking. As shown in Figure 5.22 (c), tensile strength of the SPP membrane is lowest among the investigated membranes with a value of 16.75 MPa. The tensile strength of the composite membranes increases with increasing the titania percentage in the membrane, i.e. 18.298, 20.9, 26.43 and 29 MPa for SPP/TiO_2-2.5, SPP/TiO_2-5, SPP/TiO_2-7.5 and SPP/TiO_2-10 nanocomposite membranes. The increase in stiffness and strength of the nanocomposite membranes can be explained by the incorporation of TiO_2 and their homogeneous distribution in membrane. On incorporation of TiO_2, there is increase in the formation of hydrogen bond between the OH group of PEG, TiO_2 and -SO_3H, that increases the stiffness and strength of the membranes. Other factor which contributes to increase in stiffness and strength is increase in cross-linking and IPN formation between the organic and inorganic moieties.

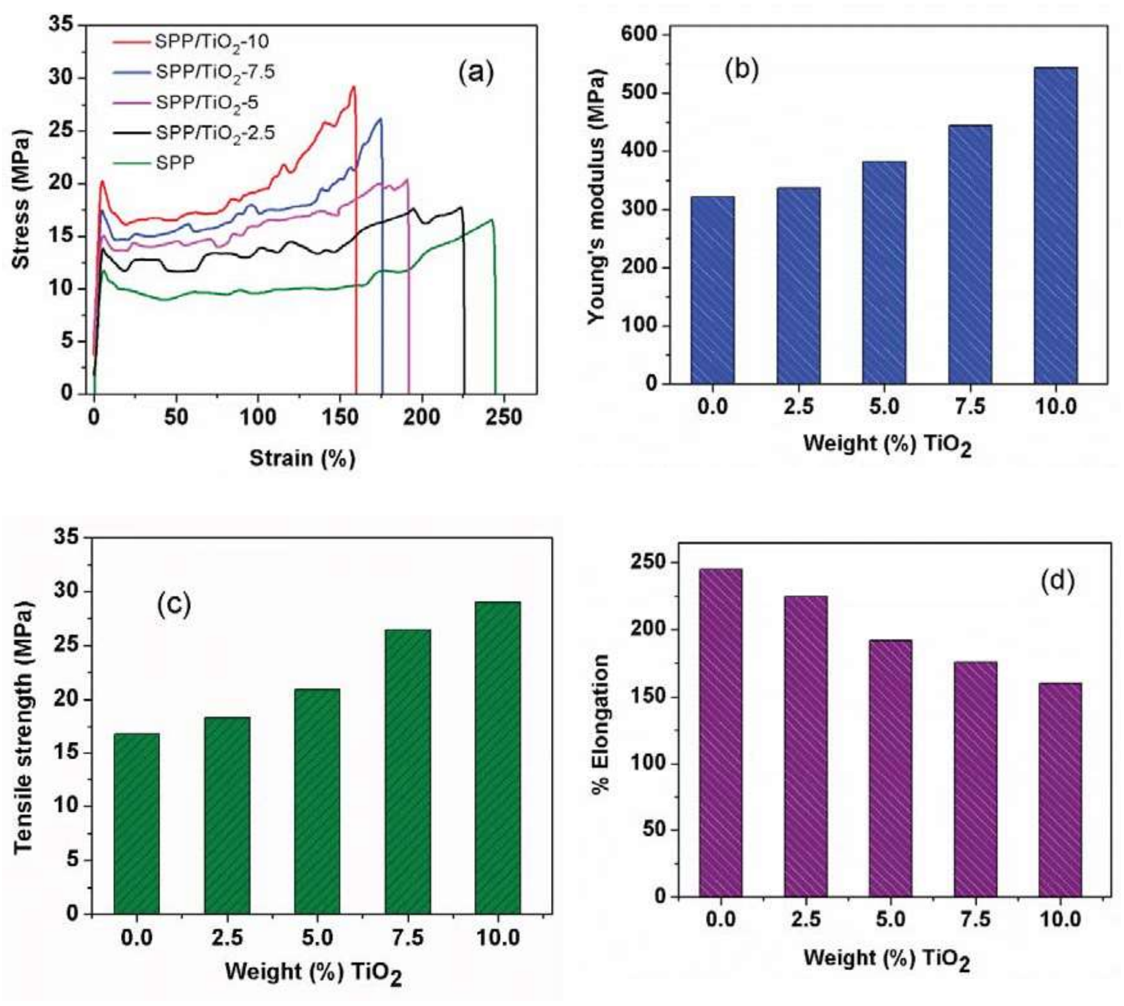

Figure 5.22: stress-strain curve (b) Young's modulus (c) Tensile strength (d) percent elongation of the membranes as a function of TiO_2 weight percentage.

Percent elongation

The percentage elongation at break, corresponding to the maximum elongation of the membrane at fracture compare to the initial length. Which is calculated by the maximum length divided by the original length, gives an information of ductility of membrane. As shown in Figure 5.22 (d), the percentage elongation of the SPP membrane is 245%. The elongation of the SPP/TiO_2 nanocomposite membranes exhibited a decreasing tendency due to the increase of TiO_2 content and reached 159% for the SPP/TiO_2-10 membrane. the decrease in percentage elongation can be explain by two factors; (i) decrease in water uptake on increasing the TiO_2 weight percentage in the membrane which decreases the polymer chain mobility, since water act as plasticizer, (ii) due to increase in cross-linking network of TiO_2 that restricted the movement of the polymer (SPEEK and PEG) chain segments.

□□□□□□*O□idative stability of SPP/TiO_2 membranes*

Oxidative stability of the membranes was evaluated by Fenton test and the results are given in Table 5.10. The results showed marginal degradation at 27°C, however, the degradation increased after treatment at 80°C. This is due to the increased water uptake. As shown in Table 5.10, at 80°C all of the hybrid membranes (SPP/TiO_2) showed higher oxidative stability than the pristine SPP membrane and the oxidative stability gradually increased on increasing of titania content within the membrane. The weight loss in SPP membrane is 28.9% whereas the SPP/TiO_2-10 membrane shows the weight reduction by 8.2%. The increase in the oxidative stability could be due to the following two reasons. Firstly, on increasing the TiO_2 percentage within the membranes, there is increase in the cross-linkable sites with IPN structure formation that reduces the water uptake at higher temperature. As the network structure formation increased, the packing density of polymer chains is also increased (reducing the free volume available for penetration of $HO^\bullet$ and $HO_2^\bullet$ radicals), which reduces the free radical attack on the polymer chain and increases the oxidative stability. Secondly, it may be due to the reinforcement effect of cross-linkage, as a polymer chain is attacked by a free radical, the dissociated molecular chain can be still attached on the polymer network by cross-linking point which increased the complete dissociation time of polymer chain under the radical attack and membrane durability.

Table 5.10: Membrane weight loss (%) after treatment in Fenton reagent at 27°C for 48 hrs and at 80°C for 1 hr.

Sample Name	% weight loss at 27 °C for 48 hrs	% weight loss at 80 °C for 1 hr
SPP	0.98	28.9
SPP/TiO_2-2.5	0.73	18.6
SPP/TiO_2-5	0.62	15.1
SPP/TiO_2-7.5	0.46	10.9
SPP/TiO_2-10	0.35	8.2

□□□□□□ *Thermal stability of SPP/TiO_2 membranes*

Thermal stability of membranes was investigated by thermogravimetric analysis. Figure 5.23 shows the thermal decomposition thermograms of SPEEK, SPP and SPP/TiO_2 nanocomposite membranes with different TiO_2 (2.5%, 5%, 7.5 and 10%) loading. All the samples showed three consecutive weight loss steps; (i) below 200°C, (ii) between 250°C and 400°C and (iii) beyond 450°C.

The initial weight loss occurs below 200 °C is associated with the loss of free and bound water within the membrane. The second step, weight loss occurs between 250-400 °C which was due to the decomposition of sulfonic acid groups and PEG and in the third step, weight loss above 450 °C, which corresponds to the decomposition of the polymer main chain. Again, from the Figure 5.23 it is observed that third weight loss temperature which was started at around 480 °C for pristine SPP membrane shifted slightly towards higher temperature 500 °C for the nanocomposite SPP/TiO_2 membranes. This may take place due to the formation of TiO_2 network. In the case of the nanocomposite membranes, the weight remaining after the polymer decomposition depended on the content of the inorganic component. That is, the weight residues of the hybrid membranes containing titania at T = 800˚C were higher than that of pristine SPP membrane. These results indicated that cross-linked titania frameworks in the hybrid membrane enhanced the thermal stability of the nanocomposite membranes. The TGA results revealed that all the membranes had fairly good thermal stability, where the onset of thermal decomposition of sulfonated moieties 250 °C occurred well above the low and medium temperature PEM fuel cell application.

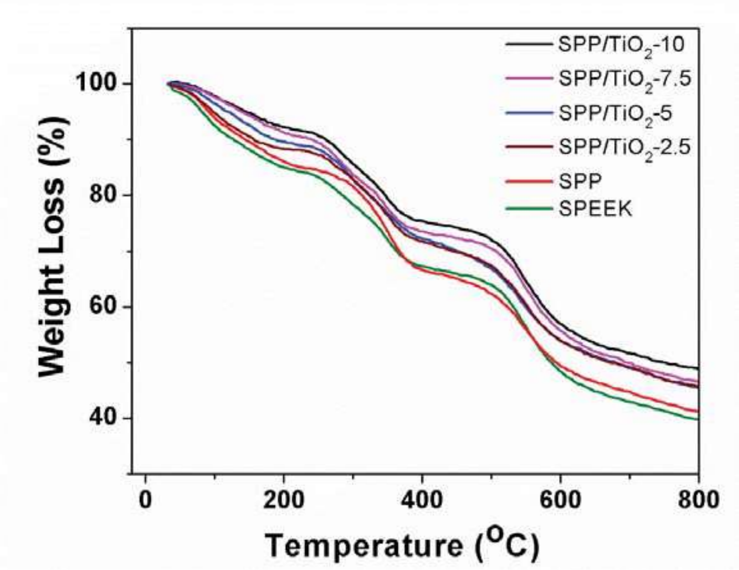

Figure 5.23: Thermo gravimetric traces of SPEEK, SPP and SPP/TiO_2 nanocomposite membranes.

□□□□□□SP□□□P□□/TiO_2 nanocomposite membrane performance evaluation in P□□ □□

As seen from the above discussions, the membrane properties are greatly affected by TiO_2 percentage in the membrane e.g. conductivity, water uptake, mechanical strength, thermal and oxidative stability etc. The membrane containing 5 wt% TiO_2 showed the highest conductivity at 60 °C among all the nanocomposite membranes. In order to understand the effect of TiO_2 addition on the membrane performance in fuel cell, MEA was prepared by using SPP/TiO_2-5 nanocomposite membrane and compared with SPP (the fuel cell performance of SPP membrane given in section 5.6.2.8). The MEA performance tests were carried out from 30 °C to 60 °C and the polarization and power density curves as a function of current density are plotted in Figure 5.24. The maximum power density, voltage and current density of SPP/TiO_2 membrane at various temperatures is given in Table 5.11 and the maximum power density, voltage and current density of SPP membrane is same as given in Table 5.6. At all temperatures, it was observed that the higher performance results for the MEA prepared by using SPP/TiO_2-5 membrane compare to SPP. At 60 °C the SPP membrane gives the maximum power density of 184 mW cm^{-2} at 460 mA cm^{-2} and at 0.4 V which is enhanced to 392.78 mW cm^{-2} at 820 mA cm^{-2} and at 0.479 V for SPP/TiO_2-5 membrane i.e. the maximum power density due to the addition of 5 wt% of TiO_2 was enhance to more than twofold higher.

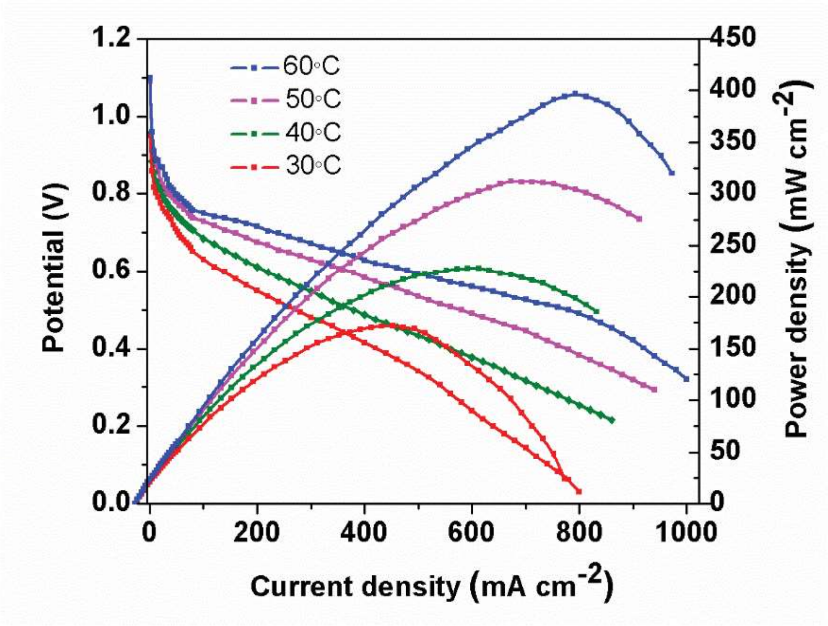

Figure 5.24: Fuel cell performance of SPP/TiO_2-5 nanocomposite membrane at various temperatures.

Table 5.11: The maximum power density, current density and voltage at 60°C of SPP/TiO_2 nanocomposite membrane.

Temperature (°C)	**Current density (mA cm^{-2})**	**Voltage (V)**	**Power density (mW cm^{-2})**
30°C	500	0.341	170.5
40°C	640	0.359	229.76
50°C	700	0.446	312.2
60°C	820	0.479	392.78

The durability studies of the membrane in the fuel cell were carried out by measurement of OCV during the 200 cycles. for both the membranes (SPP and SPP/TiO_2-5) at 60 °C and each cycle was performed after half an hour interval. The OCV profile of both the membranes as a function of number of cycles is plotted in Figure 5.25. The OCV for both the membranes increased during the first 50 cycles attributed to the activation of the MEA assembly, thereafter the OCV remained constant up to 200 cycles.

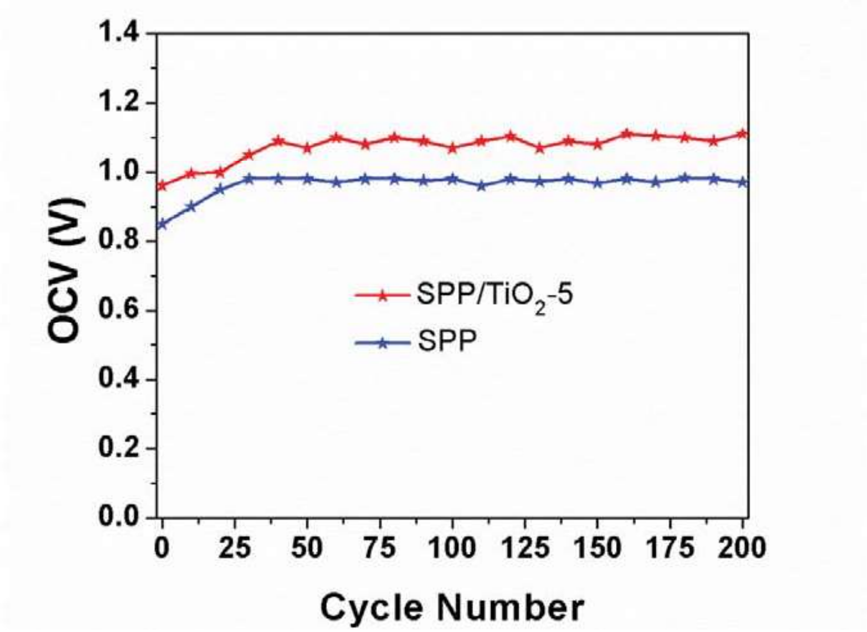

Figure 5.25: Change in OCV with number of cycles for SPP/TiO_2-5 and SPP membranes performed in H_2/O_2 fuel cell.

5.6.4 Results and discussion of SPEEK-PEG/ZrO_2 (SPP/ZrO_2) nanocomposite membranes:

The details of SPP/ZrO_2 nanocomposite membranes are given in Table 5.12. All the membranes thickness were measured after equilibrating in water for 48 hrs at room temperature.

5.6.4.1 Ion exchange capacity of SPP/ZrO_2 membranes

The IEC value of SPP and SPP/ZrO_2 nanocomposite membranes are given in Table 5.12. It can be seen in Table 5.12 that, the IEC values of membranes decreased with the increasing of ZrO_2 content, and were in the range of 1.81-1.70 meq g^{-1}. The reduction of IEC may be attributed to the two possible reasons; (i) dilution effect of the PEG and ZrO_2; since the same DS of SPEEK matrix was used here to prepare all the membranes, therefore, the sulfonic acid contents were same in all the nanocomposite membranes and on addition of PEG and ZrO_2 there is decrease in sulfonic acid group per unit weight of membrane. (ii) interaction between sulfonic and hydroxyl groups of PEG and ZrO_2 in the membrane.

Table 5.12: Details of the SPP/ZrO_2 prepared samples.

Sample designation	**SPP/ZrO_2 (W/W)**	**Thickness (□m)**	**IEC meq g^{-1}**
SPP	100/0	180±10	1.81
SPP/ZrO_2-2.5	97.5/2.5	190±10	1.77
SPP/ZrO_2-5	95/5	190±10	1.74
SPP/ZrO_2-7.5	92.5/7.5	200±10	1.72
SPP/ZrO_2-10	90/10	200±10	1.70

5.6.4.2 Morphological study of SPP/ZrO_2 membranes

Figure 5.26 (A), (B) and (C), shows the FE-SEM image of SPP/ZrO_2-2.5, SPP-ZrO_2-5 and SPP-ZrO_2-10 membranes. ZrO_2 particles identified as bright dots were observed in the Zr-mapping image shown in Figure 5.26 (a), (b) and (c). It is observed from Figure 5.26 (A), (B) and (C), that the ZrO_2 nanoparticles are evenly distributed throughout the membranes for every polymer/ZrO_2 ratio. It is also observed from Figure 5.26 (A), the *in-situ* grown ZrO_2 nanoparticles with average size is lower than 25 nm, are isolated from each other at low weight percentage of ZrO_2 (2.5%). Whereas, upon the addition of 5% ZrO_2, there is increase in the number of ZrO_2 particles and the average size of the zirconia nanoparticles is increased to 40 nm, shown in Figure 5.26 (B). On further addition (10%), the ZrO_2 particles size increased and they start agglomerating as shown in Figure 5.26 (C). These figures demonstrate various facts: first, the PEG prevents nanoparticles aggregation. Second, the synthesized nanoparticles are evenly distribution and the third is, at higher weight percentage of ZrO_2 (5 and 10%) the nanoparticles are well connected and form network like structure, which is responsible for its good form stability, mechanical strength and chemical stability that will be discussed in the coming sections.

The EDX elemental mapping of sulfur and oxygen along with zirconium is given in Figure 5.27. The mapping spectra of zirconium confirms that ZrO_2 nanoparticles are homogeneously distributed within the nanocomposite membranes. Here, it is clearly observed that the increase in the zirconium density in the membranes on increasing the ZrO_2 weight percentage in the membrane samples (Figure 5.27 B to D). Whereas, the other elements (C and S) spectra are not showing significant difference because of their high percentage within the membranes.

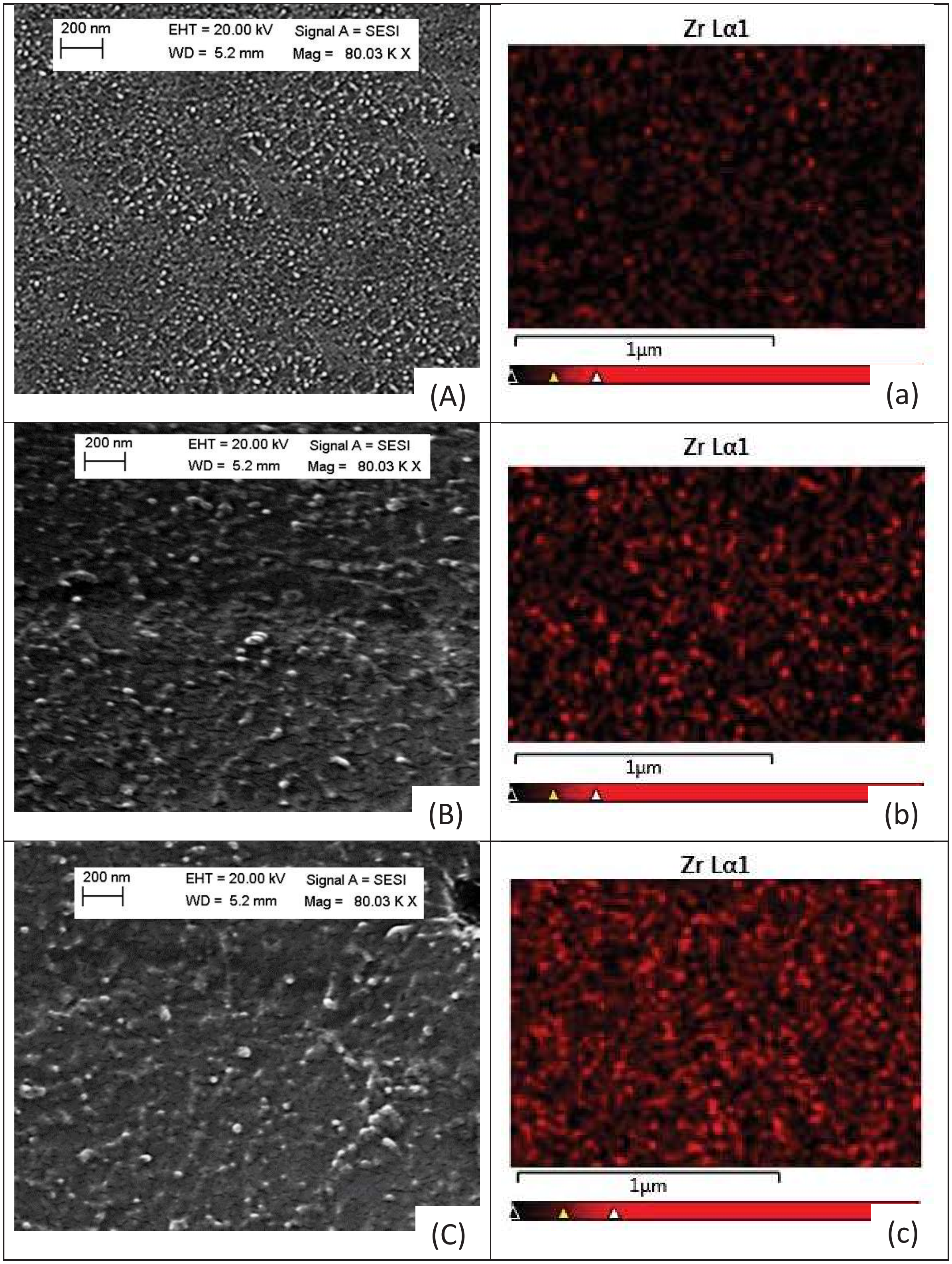

Figure 5.26: FE-SEM images of (A) SPP/ZrO_2-2.5 and (B) SPP/ZrO_2-5 (C) SPP/ZrO_2-10 and EDX images of (a) SPP/ZrO_2-2.5 and (b) SPP/ZrO_2-5 (c) SPP/ZrO_2-10.

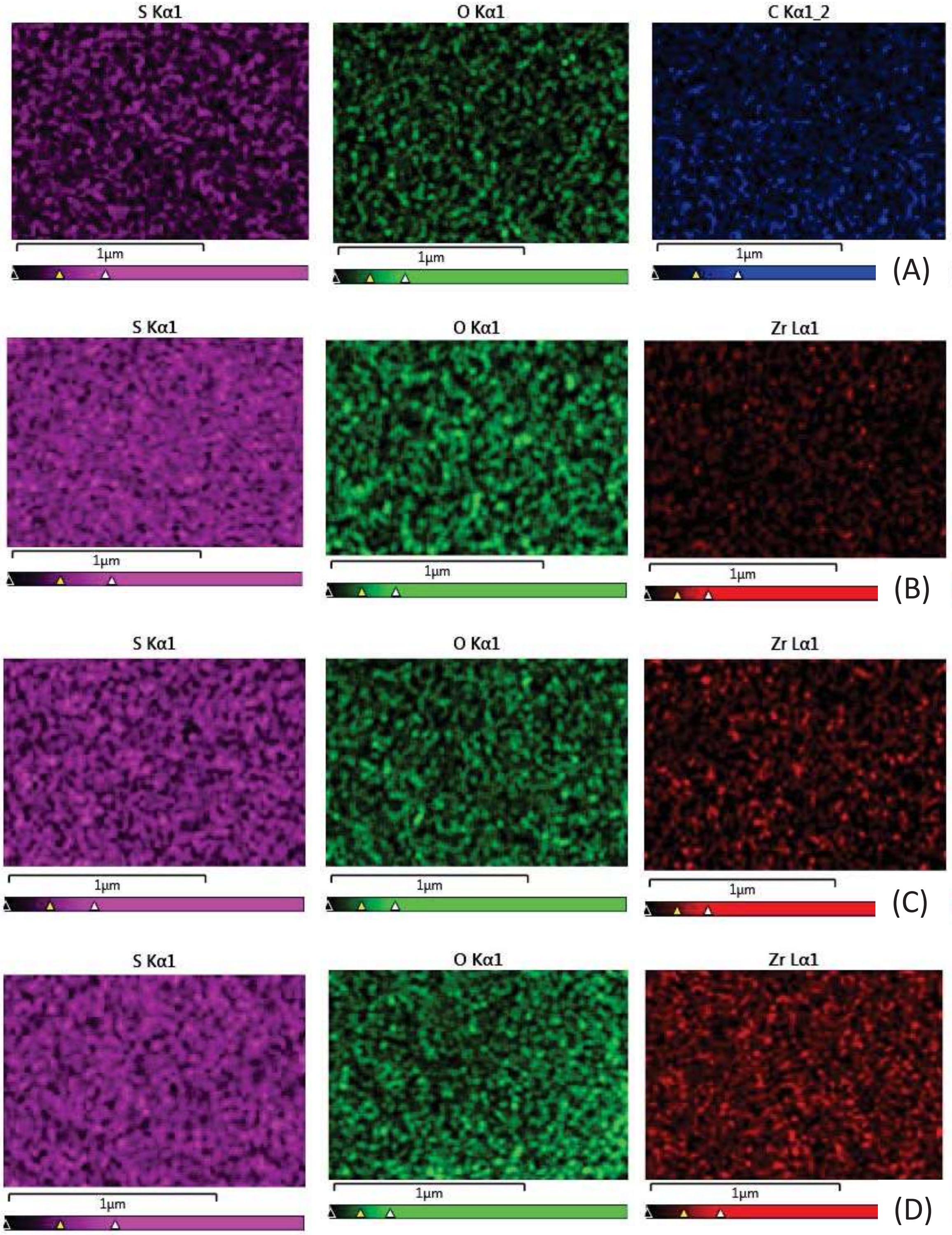

Figure 5.27: EDX elemental mapping spectra of (A) SPP (B) SPP/ZrO_2-2.5 (C) SPP/ZrO_2-5 and (D) SPP/ZrO_2-10 membranes.

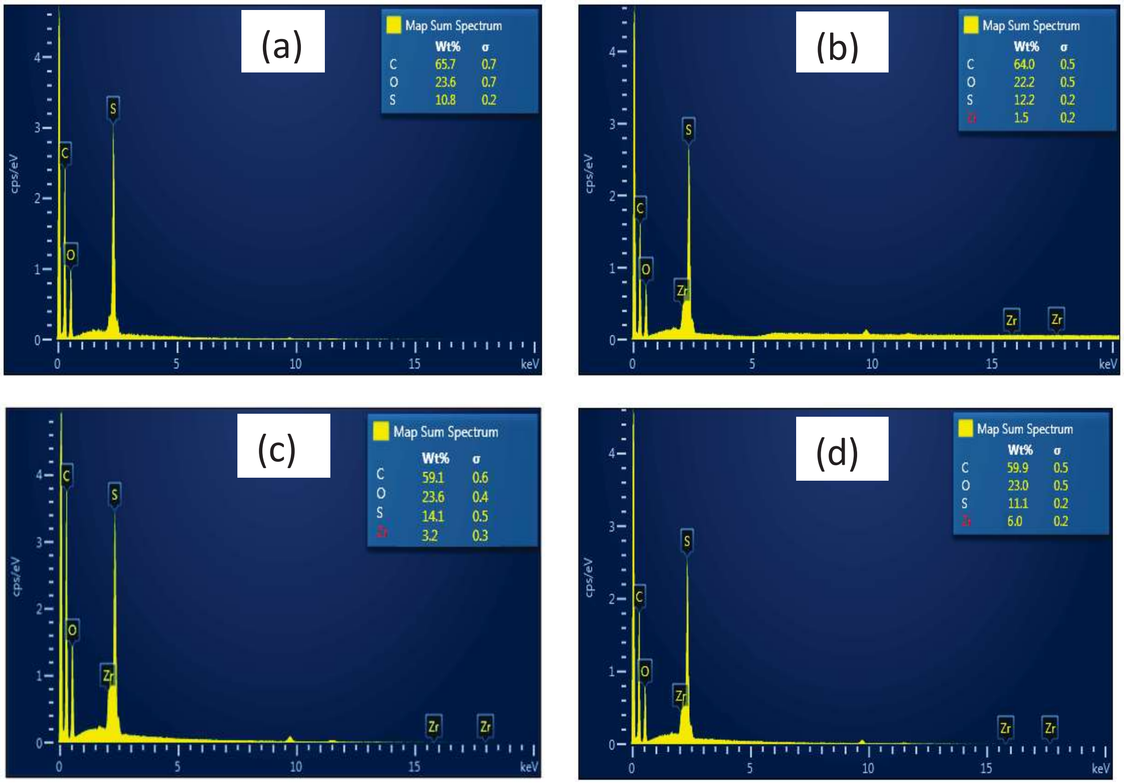

Figure 5.28: EDX spectra of (a) SPP (b) SPP/ZrO_2-2.5 (c) SPP/ZrO_2-5 and (d) SPP/ZrO_2-10 membranes.

The EDX spectra of three different nanocomposite membranes (SPP/ZrO_2-2.5, SPP/ZrO_2-5 and SPP/ZrO_2-10) along with SPP membrane are shown in Figure 5.28. It is seen that, the zirconium peak intensity increases in the membrane samples according to the zirconia precursor used for the nanoparticles synthesis. The weight percentage of the zirconium nanoparticles within the membranes (SPP/ZrO_2-2.5, SPP/ZrO_2-5 and SPP/ZrO_2-10) was obtained from the EDX spectra of the membranes and given in Table 5.13. The calculated weight percentage of zirconium and ZrO_2 by assuming the complete conversion of $Zr(OBu)_4$ precursor to ZrO_2 are also given in the Table 5.13. Here, it is clear seen that the zirconium weight percentage obtained from the EDX spectra approximately similar to the calculated zirconium weight percentage. This shows the approximately complete conversion of precursor to ZrO_2 .The difference between the calculated weight percentages of titanium and obtained from EDX spectra is increases from lower to higher weight percentage, this may be due the some amount of precursor lost during the synthesis process.

Table 5.13: Zirconium weight percentage in SPP/ZrO_2 nanocomposite membranes.

Sample name	**ZrO_2 (wt %) Calculated**	**Zr (wt %) Calculated**	**Zr (wt %) EDX spectra**
SPP/TiO_2-2.5	2.5	1.85	1.5
SPP/TiO_2-5	5	3.7	3.2
SPP/TiO_2-10	10	7.4	6

The AFM images of SPP/ZrO_2 nanocomposite membranes are given in Figure 5.29. The 2D and 3D AFM images of SPP/ZrO_2-2.5, SPP/ZrO_2-5 and SPP/ZrO_2-10 membranes, shown in Figure 5.29 (A), (B) and (C) supported the FE-SEM images given in Figure 5.26. As shown in Figure 5.29 (A), there are many small dot like particles with diameters of less than 25 nm and cross-sectional heights of about 3 nm. These particles size and density increased on increasing the ZrO_2 weight percentage in the membranes, as shown in Figure 5.29 (B) and (C), those small spherical particles are entangled chains of ZrO_2 molecules. The 3D images showed that the surface roughness of the membranes increases on increasing the ZrO_2 percentage in the membrane. For better comparison of surface variation, the roughness parameters are given in Table 5.14, where R_q, R_a and R_{max} represent the root mean square roughness, average roughness and maximum roughness respectively.

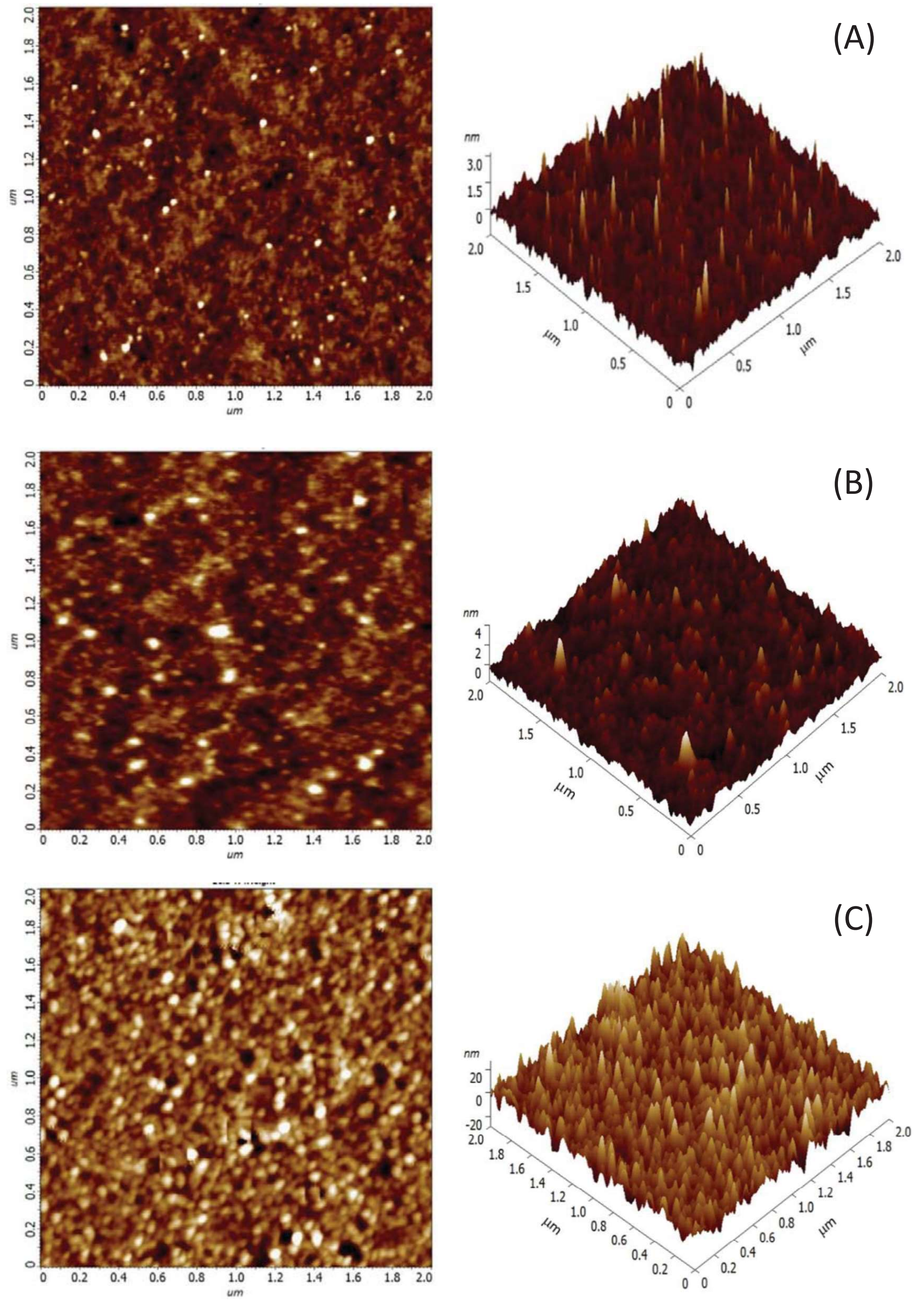

Figure 5.29: 2D and 3D AFM images of (a) SPP/ZrO$_2$-2.5 (b) SPP/ZrO$_2$-5 and (c) SPP/ZrO$_2$-10 membranes.

Table 5.14: Surface roughness parameters of SPEEK-PEG cross-linked and SPEEK-PEG/ZrO_2 nanocomposite membranes with three different weight percentage of ZrO_2 (2.5%, 5% and 10%) obtained from 2 µm × 2 µm AFM images.

Sample Name	**R_q (nm)**	**R_a (nm)**	**R_{max} (nm)**
SPP/ ZrO_2-2.5	0.334	0.249	3.194
SPP/ZrO_2-5	0.477	0.357	4.069
SPP/ZrO_2-10	5.947	4.587	27.643

5.6.4.3 Water uptake and Proton conductivity of SPEEK-PEG/ZrO_2 membranes

The water uptake and proton conductivity of SPP and SPP/ZrO_2 nanocomposite membranes with different ZrO_2 weight percentage were investigated as a function of temperature and shown in Figure 5.30 (a) and (b).

Figure 5.30 (a), shows the water uptake of the SPP and SPP/ZrO_2 nanocomposite membranes as a function of ZrO_2 content at various temperatures (30 °C, 40 °C, 50 °C, 60 °C and 80 °C). With increasing temperature, the water uptake of SPP and SPP/ ZrO_2 membranes increased due to the thermal relaxation of the polymer chains. The water uptake of the nanocomposite membranes containing ZrO_2 nanoparticles is controlled by SPP/ ZrO_2 cross-linked network structure which is hinder the chain mobility and narrow down the average distance between polymer chains that reduces the free volume capable of holding water molecules, resulting in a decrease in water uptake. As shown in Figure 5.30 (a), the water uptake of SPP/ZrO_2 nanocomposite membranes is lower than the pristine SPP membrane and it exhibited a decreasing tendency with an increase in ZrO_2 content. This can be explained by the fact that, ZrO_2 loading, the reduction in IEC and free volume becomes the primary affecting factor in the water uptake. It is also noted that the water uptake by the membranes increases gradually by increasing the equilibrating temperature, due to the increase in polymer chain movement with temperature which facilitates the increase in free volume. Similar trend were reported in SPEEK/ZrO_2 nanocomposite membranes with SPEEK of 87% DS, in literature. Where water uptake decreased with increasing in the zirconia content in the membrane.[159]

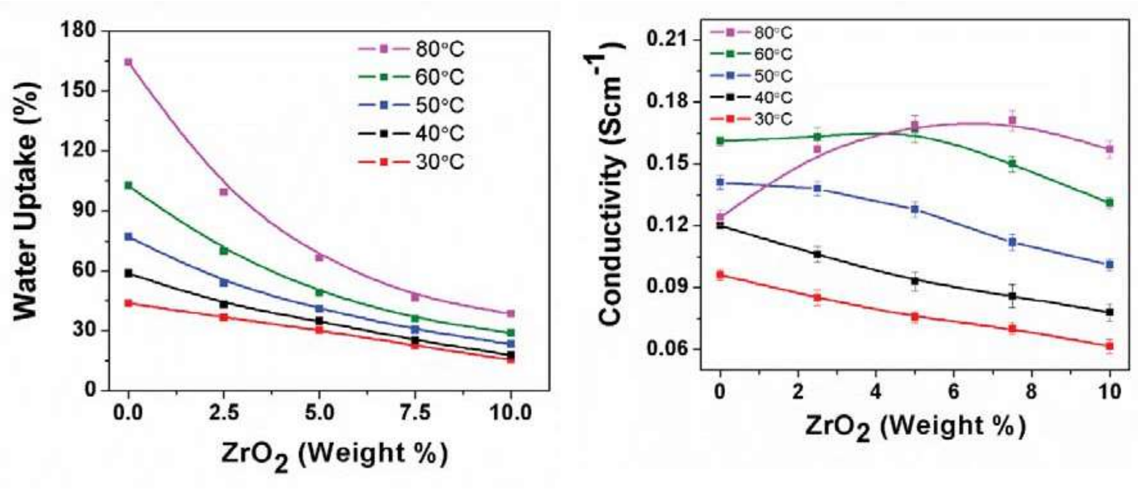

Figure 5.30: Variation of (a) water uptake and (b) conductivity as a function of ZrO_2 weight percentage in the membranes at various temperatures.

The proton conductivity of the membranes have been measured in fully hydrated condition at various temperature (30 °C, 40 °C, 50 °C, 60 °C and 80 °C) and shown in Figure 5.30 (b). On increasing the temperature, the conductivity of all the membranes increases up to 60 °C because of the thermal movement of H^+ and increase in water uptake increases the H^+ mobility in the membrane. Whereas, at 80 °C some of the membranes show lower conductivity than 60 °C mainly because of the large water uptake or H^+ dilution, it is evident from Figure 5.30. Water molecules per unit functional group (□) for the nanocomposite membranes are calculated by using Eq. 1.29.

As seen in Figure 5.31, the number of water molecules per unit sulfonic group (□) in SPP membrane is increases from 13.4 to 31.5 on increasing the equilibration temperature of membrane in water from 30 °C to 60 °C which increases the H^+ mobility within the membrane.

Whereas, at 80 °C, the λ value is increased to 50.4 which reduced the H^+ concentration and the conductivity goes down. Similarly, the composite membranes containing 2.5 weight percentage of ZrO_2 (SPP/ZrO_2-2.5), the λ value increased from 11.5 to 21.8 on increasing the temperature from 30 °C to 60 °C that facilitate the H^+ mobility and conductivity increased. But at 80 °C the conductivity is lower than 60 °C, that mainly because of the high λ value i.e. 31.2. In the case of 5 weight percentage ZrO_2 composite membrane (SPP/ZrO_2-5), the conductivity at 60°C and 80 °C are almost equal (within the error bar) and that because of the two reasons; (i) the increase in temperature increases the H^+ mobility (ii) The λ value increased to 21.2 which diluted the H^+ concentration. The increase in H^+ thermal mobility should increase the conductivity but simultaneously the dilution effect decreased the conductivity and therefore this membrane shows almost similar conductivity at 80 °C and 60 °C.

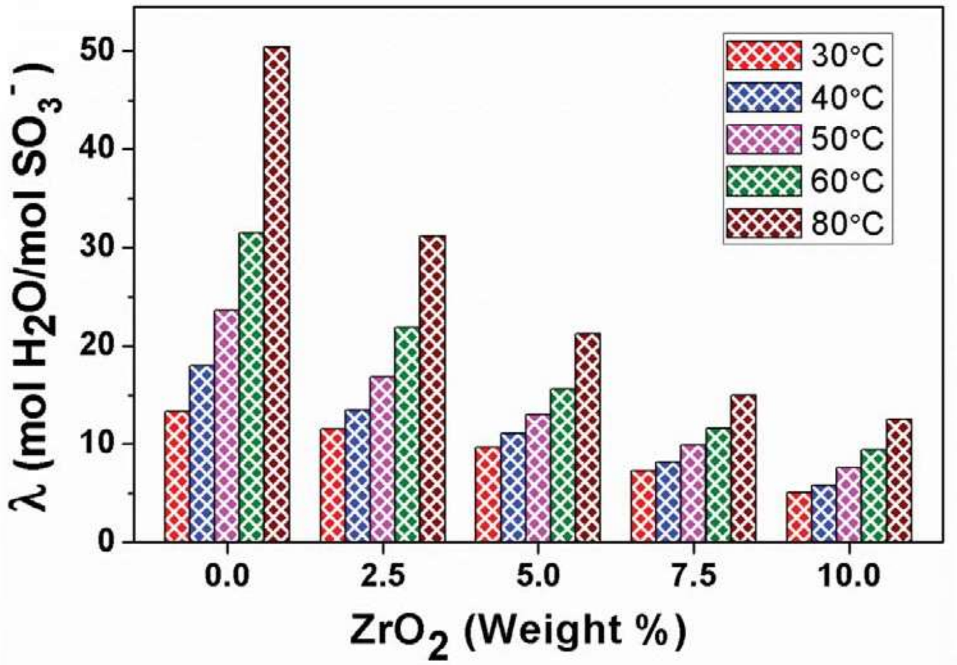

Figure 5.31: Variation of water molecules per unit functional group as a function of ZrO_2 weight percentage in the membranes at various temperatures.

The membranes that contain 7.5% and 10% ZrO_2, showed the conductivity increased from 30°C to 80 °C and that due to the increase in thermal movement of H^+ and increase in □ value which also facilitate the H^+ mobility. The □ value for SPP/ZrO_2-7.5 membrane is increased from 7.3 to 15.1 and for SPP/ZrO_2-10 membrane it is increased from 5.1 to 12.2. Here it is noticeable that, at 80°C, the SPP/ZrO_2-7.5 nanocomposite membrane has the highest conductivity among all, that may be due to the two possible reasons (i) In lower ziconia weight percentage (□ 7.5%) imbedded samples the water uptake is high the dilutes the H^+ concentration and decreased the conductivity (ii) at higher weight percentage lower IEC value and ZrO_2 network structure formation which lower the H^+ movement and conductivity.

5.6.4.4 Structural characterization of SPP/ZrO_2 membranes

The ATR-FTIR spectra of sulfonated polyether ether ketone (SPEEK), cross-linked SPP and composite cross-linked SPP/ZrO_2 with two different weight percentage of ZrO_2, 5% and 10% (SPP/ZrO_2-5,10) membranes are shown in Figure 5.32. The sulfonation of PEEK was confirmed by the two characteristic peaks of -SO_3H groups at 1020 and 1079 cm^{-1}, which are assigned to the symmetric and asymmetric stretching vibration modes of O=S=O, respectively [127]. A broad peak in the range of 3200–3700 cm^{-1} appeared in the spectra of all the samples due to the O-H stretching vibration in the hydration water and O-H groups belonging to the sulfonic acid (–SO_3H) functional group into the polymer matrix, PEG and Zr–OH. The presence of PEG is observed in particular SPP and SPP/ZrO_2 membranes at 2950-3100 cm^{-1} due to the C–H symmetric stretching bands which is absent in the spectra of SPEEK.

In the composite membranes spectrum all the typical bands of the Zirconia sol-gel materials are present. A change in the shape of the peak at 1020 cm^{-1} in the composite membranes is observed which may be due to the interaction between the sulfonic acid (–SO_3H) and Zr–OH group. The peak that appears around 450 cm^{-1} indicates the Zr-O-Zr vibrations.[255]

The peak that appears around 1530.49 – 1520.22 cm^{-1} indicates the Zr-OH bending vibrations,[256] which may overlapped by the peak C □ C stretching vibration. of the Nafion Peaks at 514.28 cm^{-1} and 513.72 cm^{-1} show the Zr-O vibrations, which are overlapped by the transmittance peaks of the Nafion . The peak at 1645 cm^{-1} was due to the carbonyl (C=O) absorption.

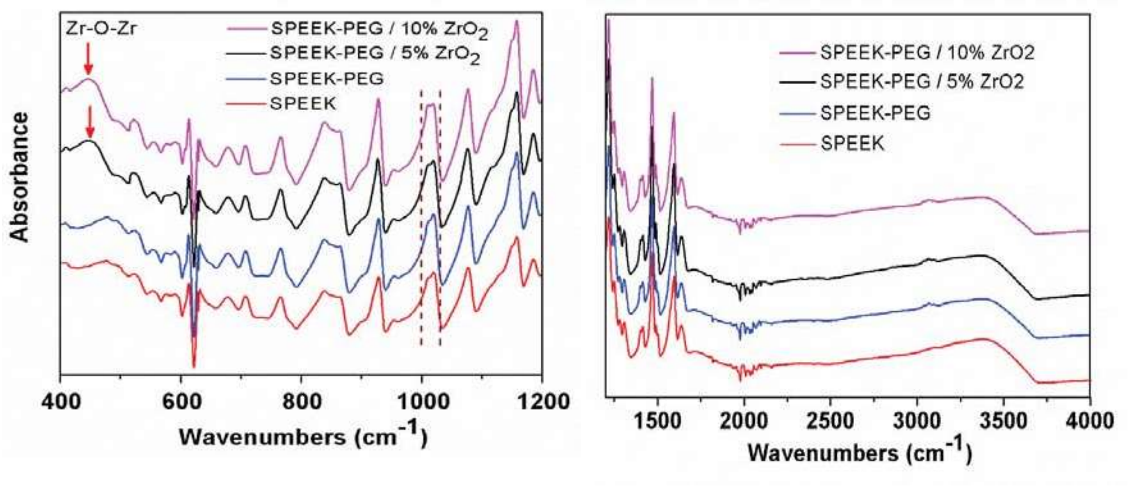

Figure 5.32: ATR-FTIR spectra of SPEEK, SPP and SPP/ZrO_2 (5% and 10%) membranes.

5.6.4.5 Mechanical Properties of SPP/ZrO_2 nanocomposite membranes

The mechanical properties of the membrane are another important parameter for fuel cell application which depends on many factors like water uptake, microstructure, temperature, preconditioning etc. The stress-strain curve of all the membranes is plotted in Figure 5.33(a). The membranes first undergo reversible elastic deformation under applied stress, as shown in the initial linear part of the stress–strain curves. Subsequently, membranes persist irreversible inelastic deformation with the increased applied stress, as shown in the curvature portion of the curves. Finally, membranes reached their fracture strength, resulting in breakage. All the samples display a sharp yield point followed by neck formation with the variation in yield stress and the yield stress increases with increasing the ZrO_2 content in the membranes. The stress-strain curves shows that the membranes brittleness increases on increasing the ZrO_2 percentage in the membrane.

In practical operation, inelastic deformation caused by excessive stress leads to the fatigue damage of the membranes, resulting in membrane failure. For better comparison, the mechanical properties e.g. Young's modulus, tensile strength and percent elongation at break were extracted from stress-strain curves and investigated specifically. The curves monotonically shifted upward to indicate increasing tensile strength, and elongation-to-break decreases in this order.

Young's Modulus and Tensile Strength

Young's modulus provides an information of the stiffness of the material which is a measure of how much it deforms elastically per unit applied stress and calculated from the slope of initial linear portion of the stress-strain curve. The values of Young's modulus of the SPP and SPP/ZrO_2 membranes are shown in Figure 5.33 (b). The Young's modulus of the SPP membrane is the lowest of all the membranes with a value of 322.15 MPa. Incorporation of ZrO_2 nanoparticles exhibited an increasing trend of Young's modulus for membranes with increasing ZrO_2 contents. The Young's modulus of the membranes SPP/ZrO_2-2.5, SPP/ZrO_2-5, SPP/ZrO_2-7.5 and SPP/ZrO_2-10 are 368.75, 400, 472 and 570 MPa respectively, indicating enhanced stiffness of the composite membranes. The tensile strength of all the membranes given in Figure 5.33 (c), tensile strength of the SPP membrane is lowest among the investigated membranes with a value of 16.77 MPa. The tensile strength of the composite membranes increases with increasing the zirconia percentage in the membrane, i.e. 18.98, 21.6, 27 and 31.53 MPa for SPP/ZrO_2-2.5, SPP/ZrO_2-5, SPP/ZrO_2-7.5 and SPP/ZrO_2-10 nanocomposite membranes. The increase in stiffness and strength of the nanocomposite membranes can be explained by the incorporation of ZrO_2 and their homogeneous distribution in membrane. On incorporation of ZrO_2, there is increase in the formation of hydrogen bond between the OH group of PEG, ZrO_2 and -SO_3H, that increases the stiffness and strength of the membranes. Other factor which contributes to increase in stiffness and strength is increase in cross-linking and IPN formation between the organic and inorganic moieties.

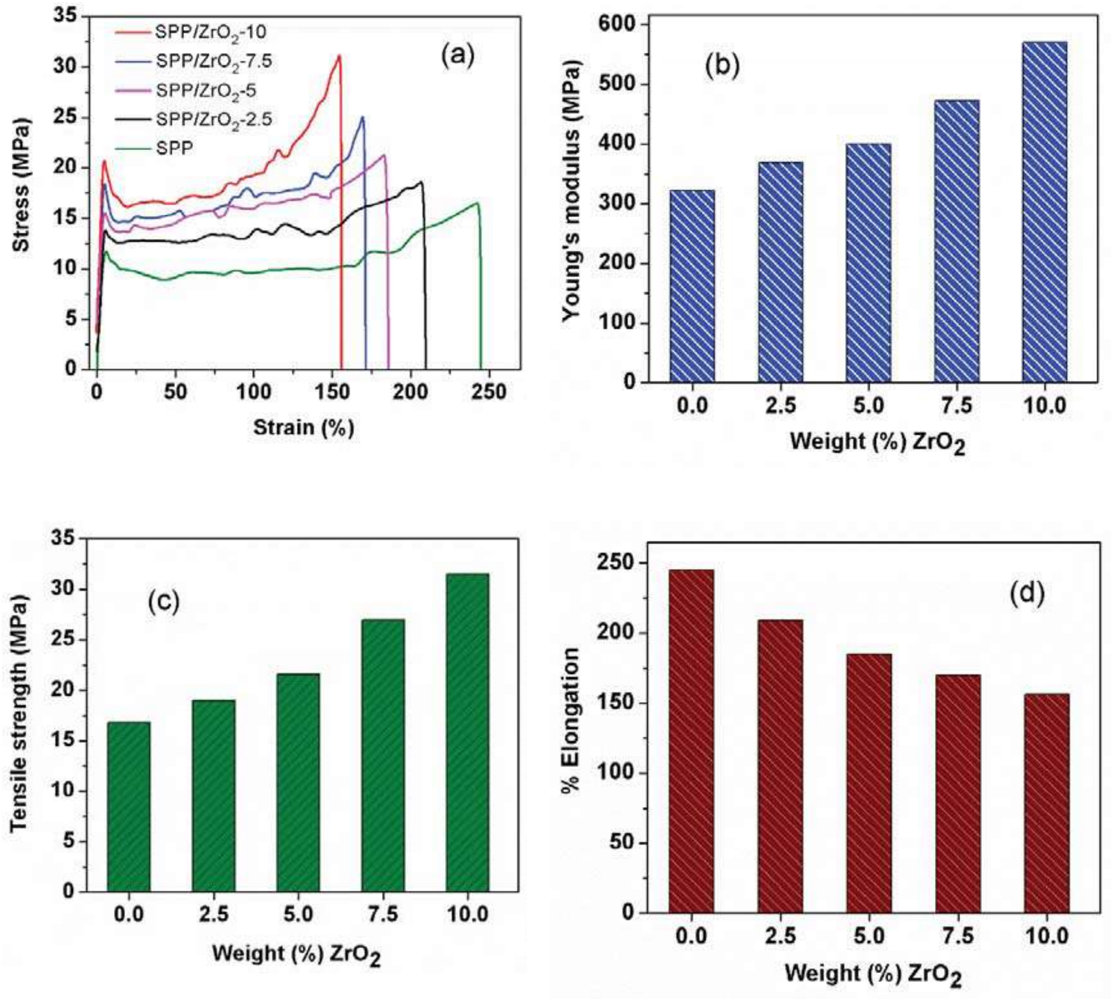

Figure 5.33: Stress-strain curve (b) Young's modulus (c) Tensile strength (d) percent elongation of the membranes as a function of ZrO_2 weight percentage.

Percent elongation

The percentage elongation at break, corresponding to the maximum elongation of the membrane at fracture compare to the initial length. Which is calculated by the maximum length divided by the original length, gives an information of ductility of membrane. As shown in Figure 5.33 (d), the percentage elongation of the SPP membrane is 245%. The elongation of the SPP/ZrO_2 nanocomposite membranes exhibited a decreasing tendency due to the increase of ZrO_2 content and reached 156% for the SPP/ZrO_2-10 membrane. the decrease in percentage elongation can be explain by two factors; (i) decrease in water uptake on increasing the ZrO_2 weight percentage in the membrane which decreases the polymer chain mobility, since water act as plasticizer, (ii) due to increase in cross-linking network of ZrO_2 that restricted the movement of the polymer (SPEEK and PEG) chain segments.

5.6.4.6 Oxidative stability of SPP/ZrO_2 membranes

Oxidative stability of the membranes was evaluated by Fenton test and the results are given in Table 5.15. The results showed marginal degradation at 27°C, however, the degradation increased after treatment at 80°C. This is due to the increased water uptake. As shown in Table 5.15, at 80°C all of the hybrid membranes (SPP/ZrO_2) showed higher oxidative stability than the pristine SPP membrane and the oxidative stability gradually increased on increasing of zirconia content within the membrane. The weight loss in SPP membrane is 28.8% whereas the SPP/ZrO_2-10 membrane shows the weight reduction by 7.8%. The increase in the oxidative stability could be due to the following two reasons. Firstly, on increasing the ZrO_2 percentage within the membranes, there is increase in the cross-linkable sites with IPN structure formation that reduces the water uptake at higher temperature. As the network structure formation increased, the packing density of polymer chains is also increased (reducing the free volume available for penetration of $HO^{\bullet}$ and $HO_2^{\bullet}$ radicals), which reduces the free radical attack on the polymer chain and increases the oxidative stability. Secondly, it may be due to the reinforcement effect of cross-linkage, as a polymer chain is attacked by a free radical, the dissociated molecular chain can be still attached on the polymer network by cross-linking point which increased the complete dissociation time of polymer chain under the radical attack and membrane durability.

Table 5.15: Membrane weight loss (%) after treatment in Fenton reagent at 27°C for 48 hrs and at 80°C for 1 hr.

Sample Name	**% weight loss at 27 °C for 48 hrs**	**% weight loss at 80 °C for 1 hr**
SPP	0.99	28.8
SPP/ZrO_2-2.5	0.78	18.1
SPP/ZrO_2-5	0.61	14.5
SPP/ZrO_2-7.5	0.52	10.5
SPP/ZrO_2-10	0.48	7.8

5.6.4. Thermal stability of SPP/ZrO_2 membranes

Thermal stability of membranes was investigated by thermogravimetric analysis. Figure 5.23 shows the thermal decomposition thermograms of SPEEK, SPP and SPP/ZrO_2 nanocomposite membranes with different ZrO_2 (2.5%, 5%, 7.5 and 10%) loading. All the samples showed three consecutive weight loss steps; (i) below 200°C, (ii) between 250°C and 400°C and (iii) beyond 450°C.

The initial weight loss occurs below 200 °C is associated with the loss of free and bound water within the membrane. The second step, weight loss occurs between 250-400 °C which was due to the decomposition of sulfonic acid groups and PEG and in the third step, weight loss above 450 °C, which corresponds to the decomposition of the polymer main chain. Again, from the Figure 5.23 it is observed that third weight loss temperature which was started at around 480 °C for pristine SPP membrane shifted slightly towards higher temperature 500 °C for the nanocomposite SPP/ZrO_2 membranes. This may take place due to the formation of ZrO_2 network. In the case of the nanocomposite membranes, the weight remaining after the polymer decomposition depended on the content of the inorganic component. That is, the weight residues of the hybrid membranes containing zirconia at T = 800°C were higher than that of pristine SPP membrane. These results indicated that cross-linked zirconia frameworks in the hybrid membrane enhanced the thermal stability of the nanocomposite membranes. The TGA results revealed that all the membranes had fairly good thermal stability, where the onset of thermal decomposition of sulfonated moieties 250 °C occurred well above the low and medium temperature PEM fuel cell application.

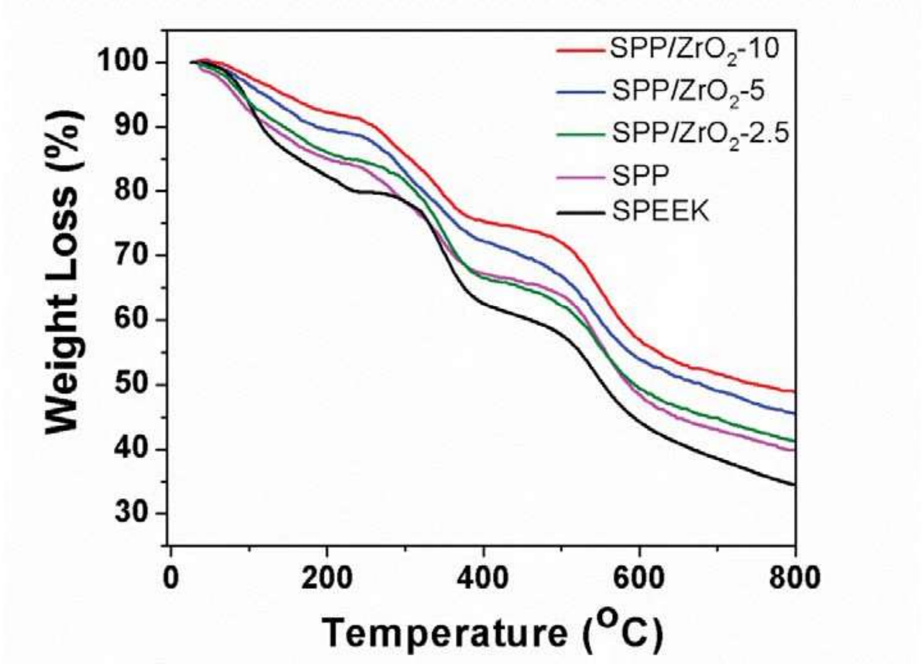

Figure 5.34: Thermo gravimetric traces of SPEEK, SPP and SPP/ZrO_2 nanocomposite membranes.

5.6.4. SPP/ZrO_2 nanocomposite membrane performance study in PEMFC

As seen from the above discussions, the membrane properties are greatly affected by ZrO_2 percentage in the membrane e.g. conductivity, water uptake, mechanical strength, thermal and oxidative stability etc. The membrane containing 5 wt.% ZrO_2 showed the highest conductivity at 60 °C among all the zirconia nanocomposite membranes. In order to understand the effect of ZrO_2 addition on the membrane performance in fuel cell, MEA was prepared by using SPP/ZrO_2-5 nanocomposite membrane and compared with SPP (the fuel cell performance of SPP membrane given in section 5.6.2.8). The MEA performance tests were carried out from 30 °C to 60 °C and the polarization and power density curves as a function of current density are plotted in Figure 5.35.

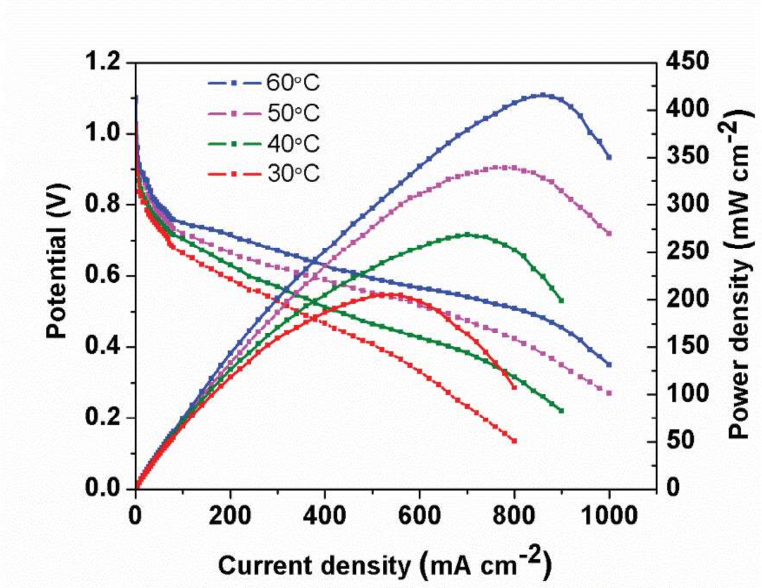

Figure 5.35: Fuel cell performance of SPP/ZrO_2-5 nanocomposite membrane at various temperatures.

The maximum power density, voltage and current density of SPP/ZrO_2 membrane at various temperatures is given in Table 5.16 and the maximum power density, voltage and current density of SPP membrane is same as given in Table 5.6. At all temperatures, it was observed that the higher performance results for the MEA prepared by using SPP/ZrO_2-5 membrane compare to SPP. As seen from Table 5.16 and Table 5.6, at 60 °C the SPP/ZrO_2-5 membrane gives the maximum power density of 425.38 mW cm^{-2} at 850 mA cm^{-2} and at 0.50 V whereas, SPP membrane showed the maximum power density of 184 mW cm^{-2} at 460 mA cm^{-2} and at 0.4 V. The maximum power density is more than two fold higher for SPP/ZrO_2-5 membrane than the pristine SPP membrane i.e. the addition of 5% of ZrO_2 enhanced the membrane performance to a significant extant.

Table 5.16: The maximum power density, current density and voltage at various temperature of SPP/ZrO_2 nanocomposite membrane.

Temperature (°C)	**Potential (V)**	**Current density (mA cm^{-2})**	**Power density (mW cm^{-2})**
30	0.36	560	204.96
40	0.39	700	278.70
50	0.44	760	338.96
60	0.50	850	425.38

The durability studies of the SPP/ZrO_2-5 membrane was measured by measuring the during 200 cycles at 60 °C and compared with the SPP membrane, plotted in Figure 5.36. The OCV for both the membranes increased during the first 50 cycles attributed to the activation of the MEA assembly, thereafter the OCV remained constant up to 200 cycles and there was no significant decrease in OCV for 200 cycles. SPEEK-PEG membrane showed slightly lower values of OCV, i.e., 0.98 V (~0.14V less) than of SPP/ZrO_2-5, which showed OCV of 1.12 V.

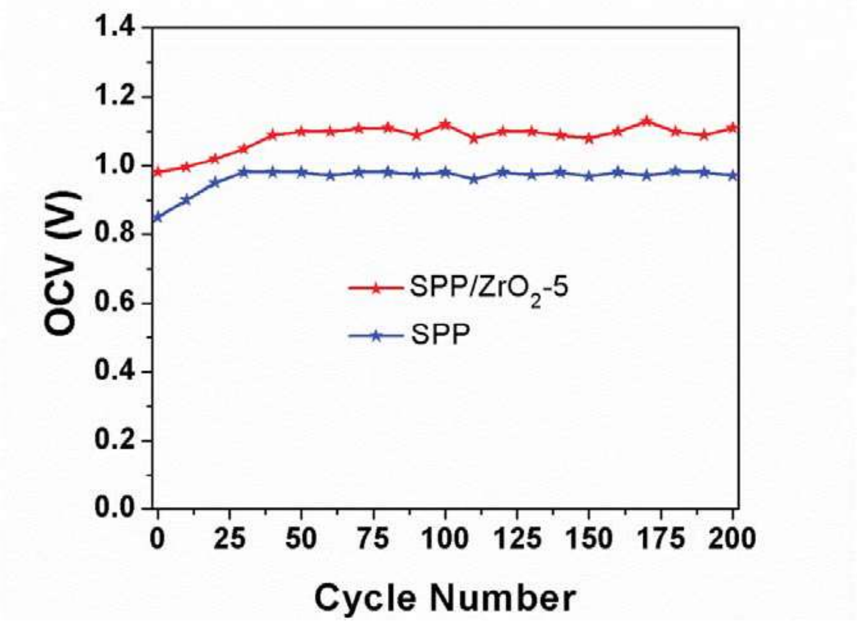

Figure 5.36: Change in OCV with number of cycles for SPP/ZrO_2 and SPP membranes performed in H_2/O_2 fuel cell.

5.7 Conclusion

A series of SPEEK-PEG/MO_2 (M= Si, Ti and Zr) nanocomposite membranes containing IPN structure were successfully fabricated with different weight percentage of MO_2. All nanoparticles were synthesized *in-situ* within the membranes using sol-gel method. Silica, titania and zirconia were synthesized by hydrolysis of TEOS, $Ti(OBu)_4$ and $Zr(OBu)_4$. The synergistic effect of cross-linking as well as inorganic additive on the membrane′s electrochemical and mechanical properties were investigated by various methods. FE-SEM and AFM images showed that the MO_2 particles are distributed homogeneously without aggregation and the average particle size silica is below 70 nm, titania is below 40 nm and zirconia is below 50 nm. The EDX elemental mapping image also supported the FE-SEM image and the silicon, titanium zirconium maps spectrum revealed the complete conversion of precursor to silica, titania and zirconia. Experimental results reveled that nanocomposite membranes had better properties than pristine SPEEK-PEG membrane e.g. conductivity, form stability, mechanical strength, thermal and oxidative stability etc. Nanocomposite membranes have shown good form stability in water up to 80 °C, whereas without nanoparticles embedded membrane has shown excessive swelling beyond 60 °C in water. Nanocomposite membranes with 10 wt% SiO_2, 7.5% TiO_2 and 7.5% ZrO_2 have shown highest conductivity and optimum water uptake at 80°C and 100% RH. All membranes have shown good mechanical properties i.e. the mechanical strength in the range of 15 to 31 MPa and the percent elongation in the range of 150 to 245%. The TGA results revealed that all the membranes had good thermal stability, where the onset of thermal decomposition 250°C occurred well above the low and medium temperature PEM fuel cell application. The composite membranes which showed highest conductivity at 60°C and 100% RH i.e. SPP/SiO_2-10, SPP/TiO_2-5 and SPP/ZrO_2-5 were studied in H_2/O_2 fuel cell and compared with pristine SPP membrane up to 60°C. At 60°C, the nanocomposite membranes showed more than two fold increased in maximum power density compare to the pristine SPP membrane. All the results indicate that the nanocomposite approach (cross-linking along with inorganic additive) enhanced the membrane properties to a great extent and the membrane can be used as an alternative in fuel cell application.

CHAPTER-6

Conclusions, Implications and Future perspectives

This thesis reports on the development and characterization of proton conductive membranes for the usage as electrolyte in PEMFC. These membranes consists of organic and organic/inorganic materials. During the entire work, the base polymer is same i.e. PEEK. The objective of the work, as highlighted in the first chapter, was to attempt different methods to synthesize SPEEK polymer based membranes which have desired properties for the fuel cell application. Various method have been used during the entire work e.g. cross-linking, blending, sol-gel etc. to achieve the target. The chapter brings out the achievements and the novel scientific understandings emerged out of this work in line with the objectives targeted and also discuss the possible future extensions of this work.

6.1 Conclusion

In the beginning, the introduction chapter gave a brief description about the proton exchange membranes acts as an electrolyte in fuel cell and earlier researchers experimental findings with advantage and disadvantages as a part of literature survey. The electrochemical and mechanical properties of a proton exchange membrane with a special focus on conductivity, water uptake, mechanical strength and chemical stability, which are the most desired properties for fuel cell have been given. A detailed discussion about the SPEEK polymer and its modification methods is also given. The membranes properties evaluation for characterization using different techniques has been elaborated in chapter 2. The next three chapters give an account of different proton exchange membranes synthesis, their characterizations, and their performance analysis in the fuel cell. The major findings and conclusions from this work are summarized as follows:

Synthesis and Characterization of SPEEK and SPEEK-PEG Cross-linked Membranes:

- Sulfonation of PEEK was done by using sulfuric acid and methane sulfonic acid (MSA), where MSA is used as diluent to control the rate of sulfonation and reduce the heterogeneity. The two concentrations of MSA investigated are namely 15% and 30%.The

15% MSA is found to be optimal and yields polymer with maximum IEC of 2.3 meq g^{-1}. The SPEEK yield obtained by this method, was more than 95%.

- The SPEEK polymer with IEC of 2 meq g^{-1} was used for the membrane synthesis and PEG was used as cross-linker. SPEEK-PEG cross-linked membranes have been prepared by using six different molecular weight of PEG (200, 400, 600, 3000, 6000 10000 Da) and the effect of the cross-linker chain length on membrane properties and morphology were investigated.
- Membranes morphology was investigated by using atomic force microscopy (AFM) and small angle X-ray scattering (SAXS), which showed that there was the formation of cluster-like structure and hydrophilic-hydrophobic phase separation occurs after cross-linking that made the membranes mechanically stronger and reduced its swelling in water at higher temperature.
- Membrane properties were found to be strongly dependent on the cross-linker chain length. PEG-400 and PEG-600 showed desirable properties in terms of overall membrane performance such as proton conductivity, mechanical strength, and membrane durability.
- These membranes have shown good form stability up to 60 °C and proton conductivity in the range of 0.070-0.095 S cm^{-1}. Highest conductivity obtained was with PEG-400 of 0.095 S cm^{-1} that is similar to that of the commercially available perflurosulfonic acid membranes. The high conductivity is a consequence of the optimum chain length of PEG required for formation of cluster structure in the membrane.
- These membranes have shown good mechanical properties after treatment in water at room temperature (20 to 25 MPa) and elevated temperature (10 to 15 MPa). All the membranes were found to be thermally stable up to 300 °C and can be used for high temperature applications.

- SPEEK-PEG-400 and SPEEK-PEG-600 cross-linked membranes performance were studied in PEMFC up to 60 °C and both the membranes showed approximately similar performance. At 60 °C the SPEEK-PEG-400 membrane showed the maximum power density of 183.04 mW cm^{-2} at 440 mA cm^{-2} and at 0.416 V and SPEEK-PEG-600 membrane showed the maximum power density of 162.40 mW cm^{-2} at 420 mA cm^{-2} and at 0.41 V.
- The methanol permeability study of SPEEK-PEG-400 membrane was carried out and compared with Nafion-117, to explore its utilization in the methanol fuel cell. It was found that it has the lower permeability of SPEEK-PEG-400 membrane compared to Nafion up to 55°C and it can be used as an alternative for methanol fuel cell.

Effect of Phosphotungstic Acid Blending on Properties and Performance of Sulfonated Poly(ether ether ketone)-Poly(ethylene glycol) Cross-linked Membranes.

- This study showed the effect of phosphotungstic acid (PWA) blending in sulfonated poly(ether ether ketone) (SPEEK) and poly(ethylene glycol) (PEG) cross-linked membrane in terms of electrochemical and mechanical properties, as PWA is a good inorganic modifier because of its unique properties like high conductivity, thermal stability, high selectivity and non-corrosive nature.
- Cross-linked SPEEK-PEG and composite cross-linked SPEEK-PEG-PWA membranes with six different weight percentage of PWA (5, 10, 20, 30, 40 and 50%) were synthesized and characterized. All the membranes were equilibrated with water at room temperature (27°C) and elevated temperature (60°C) and their properties were investigated.
- The room temperature equilibrated membranes showed increased conductivity with increasing PWA percentage in the membrane samples from 0.06 to 0.12 S cm^{-1}. All the membranes had good mechanical properties, i.e., the tensile strength in the range of 15 to 25 MPa and the percentage elongation in the range of 200 to 270 %.

- Scanning electron microscope with energy dispersive X-ray study was carried out to ascertain the tungsten concentration remaining in the membrane after water treatment at high temperature. The tungsten concentration systematically decreased with the increase in the initial PWA percentage.
- Following the treatment of membranes at 60 °C, SPEEK-PEG-10%PWA showed the highest conductivity (0.11 S cm^{-1}), high tensile strength (16 MPa) and percentage elongation (190%) among the PWA composite membranes. This membrane also showed high oxidative stability and PWA retention. Whereas, the membrane without PWA (0%PWA), the conductivity was 0.09 Scm^{-1}.The tensile strength was 19 MPa and percentage elongation was about 160%.
- The enhanced membrane properties after addition of PWA also had a significant effect on the H_2/O_2 fuel cell performance. At 60°C the cross-linked SPEEK-PEG-0%PWA membrane gave maximum power density of 153 mW cm^{-2} at 400 mA cm^{-2} and 0.4 V which was enhanced to 204 mW cm^{-2} at 520 mA cm^{-2} and 0.42 V for SPEEK-PEG-10% PWA, i.e., there was about 33% increase in the maximum power density by blending 10% PWA.

Synthesis and Characterization of Cross-linked Sulfonated poly(ether ether ketone)-poly(ethylene glycol)/MO$_2$ (M=Si, Ti and Zr) Organic-Inorganic Nanocomposite Membrane.

- A series of SPEEK-PEG/MO_2 (M=Si, Ti and Zr)nanocomposite membranes containing IPN structure were successfully fabricated. In these membranes MO_2 particles were synthesized *in-situ* within the membranes using sol-gel method by hydrolysis of TEOS (for SiO_2), $Ti(OBu)_4$ (for TiO_2) and $Zr(OBu)_4$ precursors.

- PEG act as cross-linker as well as good dispersant in the membranes. The hydrogen bond between –OH group of PEG, MO_2 and sulfonic acid (–SO_3H) facilitated better dispersion and improved the compatibility between the organic and inorganic components.
- The weight percentage of MO_2 varied within the membranes to investigate the optimum weight percentage in terms of electrochemical and mechanical properties as well as stability. In silica based nanocomposite membranes the weight percentage of silica was varied from 2.5% to 12.5% (2.5, 5, 7.5, 10 and 12.5%), and in titania and zirconia based nanocomposite membranes the weight percentage of titania and zirconia was varied from 2.5% to 10% (2.5, 5, 7.5 and 10%).
- FE-SEM and AFM images showed that the MO_2 nanoparticles were distributed homogeneously within the membranes without aggregation. The EDX mapping images of Si, Ti and Zr also supported the FE-SEM images and the elemental maps spectrum revealed the complete conversion of precursors to silica, titania and zirconia.
- Experimental results revealed that nanocomposite membranes had better properties than pristine SPEEK-PEG membrane e.g. conductivity, form stability, mechanical strength, thermal and oxidative stability etc. at a higher temperature in water.
- The nanocomposite membranes with optimum amount of MO_2 have shown good form stability in water up to 80 °C, whereas without nanoparticles added sample has shown excessive swelling beyond 60 °C in water.
- The electrochemical and mechanical properties of 10% SiO_2 embedded membrane are, maximum conductivity of 0.185 S cm^{-1} at 80°C and 100% RH; optimum water uptake of 65% with □ value 14 at 80 °C; tensile strength of 22 MPa and the percent elongation of 180%.

- The electrochemical and mechanical properties of 7.5 wt% TiO_2 imbedded membrane are, maximum conductivity of 0.180 S cm^{-1} at 80 °C and 100% RH and optimum water uptake of 56.5 with □ value 18.2; tensile strength of 26 MPa and percent elongation of 176 %.
- The electrochemical and mechanical properties of 7.5 wt% ZrO_2 imbedded membrane are, maximum conductivity of 0.171 S cm^{-1} at 80 °C and 100% RH and optimum water uptake of 46.5 with □ value 15.0; tensile strength of 27 MPa and percent elongation of 170 %.
- SPP/SiO_2-10, SPP/TiO_2-5 and SPP/ZrO_2-5 membranes showed maximum conductivity and optimum water uptake at 60°C. therefore nanocomposite membrane's performance were investigated in PEMFC and compared with pristine SPEEK-PEG membrane upto 60°C. where the nanocomposite membranes showed more than higher performance than the pristine membrane.
- At 60 °C the SPEEK-PEG membrane gives the maximum power density of 184 mW cm^{-2} at 460 mA cm^{-2} and at 0.4 V which is enhanced to 379 mW cm^{-2} at 800 mA cm^{-2} and at 0.47 V for SPP/SiO_2-10 membrane. Similarly SPP/TiO_2-5 membrane showed the maximum power density of 392.78 mW cm^{-2} at 820 mA cm^{-2} and at 0.479 V and SPP/ZrO_2-5 membrane showed the maximum power density of 425.78 mW cm^{-2} at 850 mA cm^{-2} and at 0.50 V.
- The durability studies of the membranes in the fuel cell were carried out by measurement of OCV during the 200 cycles and observed that there was no significant decrease in OCV.

In summary, three different type of PEMs have been synthesized in this work; (i) SPEEK-PEG cross linked membranes which have high conductivity (similar to the commercial membrane i.e. Nafion) and good form stability in water upto 60°C. (ii) SPEEK-PEG-PWA composite membranes which has higher conductivity than the SPEEK-PEG crosslinked membranes but the form stability was similar. (iii) SPEEK-PEG/MO_2 nanocomposite membranes which have higher conductivity and form stability (upto 80°C in water) than the SPEEK-PEG crosslinked membranes and showed good performance in PEMFC upto 60°C. A Comparison of proton conductivity and fuel cell performance (60°C) of all the three different type of membranes (which have shown the optimum electrochemical properties) is given in table 6.1. Thus in the conclusion we can say that the membranes synthesized in this work can be used as an alternative for fuel cell application

Table 6.1.: Comparison of proton conductivity and fuel cell performance (at 60°C) of membranes which have shown the optimum electrochemical properties (chapter 3 to chapter 5).

Membrane Sample	**Conductivity ($S\ cm^{-1}$)**	**Fuel cell performance**		
		Voltage (V)	**Current density ($mA\ cm^{-1}$)**	**Power density ($mW\ cm^{-1}$)**
SPEEK-PEG-400	0.150	0.416	440	183.05
SPEEK-PEG/PWA	0.115*	0.420	520	204.05
SPEEK-PEG/SiO_2	0.180	0.473	800	378.40
SPEEK-PEG/TiO_2	0.178	0.479	820	392.78
SPEEK-PEG/ZrO_2	0.179	0.501	850	425.38

* Membrane treated in water at 60°C and thereafter conductivity measurement was done at RT and 50% RH

6.2 Future perspectives

The present research work is believed to be a step towards the synthesis and characterization of SPEEK polymer based membrane. In future, there are various possibilities to extend the present work; either to improve the properties of the synthesized membranes or to investigate the membranes performance in other electrochemical applications. A brief description of the possible utility of developed membranes in various electrochemical processes is given bellow:

(i) High temperature proton exchange membrane fuel cell (HT-PEMFC):

The High temperature PEMFCs are generally operated above 120°C and under non-humidified conditions. Operation of PEMFCs above 120°C is desirable for a number of reasons:

- Elevated temperature operation enhances the kinetics of electrode reactions.
- Improves CO tolerance because at 80°C, CO adsorbs on the Pt catalyst and diminishes the fuel cell performance. To avoid this CO poisoning, the CO content has to be maintained as low as 20 ppm in the fuel stream at 80°C. CO tolerance increases to 1000 ppm at 130°C and 30,000 ppm at 200°C due to CO desorption.
- At temperatures above 120°C, flooding of the catalyst layers can be avoided due to the elimination of liquid water, the cooling system will be simplified as a result of a larger temperature difference with the ambient, waste heat may be recovered, it may be feasible to use non-precious metal catalysts.

In view of these considerations, worldwide affords are going on to develop proton exchange membranes for HT-PEMFC. An interesting approach to synthesize the membranes for HT-PEMFC is to incorporate inorganic materials as fillers in the polymer matrix. It is extensively reported in literature, the incorporation of heteropoly acids and hygroscopic oxides in polymer matrix improved the water management, proton conductivity and membrane performance at elevated temperature.

The cross-linked composite membranes synthesized in this work e.g. SPEEK-PEG/PWA, SPEEK-PEG/SiO_2, SPEEK-PEG/TiO_2 and SPEEK-PEG/ZrO_2 have possibility to work in HT-PEMFC because PWA shows good conductivity in anhydrous state and the MO_2 has good water retention properties at higher temperature. The other advantage is the leaching of PWA from the membrane will be reduce in HT-PEMFC.

(ii) Direct methanol fuel cell

Among the fuel cells, DMFC is attractive for the application of portable power source with theoretical high energy density of methanol (6100 Wh kg^{-1} at 25°C) and simple structure without reformer and humidifiers. Other attributes like quick refueling, low temperature and pressure operation, low cost of methanol and compact cell design of DMFC are also fascinating.

Despite these advantages, however, DMFC has some problems. The limits of DMFC are low efficiency and power density, which are caused by methanol permeation through the polymer membrane and slow electrochemical methanol oxidation. Ideally, the membrane in a direct methanol fuel cell should have high proton conductivity and low methanol permeability. Nafion®, which is widely used in the PEM fuel cell, is a good proton conductor when it absorbs water but has high methanol permeability. To overcome these disadvantages, a huge amount of efforts have been attempted. Among those, Various inorganic fillers such as, silica, titanium oxide, zirconium oxide, alumina and zeolite were introduced to organic/inorganic hybrid composite membranes as barrier against methanol. These hybrid membranes showed improved results in terms of low methanol permeability, high conductivity and high efficiency in DMFCs.

The membranes synthesized in this work should perform well in DMFC because the base polymer in this work is an aromatic hydrocarbon polymer which has generally lower permeability that the PFSA membranes. The other membranes developed in this work by incorporation of hygroscopic oxides along with the cross-linker should also perform well in DMFC because the hygroscopic oxides are well known for the reduction of methanol permeability through the ion exchange membrane.

Thus, these membranes have various future perspectives in the area of DMFCs. We can study the methanol permeability through these membranes and their performance analysis in DMFC.

We can also optimize the organic/inorganic components to get the maximum efficiency in DMFCs.

These membranes can find several other promising applications like,

(iii) Separation of components such as salts or acids and bases from electrolyte solutions (e.g., electro dialysis, electro-electrodialysis, bipolar electrolysis etc.),

(iv) Chlor-alkali industry for the production of alkali and chlorine,

(v) Pure water electrolysis for production of hydrogen and oxygen and or

(vi) Redox flow batteries etc.

References

1. Barbir, F., PEM fuel cells: theory and practice; Academic Press, 2012.
2. Kordesch, K. V.; Simader, G. R., Chemical Reviews 95, 191 1995.
3. Sørensen, B., Hydrogen and fuel cells: emerging technologies and applications; Academic Press, 2011.
4. Edwards, P. P.; Kuznetsov, V. L.; David, W. I.; Brandon, N. P., Energy policy 36, 4356 2008.
5. Patil, P.; Zegers, P., Journal of power sources 49, 169 1994.
6. Corbo, P.; Migliardini, F.; Veneri, O., Hydrogen fuel cells for road vehicles; Springer Science & Business Media, 2011.
7. Haseli, Y., International Journal of Hydrogen Energy 43, 9015 2018.
8. Dicks, A.; Rand, D. A. J., Fuel cell systems explained; Wiley Online Library, 2018.
9. Daud, W.; Rosli, R.; Majlan, E.; Hamid, S.; Mohamed, R.; Husaini, T., Renewable Energy 113, 620 2017.
10. Zaidi, J.; Matsuura, T., Polymer membranes for fuel cells; Springer, 2008.
11. Bagotsky, V. S., Fuel cells: problems and solutions; John Wiley & Sons, 2012.
12. McLean, G.; Niet, T.; Prince-Richard, S.; Djilali, N., International Journal of Hydrogen Energy 27, 507 2002.
13. Bischoff, M., Journal of Power Sources 160, 842 2006.
14. Amorelli, A.; Wilkinson, M.; Bedont, P.; Capobianco, P.; Marcenaro, B.; Parodi, F.; Torazza, A. Greenhouse Gas Control Technologies-6th International Conference, 2003, pp 1325.
15. Kim, Y. J.; Chang, I. G.; Lee, T. W.; Chung, M. K., Fuel 89, 1019 2010.
16. Mekhilef, S.; Saidur, R.; Safari, A., Renewable and Sustainable Energy Reviews 16, 981 2012.

17. Sotouchi, H.; Hagiwara, A., Energy Carriers And Conversion Systems With Emphasis On Hydrogen-Volume II 8, 333 2009.

18. Mahato, N.; Banerjee, A.; Gupta, A.; Omar, S.; Balani, K., Progress in Materials Science 72, 141 2015.

19. Hajimolana, S. A.; Hussain, M. A.; Daud, W. A. W.; Soroush, M.; Shamiri, A., Renewable and Sustainable Energy Reviews 15, 1893 2011.

20. Ormerod, R. M., Chemical Society Reviews 32, 17 2003.

21. Rikukawa, M.; Sanui, K., Progress in Polymer Science 25, 1463 2000.

22. Peighambardoust, S. J.; Rowshanzamir, S.; Amjadi, M., International journal of hydrogen energy 35, 9349 2010.

23. Li, X.; Faghri, A., Journal of Power Sources 226, 223 2013.

24. Tripathi, B. P.; Shahi, V. K., Progress in Polymer Science 36, 945 2011.

25. Zhang, H.; Shen, P. K., Chemical reviews 112, 2780 2012.

26. Hickner, M. A.; Ghassemi, H.; Kim, Y. S.; Einsla, B. R.; McGrath, J. E., Chemical reviews 104, 4587 2004.

27. Larminie, J.; Dicks, A., Fuel cell systems explained, 67 2003.

28. Blomen, L. J.; Mugerwa, M. N., Fuel cell systems; Springer Science & Business Media, 2013.

29. Hickner, M.; Pivovar, B., Fuel cells 5, 213 2005.

30. Peckham, T. J.; Holdcroft, S., Advanced materials 22, 4667 2010.

31. Eikerling, M.; Kornyshev, A., Journal of electroanalytical chemistry 502, 1 2001.

32. Eikerling, M.; Kornyshev, A.; Kuznetsov, A.; Ulstrup, J.; Walbran, S., The Journal of Physical Chemistry B 105, 3646 2001.

33. Kim, Y. S.; Dong, L.; Hickner, M. A.; Glass, T. E.; Webb, V.; McGrath, J. E., Macromolecules 36, 6281 2003.

34. Siu, A.; Schmeisser, J.; Holdcroft, S., The Journal of Physical Chemistry B 110, 6072 2006.

35. Kreuer, K., Journal of membrane science 185, 29 2001.

36. Laberty-Robert, C.; Valle, K.; Pereira, F.; Sanchez, C., Chemical Society Reviews 40, 961 2011.

37. Büchi, F. N.; Gupta, B.; Haas, O.; Scherer, G. G., Electrochimica Acta 40, 345 1995.

38. Guo, Q.; Pintauro, P. N.; Tang, H.; O'Connor, S., Journal of Membrane Science 154, 175 1999.

39. Hou, H.; Di Vona, M. L.; Knauth, P., ChemSusChem 4, 1526 2011.

40. Ogumi, Z.; Kuroe, T.; Takehara, Z. i., Journal of the Electrochemical Society 132, 2601 1985.

41. Ogumi, Z.; Takehara, Z.; Yoshizawa, S., Journal of the Electrochemical Society 131, 769 1984.

42. Vebrugge, M., Journal of electrochemical society 136, 417 1989.

43. Ren, X.; Zawodzinski, T. A.; Uribe, F.; Dai, H.; Gottesfeld, S., ECS Proceedings Volumes 1995, 284 1995.

44. Perry, M. L.; Fuller, T. F., Journal of the electrochemical society 149, S59 2002.

45. Page, K. A.; Rowe, B. W., Polymers for Energy Storage and Delivery: Polyelectrolytes for Batteries and Fuel Cells, 147 2012.

46. Peinemann, K.-V.; Nunes, S. P., Membranes for energy conversion; John Wiley & Sons, 2008.

47. Savadogo, O., Journal of New Materials for Electrochemical Systems 1, 47 1998.

48. Lee, J. S.; Quan, N. D.; Hwang, J. M.; Lee, S. D.; Kim, H.; Lee, H.; Kim, H. S., JOURNAL OF INDUSTRIAL AND ENGINEERING CHEMISTRY-SEOUL- 12, 175 2006.

49. Cohen, S. G.; Wolosinski, H. T.; Scheuer, P. J., Journal of the American Chemical Society 71, 3439 1949.

50. Prober, M., Journal of the American Chemical Society 75, 968 1953.

51. Hodgdon Jr, R. B., Journal of Polymer Science Part A-1: Polymer Chemistry 6, 171 1968.

52. Savadogo, O., Journal of Power Sources 127, 135 2004.

53. Kerres, J. A., Journal of Membrane Science 185, 3 2001.

54. Li, J.; Sato, K.; Ichiduri, S.; Asano, S.; Ikeda, S.; Iida, M.; Oshima, A.; Tabata, Y.; Washio, M., European Polymer Journal 40, 775 2004.

55. Li, J.; Sato, K.; Ichizuri, S.; Asano, S.; Ikeda, S.; Iida, M.; Oshima, A.; Tabata, Y.; Washio, M., European polymer journal 41, 547 2005.

56. Sato, K.; Ikeda, S.; Iida, M.; Oshima, A.; Tabata, Y.; Washio, M., Nuclear Instruments and Methods in Physics Research Section B: Beam Interactions with Materials and Atoms 208, 424 2003.

57. Huslage, J.; Rager, T.; Schnyder, B.; Tsukada, A., Electrochimica acta 48, 247 2002.

58. Schmidt, T.; Simbeck, K.; Scherer, G., Journal of the Electrochemical Society 152, A93 2005.

59. Büchi, F. N.; Gupta, B.; Haas, O.; Scherer, G. G., Journal of the Electrochemical Society 142, 3044 1995.

60. Nasef, M. M.; Saidi, H.; Nor, H. M.; Foo, O. M., Journal of applied polymer science 76, 1 2000.

61. Nasef, M. M.; Saidi, H., Journal of membrane science 216, 27 2003.

62. Kallio, T.; Jokela, K.; Ericson, H.; Serimaa, R.; Sundholm, G.; Jacobsson, P.; Sundholm, F., Journal of applied electrochemistry 33, 505 2003.

63. Chen, J.; Asano, M.; Maekawa, Y.; Yoshida, M., Journal of Membrane Science 277, 249 2006.

64. Park, C. H.; Lee, C. H.; Guiver, M. D.; Lee, Y. M., Progress in Polymer Science 36, 1443 2011.

65. Flint, S. D.; Slade, R. C., Solid State Ionics 97, 299 1997.

66. Chen, S.-L.; Krishnan, L.; Srinivasan, S.; Benziger, J.; Bocarsly, A., Journal of membrane science 243, 327 2004.

67. Savinell, R. F.; Litt, M. H.; Google Patents: 1996.

68. Savinell, R. F.; Litt, M. H.; Google Patents: 1998.

69. Wainright, J.; Wang, J. T.; Weng, D.; Savinell, R.; Litt, M., Journal of the Electrochemical Society 142, L121 1995.

70. Wang, J.; Wainright, J.; Yu, H.; Litt, M.; Savinell, R., ECS Proceedings Volumes 1995, 202 1995.

71. Blonsky, P. M.; Shriver, D.; Austin, P.; Allcock, H., Journal of the American Chemical Society 106, 6854 1984.

72. Allcock, H. R.; Fitzpatrick, R. J.; Salvati, L., Chemistry of materials 3, 1120 1991.

73. Wycisk, R.; Pintauro, P. N., Journal of membrane science 119, 155 1996.

74. Hergenrother, P. M.; Levine, H. H., Journal of Polymer Science Part A-1: Polymer Chemistry 5, 1453 1967.

75. Kopitzke, R.; Linkous, C.; Nelson, G., Journal of Polymer Science Part A: Polymer Chemistry 36, 1197 1998.

76. Kobayashi, T.; Rikukawa, M.; Sanui, K.; Ogata, N., Solid state ionics 106, 219 1998.

77. Rusanov, A. L.; Belomoina, N. M.; Bulycheva, E. G.; Yanul, N. A.; Likhatchev, D. Y.; Dobrovolskii, Y. A.; Iojoiu, C.; Sanchez, J.-Y.; Voytekunas, V. Y.; Abadie, M. J., High Performance Polymers 20, 627 2008.

78. Wu, H.-L.; Ma, C.-C. M.; Liu, F.-Y.; Chen, C.-Y.; Lee, S.-J.; Chiang, C.-L., European Polymer Journal 42, 1688 2006.

79. Nolte, R.; Ledjeff, K.; Bauer, M.; Mülhaupt, R., Journal of Membrane Science 83, 211 1993.

80. Kim, Y. S.; Einsla, B.; Sankir, M.; Harrison, W.; Pivovar, B. S., Polymer 47, 4026 2006.

81. Zaidi, S. J.; Mikhailenko, S. D.; Robertson, G.; Guiver, M.; Kaliaguine, S., Journal of Membrane Science 173, 17 2000.

82. Nagarale, R.; Gohil, G.; Shahi, V. K., Journal of Membrane Science 280, 389 2006.

83. Mikhailenko, S. D.; Wang, K.; Kaliaguine, S.; Xing, P.; Robertson, G. P.; Guiver, M. D., Journal of Membrane Science 233, 93 2004.

84. Mikhailenko, S.; Zaidi, S.; Kaliaguine, S., Catalysis Today 67, 225 2001.

85. Li, W.; Wang, G.; Jiang, Z.; Liu, C.; Huo, P.; Zhang, S., Journal of Applied Polymer Science 1312014.

86. Zhang, Y. P.; Yue, M. Z.; Chen, Y. Advanced Materials Research, 2011, pp 3032.

87. Genies, C.; Mercier, R.; Sillion, B.; Cornet, N.; Gebel, G.; Pineri, M., Polymer 42, 359 2001.

88. Faure, S.; Pineri, M.; Aldebert, P.; Mercier, R.; Sillion, B.; Google Patents: 2002.

89. Cornet, N.; Diat, O.; Gebel, G.; Jousse, F.; Marsacq, D.; Mercier, R.; Pineri, M., Journal of new materials for electrochemical systems 3, 33 2000.

90. Grubb, W.; Niedrach, L., Journal of the Electrochemical Society 107, 131 1960.

91. Dockheer, S. M.; Gubler, L.; Bounds, P. L.; Domazou, A. S.; Scherer, G. G.; Wokaun, A.; Koppenol, W. H., Physical Chemistry Chemical Physics 12, 11609 2010.

92. Dockheer, S. M.; Gubler, L.; Koppenol, W. H., Physical Chemistry Chemical Physics 15, 4975 2013.

93. Yu, J.; Yi, B.; Xing, D.; Liu, F.; Shao, Z.; Fu, Y.; Zhang, H., Physical Chemistry Chemical Physics 5, 611 2003.

94. Wang, J.-T.; Savinell, R.; Wainright, J.; Litt, M.; Yu, H., Electrochimica Acta 41, 193 1996.

95. Wang, J.-T.; Wainright, J.; Savinell, R.; Litt, M., Journal of Applied Electrochemistry 26, 751 1996.

96. Wainright, J. S.; Wang, J.-t.; Savinell, R. F. Energy Conversion Engineering Conference, 1996. IECEC 96., Proceedings of the 31st Intersociety, 1996, pp 1107.

97. Peron, J.; Ruiz, E.; Jones, D. J.; Rozière, J., Journal of Membrane Science 314, 247 2008.

98. Xu, H.; Chen, K.; Guo, X.; Fang, J.; Yin, J., Polymer 48, 5556 2007.

99. Wang, J.; Lin, W.; Weber, M.; Wasmus, S.; Savinell, R., Electrochimica acta 43, 3821 1998.

100. Weber, M.; Wang, J. T.; Wasmus, S.; Savinell, R., Journal of the Electrochemical Society 143, L158 1996.

101. Staiti, P.; Lufrano, F.; Arico, A.; Passalacqua, E.; Antonucci, V., Journal of Membrane Science 188, 71 2001.

102. Genies, C.; Mercier, R.; Sillion, B.; Petiaud, R.; Cornet, N.; Gebel, G.; Pineri, M., Polymer 42, 5097 2001.

103. Tang, H.; Pintauro, P. N., Journal of applied polymer science 79, 49 2001.

104. Tang, H.; Pintauro, P. N.; Guo, Q.; O'Connor, S., Journal of applied polymer science 71, 387 1999.

105. Wrasidlo, W.; Augl, J., Journal of Polymer Science Part A-1: Polymer Chemistry 7, 3393 1969.

106. Kopitzke, R. W.; Linkous, C. A.; Anderson, H. R.; Nelson, G. L., Journal of the Electrochemical Society 147, 1677 2000.

107. Klein, D. J.; Modarelli, D. A.; Harris, F. W., Macromolecules 34, 2427 2001.

108. Schönberger, F.; Hein, M.; Kerres, J., Solid State Ionics 178, 547 2007.

109. Xu, T.; Wu, D.; Wu, L., Progress in Polymer Science 33, 894 2008.

110. Roziere, J.; Jones, D. J., Annual Review of Materials Research 33, 503 2003.

111. Smitha, B.; Sridhar, S.; Khan, A., Journal of membrane science 259, 10 2005.

112. Shao, Y.; Yin, G.; Wang, Z.; Gao, Y., Journal of Power Sources 167, 235 2007.

113. Peighambardoust, S.; Rowshanzamir, S.; Amjadi, M., International journal of hydrogen energy 35, 9349 2010.

114. Authayanun, S.; Im-Orb, K.; Arpornwichanop, A., Chinese Journal of Catalysis 36, 473 2015.

115. Bose, S.; Kuila, T.; Nguyen, T. X. H.; Kim, N. H.; Lau, K.-t.; Lee, J. H., Progress in Polymer Science 36, 813 2011.

116. Huang, R.; Shao, P.; Burns, C.; Feng, X., Journal of applied polymer science 82, 2651 2001.

117. Jin, X.; Bishop, M. T.; Ellis, T. S.; Karasz, F. E., Polymer International 17, 4 1985.

118. Kim, Y. S.; Hickner, M. A.; Dong, L.; Pivovar, B. S.; McGrath, J. E., Journal of Membrane Science 243, 317 2004.

119. Takamuku, S.; Jannasch, P., Advanced Energy Materials 2, 129 2012.

120. Ingratta, M.; Jutemar, E. P.; Jannasch, P., Macromolecules 44, 2074 2011.

121. Li, N.; Hwang, D. S.; Lee, S. Y.; Liu, Y.-L.; Lee, Y. M.; Guiver, M. D., Macromolecules 44, 4901 2011.

122. Zhang, X.; Hu, Z.; Luo, L.; Chen, S.; Liu, J.; Chen, S.; Wang, L., Macromolecular Rapid Communications 32, 1108 2011.

123. Lee, S. Y.; Kang, N. R.; Shin, D. W.; Lee, C. H.; Lee, K.-S.; Guiver, M. D.; Li, N.; Lee, Y. M., Energy & Environmental Science 5, 9795 2012.

124. Kim, T.; Choi, Y.-W.; Kim, C.-S.; Yang, T.-H.; Kim, M.-N., Journal of Materials Chemistry 21, 7612 2011.

125. So, S. Y.; Yoon, Y. J.; Kim, T.-H.; Yoon, K.; Hong, Y. T., Journal of Membrane Science 381, 204 2011.

126. Weissbach, T.; Tsang, E. M.; Yang, A. C.; Narimani, R.; Frisken, B. J.; Holdcroft, S., Journal of Materials Chemistry 22, 24348 2012.

127. Mikhailenko, S. D.; Robertson, G. P.; Guiver, M. D.; Kaliaguine, S., Journal of membrane science 285, 306 2006.

128. Kanakasabai, P.; Deshpande, A. P.; Varughese, S., Journal of Applied Polymer Science 127, 2140 2013.

129. Arigonda, M.; Deshpande, A. P.; Varughese, S., Journal of Applied Polymer Science 127, 5100 2013.

130. Patil, Y.; Kulkarni, S.; Mauritz, K. A., Journal of Applied Polymer Science 121, 2344 2011.

131. Branco, C. M.; Sharma, S.; de Camargo Forte, M. M.; Steinberger-Wilckens, R., Journal of Power Sources 316, 139 2016.

132. Wu, H.-L.; Ma, C.-C. M.; Li, C.-H.; Lee, T.-M.; Chen, C.-Y.; Chiang, C.-L.; Wu, C., Journal of membrane science 280, 501 2006.

133. Wu, H. L.; Ma, C. C. M.; Kuan, H. C.; Wang, C. H.; Chen, C. Y.; Chiang, C. L., Journal of Polymer Science Part B: Polymer Physics 44, 565 2006.

134. Pasupathi, S.; Ji, S.; Bladergroen, B. J.; Linkov, V., International Journal of Hydrogen Energy 33, 3132 2008.

135. Giffin, G. A.; Galbiati, S.; Walter, M.; Aniol, K.; Ellwein, C.; Kerres, J.; Zeis, R., Journal of Membrane Science 535, 122 2017.

136. Zhang, H.; Li, X.; Zhao, C.; Fu, T.; Shi, Y.; Na, H., Journal of Membrane Science 308, 66 2008.

137. Li, H.; Zhang, G.; Ma, W.; Zhao, C.; Zhang, Y.; Han, M.; Zhu, J.; Liu, Z.; Wu, J.; Na, H., international journal of hydrogen energy 35, 11172 2010.
138. Yang, T., International Journal of Hydrogen Energy 33, 6772 2008.
139. Kerres, J., Fuel Cells 5, 230 2005.
140. Helmer-Metzmann, F.; Osan, F.; Schneller, A.; Ritter, H.; Ledjeff, K.; Nolte, R.; Thorwirth, R.; US Patents: 1995.
141. Mao, S. S.; Hamrock, S. J.; Ylitalo, D. A.; US Patents: 2000.
142. Yen, S.-P. S.; Narayanan, S. R.; Halpert, G.; Graham, E.; Yavrouian, A.; US Patents: 1998.
143. Kerres, J.; Zhang, W.; Jorissen, L.; Gogel, V., Journal of New Materials for Electrochemical Systems 5, 97 2002.
144. Kerres, J.; Ullrich, A.; Hein, M.; Gogel, V.; Friedrich, K.; Jörissen, L., Fuel Cells 4, 105 2004.
145. Yen, S.-P. S.; Narayanan, S. R.; Halpert, G.; Graham, E.; Yavrouian, A.; US Patent: 1998.
146. Gupta, D.; Choudhary, V., international journal of hydrogen energy 36, 8525 2011.
147. Hande, V. R.; Rao, S.; Rath, S.; Thakur, A.; Patri, M., Journal of Membrane Science 322, 67 2008.
148. Fang, C.; Toh, X. N.; Yao, Q.; Julius, D.; Hong, L.; Lee, J. Y., Journal of Power Sources 226, 289 2013.
149. Saccà, A.; Carbone, A.; Pedicini, R.; Marrony, M.; Barrera, R.; Elomaa, M.; Passalacqua, E., Fuel Cells 8, 225 2008.
150. Misono, M., Chemical communications, 1141 2001.
151. Ramani, V.; Kunz, H.; Fenton, J., Electrochimica Acta 50, 1181 2005.
152. Zaidi, S. J.; Mikhailenko, S.; Robertson, G.; Guiver, M.; Kaliaguine, S., Journal of Membrane Science 173, 17 2000.

153. Ponce, M.; Prado, L. d. A.; Silva, V.; Nunes, S., Desalination 162, 383 2004.

154. Colicchio, I.; Wen, F.; Keul, H.; Simon, U.; Moeller, M., Journal of Membrane Science 326, 45 2009.

155. Oh, S.; Yoshida, T.; Kawamura, G.; Muto, H.; Sakai, M.; Matsuda, A., Journal of Power Sources 195, 5822 2010.

156. Doğan, H.; Inan, T. Y.; Unveren, E.; Kaya, M., international journal of hydrogen energy 35, 7784 2010.

157. Ismail, A.; Othman, N.; Mustafa, A., Journal of membrane science 329, 18 2009.

158. Nunes, S.; Ruffmann, B.; Rikowski, E.; Vetter, S.; Richau, K., Journal of Membrane Science 203, 215 2002.

159. Silva, V.; Ruffmann, B.; Silva, H.; Gallego, Y.; Mendes, A.; Madeira, L.; Nunes, S., Journal of Power Sources 140, 34 2005.

160. Roelofs, K. S.; Hirth, T.; Schiestel, T., Journal of Membrane Science 346, 215 2010.

161. Colicchio, I.; Demco, D. E.; Baias, M.; Keul, H.; Moeller, M., Journal of Membrane Science 337, 125 2009.

162. Sambandam, S.; Ramani, V., Journal of power sources 170, 259 2007.

163. Di Vona, M. L.; Ahmed, Z.; Bellitto, S.; Lenci, A.; Traversa, E.; Licoccia, S., Journal of membrane science 296, 156 2007.

164. Dou, Z.; Zhong, S.; Zhao, C.; Li, X.; Fu, T.; Na, H., Journal of Applied Polymer Science 109, 1057 2008.

165. Gashoul, F.; Parnian, M. J.; Rowshanzamir, S., International Journal of Hydrogen Energy 42, 590 2017.

166. Kalappa, P.; Lee, J. H., Polymer international 56, 371 2007.

167. Chang, J.-H.; Park, J. H.; Park, G.-G.; Kim, C.-S.; Park, O. O., Journal of Power Sources 124, 18 2003.

168. Karthikeyan, C.; Nunes, S.; Schulte, K., European polymer journal 41, 1350 2005.

169. Gosalawit, R.; Chirachanchai, S.; Shishatskiy, S.; Nunes, S. P., Journal of Membrane Science 323, 337 2008.

170. Şengül, E.; Erdener, H.; Akay, R. G.; Yücel, H.; Bac, N.; Eroğlu, İ., international journal of hydrogen energy 34, 4645 2009.

171. Tchicaya-Bouckary, L.; Jones, D.; Roziere, J., Fuel Cells 2, 40 2002.

172. Ruffmann, B.; Silva, H.; Schulte, B.; Nunes, S., Solid State Ionics 162, 269 2003.

173. Tripathi, B. P.; Kumar, M.; Shahi, V. K., Journal of Membrane Science 327, 145 2009.

174. Paturzo, L.; Basile, A.; Iulianelli, A.; Jansen, J. C.; Gatto, I.; Passalacqua, E., Catalysis today 104, 213 2005.

175. Iulianelli, A.; Clarizia, G.; Gugliuzza, A.; Ebrasu, D.; Bevilacqua, A.; Trotta, F.; Basile, A., international journal of hydrogen energy 35, 12688 2010.

176. Iulianelli, A.; Gatto, I.; Trotta, F.; Biasizzo, M.; Passalacqua, E.; Carbone, A.; Bevilacqua, A.; Clarizia, G.; Gugliuzza, A.; Basile, A., International Journal of Hydrogen Energy 38, 551 2013.

177. Di Vona, M. L.; Ahmed, Z.; Bellitto, S.; Lenci, A.; Traversa, E.; Licoccia, S., Journal of membrane science 296, 156 2007.

178. Parnian, M. J.; Rowshanzamir, S.; Prasad, A. K.; Advani, S. G., Journal of Membrane Science 556, 12 2018.

179. Bello, M.; Zaidi, S. J.; Rahman, S., Journal of Membrane Science 322, 218 2008.

180. Electrochemistry, P.; Elements, C.; Equivalent, C.; Models, C., Appl Note AC 286, R491 2010.

181. Kauffman, G. B., Angewandte Chemie International Edition 48, 1532 2009.

182. Barsoukov, E.; Macdonald, J. R., Impedance spectroscopy: theory, experiment, and applications; John Wiley & Sons, 2018.

183. Cesiulis, H.; Tsyntsaru, N.; Ramanavicius, A.; Ragoisha, G. In Nanostructures and Thin Films for Multifunctional Applications; Springer, 2016.

184. Navarra, M.; Abbati, C.; Scrosati, B., Journal of power sources 183, 109 2008.

185. Appetecchi, G.; Croce, F.; Persi, L.; Ronci, F.; Scrosati, B., Electrochimica Acta 45, 1481 2000.

186. Suart, B., Google Scholar2004.

187. Griffiths, P. R.; De Haseth, J. A., Fourier transform infrared spectrometry; John Wiley & Sons, 2007.

188. Mojet, B. L.; Ebbesen, S. D.; Lefferts, L., Chemical Society Reviews 39, 4643 2010.

189. Zhou, W.; Wang, Z. L., Scanning microscopy for nanotechnology: techniques and applications; Springer science & business media, 2007.

190. Brodusch, N.; Demers, H.; Gauvin, R., Field Emission Scanning Electron Microscopy: New Perspectives for Materials Characterization; Springer, 2017.

191. Van Bokhoven, J. A.; Lamberti, C., X-ray absorption and X-ray emission spectroscopy: theory and applications; John Wiley & Sons, 2016.

192. Eaton, P.; West, P., Atomic force microscopy; Oxford University Press, 2010.

193. Haugstad, G., Atomic force microscopy: understanding basic modes and advanced applications; John Wiley & Sons, 2012.

194. Khulbe, K. C.; Feng, C.; Matsuura, T., Synthetic polymeric membranes: characterization by atomic force microscopy; Springer Science & Business Media, 2007.

195. De Oliveira, R.; Albuquerque, D.; Cruz, T.; Yamaji, F.; Leite, F. In Atomic force microscopy-imaging, measuring and manipulating surfaces at the atomic scale; InTech, 2012.

196. Porod, G.; Small-Angle, X.; Academic Press, Londres: 1982.

197. Gille, W., Particle and particle systems characterization: small-angle scattering (SAS) applications; CRC Press, 2016.

198. Schnablegger, H.; Singh, Y., Anton Paar GmbH2013.

199. Michler, G. H.; Baltá-Calleja, F. J., Mechanical properties of polymers based on nanostructure and morphology; CRC Press, 2016.

200. Landel, R. F.; Nielsen, L. E., Mechanical properties of polymers and composites; CRC press, 1993.

201. Schümann, K.; Röhr, U.; Schmitz, K.-P.; Grabow, N., Current Directions in Biomedical Engineering 2, 649 2016.

202. Hatakeyama, T.; Quinn, F., Thermal analysis: fundamentals and applications to polymer science; [sl], 1999.

203. Brown, M.; London: Chapman and Hall.

204. Helmer-Metzmann, F.; Osan, F.; Schneller, A.; Ritter, H.; Ledjeff, K.; Nolte, R.; Thorwirth, R. in U.S.; Patent, U. S., Ed.: 1995.

205. Mao, S. S.; Hamrock, S. J.; Ylitalo, D. A.; US Patent: 2000, p 68.

206. Parnian, M. J.; Rowshanzamir, S.; Gashoul, F., Energy 125, 614 2017.

207. Pedersen, J. S., Journal of Applied Crystallography 27, 595 1994.

208. Ashcroft, N. W.; Lekner, J., Physical Review 145, 83 1966.

209. Debye, P.; Anderson Jr, H.; Brumberger, H., Journal of Applied Physics 28, 679 1957.

210. Li, B.; Kim, Y. S.; Mukundan, R.; Wilson, M. S.; Welch, C.; Fenton, J.; Borup, R. L., ECS Transactions 33, 913 2010.

211. Park, J.-S.; Krishnan, P.; Park, S.-H.; Park, G.-G.; Yang, T.-H.; Lee, W.-Y.; Kim, C.-S., Journal of Power Sources 178, 642 2008.

212. Mukoma, P.; Jooste, B.; Vosloo, H., Journal of Membrane Science 243, 293 2004.

213. Gebel, G.; Diat, O., Fuel Cells 5, 261 2005.

214. Gierke, T.; Munn, G.; Wilson, F., Journal of Polymer Science: Polymer Physics Edition 19, 1687 1981.

215. Gebel, G., Polymer 41, 5829 2000.

216. Takimoto, N.; Wu, L.; Ohira, A.; Takeoka, Y.; Rikukawa, M., Polymer 50, 534 2009.

217. Yang, B.; Manthiram, A., Journal of Power Sources 153, 29 2006.

218. Kreuer, K.; Ise, M.; Fuchs, A.; Maier, J., Le Journal de Physique IV 10, Pr7 2000.

219. Luu, D. X.; Cho, E.-B.; Han, O. H.; Kim, D., The Journal of Physical Chemistry B 113, 10072 2009.

220. Marx, C. L.; Caulfield, D. F.; Cooper, S. L., Macromolecules 6, 344 1973.

221. Reyna-Valencia, A.; Kaliaguine, S.; Bousmina, M., Journal of applied polymer science 98, 2380 2005.

222. He, S.; Jia, H.; Lin, Y.; Qian, H.; Lin, J., Polymer Composites 37, 2632 2016.

223. Sangeetha Rani, G.; Beera, M. K.; Pugazhenthi, G., Journal of Applied Polymer Science 1242012.

224. Kim, D. J.; Jo, M. J.; Nam, S. Y., Journal of Industrial and Engineering Chemistry 21, 36 2015.

225. Xu, X. L.; Zhang, G.; Wang, Z.; Zhao, C.; Na, H., Journal of applied polymer science 103, 4020 2007.

226. Kourasi, M.; Wills, R.; Shah, A.; Walsh, F., Electrochimica Acta 127, 454 2014.

227. Giordano, N.; Staiti, P.; Hocevar, S.; Arico, A., Electrochimica Acta 41, 397 1996.

228. Kozhevnikov, I. V., Chemical Reviews 98, 171 1998.

229. Maksimov, G. M., Russian Chemical Reviews 64, 445 1995.

230. Zhou, Y.; Yang, J.; Su, H.; Zeng, J.; Jiang, S. P.; Goddard, W. A., Journal of the American Chemical Society 136, 4954 2014.

231. Janik, M. J.; Campbell, K. A.; Bardin, B. B.; Davis, R. J.; Neurock, M., Applied Catalysis A: General 256, 51 2003.

232. Wu, Q.; Xie, X., Materials Science and Engineering: B 96, 29 2002.

233. Bardin, B. B.; Bordawekar, S. V.; Neurock, M.; Davis, R. J., The Journal of Physical Chemistry B 102, 10817 1998.

234. Knoth, W. H.; Harlow, R. L., Journal of the American Chemical Society 103, 4265 1981.

235. Kim, Y. S.; Wang, F.; Hickner, M.; Zawodzinski, T. A.; McGrath, J. E., Journal of Membrane Science 212, 263 2003.

236. Sekhon, S.; Park, J.-S.; Cho, E.; Yoon, Y.-G.; Kim, C.-S.; Lee, W.-Y., Macromolecules 42, 2054 2009.

237. Kusoglu, A.; Tang, Y.; Santare, M. H.; Karlsson, A. M.; Cleghorn, S.; Johnson, W. B., Journal of Fuel Cell Science and Technology 6, 011012 2009.

238. Scott, J. I.; Xue, X.; Wang, M.; Kline, R. J.; Hoffman, B. C.; Dougherty, D.; Zhou, C.; Bazan, G.; O'Connor, B. T., ACS applied materials & interfaces 8, 14037 2016.

239. Asano, N.; Aoki, M.; Suzuki, S.; Miyatake, K.; Uchida, H.; Watanabe, M., Journal of the American Chemical Society 128, 1762 2006.

240. Knauth, P.; Hou, H.; Bloch, E.; Sgreccia, E.; Di Vona, M., Journal of Analytical and Applied Pyrolysis 92, 361 2011.

241. Nagarale, R.; Shin, W.; Singh, P. K., Polymer Chemistry 1, 388 2010.

242. Jaafar, J.; Ismail, A.; Matsuura, T.; Nagai, K., Journal of membrane science 382, 202 2011.

243. Şengül, E.; Erdener, H.; Akay, R. G.; Yücel, H.; Baç, N.; Eroğlu, İ., international journal of hydrogen energy 34, 4645 2009.

244. Lee, C. H.; Hwang, S. Y.; Sohn, J. Y.; Park, H. B.; Kim, J. Y.; Lee, Y. M., Journal of power sources 163, 339 2006.

245. Kim, J. Y.; Mulmi, S.; Lee, C. H.; Park, H. B.; Chung, Y. S.; Lee, Y. M., Journal of membrane science 283, 172 2006.

246. Dong, H.; Chen, Y.-C.; Feldmann, C., Green Chemistry 17, 4107 2015.

247. Hunter, R. J., Foundations of colloid science; Oxford university press, 2001.

248. Yang, H.-C.; Hou, J.; Chen, V.; Xu, Z.-K., Journal of Materials Chemistry A 4, 9716 2016.

249. Reinholdt, M. X.; Kaliaguine, S., Langmuir 26, 11184 2010.

250. Catauro, M.; Renella, R.; Papale, F.; Ciprioti, S. V., Materials Science and Engineering: C 61, 51 2016.

251. Deng, Q.; Moore, R.; Mauritz, K. A., Journal of Applied Polymer Science 68, 747 1998.

252. León, A.; Reuquen, P.; Garín, C.; Segura, R.; Vargas, P.; Zapata, P.; Orihuela, P. A., Applied Sciences 7, 49 2017.

253. Órdenes-Aenishanslins, N. A.; Saona, L. A.; Durán-Toro, V. M.; Monrás, J. P.; Bravo, D. M.; Pérez-Donoso, J. M., Microbial cell factories 13, 90 2014.

254. Satterfield, M. B.; Majsztrik, P. W.; Ota, H.; Benziger, J. B.; Bocarsly, A. B., Journal of Polymer Science Part B: Polymer Physics 44, 2327 2006.

255. Das, I.; Chattopadhyay, S.; Mahato, A.; Kundu, B.; De, G., RSC Advances 6, 59030 2016.

256. Mokhtaruddin, S. R.; Mohamad, A. B.; Loh, K. S.; Kadhum, A. A. H., Malaysian Journal of Analytical Sciences 20, 670 2016.

257. Tazi, B.; Savadogo, O., Journal of New Materials for Electrochemical Systems 4, 187 2001.

258. Dimitrova, P.; Friedrich, K.; Stimming, U.; Vogt, B., Solid State Ionics 150, 115 2002.

259. Zhang, Y.; Zhang, H.; Bi, C.; Zhu, X., Electrochimica Acta 53, 4096 2008.

APPENDIX

Figure A1: Schematic of the impedance analyzer

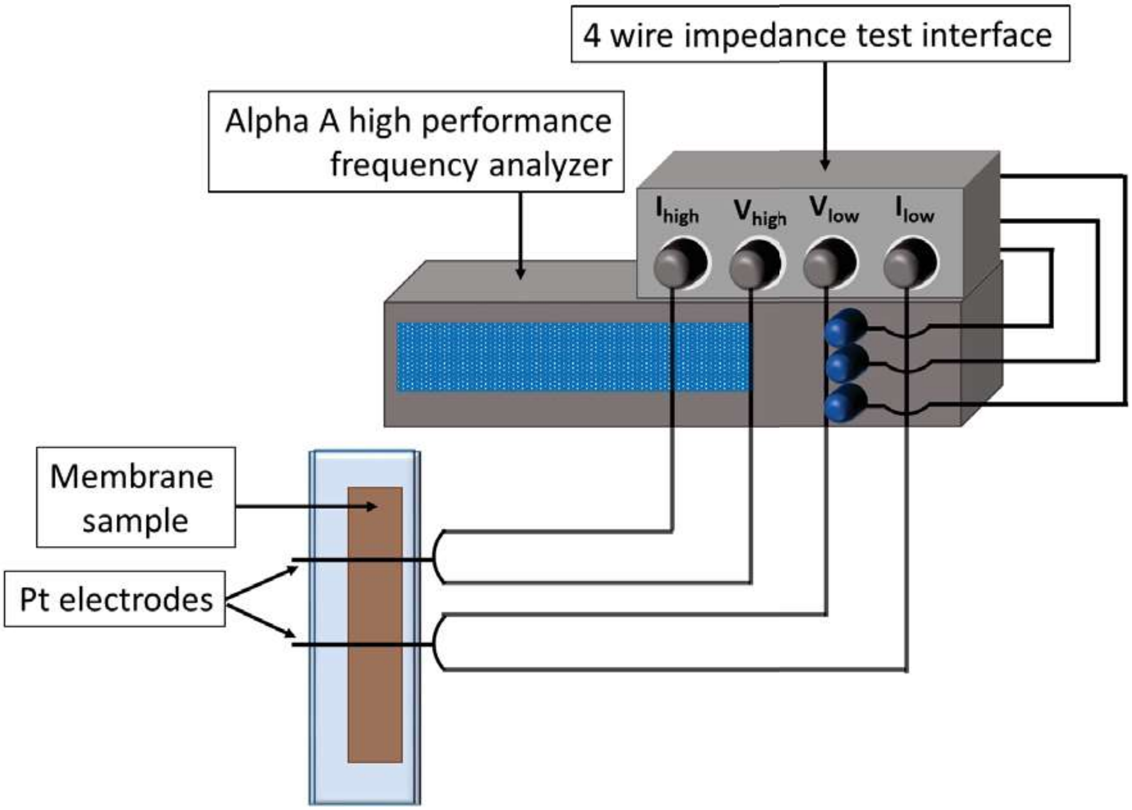

A comparison between the conductivity data given in literature for Nafion/HPA and SPEEK/HPA based membrane and the conductivity of the present membrane is given below. .

Table A1: Comparison of conductivity of PWA and PMA acid based membranes given in literature and the present work.

Membrane	**Additives**	**Proton Conductivity**	**Comments**	**Ref.**
Nafion	$H_3PW_{12}O_{40}$, $H_3PMo_{12}O_{40}$ $H_4SiW_{12}O_{40}$	(1.5-9.5) × 10^{-2} S cm^{-1} at 100 °C and 100% RH	Water uptake increased up to 95% with $H_3PMo_{12}O_{40}$	**257**
Nafion	$H_3PMo_{12}O_{40}$	3.5 × 10^{-1} S cm^{-1} at 80 °C and 100% RH	Decreased methanol permeation rate	**258**
SPEEK	$H_3PW_{12}O_{40}$, $H_3PMo_{12}O_{40}$ $Na_2HPW_{12}O_{40}$	More than 10^{-2} S cm−1 at 20 °C 1.1 × 10−1 S cm−1 at 120 °C and 55% RH		**81**
SPEEK	$Cs_{2.5}H_{0.5}PW_{12}O_{40}$ on Pt	5.3 × 10^{-2} S cm^{-1} at 60 °C and 100% RH	**Improved stability**	**259**
Membrane synthesized in the present study				
SPEEK	10% PWA	5.0 × 10^{-2} S cm^{-1} at 27 °C and 100% RH	**high retention of PWA in the membrane sample**	
SPEEK	10% PWA	1.1 × 10^{-1} S cm^{-1} at 60 °C and 100% RH		